Allosteric regulation of the bacterial K^+ channel KtrAB

Dissertation

zur Erlangung des Doktorgrades

der Naturwissenschaften

vorgelegt beim Fachbereich 14

Biochemie, Chemie und Pharmazie

der Johann Wolfgang Goethe-Universität

in Frankfurt am Main

von

Janina Stautz

aus Limburg an der Lahn

Frankfurt am Main, 2021

(D 30)

“I am a firm believer, that without speculation there is no good and original observation.”
(Charles Darwin)

Vom Fachbereich 14 Biochemie, Chemie und Pharmazie der
Johann Wolfgang Goethe-Universität als Dissertation angenommen.

Dekan: Prof. Dr. Clemens Glaubitz

1. Gutachterin: Prof. Dr. Inga Hänelt
2. Gutachter: Prof. Dr. Klaas Martinus Pos

Datum der Disputation:

Table of content

Declaration of scientific collaborations I

Summary V

Zusammenfassung XI

1 Introduction 1

1.1 Bacterial tolerance and intrinsic resistance to extreme environmental conditions 1

1.1.1 Attachment of bacteria to a surface and biofilm formation 1

1.1.2 Intrinsic resistance to antibiotics 2

1.1.3 Bacterial resistance to organic solvents 2

1.1.4 Adaptation to acidity and alkalinity 3

1.1.5 Bacterial life under extreme temperatures 3

1.1.6 Adaptation to osmotic stress 4

1.1.7 Regulation of osmoregulatory proteins by lipids 5

1.2 Cellular functions depend on the ion distribution across the membrane 7

1.3 Variety of bacterial potassium translocation systems fulfil different tasks in potassium homeostasis 8

1.4 General architecture and main features of K^+ channels 11

1.5 KcsA, the paradigm of K^+ channels 12

1.6 Regulation of K^+ channels by RCK domains 14

1.6.1 Proposed mechanisms of K^+ translocation meditated by RCK-regulated K^+ channel 17

1.6.2 Ca^{2+}-activated K^+ channel MthK 17

1.6.3 Ca^{2+}- and nucleotide-regulated K^+ channel GsuK 21

1.7 Superfamily of K^+ transporter (SKT) 23

1.7.1 Potassium uptake by the multiligand-regulation potassium channels KtrAB and TrkAH 26

1.7.2 H^+- and ATP-dependent K^+ translocating system TrkAH 26

1.7.3 KtrAB – the Na^+-, ATP- and $\Delta\Psi$-activated bacterial K^+ uptake system 30

2 Motivation and Objectives 35

3 Material 37
3.1 Chemicals and Consumables 37
3.2 Buffers, Solutions and Media 39
3.3 Bacterial strains, plasmids, and primers 42
4 Methods 47
4.1 Molecular biology 47
4.1.1 Isolation of genomic DNA from *B. subtilis* 47
4.1.2 Plasmid isolation from *E. coli* 47
4.1.3 Agarose gel electrophoresis 48
4.1.4 Polymerase chain reaction (PCR) for site-directed mutagenesis 48
4.1.5 FX cloning 49
4.1.6 In-Fusion® cloning to generate msfGFP fusion constructs 49
4.1.7 Cloning of pMUTIN4 containing $ktrA_{msfGFP}$ 50
4.2 Microbiology 51
4.2.1 Preparation of *E. coli* competent cells and transformation 51
4.2.2 Transformation of *Bacillus subtilis* cells 51
4.2.3 Verification of integration at the *amyE* locus by starch assay 52
4.2.4 Complementation in *B. subtilis* cells 52
4.2.5 Fluorescence microscopy of *B. subtilis* 52
4.2.5.1 Abolishment of membrane potential prior to microscopy 53
4.2.5.2 Time-lapse microscopy 54
4.2.6 Whole-cell K^+ uptake experiments in *E. coli* LB2003 cells 54
4.2.6.1 Potassium-free cells 54
4.2.6.2 Potassium uptake assay 55
4.3 Protein biochemistry 56
4.3.1 SDS PAGE 56
4.3.2 Western blot 57
4.3.3 Blue Native PAGE 57
4.3.4 Purification of 3C protease 57
4.3.5 Overproduction and purification of KtrA from *Vibrio alginolyticus* 58
4.3.6 Production and purification of KtrAB/KtrB and variants thereof 59

4.3.6.1 Protein overproduction 59
4.3.6.2 Solubilisation and purification of KtrAB/KtrB from isolated membranes 60
4.3.6.3 Production and purification of the native assembled KtrAB complex 60
4.3.6.4 Purification of the natively assembled complex via ATP agarose 61
4.3.7 PEGylation of KtrAB and KtrB 62
4.3.8 Reconstitution of KtrAB/KtrB into a lipidic environment 62
4.3.8.1 Preparation of *E. coli* polar lipids from *E. coli* total lipid extract 62
4.3.8.2 Preparation of different liposomes 62
4.3.8.3 BioBeads activation 63
4.3.8.4 Reconstitution of KtrB/KtrAB into pre-formed liposomes 63
4.3.8.5 Verification of reconstitution efficiency by resolubilisation 63
4.3.8.6 Production and purification of MSP2N2 64
4.3.8.7 Reconstitution into MSP2N2 nanodiscs 64
4.4 Biochemical and biophysical methods 65
4.4.1 ACMA assay 65
4.4.2 Isothermal titration calorimetry (ITC) 65
4.4.3 Scintillation proximity assay (SPA) 66
4.4.4 Differential scanning fluorimetry (DSF) 66
4.4.5 Thin layer chromatography (TLC) 67
4.4.6 Electron microscopy (EM) 68
4.4.6.1 Preparation of negative stained samples 68
4.4.6.2 Sample vitrification 68
4.4.6.3 Cryo-EM image recording and processing 69
4.4.6.4 Model building 69
4.4.7 Laser-induced Liquid Bead Ion Desorption-Mass Spectroscopy (LILBID-MS) 69
4.4.8 Electron paramagnetic resonance (EPR) spectroscopy 70
4.4.8.1 Purification and spin-labelling of KtrAB variants 70
4.4.8.2 Double electron-electron resonance (DEER) measurements 70

4.4.9 Molecular dynamics (MD) simulations of KtrB in the ADP-bound conformation 72

5 Results 73

5.1 Localisation and assembly of KtrAB in *B. subtilis* cells 73

5.1.1 Localisation of $KtrB_{msfGFP}$ within the membrane upon osmotic stress and different lipid environments 73

5.1.2 Assembly of the KtrAB complex in *B. subtilis* 76

5.1.3 Localisation of $KtrA_{msfGFP}$ expressed under a xylose-inducible promoter .. 79

5.1.3.1 Xylose screening for optimal expression levels 80

5.1.3.2 Effect of osmotic stress on the localisation of $KtrA_{msfGFP}$ in cells lacking endogenous uptake systems 81

5.1.3.3 Time-dependent localisation of $KtrA_{msfGFP}$-KtrB and the effect of membrane potential loss 83

5.2 Structural and functional analysis of the unique KtrAB complex in its native assembly 85

5.2.1 Overcoming the non-physiological ‘sandwich’ assembly of the KtrAB complex 85

5.2.1.1 PEGylation of free KtrB to avoid association to the KtrAB complex... 85

5.2.1.2 Mixing of purified KtrBNH3 with an excess of purified KtrAC3H 88

5.2.1.3 Pull-out purification of tag-less KtrB with KtrAC3H 89

5.2.2 Optimising single-particle cryo-EM analysis of the native KtrAB assembly... 93

5.2.2.1 Cryo-EM maps of the KtrAB complex..... 93

5.2.2.2 Cryo-EM map of KtrAB complex purified via ATP agarose..... 97

5.2.2.3 Conformational flexibility of the intramembrane gating loop in the dependence of nucleotides 100

5.2.3 Analysis of nucleotide binding to KtrA to illuminate regulation by ATP and ADP 102

5.2.3.1 Isothermal titration calorimetry to determine affinity of KtrA for ATP and ADP 102

5.2.3.2 Competitive nucleotide binding analysed by Scintillation Proximity Assay..... 103

5.2.3.3 Effect of nucleotides on the thermostability of KtrA 105

5.2.3.4 Nucleotide-induced conformational changes of KtrA 107
5.2.3.5 Excluding ATP hydrolysis during sample preparation 109
5.2.4 Detailed structural analysis of the high-resolution structure of KtrAB in the ADP-bound state 111
5.2.4.1 Regulation of K^+ flux by the selectivity filter and the intramembrane loop 112
5.2.4.2 Stabilisation of the inter-subunit connecting D1M2 helix 116
5.2.4.3 Identification of a new feature in the KtrAB complex: The N temini of KtrB 117
5.2.5 MD simulations of the KtrB dimer in a lipid environment 121
5.2.6 Conformational flexibility of the intramembrane gating loop in the dependence of lipids and KtrB's N terminus 123
5.2.7 Lipids and their role in regulating KtrAB 126
5.2.7.1 Effect of cardiolipin on the activity of KtrB 126
5.2.7.2 Reconstitution of KtrAB in nanodiscs for structural analysis 128
6 Discussion 131
6.1 New structural and functional insights lead to an adapted proposed gating mechanism for KtrAB from *V. alginolyticus* 131
6.2 Interaction of KtrB's N terminus with the membrane 134
6.3 Possible role of KtrB's N terminus in channel inactivation 137
6.4 Conservation of KtrBs' N termini within KtrAB homologues 140
6.5 New insights into KtrAB gating by nucleotide binding to the N lobes of the RCK ring 142
6.6 Features of KtrAB gating are shared among potassium channels 145
6.7 Outlook 148
7 Supplementary Information 151
8 References 165
9 Abbreviations 183
10 Acknowledgement ..... **Fehler! Textmarke nicht definiert.**
11 Eidesstattliche Erklärung ..... **Fehler! Textmarke nicht definiert.**
12 Curriculum Vitae ..... **Fehler! Textmarke nicht definiert.**

Declaration of scientific collaborations

Except where stated otherwise by references or acknowledgements, the work presented was generated by myself under the supervision of my advisor during my doctoral studies. All contributions from colleagues are explicitly referenced in the thesis. The material listed below was obtained in the context of collaborative research.

Figure 12: Distribution of $KtrB_{msfGFP}$-KtrA within the membrane comprising different lipid compositions, Figure 15: Expression of $KtrA_{msfGFP}$ under its native promoter. KtrB expression was induced by the addition of IPTG, Figure 17: Xylose screening for optimal expression levels & Figure 18: Distribution of $KtrA_{msfGFP}$ in different *B. subtilis* strain backgrounds and under different osmotic conditions: Fluorescence microscopy was performed in collaboration with Dr. Henrik Strahl, Centre for Bacterial Cell Biology (CBCB), Newcastle upon Tyne. Furthermore, *B. subtilis* strains and integration vectors were provided by Henrik Strahl. Cloning of GFP fusion constructs, strain construction, cell growth, imaging and analysis were performed by myself.

Figure 19: Time-lapse microscopy of *B. subtilis ktrAB::kan* expressing *$ktrA_{msfgfp}$-ktrB* and the effect of membrane potential loss: Time-lapse microscopy was set up by Dr. Henrik Strahl, Centre for Bacterial Cell Biology (CBCB), Newcastle upon Tyne. CCCP experiments of $KtrA_{msfGFP}$-KtrB were performed by myself, while control experiment was performed by James Grimshaw, Centre for Bacterial Cell Biology (CBCB), Newcastle upon Tyne.

Figure 20: PEGylation of $KtrB_{E449C}$ and $KtrAB_{E449C}$: Plasmids were prepared by Natalie Bärland, Institute of Biochemistry, Goethe-University Frankfurt. Expression, purification, PEGylation, SDS PAGE and Western blotting were performed by myself.

Figure 21: KtrAB assembly by mixing of individually purified KtrA and KtrB subunits: Plasmids pBKtrANH3, pBKtrBC3H and pBKtrBNH3 were prepared by Marina Schrecker, Institute of Biochemistry, Goethe-University. Protein production and purification were performed by myself.

Figure 22: Establishing a pull-out purification of tag-less KtrB with His-tagged KtrA to saturate all KtrB subunits within the membrane: LILBID-MS was performed by Dr. Jan Hoffmann, Institute of Physical and Theoretical Chemistry, Goethe-University Frankfurt. Negative staining electron microscopy was performed by Dr. Susann

Kaltwasser, Max Planck Institute of Biophysics, Frankfurt and Marina Schrecker, Institute of Biochemistry, Goethe-University. Protein production, purification, SEC, SDS PAGE and BN PAGE was performed by myself.

Figure 23: Large-scale purification of the native KtrAB complex assembly for cryo-EM analysis: Grid preparation and data collection Titan Krios G3i were performed with the help of Dr. Susann Kaltwasser, Max Planck Institute of Biophysics, Frankfurt and Marina Schrecker, Institute of Biochemistry, Goethe-University, Frankfurt. Classification and structural analysis were performed by Dr. Janet Vonck, Max Planck Institute of Biophysics, Frankfurt. Purification and sample preparation was performed by myself.

Figure 24: The resolution revolution in cryo-EM maps of the native KtrAB assembly & Figure 25: Cryo-EM structure of the native KtrAB complex assembly with a resolution of 2.8 Å: Grid optimisation and preparation as well as automated data acquisition at a Titan Krios G3i was performed with the help of Dr. Susann Kaltwasser, Max Planck Institute of Biophysics, Frankfurt. Data processing and structural analysis were performed by Dr. Janet Vonck, Max Planck Institute of Biophysics, Frankfurt. Protein purification and sample preparation was performed by myself.

Figure 26: Purification of KtrAB via ATP agarose for cryo-EM: Negative staining electron microscopy, cryo-EM grid preparation and data acquisition at a Titan Krios G3i were performed with the help of Dr. Susann Kaltwasser, Max Planck Institute of Biophysics, Frankfurt. Purification, sample preparation, SDS PAGE and DSF measurements were perfomed by myself.

Figure 27: Dynamics of the intramembrane loop of detergent-solubilised KtrAB in the dependence of nucleotides & Figure 41: Dynamics of the intramembrane loop of KtrAB in the dependence of KtrBs' N termini and a lipid environment: Protein purification, sample preparation was prepared together with Dr. Dorith Wunnicke-Kortz, Institute of Biochemistry, Goethe-University, Frankfurt, who performed the DEER measurements and data analysis.

Figure 31: 2D class averages of KtrA in the presence of different ligands: Sample preparation, 2D classification and evaluation of the data was performed by Celina Thiel, Institute of Biochemistry, Goethe-University, Frankfurt, under my supervision. Data collection was performed by Dr. Susann Kaltwasser, Max Planck Institute of Biophysics, Frankfurt.

Figure 32: Elimination of possible ATP hydrolysis during KtrAB sample preparation for cryo-EM: Purification of KdpFABC was performed by Jakob M. Silberberg, Institute of Biochemistry, Goethe-University, Frankfurt. Cryo-EM grid preparation and data acquisition at a Titan Krios G3i were performed with the help of Dr. Susann Kaltwasser, Max Planck Institute of Biophysics, Frankfurt. Data processing and structural analysis were performed by Dr. Janet Vonck, Max Planck Institute of Biophysics, Frankfurt. Purification of KtrAB and TLC were performed by myself.

Figure 35: K^+ uptake by *E. coli* LB2003 cells producing KtrAB pore variants: Several replicates of uptake experiments were performed by David Griwatz, Institute of Biochemistry, Goethe-University, Frankfurt, under my supervision. Cloning of variant was performed by myself. Initial measurements were performed by myself.

Figure 38: Structural effect of N terminus deletion on the KtrAB complex: Sample preparation was performed by David Griwatz, Institute of Biochemistry, Goethe-University, Frankfurt, during his Master thesis under my supervision. Grid preparation and data acquisition at a Titan Krios G3i were performed by myself with the help of Dr. Susann Kaltwasser, Max Planck Institute of Biophysics, Frankfurt. Data analysis, processing and model building were performed by Dr. Janet Vonck, Max Planck Institute of Biophysics, Frankfurt.

Figure 39: K^+ uptake by KtrAB variants with modified N termini: Cloning of variants and uptake measurements were performed in triplicates by David Griwatz and his Bachelor student Katja Ohlemüller, Institute of Biochemistry, Goethe-University, Frankfurt.

Figure 40: All-atom MD simulations of a KtrB dimer in a lipid environment: MD simulation and analysis was performed by Dr. Ahmad Reza Mehdipour, Center for Molecular Modeling, Ghent University.

Figure 43: Reconstitution of KtrAB into MSP2N2 nanodiscs for structural analysis: Grid preparation and data acquisition at a Titan Krios G3i were performed by myself with the help of Dr. Susann Kaltwasser, Max Planck Institute of Biophysics, Frankfurt. Data analysis and processing were performed by Dr. Janet Vonck, Max Planck Institute of Biophysics, Frankfurt. Purification, reconstitution, and sample preparation were performed by myself.

Whenever a figure, table or text is identical to a previous publication, it is stated explicitly in the thesis that copyright permission and/or co-author agreement has been obtained.

Summary

K^+ homeostasis in bacteria is essential for the survival of an individual cell and of a bacterial community. It plays a role in osmoregulation, pH homeostasis, regulation of protein synthesis, enzyme activation, membrane potential adjustment and electrical signalling. A key player in the adaptation to hyperosmotic stress and for daily maintenance of potassium (K^+) homeostasis is the bacterial K^+ channel KtrAB. The system is present in Gram-positive bacteria like *Bacillus subtili*s and Gram-negative bacteria like *Vibrio alginolyticus*, in which it functions as an ATP-, Na^+- and ΔΨ-dependent K^+ uptake system. KtrAB consists of the transmembrane subunit KtrB, which forms a functional dimer in the membrane with two individual pores, and the cytosolic regulatory subunit KtrA, which forms a homooctameric gating ring that associates to the KtrB dimer. KtrB belongs to the superfamily of potassium transporter (SKT), which exist in all domains of life, except animals. Members of the SKT most likely evolved from 2-TM potassium channels like KcsA by gene duplication and gene fusion. Therefore, a KtrB protomer consists of four non-identical, covalently fused M1PM2 motifs, each of which is made of two transmembrane (M) helices that are connected by the pore helix and the pore loop (P). The four motifs, referred to as D1-D4, are pseudo-fourfold symmetrically arranged around a central axis forming the pore. The pore helices form a reduced selectivity filter, which plays a crucial role in ion selectivity. Just below the SF, the intramembrane loop of helix D3M2 and a highly conserved arginine of D4M2 regulate ion flux as gate. Subunit KtrA belongs to the family of regulator of K^+ conductance (RCK) proteins. By cytosolically assembling to KtrB, it confers K^+ selectivity, Na^+ and ATP dependency as well as an increased uptake velocity to the system. The KtrA ring binds ATP and ADP to the conserved Rossman fold in a competitive manner, which induces conformational changes to a square-shaped and oval-shaped conformation, respectively. The conformational changes in the octameric ring result in channel activation and inactivation, respectively. The interaction between the KtrB dimer and the octameric KtrA is mediated by so-called tip contacts of a helical hairpins at the end of helices D1M2 with KtrAs in the ATP-bound conformation. This interaction gets more pronounced in the ADP-bound conformation, as the D1M2 helices extend and protrude into the KtrA ring. Furthermore, the C termini of the KtrB dimer interact with KtrA. However, it is so far not understood how conformational changes in KtrA are transmitted to the pore-forming subunit KtrB, allowing the opening of the gate. In other RCK-gated K^+ channel, like MthK and GsuK, the RCK domains are covalently fused to the transmembrane domains, which is why conformational changes in the RCK domain are suggested to be communicated via a flexible linker. Since KtrAB lacks this linker, it is not surprising, that an adapted gating mechanism applies for the system. Unfortunately, all

available data does not allow to elucidate the gating mechanism in molecular detail. Therefore, the KtrAB complex was further investigated in this thesis, addressing complex localisation and assembly as well as channel gating by in vivo and in vitro approaches.

As a membrane-embedded protein, KtrB is surrounded by lipids, which can have an effect on the localisation as well as on the activity of the protein. To analyse, whether the localisation of the complex depends on the lipid composition or osmotic conditions, the distribution of KtrAB within the membrane was investigated in *B. subtilis* by applying osmotic stress or using strains that either lack cardiolipin (CL) or phosphatidylethanolamine (PE). To visualise the localisation of KtrAB within the membrane of *B. subtilis* cells, KtrB was fused to msfGFP and fluorescence microscopy was performed. Microscopy revealed that at all tested conditions the fluorescently-labelled variant of the KtrAB complex was homogenously distributed throughout the membrane. While this excluded that the system co-localises with lipid patches, it remains elusive whether lipids influence the activity of KtrAB in more general. Fluorescence microscopy was further used to study, whether the interaction and assembly of the two non-covalently linked subunits, KtrA and KtrB, is a dynamic process. For this purpose, the distribution of $KtrA_{msfGFP}$-KtrB was analysed under various conditions and in different cell backgrounds lacking endogenous K^+ uptake systems like KtrAB, KtrCD and KimA. Although it was expected that KtrA would localise at the membrane interacting with KtrB, $KtrA_{msfGFP}$ was diffusely distributed throughout the whole cytosol at all tested conditions. Time-lapse microscopy was performed to investigate complex assembly/disassembly over time. Interestingly, after 8 h the diffuse pattern of fluorescence signal changed to small bright clusters located towards the membrane. However, this observation was uncovered as a non-specific artifact upon depolarisation, which is why none of the microscopic attempts allowed to identify the assembly of the two subunits. The reason remains elusive as the msfGFP-fused construct was shown to functionally assemble in *Escherichia coli*.

To better understand the molecular basis of complex assembly and the mechanism of channel gating, KtrAB was further investigated by in vitro approaches. Therefore, KtrAB from *V. alginolyticus* was heterologous produced in and purified from *E. coli* cells. At first, the purification was optimised, as so far, a non-physiological $KtrB_2A_8B_2$ assembly, called ’sandwich’ assembly, was purified. This assembly hampered structural and functional approaches, particularly the reconstitution of the complex into membrane scaffolds. Therefore, different strategies were tested to avoid the attachment of a second KtrB dimer. While sterically hindering the assembly via PEGylation of free KtrB and mixing of individually purified KtrB with an excessive amount of KtrA was unsuccessful, a pull-out strategy, in which $KtrB_2$ in the membrane was saturated with $KtrA_8$ prior solubilisation, resulted in the purification of the intact $KtrB_2A_8$ complex. The correct assembly was confirmed by SEC, blue native PAGE, negative staining EM, and LILBID-MS. An initial cryo-EM dataset of the native assembly resulted in 7 Å resolution density map, but to

further illuminate molecular details of the system a higher resolution was required. Therefore, sample and grid quality were improved, which finally resulted in an increased resolution of 2.8 Å. While all samples were prepared in the presence of excessive ATP and $MgCl_2$ to stabilise the active, ATP-bound conformation, all six structures obtained in this thesis were obtained in the ADP-bound state, including the extended D1M2 helices and the oval-shaped KtrA ring. Even after purification via ATP agarose, the obtained 2.5 Å resolution structure of KtrAB still adopted the ADP-bound conformation. The high-resolution map unambitiously allowed to identify ADP bound to the N lobes of KtrA. The overall binding was similar to what was previously observed in an X-ray structure of KtrA from *B. subilits*, yet the coordination of the phosphates from the ADP molecules is slightly different. It is accomplished by the positive charges of an arginine and a magnesium ion, while previously no Mg^{2+}, but other arginines were described to be involved. The lack of ATP binding was further confirmed by pulsed EPR measurements, for which a spin label (MTS) was introduced into the intramembrane loop. As conformational changes in KtrA upon ATP binding should change the flexibility of the intramembrane loop for gating, a shift in the distance distribution was expected when comparing the presence of ADP or ATP. However, nearly identical distance distributions were observed for detergent-solubilised KtrAB in the presence of ADP and ATP. Therefore, the nucleotide binding to KtrA was further analysed using different techniques. Binding affinities of ADP and ATP to purified KtrA were determined by ITC, revealing similar affinities in the low micromolar range, with a slight preference of ADP (K_d= 2.4 µM) over ATP (K_d= 3.4 µM). The binding behaviour was further assessed by SPA, performing a competition assay to determine IC_{50} values for the different nucleotides. In line with the ITC data, the IC_{50} values were in the low micro molar range, indicating that both nucleotides should be replaceable by one another. A first fundamental difference upon the binding of the two nucleotides to KtrA was observed in DSF measurements, analysing the thermostability of the KtrA ring. While an increase in melting temperature was determined in the presence of both nucleotides, the presence of ADP caused a much stronger stabilisation than ATP (increase of 20°C and 8°C, respectively). Nevertheless, also in this approach both nucleotides could be exchanged for one another, as demonstrated by shifting the melting temperatures from one complex to the other. As each individual approach showed that exchange and binding of nucleotides to the KtrA ring is possible, negative staining EM was performed to analyse, whether the binding induces the previously described conformational changes. In fact, in the presence of ATP and $MgCl_2$, the majority of the particles adopted the square-shaped conformation, while in the presence of ADP and $MgCl_2$ or only $MgCl_2$, the KtrA particles were predominantly in the oval-shaped conformation. Therefore, it was even more surprising that all structural approaches of KtrAB resulted in an ADP-bound conformation. To exclude, that the supplied ATP was hydrolysed during the sample preparation, ATPase activity of the purified KtrAB sample was eliminated, and a sample in the presence of the

non-hydrolysable ATP analogue AMP-PCP was analysed by cryo-EM. Surprisingly, the structure was again obtained in the ADP-bound conformation and by thin-layer chromatography it was shown, that the purified complex is most likely co-purified with ADP. Altogether, it appears, that while the isolated KtrA ring can bind both nucleotides resulting in different conformations, the presence of KtrB in the KtrAB complex, does not allow the ATP-bound, active conformation in the detergent-solubilised sample, indicating that an additional factor is required to exchange ADP to ATP during activation.

The obtained high resolution, however, allowed to resolve molecular details of the inactive state that were so far unknown. The selectivity filter and the intramembrane loop were well resolved and a K^+ could be identified er at a position corresponding to S3 in canonical K^+ selectivity filters. Below the selectivity filter, the intramembrane loop adopted a closed conformation, mainly stabilised by interactions with the D1M2 helix, blocking the pore for ion flux. A conserved lysine (K325) was shown to form a salt bridge with the C terminus of the neighbouring KtrB subunit, further sterically blocking the pore. The gating arginine (R427) is coordinated by residue Q99, forming an additional electrostatic barrier in the pore. Both residues, K325 and Q99 have been shown to be important for the stabilisation of the closed pore, as their substitution to an alanine increased the uptake velocity. Further, the coordination of the extended D1M2 helices was shown to be established via several hydrophobic and hydrophilic interaction with the N lobes of KtrA and an inter-subunit salt bridge between R117 in KtrB and E38 in KtrA. Interestingly, in all obtained cryo-EM maps, so far unknown densities near the extended D1M2 helices, lying flat on top of the KtrA ring, were observed, which were identified as the N termini of KtrB. The N termini extensively interact with both the N lobes of KtrA and the extended D1M2 helices of KtrB. A first hypothesis that this interaction network stabilised the ADP-bound, inactive conformation was disproved, as a structure of a variant with residues 2-19 of the N termini deleted did not affect the ADP-bound conformation. However, whole-cell uptake experiments revealed that the deletion of the N terminus has a drastic effect on the activity of the KtrAB complex. In the absence of the N termini, the uptake velocity (V_{max}) was significantly reduced from 190 $nmol*mg^{-1}*min^{-1}$ to 46 $nmol*mg^{-1}*min^{-1}$ when compared to wildtype KtrAB. A more detailed analysis showed that mutating a cluster of positively charged residues (K16, R17, K19, K21) reduced the V_{max} already to half the velocity of the wildtype, while mutating a hydrophobic patch at the N terminus did not show a reduction in V_{max}. As especially the positive charges appeared to be crucial for the activity of KtrAB it was speculated that, similar to what is known for other osmoprotective systems like OpuA, BetP or ProP, the N termini interact with the negatively charged headgroups of the lipid bilayer, inducing the active, conductive state triggered by the binding of ATP. Preliminary MD simulations confirm the interaction of the N termini with the membrane. To further support this hypothesis, the flexibility of the intramembrane loop of KtrAB reconstituted in liposomes was investigated by another set of pulsed EPR measurements.

In fact, in the presence of lipids a nucleotide-dependent flexibility of the intramembrane loop was observed. In the presence of ADP, a mean distance distribution at 3.3 nm was detected. This distance distribution was comparable to the previously mentioned measurements of KtrAB in detergents micelles and most likely corresponds to the closed conformation. In contrast, in the presence of ATP the mean distance distribution was shifted to 3.7 nm, suggesting a conformational change to the open conformation. To understand the role of the N termini in this regard, the same measurements were repeated in the absence of the N termini. Interestingly, similar to the detergent-solubilised sample, no clear shift in the mean distance distribution could be observed in the presence of ATP, indicating that the N termini together with the membrane and ATP are required for the conformational transition to the open state.

To better understand the role of lipids, KtrB was reconstituted into *E. coli* polar lipid liposomes supplemented with different concentrations of CL. An ACMA-based flux assay revealed that increasing concentrations of CL increased the flux rate of K^+, showing an influence of lipids on KtrB's activity for the first time. As this supported the idea that for activation of KtrAB a lipid environment is required, the reconstitution of the complex into nanodiscs was established for further structural analysis. After initial optimisation, a cryo-EM dataset in the presence of ATP and $MgCl_2$ resulted in a first low-resolution density map (6 Å). Although the resolution was rather low, it was obvious that the overall architecture again resembled the ADP-bound conformation. However, the MSP was tightly wrapped around the membrane helices, missing the lipid surface which most likely is required for the interaction of the N terminus.

Altogether, the presented data clearly showed that the activation of the KtrAB complex does not only require the exchange of ADP to ATP in the KtrA ring. Instead, an allosteric network combining nucleotide-dependent conformational changes and the interaction of the identified N termini with the membrane is necessary to allow K^+ flux via KtrAB.

Zusammenfassung

Die K^+-Homöostase ist für das Überleben einer einzelnen Zelle und einer bakteriellen Gemeinschaft von wesentlicher Bedeutung. Hierbei ist K^+ in einer Vielzahl lebenswichtiger Prozesse, wie der Osmoregulation, der pH-Homöostase, der Regulierung der Proteinsynthese, der Enzymaktivierung, der Anpassung des Membranpotenzials und der elektrischen Signalübertragung, involviert. Bei der Anpassung an hyperosmotischen Stress und bei der täglichen Aufrechterhaltung der Kalium-Homöostase spielt wiederum der bakterielle K^+-Kanal KtrAB eine Schlüsselrolle. Das System kommt sowohl in Grampositiven Bakterien, wie *Bacillus subtilis*, als auch Gramnegativen Bakterien, wie *Vibrio alginolyticus,* vor, in welchen es als ATP-, Na^+- und $\Delta\Psi$-abhängiges K^+-Aufnahmesystem funktioniert. KtrAB besteht aus der Transmembran-Untereinheit KtrB, die in der Membran als funktionelles Dimer zwei individuellen Poren bildet, und der zytosolisch-regulatorischen Untereinheit KtrA, die einen homooktameren Ring bildet und mit dem KtrB-Dimer assoziiert. KtrB gehört zur Superfamilie der Kaliumtransporter (SKT), die in allen Lebensbereichen, mit Ausnahme der Tiere, vorkommen. Mitglieder der SKT haben sich wahrscheinlich aus 2-TM-Kaliumkanälen wie KcsA durch Genduplikation und Genfusion entwickelt. Daher besteht ein KtrB-Protomer aus vier nicht identischen, kovalent fusionierten M1PM2-Motiven, von denen jedes aus zwei Transmembranhelices (M) besteht, die durch die Porenhelix und die Porenschleife (P) verbunden sind. Diese vier Motive, die als D1-D4 bezeichnet werden, sind um eine zentrale Achse angeordnet, und bilden die Poren. Die Porenhelices formen einen reduzierten Selektivitätsfilter (SF), der eine entscheidende Rolle bei der Ionenselektivität spielt. Direkt unterhalb des SF regulieren die Intramembranschleife von Helix D3M2 und ein hochkonserviertes Arginin von Helix D4M2 den Ionenfluss. Die Untereinheit KtrA gehört zur Familie der RCK-Proteine (Regulatoren von K^+ Leitfähigkeit). Durch die Interaktion von KtrA mit KtrB wird das KtrAB System selektiv für K^+ und translozíert dieses nur in Abhängigkeit von Na^+ und ATP und mit einer höheren Aufnahmegeschwindigkeit. Der oktamere KtrA-Ring bindet ATP und ADP kompetitiv an die konservierte Rossman-Faltung, wodurch eine Konformationsänderungen in eine quadratische bzw. ovale Konformation ausgelöst wird. Dies wiederum führt zu einer Aktivierung oder Inaktivierung des Kanals. Beide Untereinheiten interagieren zum einen über die C-Termini von KtrB und zum anderen über die D1M2-Helices, die je nach gebundenem Nukleotid entweder eine helikale Haarschleife bilden oder eine elongierte Konformation einnehmen, miteinander. Bislang ist jedoch nicht geklärt, wie Konformationsänderungen in KtrA auf die porenbildende Untereinheit KtrB übertragen werden. In anderen RCK-gesteuerten K^+-Kanälen, wie MthK und GsuK, sind die RCK-Domänen kovalent an die Transmembrandomänen fusioniert. Deshalb wird

angenommen, dass Konformationsänderungen in der RCK-Domäne über einen flexiblen Linker übertragen werden. Da dieser Linker in KtrAB fehlt, ist es nicht überraschend, dass für das System ein angepasster Regulationsmechanismus gilt. Leider verwehren die verfügbaren Daten, eine detaillierte Aufklärung des Regulationsmechanismus. Daher wurde der KtrAB-Komplex in dieser Arbeit weiter untersucht, wobei die Lokalisierung und die Assemblierung des Komplexes sowie das Regulierung des Kanals mit Hilfe von in vivo- und in vitro-Ansätzen analysiert wurden.

Als Membranprotein ist KtrB von Lipiden umgeben, die sowohl die Lokalisierung als auch die Aktivität des Proteins beeinflussen können. Um zu analysieren, ob die Lokalisierung des Komplexes von der Lipidzusammensetzung oder den osmotischen Bedingungen abhängt, wurde die Verteilung von KtrAB innerhalb der Membran von *B. subtilis* mittels Fluoreszenzmikroskopie untersucht. Dazu wurden die Zellen osmotischem Stress ausgesetzt oder es wurden *B. subtilis* Stämme verwendet, denen entweder Cardiolipin (CL) oder Phosphatidylethanolamin (PE) fehlt. Die Mikroskopie ergab, dass der KtrAB-Komplex unter allen getesteten Bedingungen homogen in der Membran verteilt war. Dies schließt zwar aus, dass das System mit Clustern von Lipiden zusammen lokalisiert, aber es bleibt unklar, ob Lipide die Aktivität von KtrAB im Allgemeinen beeinflussen. Zusätzlich wurde analysiert, ob es sich bei der Interaktion und der Assemblierung der beiden nicht kovalent verbundenen Untereinheiten KtrA und KtrB um einen dynamischen Prozess handelt. Zu diesem Zweck wurde die Verteilung von $KtrA_{msfGFP}$ unter verschiedenen Bedingungen und in verschiedenen Zellhintergründen, denen endogene K^+-Aufnahmesysteme, wie KtrAB, KtrCD und KimA, fehlen, analysiert. Obwohl erwartet wurde, dass KtrA an der Membran lokalisiert ist, um mit KtrB zu interagiert, war $KtrA_{msfGFP}$ über das gesamte Zytosol verteilt. Mit Hilfe der Zeitraffermikroskopie wurde die Assemblierung des Komplexes in Abhängigkeit der Zeit beobachtet. Interessanterweise veränderte sich das diffuse Muster des Fluoreszenzsignals nach 8 Stunden zu kleinen hellen Clustern, die sich in der Nähe der Membran befanden. Diese Beobachtung wurde jedoch als unspezifisches Artefakt der Depolarisierung aufgedeckt, weshalb keiner der mikroskopischen Versuche die Assemblierung der beiden Untereinheiten identifizieren konnte. Der Grund dafür bleibt rätselhaft, da sich das mit msfGFP fusionierte Konstrukt in *Escherichia coli* funktionell assemblierte.

Um die molekulare Grundlage des Komplexaufbaus und den Regulationsmechanismus besser zu verstehen, wurde KtrAB mit in vitro-Ansätzen weiter untersucht. Dazu wurde KtrAB aus *V. alginolyticus* heterolog in *E. coli* Zellen produziert und gereinigt. Zunächst wurde die Reinigung optimiert, da bisher eine unphysiologische $KtrB_2A_8B_2$-Assemblierung, gereinigt wurde. Diese Anordnung erschwerte strukturelle und funktionelle Ansätze, insbesondere die Rekonstitution des Komplexes in Membranumgebungen. Daher wurden verschiedene Strategien getestet, um die Anlagerung eines zweiten KtrB-Dimers zu verhindern. Während die sterische Verhinderung der Assemblierung durch PEGylierung

von freiem KtrB und das Mischen von gereinigtem KtrB mit einer Überschuss an KtrA erfolglos war, führte eine Pull-out-Strategie zur Reinigung des intakten $KtrB_2A_8$-Komplexes. Ein erster Kryo-EM-Datensatz des nativ-assemblierten Komplex ergab eine 3D-Elektronendichte mit einer Auflösung von 7 Å. Um jedoch weitere molekulare Details des Systems zu beleuchten, war eine höhere Auflösung erforderlich. Daher wurde die Qualität der EM-Proben verbessert, was schließlich zu einer erhöhten Auflösung von 2.8 Å führte. Während alle Proben in Gegenwart von überschüssigem ATP und $MgCl_2$ hergestellt wurden, um die aktive, ATP-gebundene Konformation zu stabilisieren, wurden alle sechs in dieser Arbeit erhaltenen Strukturen in der ADP-gebundenen Konformation beobachtet. Selbst nach der Reinigung über ATP-Agarose nahm die erhaltene 2.5 Å-Struktur immer noch die ADP-gebundene Konformation an. Die hochauflösenden 3D-Elektronendichte erlaubten es, an KtrA gebundenes ADP zu identifizieren, wodurch klar wurde, dass keine ATP-Bindung stattgefunden hat. Dies wurde zusätzlich im Zuge von gepulsten ESR-Messungen bestätigt, bei denen ein Spin-Label (MTS) in die Intramembranschleife eingebracht wurde. Da die Konformationsänderungen in KtrA bei ATP-Bindung die Flexibilität der Intramembranschleife für die Regulation verändern sollten, wurde eine Verschiebung der Abstandsverteilung, in Abhängigkeit von ADP und ATP, erwartet. Allerdings wurden nahezu identische Abstandsverteilungen für den solubilisierten KtrAB Komplex in Gegenwart von ADP und ATP beobachtet. Um den Effekt der Nukleotidbindung an KtrA besser zu verstehen, wurde mit verschiedenen Techniken die Bindung von ATP und ADP analysiert. Die Bindungsaffinitäten von ADP und ATP an gereinigtes KtrA wurden mittels ITC bestimmt und ergaben ähnliche Affinitäten im niedrigen mikromolaren Bereich, mit einer leichten Bevorzugung von ADP (K_d= 2,4 µM) gegenüber ATP (K_d= 3,4 µM). Das Bindungsverhalten wurde, zur Bestimmung der IC_{50}-Werte für die verschiedenen Nukleotide, weiter durch SPA analysiert. In Übereinstimmung mit den ITC-Daten lagen die IC_{50}-Werte im niedrigen mikromolaren Bereich, was darauf hindeutet, dass beide Nukleotide miteinander austauschbar sein sollten. Ein erster grundlegender Unterschied bei der Bindung der beiden Nukleotide an KtrA wurde bei DSF-Messungen beobachtet, bei denen die Thermostabilität des KtrA-Rings analysiert wurde. Während in Anwesenheit beider Nukleotide die Schmelztemperatur stieg, bewirkte die Anwesenheit von ADP eine wesentlich stärkere Stabilisierung als ATP. Dennoch konnten auch bei diesem Ansatz beide Nukleotide gegeneinander ausgetauscht werden. Da jeder einzelne Ansatz zeigte, dass der Austausch und die Bindung von Nukleotiden an den KtrA-Ring möglich ist, wurde mittels Negativkontrastierung und anschließender EM analysiert, ob die Bindung die zuvor beschriebenen Konformationsänderungen hervorruft. Tatsächlich war die Mehrzahl aller Partikel in Gegenwart von ATP und $MgCl_2$ in der quadratischen Konformation, während die KtrA-Partikel in Gegenwart von ADP und $MgCl_2$ oder nur $MgCl_2$ überwiegend die ovale Konformation aufwiesen. Umso überraschender war es, dass alle Strukturen von KtrAB auf eine ADP-gebundene Konformation

hinausliefen. Um auszuschließen, dass das zugeführte ATP während der Probenpräparation hydrolysiert wurde, wurde die ATPase-Aktivität der gereinigten KtrAB-Probe ausgeschlossen und eine Probe in Gegenwart des nicht hydrolysierbaren ATP-Analogons AMP-PCP mittels Kryo-EM analysiert. Überraschenderweise wurde die Struktur wieder in der ADP-gebundenen Konformation beobachtet. Mit Hilfe einer Dünnschichtchromatographie wurde gezeigt, dass ADP höchstwahrscheinlich zusammen mit dem Komplex gereinigt wird. Insgesamt zeigt sich, dass der KtrAB-Komplex im Gegensatz zum isolierten KtrA Ring, die ATP-gebundene, aktive Konformation nicht zulässt, was darauf hindeutet, dass ein zusätzlicher Faktor für den Austausch von ADP gegen ATP zur Aktivierung des KtrAB-Komplexes erforderlich ist.

Die erzielte hohe Auflösung ermöglichte es jedoch, molekulare Details des inaktiven Zustands zu klären, die bisher unbekannt waren. Der Selektivitätsfilter und die Intramembranschleife wurden gut aufgelöst, und ein K^+ konnte im Selektivitätsfilter an einer Position identifiziert werden, die der S3 Position in kanonischen K^+-Selektivitätsfiltern entspricht. Unterhalb des Selektivitätsfilters nahm die Intramembranschleife eine geschlossene Konformation an, die hauptsächlich durch Wechselwirkungen mit der D1M2-Helix stabilisiert wird. Es wurde gezeigt, dass ein konserviertes Lysin (K325) eine Salzbrücke mit dem C-Terminus der benachbarten KtrB-Untereinheit bildet, wodurch die Pore weiter sterisch blockiert wird. Das konservierte Arginin (R427) wird durch den Rest Q99 koordiniert und bildet eine zusätzliche elektrostatische Barriere in der Pore. Es konnte gezeigt werden, dass beide Reste, K325 und Q99, wichtig für die Stabilisierung der geschlossenen Pore sind, da ihre Substitution die Aufnahmegeschwindigkeit erhöht. Außerdem wurde gezeigt, dass die Koordination der elongierten D1M2-Helices über mehrere hydrophobe und hydrophile Wechselwirkungen mit KtrA erfolgt. Außerdem wird eine Salzbrücke zwischen R117 in KtrB und E38 in KtrA gebildet. Interessanterweise wurden in allen erhaltenen 3D- Elektronendichten bisher unbekannte Dichten in der Nähe der elongierten D1M2-Helices, die flach auf dem KtrA-Ring liegen, beobachtet. Diese wurden als N-Termini von KtrB identifiziert. Die N-Termini interagieren umfassend sowohl mit KtrA als auch mit den elongierten D1M2-Helices von KtrB. Eine erste Hypothese, dass dieses Interaktionsnetzwerk die ADP-gebundene, inaktive Konformation stabilisiert, wurde widerlegt, da die Struktur einer Variante, bei der die Reste 2-19 der N-Termini entfernt wurden, die ADP-gebundene Konformation nicht beeinflusste. Experimente zur K^+-Aufnahme in Zellen zeigten jedoch, dass die Deletion des N-Terminus drastische Auswirkungen auf die Aktivität des KtrAB-Komplexes hat. In Abwesenheit des N-Terminus war die Aufnahmegeschwindigkeit (V_{max}) im Vergleich zum Wildtyp-KtrAB deutlich von 190 $nmol*mg^{-1}*min^{-1}$ auf 46 $nmol*mg^{-1}*min^{-1}$ reduziert. Eine detailliertere Analyse zeigte, dass die Mutation eines Clusters von positiv geladenen Resten (K16, R17, K19, K21) den V_{max}-Wert bereits auf die Hälfte der Geschwindigkeit des Wildtyps reduzierte. Die Mutation eines hydrophoben Bereichs am N-Terminus zeigte hingegen keine Verringerung des

V_{max}-Wertes. Da insbesondere die positiven Ladungen für die Aktivität von KtrAB entscheidend zu sein scheinen, wurde spekuliert, dass, ähnlich wie bei anderen osmoprotektiven Systemen, wie z.B. OpuA, BetP oder ProP, die N-Termini von KtrB mit den negativ geladenen Kopfgruppen der Lipiddoppelschicht interagieren und zusammen mit ATP den aktiven, leitfähigen Zustand auslösen. Vorläufige MD-Simulationen bestätigen die Interaktion der N-Termini mit der Membran. Um diese Hypothese zusätzlich zu untermauern, wurde durch eine weitere Reihe von gepulsten ESR-Messungen die Flexibilität der Intramembranschleife von KtrAB, welches in Liposomen rekonstituiert wurde, untersucht. In der Tat wurde in Gegenwart von Lipiden eine nukleotidabhängige Flexibilität der Intramembranschleife beobachtet. In Anwesenheit von ADP wurde eine mittlere Abstandsverteilung von 3.3 nm festgestellt, welche höchstwahrscheinlich der geschlossenen Konformation entspricht. Im Gegensatz dazu war die mittlere Abstandsverteilung in Gegenwart von ATP auf 3.7 nm verschoben, was auf eine Konformationsänderung zur offenen Konformation hindeutet. Um die Rolle der N-Termini in diesem Zusammenhang zu verstehen, wurden die gleichen Messungen in Abwesenheit der N-Termini wiederholt. Interessanterweise konnte hier in Gegenwart von ATP keine deutliche Verschiebung der mittleren Abstandsverteilung beobachtet werden. Das lässt darauf schließen, dass die N-Termini, zusammen mit der Membran und ATP, für den Konformationsübergang in den offenen Zustand erforderlich sind.

Um die Rolle der Lipide besser zu verstehen, wurde KtrB in Liposomen rekonstituiert, die aus polaren *E. coli* Lipiden in Kombination mit verschiedenen CL-Konzentrationen hergestellt wurden. Ein ACMA-basierter K^+-Translokations-Assay zeigte, dass steigende CL-Konzentrationen die Translokationsrate von K^+ erhöhten. Hiermit wurde zum ersten Mal ein Einfluss der Lipide auf die Aktivität von KtrB gezeigt. Da dies die Idee unterstützt, dass für die Aktivierung von KtrAB eine Lipidumgebung erforderlich ist, wurde die Rekonstitution des KtrAB Komplexes in Nanodiscs für weitere Strukturanalysen etabliert. Nach einer ersten Optimierung führte ein Kryo-EM-Datensatz in Gegenwart von ATP und $MgCl_2$ zu einer ersten 3D-Elektronendichte mit niedriger Auflösung (6 Å). Obwohl die Auflösung eher gering war, war es offensichtlich, dass die Gesamtarchitektur wieder der ADP-gebundenen Konformation ähnelte. Allerdings war das MSP eng um die Membranhelices gewickelt, so dass die Lipidoberfläche fehlte, die höchstwahrscheinlich für die Interaktion mit dem N-Terminus erforderlich ist.

Insgesamt zeigen die vorgestellten Daten deutlich, dass die Aktivierung des KtrAB-Komplexes nicht nur den Austausch von ADP zu ATP im KtrA-Ring erfordert. Stattdessen ist ebenfalls ein allosterisches Netzwerk aus nukleotidabhängigen Konformationsänderungen und der Interaktion der identifizierten N-Termini mit der Membran notwendig, um den K^+-Fluss durch KtrAB zu ermöglichen.

1 Introduction

1.1 Bacterial tolerance and intrinsic resistance to extreme environmental conditions

Bacteria are very versatile organisms and they can occupy all available niches on Earth, as well as niches in Space (Merino et al, 2019). In these environments, extremely harsh conditions exist, including high ultraviolet radiation, drastic changes in temperature, pH and salinity as well as the presence of organic solvents and antibiotics (Rothschild & Mancinelli, 2001). All microorganisms, either planktonic or sessile, surviving under these conditions, exhibit specific adaptation mechanisms and intrinsic resistances.

1.1.1 Attachment of bacteria to a surface and biofilm formation

One of the most distributed and successful strategies to adapt and survive under all kind of extreme environmental conditions is the formation of biofilms. By attaching to surfaces, the cells can form biofilms, in which they are embedded in a matrix consisting of extracellular polymeric substances (EPS) (Yin et al, 2019). This lifestyle provides bacteria with many advantages. They benefit from high nutrient availability at the surfaces and utilisation of surface-originated elements in the metabolism, as well as from the protection against environmental hazards. For example, it has been shown that surface-attached biofilms are 100 to 1,000 times more resistant to antibiotics and disinfecting agents compared to planktonic bacteria (Smith & Hunter, 2008; Stewart & William Costerton, 2001). Bacteria can adhere to a large variety of biotic and abiotic surfaces, including glass, metals, different polymers, other bacteria and eukaryotic tissues, as well as water system piping and natural aquatic systems (Donlan, 2002; Tuson & Weibel, 2013). While this lifestyle is advantageous for bacteria, it can result in a wide range of consequences for humans, ranging from infections to contamination of food products in processing facilities. It has been estimated that 80% of all medical infections are biofilm-derived and a good understanding, on how bacterial cells attach to biotic and abiotic surfaces is required to effectively fight bacterial biofilms (Harro et al, 2010). The attachment of cells, which is the initiation of a biofilm formation, is a complex multistage process, which includes locating, approaching, and sensing the proximity of the surface. In each step, gradients of physiochemical or/and biological signals from the cells immediate surrounding are considered and the cells respond accordingly. The interaction of bacteria with the surface is further influenced by the interplay of properties from the bacterium, the substratum as well as the liquid medium (Cheng et al, 2019; Donlan, 2002). For the substratum the topology or roughness, the hydrophobicity as well as the presence of a conditioning film

are important variables. Furthermore, the flow velocity, pH, temperature, concentrations of cations and the presence of antimicrobial agents in the surrounding liquid can have an effect in the process of attachment. In addition, the interaction of bacterial cells with a surface varies dependent on cell surface structure like hydrophobicity, the presence of fimbriae and flagella as well as on the production of EPS (Donlan, 2002). Altogether, the attachment of microorganism to surfaces is a very complex process and the detailed mechanisms are so far not fully understood.

1.1.2 Intrinsic resistance to antibiotics

Not only for microorganism within a bacterial biofilm, but universally and naturally occurring within all bacteria species is the intrinsic resistance to different classes of antibiotics (Cox & Wright, 2013). For example, intrinsic antibiotic resistance is responsible for multi-drug resistant (MDR) phenotypes of many Gram-negative bacteria. The outer membrane of Gram-negative bacteria is impermeable to many molecules and therefore protects the cells from several antibiotics (Nikaido, 1994). Furthermore, several MDR efflux pumps are expressed to actively reduce the intracellular concentration of antibiotic drugs, which allows cell survival. Screening of gene inactivation and transposon insertion revealed a wide range of additional genetic loci that contribute to the intrinsic susceptibility (Blake & O'Neill, 2013; Fajardo et al, 2008; Gomez & Neyfakh, 2006; Liu et al, 2010). All these elements together are referred to as the ‘intrinsic resistome’, which represents an attractive target for the identification of antibiotic adjuvants that support the activity of existing antibiotics, as the intrinsic resistance in bacteria drastically limits the therapeutic options. Therefore, it appears significantly important to develop additionally strategies to treat bacterial infections. Here, other bacterial intrinsic resistances and tolerances should be considered and studied in detail, to harness the capacities of environmental bacteria more efficiently.

1.1.3 Bacterial resistance to organic solvents

In 1989, the occurrence of organic solvent-tolerant bacteria has been described for the first time (Inoue, 1989). Although, organic solvents are known to be extremely toxic to microbial cells by disrupting the lipid bilayer, bacterial species like the Gram-negative *Pseudomonas* and *Eschericha coli (E. coli)* (Aono et al, 1991; Cruden et al, 1992), as well as the Gram-positive *Bacillus* or *Rhodococcus* (Paje et al, 1997; Sardessai & Bhosle, 2003) were shown to survive at high concentrations of toluene, p-xylene, or benzene. Mechanisms involved in this tolerance comprise modifications in the cell envelope to increase membrane rigidity and decrease permeability, special solvent-inactivating enzymes, and active efflux by solvent efflux pumps or release of solvent-containing

membrane vesicles (Sardessai & Bhosle, 2002). Making use of these mechanisms shows a great potential in industrial and environmental biotechnology (Torres et al, 2011).

1.1.4 Adaptation to acidity and alkalinity

Extremely high and low pH conditions are present in different ecosystems on Earth and living bacteria have been isolated from environments with a pH ranging from 0 to 12.5 (Merino et al, 2019). The environmental pH has a significant effect on microorganisms, as the majority of bacteria must maintain a near neutral cytoplasmic pH to enable cellular functions for survival and metabolism. Furthermore, the intracellular proton concentration is involved in cellular bioenergetics, and the proton gradient across the membrane significantly contributes to the proton motif force, which is a central energy currency. Therefore, under acidic conditions the expression and activity of proteins or pathways that result in an efflux or consumption of cytoplasmic protons is stimulated. In contrast, under alkalic conditions, pH homeostasis is maintained by the active accumulation or generation of protons in the cytoplasm. In addition, the cells undergo passive adjustments including alterations of membrane permeability to protons, by making the membrane less fluid, denser, or thicker (Sohlenkamp, 2017). Insights into the structure and function of molecules and regulators of pH homeostasis allows to understand the molecular basis of the strategies for adaptation to alkalic and acidic conditions (Krulwich et al, 2011). Since these adaptation mechanisms enable for example *Helicobacter pylori* to colonise the highly acidic surface of the human stomach, these insights might help to target certain pathogens more accurately.

1.1.5 Bacterial life under extreme temperatures

In addition to extreme pH conditions, temperatures ranging from -98.6°C to 495°C can be found on Earth. The temperature range in which metabolising bacteria have been reported is currently between -20°C and 122°C, while survival has been observed from -25°C to 130°C. Even from deep sea vents, which can reach temperatures of 340°C, bacteria could be isolated. These extreme temperatures affect the cells in many ways. Very low temperatures decrease the fluidity of the membranes, disrupt membranes by ice crystal formation, slow down chemical reactions and diffusions, and inactivate proteins. On the other hand, very high temperatures denature proteins and nucleic acids, and an increased fluidity of the membrane impairs metabolic processes. In general, to survive under these extreme temperatures, the environment generally involves either high salinity or pressure conditions. In cold environments high concentrations of salt lower the freezing point, while high pressure at extreme high temperature allows water to remain liquid (Merino et al, 2019). Furthermore, to avoid freezing and ice crystal formation, cells produce intracellular substances, such as glycerol or antifreeze proteins which lower the freezing point. To

increase the fluidity of the membranes the fraction of unsaturated lipids increases (Beales, 2004; Russell, 1990). In contrast, at extreme high temperatures, the ratio of saturated to unsaturated lipids increases to limit the fluidity of the cell membranes. To avoid protein denaturation and allow protein and enzyme activity at elevated temperatures, the thermo-adapted proteins have additional secondary ionic and covalent bonds, as well as a special amino acid usage to stabilise folding (Wang et al, 2015).

1.1.6 Adaptation to osmotic stress

One further environmental parameter for which bacteria have developed an adaptation mechanism, is the osmolarity and salinity of the environment. Saline environments comprise a large portion of the Earth and range from marine environments, hot springs, to soda lakes and salt inclusions (Merino et al, 2019). Osmotic fluctuations can be caused by periods of low and high rainfall, changes in the concentration of external nutrient solutions, or accumulation of metabolic products. Furthermore, pathogenic bacteria face hyperosmotic stress upon invading a mammalian host, as for instance in the urinary tract the urea concentration can increase up to 1.5 M (Culham et al, 2018). Facing these drastic changes, bacteria need to react instantaneously to survive.

When bacteria are facing sudden osmotic down shock, massive influx of water increases the turgor pressure within milliseconds to a degree that cannot be restrained by the cell wall (Buda et al, 2016). Therefore, the cells have to release cytoplasmic low molecular weight solutes *via* mechanosensitive or stretch-activated channels like MscL, MscM and MscS. This is followed by efflux of cytoplasmic water, enabling the cells to recover the turgor pressure and ensure their survival (Levina et al, 1999; Sleator & Hill, 2002; Wilson et al, 2013).

In contrast, sudden external hyperosmotic conditions induce the release of water from cells, which would, without any adaptation, lead to cell death due to plasmolysis. In order to adapt to these conditions, bacterial cells have developed two major strategies. The ‘salt-in strategy’ involves the continuous accumulation of molar concentration of K^+ in the cytoplasm. Since such high intracellular K^+ concentrations are toxic for the majority of bacterial cells on a long term and requires an adaptation of the cellular enzymatic machinery, this strategy is only used by a small number of halophiles, which permanently live under elevated salt concentrations (Epstein, 1986; Stumpe & Bakker, 1997; Ventosa et al, 1998). This prevents the loss of water and restores turgor pressure, as the ions increase the osmolarity inside the cell. Much more widespread is the so called ‘salt-out strategy’, which as well comprises the initial rapid uptake of K^+. However, in a second phase of adaptation K^+ is replaced by other osmoprotective compounds either by uptake or de-novo synthesis. These small osmoprotective compounds, compatible solutes, are in general uncharged or zwitterionic and include polyols, sugars, amino acids and derivates

thereof such as glycine betaine and ectoine (Ventosa et al, 1998). The osmotic pressure of the cytosol is then further balanced by the compatible solutes and no further adaptation of the intracellular machineries is required.

Along with this primary adaptations, bacterial cells undergo several further passive and active adjustments during osmotic stress. Prior to K^+ uptake, water efflux results in shrinkage of the cell, which alters the cytoplasmic solute concentration and the turgor pressure of the cell. While respiration and majority of active transport activities are halted, the internal pH gradient and ATP level are transiently increased (Wood, 1999). Furthermore, the lipid composition of the membrane is adjusted. Besides variation of phospholipid headgroups, hydrogen-bonding, length and saturation of the acyl chains, membrane tension, lateral pressure, and the curvature changes. Osmoprotective proteins in fact sense these cellular changes like the ionic strength inside the cell, lipid headgroups or saturation, as well as ion gradients across membranes or altered force fields induced by changes in membrane potential, which in consequence regulates the activity of the proteins (Poolman et al, 2004). Here, for many transporters and channels, an interaction with the lipid membrane has been shown to play a crucial role in the regulation.

1.1.7 Regulation of osmoregulatory proteins by lipids

Proteins which are embedded in the membrane are surrounded by different lipid molecules that can interact with the protein. These lipids are referred to as annular lipids and they are less mobile compared to those in the bulk phase of the membrane. However, they can be exchanged in a time scale of (sub)microseconds with bulk lipids (Lee, 2003). In addition to these lipids, the presence of non-annular lipids, which can be tightly bound to the protein between transmembrane helices or at protein interfaces, have been suggested to influence protein functions. Bacterial membranes present a large diversity of lipids, including the most common phosphatidylethanolamine (PE), phosphatidylglycerol (PG), cardiolipin (CL), and the less frequent lysyl-phosphatidylglycerol (LPG), phosphatidylinositol (PI), phosphatidic acid (PA) and phosphatidylserine (PS), as well as a variety of other membrane lipids, such as ornithine lipids (OL), glycolipids (GL), glycophospholipids (GLP), sphingolipids (SL) or hopanoids (HOP). Different bacterial species display different composition and even cells belonging to a single species can have varied lipid composition depending on the environmental conditions. Membranes of the model organisms *E. coli* predominantly consist of PE, PG and CL. For *B. subtilis* the presence of LPG, GL, and GPL is additionally described to the presence of the most common lipids PE, PG and CL (Sohlenkamp & Geiger, 2016). Upon increased salt concentration the concentration of anionic phospholipids (PG, CL) increase, whereas the fraction of zwitterionic phospholipids (PE) decreases. Whether CL or PG dominates depends on the organism, but in general the behaviour is shared by Gram-positive and Gram-negative as well as halophilic and halotolerant bacteria. These variations in lipid

composition have been shown to regulate mechanosensitive channel as well as several osmolyte transporter during the adaptation to osmotic stress (Poolman et al, 2004). The best studied osmolyte transporter are the ABC (ATP-binding cassette) transporter OpuA from *Lactococcus lactis* (Biemans-Oldehinkel et al, 2006; Sikkema et al, 2020), the Na^+-coupled transporter BetP from *Corynebacterium glutamicum* (Ochrombel et al, 2011; Rübenhagen et al, 2000) and the H^+-coupled transporter ProP from *E. coli*, which all have been described to be influenced by the interaction with the membrane. For example, OpuA is activated by an increased concentration of internal ions. At the same time its activity strongly dependents on the fraction of anionic lipids in the membrane. It was demonstrated that the CBS domain (cystathionine-β-synthase) of the protein is responsible for the osmosensing, and mutagenesis of the cationic residues affected the ionic strength gating and lipid dependency (Biemans-Oldehinkel et al, 2006; Karasawa et al, 2011). Recently, an additional motif of positive charges was identified located in close proximity of the membrane, in a helix-turn-helix (HTH) motif of the nucleotide binding domain (NBD), which was shown to be responsible for the lipid dependent activation of the transporter (Sikkema et al, 2020). Therefore, it is suggested, that these domains interact with the negative charged lipids of the membrane by electrostatic interactions, inducing an inactive state of the transporter. Upon increasing intracellular ionic strength this electrostatic interaction weakens, which results in a repulsion of the sensor, inducing conformational changes towards the active state of the transporter. The interplay between the residues in the HTH motif and the CBS domain remains elusive. Similar, the activation of BetP is dependent on the internal osmolality and the proportion of the anionic lipid PG (Rübenhagen et al, 2000). Responsible for this effect is the C-terminal domain of BetP, which is described to form a sensor for K^+. With a net charge of approximately +10 the sensor appears to interact the anionic membrane surface, which gets weakened at an excess of K^+ (Rübenhagen et al, 2001). Protein-lipid interaction of ProP is less understood; however, it has been proposed, that ProP co-localises together with CL at the cell poles and that the activity also depends on the CL and PG content of the membrane, most likely by interactions with the C-terminal peptide of ProP (Culham et al, 2018; Tsatskis et al, 2005). Since the adjustment of the lipid composition and interaction with osmoregulatory proteins seem to be crucial for the adaption to osmotic stress, it appears plausible that other systems, which are also involved in osmoadaptation, might as well be regulated by the lipid environment.

1.2 Cellular functions depend on the ion distribution across the membrane

In addition to the major role in the rapid adaptation to hyperosmotic stress, K^+ in general fulfils a broad spectrum of tasks. In prokaryotes it is involved in essential cellular processes, including pH stress response (Booth, 1985), maintaining of turgor pressure and membrane potential (Epstein, 2003; Schultz & Solomon, 1961), regulation of protein synthesis, enzyme activation (Nissen et al, 2000; Rozov et al, 2019), and electrical signalling in biofilms (Beagle & Lockless, 2020; Prindle et al, 2015). K^+ is the most abundant intracellular monovalent cation in all living organisms and cell functions are adapted to high millimolar internal K^+ concentration. Prokaryotic cells can accumulate K^+ 10^3 to 10^5-fold compared to the external K^+ concentration, under normal condition internal K^+ concentrations range from 300 to 500 mM (Schultz & Solomon, 1961). In contrast, the pre-dominant cation on the extracellular side is sodium (Na^+). It is usually present in 10-fold access compared to the inside of the cell, as an internal Na^+ concentration above 10 mM is already toxic for the cells (Carden et al, 2003; Gorecki et al, 2014; Munns & Tester, 2008). This non-equilibrated ion distribution contributes to the electrical potential across the membrane ($\Delta\psi$), which drives essential process like ATP hydrolysis, secondary active transport processes across the membrane, electrical signalling, or flagella movement. Therefore, microbial physiology and cell function strongly relies on the defined partition of ions across the membrane. In addition to the essential K^+ and Na^+ gradients, the major contribution to the cell's membrane potential of respiring bacteria is the electron transport chain (ETC), which pumps out protons from the cytosol to the extracellular side or periplasm. This electrical gradient together with the chemical H^+ gradient are the main contributor to the proton motif force and result in a membrane potential in the order of -150 mV in a metabolising bacterium (Figure 1) (Felle et al, 1980; Stautz et al, 2021). Another factor that contributes to the negative resting membrane potential is the Donnan potential, which arises from intracellular impermeable, negatively charged macromolecules including DNA or RNA (Eisenberg & Crothers, 1979). This inside-negative membrane potential allows bacteria to enrich positively charged ions within the cell relative to their external concentrations. However, due to the positive charge, the ions are impermeable to the membrane and can only cross the bilayer through specific membrane spanning transport proteins. Based on the transport mechanism, the proteins are divided in three general groups: pumps or primary active carriers/transporters, secondary active carriers/transporters, and channels. Primary and secondary active transporters move ions actively against gradients under consumption of ATP and by utilising the gradient of a co-translocated ion, respectively. In contrast, channels allow passive flux of ions across the membrane along the electrochemical gradient (Gadsby, 2009; Gouaux & Mackinnon, 2005).

1.3 Variety of bacterial potassium translocation systems fulfil different tasks in potassium homeostasis

To allow the broad-spectrum K^+ has to fulfil, bacterial cells have a number of K^+ translocating systems from all three protein classes mentioned above. The systems are present at different combination in bacteria and their activity depends on different cellular conditions. Identified system are not limited to one organism, but are widely spread among different prokaryotic species and the combination of the different channels and transporters influences the bacterium's unique physiology (Figure 1) (Epstein, 2003; Stautz et al, 2021). The molecular details and the physiological roles of many of these systems remain unknown and are still being discovered. Best described is the K^+ homeostasis in *Escherichia coli* and *Bacillus subtilis*, in which several K^+-translocating systems are known to maintain the outward-directed K^+ gradient.

To release intracellular K^+, *E. coli* possesses three main mechanosensitive channels MscL, MscM and MscS, which are activated dependent on membrane tension. Upon hypoosmotic shock they release potassium together with other osmolytes, followed by water diffusion, resulting in turgor pressure recovery (Levina et al, 1999; Sukharev et al, 1994). In addition, the glutathione-controlled K^+/H^+ antiporter Kef (K^+ efflux) is involved in K^+ efflux (Bakker et al, 1987; Roosild et al, 2010). By a controlled acidification it protects the cell against detrimental effects of electrophilic compounds (Healy et al, 2014).

For K^+ uptake in *E. coli* cells three different systems were identified: Trk (transport of K^+), Kup (K^+ uptake) and Kdp (K^+ dependent P-type ATPase) (Epstein & Kim, 1971; Rhoads & Epstein, 1977; Schleyer & Bakker, 1993). For everyday challenges and adaption to osmotic stress, the constitutively expressed Trk system is predominantly responsible (Rhoads & Epstein, 1977). The channel is active at external K^+ concentration >200 µM and neutral to alkaline pH. By use of the pmf it accumulates K^+ by 150-fold. Trk consists of a dimer of the pore-forming transmembrane subunit TrkH, and a tetramer of the regulating, ligand-binding RCK (regulator of conductance of K^+) domain. It has an apparent affinity for K^+ of around 1.5 mM and takes up K^+ with a maximal uptake rate of 300-500 $\mu mol*g^{-1}*min^{-1}$ in a H^+ and ATP-dependent manner (Cao et al, 2013; Epstein et al, 1993; Stumpe & Bakker, 1997). The transmembrane channel subunit TrkH belongs to the superfamily of potassium transporters (SKT). When the external K^+ is limited (<100 µM) and Trk fails to take up potassium, the high-affinity potassium uptake system Kdp is produced and ensures the accumulation of K^+ with a moderate uptake rate (100-150 $\mu mol*g^{-1}*min^{-1}$) fuelled by ATP hydrolysis. Kdp is a primary active K^+ pump and consists of the four subunits KdpF, KdpA, KdpB and KdpC, which allows K^+ uptake by the combination of two half-channels formed by the K^+ channel-like subunit KdpA, which as well belongs to the SKT family, and the P-type ATPase KdpB (Silberberg et al, 2021; Stock et al, 2018). Under acidic pH, the secondary active K^+/H^+ symporter Kup has a particular

high activity and exhibits K^+ translocation with similar rates to that of Trk but shows a slightly increased affinity towards K^+ (0.5 mM). The transporter accumulates K^+ against its concentration gradient by the co-transport of protons along the concentration gradient (Epstein et al, 1993; Trchounian & Kobayashi, 1999; Zakharyan & Trchounian, 2001).

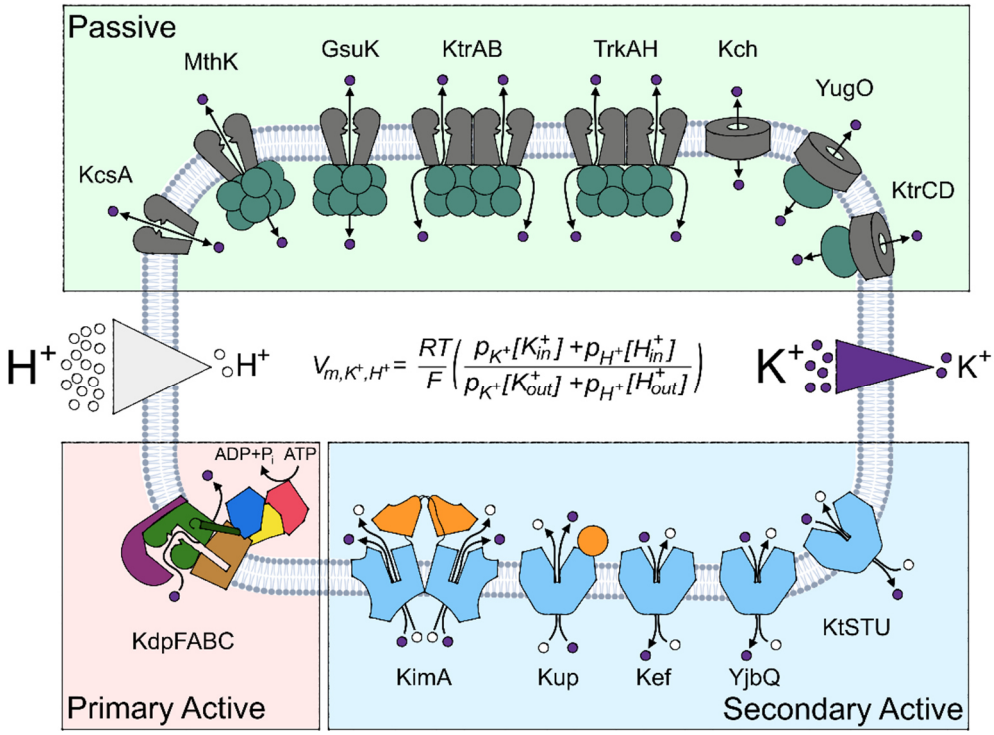

Figure 1: Overview of identified bacterial K^+ translocation system. Bacterial cells have a number K^+ translocation systems, including channels, primary and secondary active transporters. The systems are present at different combination in bacteria and their activity depends on different conditions. They need to work in a concerted and controlled fashion to maintain an outward-directed K^+ gradient. The K^+ gradient contributes to the membrane potential, which in addition is established by the H^+ gradient. The Goldman Katz equation can be used to calculate the membrane potential in the dependence of the permeability (P) for different ions. R is the gas constant, T is the temperature, and F is the Faraday constant. Figure was adapted from Stautz et al. (2021).

In *B. subtilis* efflux of K^+ is mediated by several mechanosensitive channels, as well as the K^+/H^+ antiporter KhtSTU and potentially CpaA (formerly YjbQ). For the latter two the physiological role is unknown. Further, K^+ channel YugO, was recently identified to be involved in electrical signalling within biofilms, where it releases K^+ which induces a depolarisation of the neighbouring cell for the communication of the metabolic state of the interior cells of a biofilm (Prindle et al, 2015).

Likewise in *E. coli*, multiple K^+ uptake systems are present in *B. subtilis* cells. Here, first structural insights into the transport mechanism of K^+ by the KUP family was gained on KimA from *B. subtilis* (Tascon et al, 2020). In line with what was predicted for Kup from *E. coli*, the protein adopts a different overall and pore structure when compared to the other K^+-transporting system (Sato et al, 2014). KimA consists of a homodimer in the

membrane, of which each monomer adopts a LeuT fold, and a regulatory domain in the cytoplasm (Tascon et al, 2020). In addition to the H^+/K^+ symporter KimA, the K^+ channels KtrAB and KtrCD are mainly responsible for K^+ uptake (Holtmann et al, 2003). KtrAB and KtrCD are homologues of each other and of TrkAH, however, KtrCD has a 10-fold lower affinity for K^+ and can be modulated by glutamate (Krüger et al, 2020). Similar to Trk, the dimeric channel subunits KtrB and KtrD belong to the SKT family and assemble with a cytosolic regulatory RCK ring, KtrA and KtrC, respectively, which are made of eight RCK proteins (Holtmann et al, 2003). While the *ktrC* and *ktrD* genes are constitutively expressed, the expression of *ktrAB* and *kimA* is controlled by a riboswitch, which responds to the internal concentration of cyclic di-adenosine monophosphate (c-di-AMP). The binding of c-di-AMP to the riboswitch prevents the expression of the underlying genes encoding for channel and transporter subunits, thereby regulating potassium uptake (Gundlach et al, 2017; Nelson et al, 2013). In addition to the regulation on the genetic level, c-di-AMP was shown to regulate KtrAB and KimA by binding to the proteins, inducing inactivation (Gundlach et al, 2019). The KtrAB complex is further regulated binding of ATP or ADP to the RCK ring and for homologues from other organisms it was shown, that they as well depend on $\Delta\Psi$ and the presence of Na^+ (Kröning et al, 2007; Matsuda et al, 2004; Tholema et al, 2005).

1.4 General architecture and main features of K^+ channels

The history of research on ion channels already began in 1953, when Hodgkin and Huxley published their findings on action potentials in the squid axon, which included changes in membrane permeability for Na^+ and K^+ ions. Few years later, this permeability was attributed to ion channels (Hodgkin & Huxley, 1952) and concepts for ion selectivity, conductance and gating were suggested (Armstrong & Bezanilla, 1973; Hille, 1970; Hille, 1971; Hille, 1973). By identifying the Shaker K^+ channel gene from *Drosophila melanogaster*, the amino acid sequence of a K^+ channel was revealed for the first time, which allowed to identify the residues that are responsible for the specific features of a channel. It was concluded that the architecture of most of the K^+ channel had to be tetramers that encircle a central pore, which contains a signature sequence for ion selectivity. The signature sequence -TVGYG- motif was identified to be responsible for K^+ selectivity. In 1998 the first atomic structure of the prokaryotic K^+ channel KcsA from *Streptomyces lividans* (*S. lividans*) was determined, which tremendously moved forward the mechanistical understanding of ion channels (Doyle et al, 1998). In 2003, MacKinnon, the senior author who solved the KscA structure, was awarded the Nobel Prize in Chemistry for his ground-breaking research on potassium channels. Since then, many more structures of K^+ channels were solved. In general, many of them share a common tetrameric architecture, which arranges from the assembly of four TM1-P-TM2 motifs (also referred as M1PM2 motifs). Each M1PM2 motif, consists of two transmembrane (TM1 and TM2) helices connected by a pore (P) domain, which includes the pore helix and the pore loop. The organisation around a fourfold or pseudo-fourfold symmetry axis provides the ion permeation pathway. Despite this typical architecture, K^+ channels can be divided in three major classes depending on their structure and function: the 2-TM/P, the 4-TM/2P or the 6-TM/P channels (Kubo et al, 1993). 2-TM/P channels consist of one M1PM2 motif, which assembles as a tetramer, and include the subgroup of homotetrameric inward-rectifying K^+ channels (Kir) as well as many procaryotic channels (Figure 2 A) (Hibino et al, 2010). 4-TM/2P channels, also known as K2P channels, form homodimers of two subunits, with each two pore regions and four transmembrane helices (two fused M1PM2 motifs) and include outward rectifier and open rectifier (or ‘leak’) channels. (Figure 2 B) (Goldstein et al, 1998). In contrast, the protomers of 6-TM/P channels consist of only one M1PM2 motif and of four additional N-terminal helices (S1-S4), which as well form a homotetramer. Functionally, 6-TM/P channels are often voltage-gated K^+ channels (Kv) (Figure 2 C) (Kim & Nimigean, 2016).

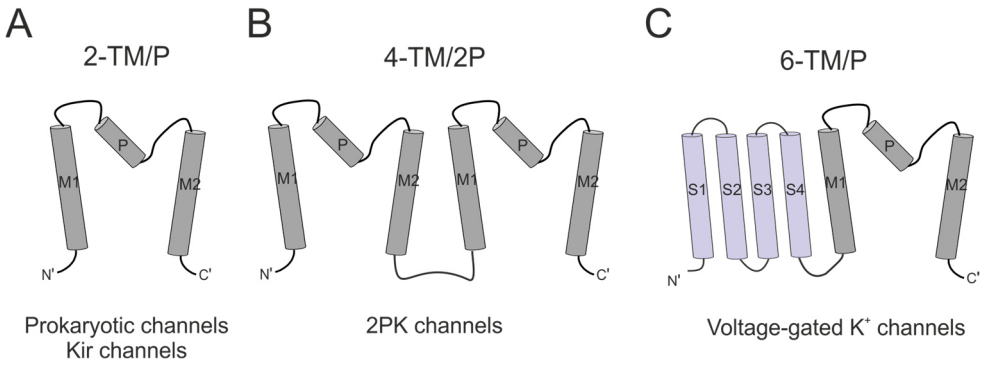

Figure 2: **Topology of the three main classes of K^+ channels**. A) Topology model of a 2-TM/P protomer, which forms a homotetramer of four M1PM2 motifs. Each channel protomer consists of 2 transmembrane helices (M1 and M2), which are connected by a pore helix and pore loop (P). B) 4-TM/2 channels are formed by a homodimer. Each protomer consists of two covalently fused M1PM2 motifs. C) For 6-TM/2P channels, four additional helices are fused to the M1PM2 motif (S1-S4, colored in lilac), which are not involved in the formation of the pore in a tetrameric assembly.

1.5 KcsA, the paradigm of K^+ channels

As mentioned above, the best-studied 2-TM channel is KscA, which is highly selective for K^+. The channel was shown to be activated following a downshift of the intracellular pH (Hirano et al, 2011) and the gating is voltage-dependent, with increased open probability upon depolarisation (Cordero-Morales et al, 2006). KcsA forms a homotetramer, with each subunit consisting of an M1PM2 motif (Figure 3 A). The pore is formed by the TM section of the helices, the short pore helices, and the subsequent pore loops. Therefore, the four M1PM2 motifs are oriented towards each other forming a central pore (Figure 3 B). The pore loop forms the major constriction of the pore and the selectivity filter, which harbors the amino acid sequence N'-TVGYG-C'. The selectivity filter is 12 Å long and ~3 Å wide and contains 4 K^+ binding sites, referred to as S1-S4 (Figure 3 C). The binding sites are lined by carbonyl oxygen atoms, which octahedrally coordinate dehydrated K^+, similar to how water coordinates hydrated K^+. The architecture of the SF results in a low energetic effort for dehydration of K^+, which allows conductance of potassium at nearly diffusion limit and results in the discrimination against other ions like the prevalent smaller Na^+. Once the channel is activated, up to 10^8 ions per second are translocated for ~ 200 milliseconds until channel inactivation (Morais-Cabral et al, 2001; Xu & McDermott, 2019). The long-proposed mechanism for potassium ion conduction suggested co-translocation of K^+ together with water, occurring by the occupancy of alternating binding sites (S1 and S3 or S2 and S4) from ions in a water solution, due to the strong electrostatic repulsion between the dehydrated ions (Morais-Cabral et al, 2001; Zhou et al, 2001). This hypothesis was challenged by a mechanism called 'direct knock-on' mechanism (Kopec et al, 2018; Köpfer et al, 2014; Öster et al, 2019). Here, a direct repulsion of the dehydrated ions, which are coordinated in adjacent binding sites allows the rapid ion conduction through the pore.

Once K^+ is released from the selectivity filter, it gets rehydrated in an energetically favorable event. Below the selectivity filter a large vestibule is separated from the cytoplasm by a helical bundle formed by the C-terminal end of TM2. This helical bundle functions as a second gating point for ion flux, as it can adopt an open and closed conformation. While in the active conformation the helical bundle widens the vestibule below the selectivity filter up to 22 Å allowing K^+ flux, in the inactive state the pore is restricted by a hydrophobic barrier as residues V115 narrow down the pore avoiding ion permeation (Figure 3 C,D) (Cuello et al, 2017; Uysal et al, 2009). The opening is induced by the protonation of residues such as H25, E118 and E120, which disrupts hydrogen bonds in the helical bundle, thus opening the gate (Imai et al, 2010; Thompson et al, 2008). This open conformation was described to be stabilised by the interaction of the N-terminal residues of TM1 with the membrane. Upon deletion of the first 22 N-terminal residues, the open probability (P_{open}) was drastically reduced. This effect could be assigned to two positively charged residues of this region, which showed a similar decrease in P_{open} upon neutralisation (Iwamoto & Oiki, 2013). Unfortunately, these residues are structurally not resolved.

Within a millisecond timescale, the ion flux through KcsA is stopped by a C-type inactivation. The exact molecular mechanism of C-type inactivation is still under debate and different scenarios are suggested: In the activation-coupled inactivation hypothesis, the selectivity filter undergoes conformational changes due to allosteric coupling with the helical bundle, inducing a collapsed selectivity filter, which does no longer conduct ions (Cuello et al, 2017; Cuello et al, 2010a; Cuello et al, 2010b). A second hypothesis describes an inactivation of K^+ flux, which is linked to ion occupancy at specific sites of the selectivity filter. Here, ion binding at the S2 site leads to the deformation at the S3 site, blocking ion flux and thus inducing inactivation. Finally, the so-called ion dilation hypothesis includes the expansion of the outermost site of the selectivity filter, reducing the selectivity for K^+. This in consequence is suggested to allow the binding of partially dehydrated Na^+ ions, preventing the entrance of K^+ into the selectivity filter. Subsequently, the diffusion of bound K^+ out of dilated selectivity filter is described to induce further dilation, allowing the permeation of partially dehydrated Na^+ (Hoshi & Armstrong, 2013). Despite the difference of all three hypothesis, once C-type inactivation is completed, conformational changes within the selectivity filter are supposed to stop the translocation of K^+, even though the helical bundle is still open (Xu & McDermott, 2019). While the selectivity filter recovers to its conductive state, the helical bundle rearranges and prevents further ion translocation (Cuello et al, 2017).

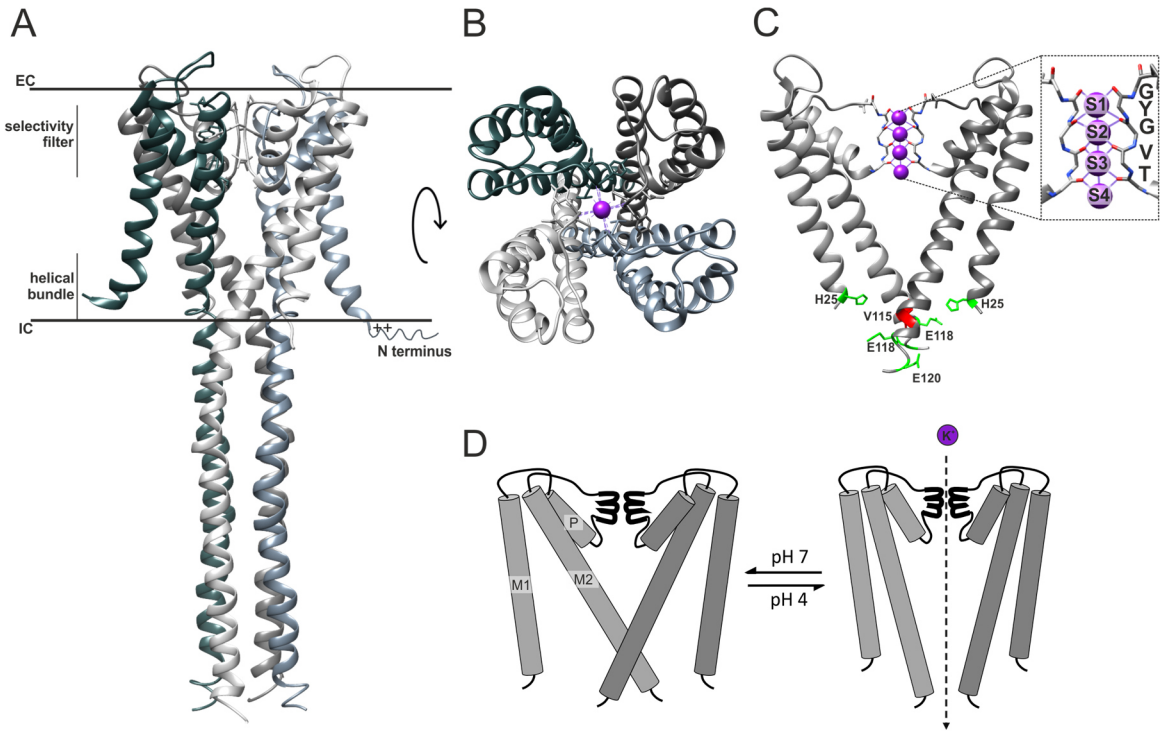

Figure 3: The 2-TM K^+ channel KscA from *S. lividans*. A) Structure of the tetrameric assembled KscA channel (PDB: 3EFF), which consists of a transmembrane domain and helices that extend into the cytoplasm. The selectivity filter is responsible for K^+ selectivity and K^+ translocation is regualted by a helical bundel. The N terminus is formed by a helical stretch of 22 amino acids, which is located in close proximity to the membrane, suggesting stabilising interactions with the lipids. B) Top-view of KscA shows that the four M1PM2 motifs orient around a central axis forming the pore for ion translocation. C) Zoom-in into the M1PM2 motif to highight the selectivity filter, which is formed by the highly conserved N'-TVGYG-C' in the P loops. The selectivity filter habors four K^+ binding sites (S1-S4), which coordinate dehydrated K^+ ions. A second constriction of the ion permeation pathway is formed by a hydrophobic gate in the helical bundle by residue V115 (colored in red). The residue which are protonated during activation are highlighted in green (H25,E118,E120). D) Cartoon of helical bundle gate mechanism. Upon a pH shift, the helical bundle reorrients and opens the ion pathway, allwoing ion flux. Cartoon was adaptated from Stautz et al. (2021).

1.6 Regulation of K^+ channels by RCK domains

Although, all 2-TM K^+ channels are arranged as tetramers of M1PM2 motifs, forming a central pore with a similar mechanism for ion translocation, yet the regulation of channel activity varies. While KscA is mainly regulated by pH, other potassium channels contain an additional domain, which functions as a sensor- (like voltage sensor domains (VSD)) or as ligand-binding domains. Out of 270 prokaryotic genomes more than half of the identified K^+ channels are regulated by a C- terminal cytoplasmic ligand-binding RCK (Jiang et al, 2001; Loukin et al, 2005). These domains assemble as an octameric ring and form a complex with the pore forming transmembrane subunit. Generally, the octameric assembly can result from five different assemblies (Figure 4): (A) a single domain is fused to the C terminus of a 2-TM domain, with a second soluble RCK domain, which is separately expressed via an alternative translation start on the same gene; (B) two tandem RCK domains are fused to the C terminus of a 2-TM domain, which can additionally contain

a VSD at the N terminus; (C) the N and C termini of the 2-TM domain are each fused to a RCK domain; (D) a soluble protein consisting of two tandem RCK domains; or (E) a soluble protein consisting of one RCK domains (Schrecker et al, 2019). As individual soluble proteins (D, E) they assemble to members of the superfamily of K^+ transporters (SKT, cf. 1.7), like TrkH and KtrB.

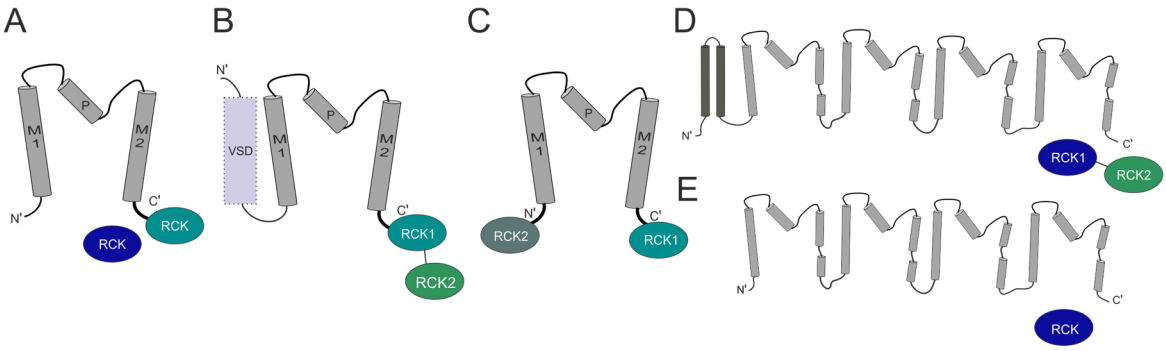

Figure 4: Topology of RCK-gated channels. Five different arrangements of the pore-forming subunits (M1PM2) and RCK domains are possible. A) One RCK domain is fused to the C terminus of the transmembrane domain, while a second soluble RCK domain is expressed through a second start codon. B) Two tandem RCK domains are fused to the C termiunus of the M1PM2 motif. C) Both, the N and C terminus of the pore-forming transmembrane helices are fused to a RCK domain. D) A soluble protein of two tandem RCK domains or E) a soluble protein consisting of a single RCK domain assemble to transmembrane subunits. Transmembrane domains are colored in grey, while the different RCK domains are colored in different shades of blue and green. Colors were maintained in all figures, if not stated otherwise.

Although the arrangement of RCK-gated channels varies, all structurally characterised octameric RCK rings consist of a tetramer of dimers (Figure 5). The dimer is formed by one up and one down RCK domain, therefore resembles two layers (Figure 5 A). The domains within one layer do not make direct contact but interaction is mediated by intervening domains from the other layer (Albright et al, 2006) The dimerization area between an up and down subunit is called dimer-hinge interface (Figure 5 A). The ring assembly is established through interaction between dimers, generating dimer-to-dimer interfaces (Figure 5 B). Each RCK domain consist of a conserved N lobe and less conserved C lobe (Figure 5 A). The N lobes form the inner ring, and a crossover helix extends over to the partner subunit of the dimer, followed by the C lobes, which are oriented to the periphery. The N lobe contains the highly conserved Rossman fold, which consists of alternating alpha helices and beta strands. Those RCK domains that bind nucleotides show the characteristic GxGxxG…D/E motif in the N lobe (Wierenga et al, 1986). In general, ligand binding can occur either within the N lobe, at the interface between the N and C lobe, and/or within the C lobe. Here, a wide range of ligands is known to bind to RCK domains. In addition to nucleotides like ATP, ADP, AMP, NAD(H) and c-di-AMP, several mono- and divalent cations like Na^+ and Ca^{2+}, Mg^{2+} or Zn^{2+} are known to bind to different sites in RCK rings, inducing conformational changes which either result in inactivation or activation of the channel (Schrecker et al, 2019). Although numerous K^+

channels are known to be regulated by RCK domains, the detailed understanding of the gating mechanism is still limited. In the following section, exemplary mechanisms of RCK-gated K^+ channels, which are structurally investigated, are summarised.

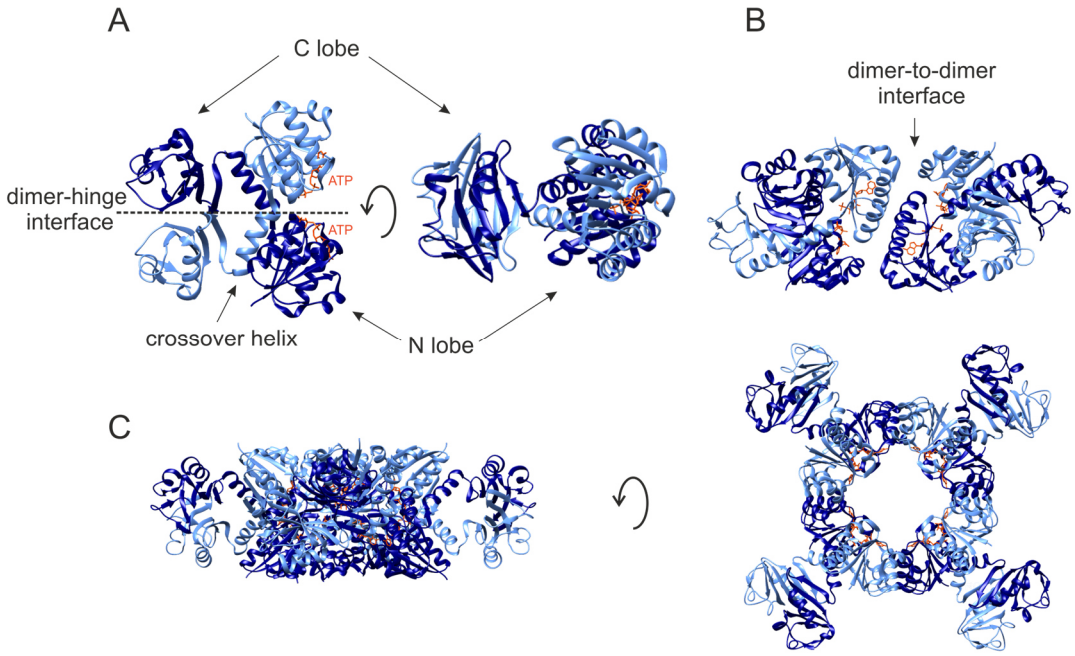

Figure 5: Assembly of an octameric RCK ring. As an example a ring of soluble RCK proteins KtrA is shown (PDB: 4J90). All structurally characterised RCK domains consist of a tetramer of dimers. A) A dimer is formed by an up and down protomer, which are interacting at the dimer-hinge interface. The interaction is established by the crossover helix. Each protomer consists of a conserved N lobe and a less conserved C lobe. The N lobe contains the conserved GxGxxG…D/E motif, which in the case of KtrA binds nucleotides (ATP shown in red). B) The ring assembly is established through interaction between dimers, generating dimer-to-dimer interfaces. C) In the octameric assembly, the N lobes form the inner ring, while the C lobes reach to periphery.

1.6.1 Proposed mechanisms of K^+ translocation meditated by RCK-regulated K^+ channel

In general, a common mechanism for all RCK-regulated K^+ channels appears not to exist. As highlighted above, the assembly of octameric rings varies, which in consequence requires adapted mechanism of how the RCK rings regulate the pore region. Furthermore, different ligands bind to different sites, inducing multiple effects on the conformation of the RCK ring. Therefore, the expansion of the ring varies, involving either the whole ring or only specific parts like the N domain of one layer. In addition, the respective transmembrane domains are variable, forming either one or two pores with their intramembrane gates at various positions (Schrecker et al, 2019). However, based on available functional and structural data, three general steps of the regulatory mechanism are widely accepted (Chakrapani & Perozo, 2007; Hite & MacKinnon, 2017; Jiang et al, 2002a; Kong et al, 2012; Niu et al, 2004). In the first step, ligands bind to the RCK domains and induce conformational changes in the gating ring. Second, these arrangements are transferred to the pore, either via a flexible linker connecting the RCK ring with the transmembrane domain and/or via the interface between the assembled gating rings and the pore forming subunits as well as via additional membrane-bound domains. Third, the resulting conformational rearrangements open the pore restriction, the gate, allowing potassium flux. Nevertheless, several variations are observed in different RCK-gated K^+ channels, and an allosteric network seems to be required to regulate the K^+ translocating systems.

1.6.2 Ca^{2+}-activated K^+ channel MthK

One of the best structurally studied systems is the K^+ channel MthK from *Methanothermobacter thermautotrophicus*, which is described to be a homologue of the human BK channel. It is activated by allosteric binding of Ca^{2+} to the RCK domain, which leads to conformational changes allowing the flux of K^+ with a similar rate as observed for KscA. However, the physiological role of MthK, is so far not fully understood. While the homologues channels CglK from *Corynebacterium glutamicum* or CaK from cyanobacterium S*ynechocystis sp*. are described to be involved in pH homeostasis and cell growth at acidic pH (Follmann et al, 2009) or in regulation of membrane potential and the tolerance to heavy metals (Checchetto et al, 2013), no data is available connecting one of these cellular processes to MthK.

Despite the uncertainties about the physiological role, the structure of the K^+ channel is studied in great detail. It is arranged as a tetrameric 2-TM K^+ channel similar to KscA, but instead of the elongated helices reaching into the cytoplasm, an RCK domain is covalently fused to the C terminus of the TM2 via a flexible linker (Figure 4 A, Figure 6) (Jiang et al, 2002a; Jiang et al, 2002b). An additional, soluble RCK domain is encoded downstream a

second start codon in the *mthK* gene (M107), which forms a dimer with the RCK domain tethered to the TM domain, resulting in an octameric ring in the tetrameric arrangement. The TM domain contains the classical N'-TVGYG-C' selectivity filter, as described for KscA and provides high selectivity for K^+. Upon binding of Ca^{2+} to the RCK domain the system is activated, while the absence of Ca^{2+} induces the inactive conformation. Additionally, the system is further regulated by pH. Here, a shift to a lower internal pH decreases the activation because protonation of the RCK ring destabilising Ca^{2+} binding (Pau et al, 2010). For the isolated gating ring it was shown that both the pH and Ca^{2+} influence the oligomeric state (Ye et al, 2006).

Therefore, the regulation of MthK upon activation and inactivation depends on several conformational rearrangements. In the inactive Ca^{2+}-free conformation of MthK, the TM2 helices are lining the pore and are forming a helical bundle crossing at the intracellular side (Figure 6 A, E). Here, a hydrophobic gate is formed by residue L95 and I99, which narrows down the pore, making the channel impermeable for ions (Fan et al, 2020). The flexible C- linker, which tethers the RCK domain to TM2, lies flat on the N lobe of the RCK ring and establishes contact via several hydrophobic and salt bridge interactions, possibly stabilising the inactive state. The RCK ring adopts a four-fold symmetric octameric ring similar to the isolated RCK ring in the absence of Mg^{2+} (Figure 6 B) (Ye et al, 2006). MD simulations revealed a slight ridged body movement of the RCK ring in the inactive conformation, tilting the gating ring towards the membrane without leading to channel activation as the hydrophobic gate remains closed (Fan et al, 2020). This rocking motion seems to be caused by bending of TM2 and the flexible C-linker, which alternates between interacting with the N lobe and the phospholipid headgroups.

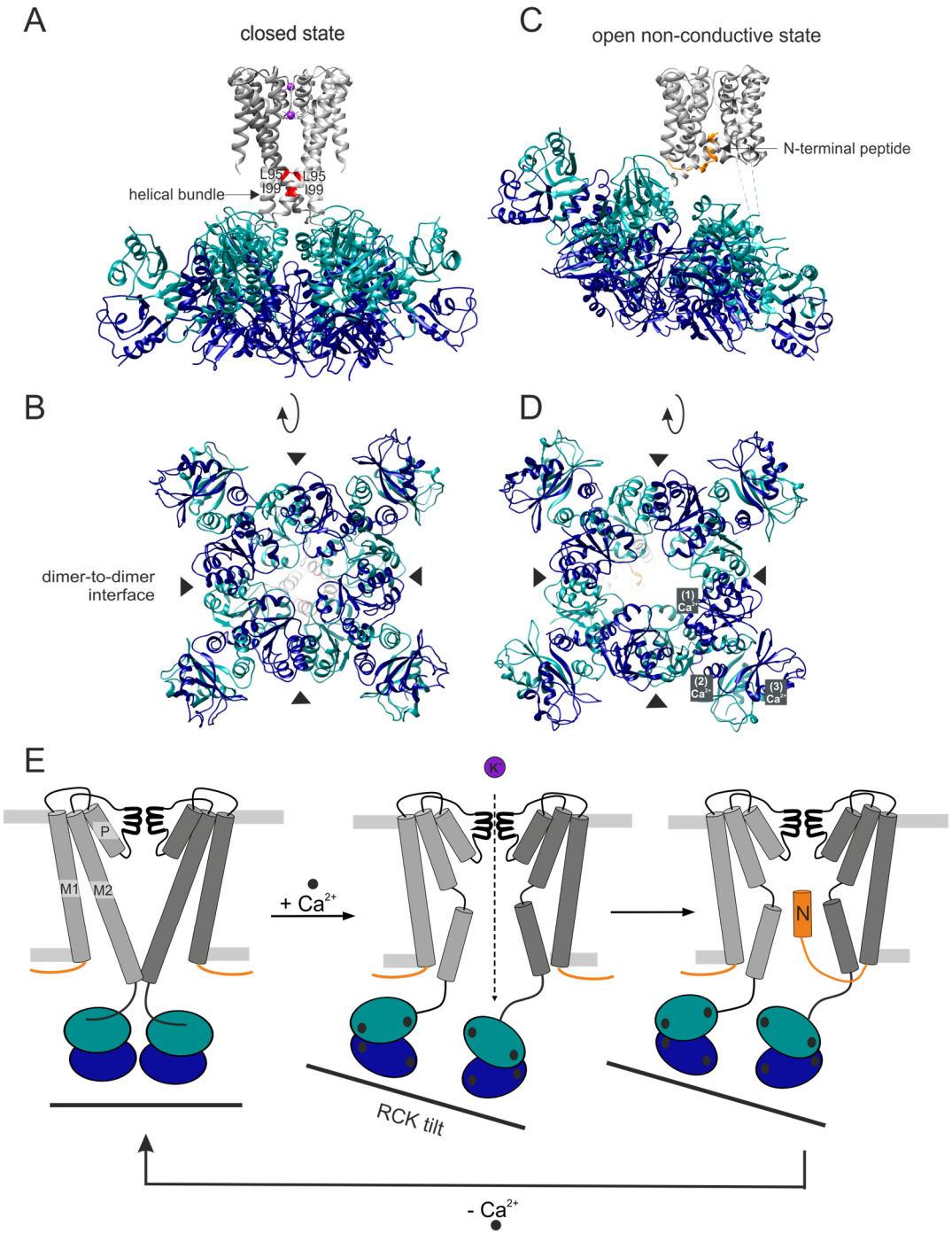

Figure 6: Ca^{2+}-gated K^+ translocation by the MthK channel. A) Structure of the MthK channel from *M. thermoautotrophicus* in the closed state (PDB: 6U6D). A tetrameric transmembrane domain is regulated by an octameric RCK ring. One RCK domain is covalently fused to the M1PM2 motif, while the second domain assembles as a soluble protein. In the absence of Ca^{2+}, the helical bundle restricts the ion pathway and a hydrophobic gate is formed by residues L95 and L99 (shown in red). The C-linker lies flat on the RCK domain, and the gating ring adopts a four-fold symmetry. B) Bottom-view of the octameric gating ring. Dimer-to-dimer interfaces are highlighted with black triangles. C) Structure of MthK in the presence of Ca^{2+} (PDB: 6U68). The channel gets activated by rocking of the RCK domain upon binding of Ca^{2+}, which opens the helical bundle allowing K^+ flux. The shown structure presents the open, non-conductive state, where ion translocation is already hindered due to N-type activation. The N-terminal peptide (orange) of one protomer blocks the pore. D) The RCK domain not only bends towards the membrane, but also the four-fold symmetry gets lost as obvious from the bottom views. Three independent Ca^{2+} binding sites are known. One is located within the N lobe, the second one is found in the dimer-hinge interface at the crossover-helix and the third one is at the interface of the C lobes. E) Cartoon illustration of the Ca^{2+}-gated mechanism. Shown are the closed conformation (left), the open, conductive conformation (middle), and the open, non-conductive state (right). Cartoon was adapted from Stautz et al.(2021).

Upon binding of Ca^{2+} to the RCK ring, the channel opens and allows the translocation of K^+ (Figure 6 C, E). Three independent Ca^{2+} binding sites were identified in each domain of the octameric gating ring (Figure 6 D). One binding site is located within the N lobe and includes coordination of Mg^{2+} by crucial negatively charged residues D184, E210 and E212. A mutation to uncharged amino acids causes a loss of Ca^{2+} binding at this site. A second binding site is found in the dimer-hinge interface at the cross-over helices and residues E248 from the own RCK domain and E266 from the adjacent RCK domain are involved in coordination. The third binding site was identified at the interface of the C lobes and Ca^{2+} was shown to be coordinated by residue D305 from one RCK domain and E326 from the neighbouring domain. Binding to the latter two sites is sufficient for activation (Pau et al, 2011). The energy resulting from Ca^{2+} binding allows the breaking of protein-protein interactions in the four dimer-to-dimer interfaces, which in consequence induces the loss of the four-fold symmetry of the RCK ring. Subsequently, the ring shows large tilts of different angles towards the membrane similar to the observations from MD simulations of the closed channel (Figure 6 C, D, E). For Ca^{2+}-bound structures, however, different degrees of tilts were structurally identified, indicating an increased dynamic. These large structural changes within the gating ring result in a displacement of the C-linker and in a wrenching of the last two helical turns of TM2, which allows the helices to kink open at a highly conserved hinge glycine, and thereby opening the helical bundle (Fan et al, 2020; Jiang et al, 2002a). K^+ flux is enabled for four to five seconds until the ion translocation is stopped by an N-type inactivation (Kuo et al, 2008). The N-terminal peptide of TM1 from one subunit plugs into the pore and interacts via its hydrophobic residues with the hydrophobic inner pore (Figure 6 C, E). Additionally, interactions of charged residues from the N-terminal plug and the pore are required for effective blocking (Fan et al, 2020; Kuo et al, 2008). For the ‘resetting’ of the system, the N-terminal peptide has to be released from the pore, which possibly occurs together with the release of Ca^{2+} from the RCK domain.

1.6.3 Ca^{2+}- and nucleotide-regulated K^+ channel GsuK

Another prokaryotic K^+ channel, which is regulated by an RCK domain, is GsuK from *Geobacter sulfurreducens*. The activation of the channel is induced by binding of NAD^+ and ADP to the gating ring, while binding of Ca^{2+} deactivates the channel. Until now, there is no information on the physiological role and no close homologues have been described. However, as the assembly of its RCK domain resembles the RCK domain of the eukaryotic Slo channels, GsuK is studied as a model system although it lacks the specific voltage sensor (Kong et al, 2012).

The GsuK channel is a tetrameric 2-TM channel, with a tandem of two RCK domains (RCK1 and RCK2) fused to the C terminus of each M1PM2 domain (Figure 4 B), therefore forming an octameric ring which regulates the channel (Figure 7 A). The selectivity filter sequence N-TLGFG-C is modified compared to the classical selectivity filter N-TVGYG-C, resulting in a reduced selectivity for K^+ over Na^+ (Figure 7 B). Structural analysis of the closed, non-conductive Mg^{2+}-bound conformation revealed, that the TM2 helices from GsuK are about two helical turns longer (7 amino acids) compared to those of MthK, and they form three segments, which are referred to as TM2a, 2b and 2c. Furthermore, the helices are not forming a helical bundle and are more parallel compared to the same helices in MthK and KscA, resulting in a large water-filled vestibule below the selectivity filter (Figure 7 B). Only the TM2c segments reorient towards the pore and form a restriction at the very end of the channel, with residues L117 presenting the hydrophobic barrier that avoids K^+ flux. Following this position, a short flexible linker tethers the N terminus of the RCK1 domain to the transmembrane helix. At this connecting stretch, a cluster of several positively charged residues was identified, which is speculated to participate in channel gating by interaction with the negatively charged lipid surface. The orientations of the gating ring in regard to the pore, is about 50° rotated relative to MthK, which could contribute to a varied gating mechanism. Each of the two tandem RCK domains consists of an N lobe, which adopts the Rossman-fold, and a C lobe, similar as described above (Figure 7 C). Interestingly, in GsuK the interaction between the N and C lobes lacks parts of the cross-over helices and therefore the extensive dimer-hinge interface is impaired. Instead, a shorter helix with a different orientation in RCK2 establishes the interaction, which results in a swapped and loosely packed C lobe. The conserved GxGxxG…D/E motif, which is required for nucleotide binding, is only present in the RCK2 domain. Ca^{2+} binds to the dimer-to-dimer interface at so called Ca^{2+} bowls, which deactivates the channel as the closed conformation of the gating ring is stabilised. The ions are coordinated by residues T183, T214 and N140 from RCK1 as well as by residues G449, N450 and Q453 from RCK2. As the gating ring is formed by two different RCK domains, the variations between the up and down domain result in the loss of the two-fold symmetry within the gating ring, which is observed in MthK. Single channel recordings of GsuK

showed that the binding of ADP or NAD^+ to the N lobe of RCK2 activates the channel and allows K^+ flux. It is suggested that an expansion of the gating ring upon nucleotide binding induces the conformational changes within the pore-lining helices via the flexible linker, resulting in the active state (Figure 7 D). However, no structural information of the nucleotide-bound, active state is available. Instead, the structure of a variant L97D, which revealed an increased P_o and enhanced channel conductance, was obtained. This variant appears to promote the bending of the inner helices at the conserved hinge glycine (G92) inducing an opening of the pore, however, the gating ring remains bound to inactivating Ca^{2+}. The structure was interpreted to represent an intermediate state and it was hypothesised that an expansion of the gating ring in wildtype GsuK would allow the movements of TM2b and TM2c, which would lead to the rotation of L117 away from the ion permeation pathway, enabling K^+ flux. In addition to nucleotides and Ca^{2+}, a high-affinity binding site for Zn^{2+} was identified in the RCK domain. However, its functional role remains elusive.

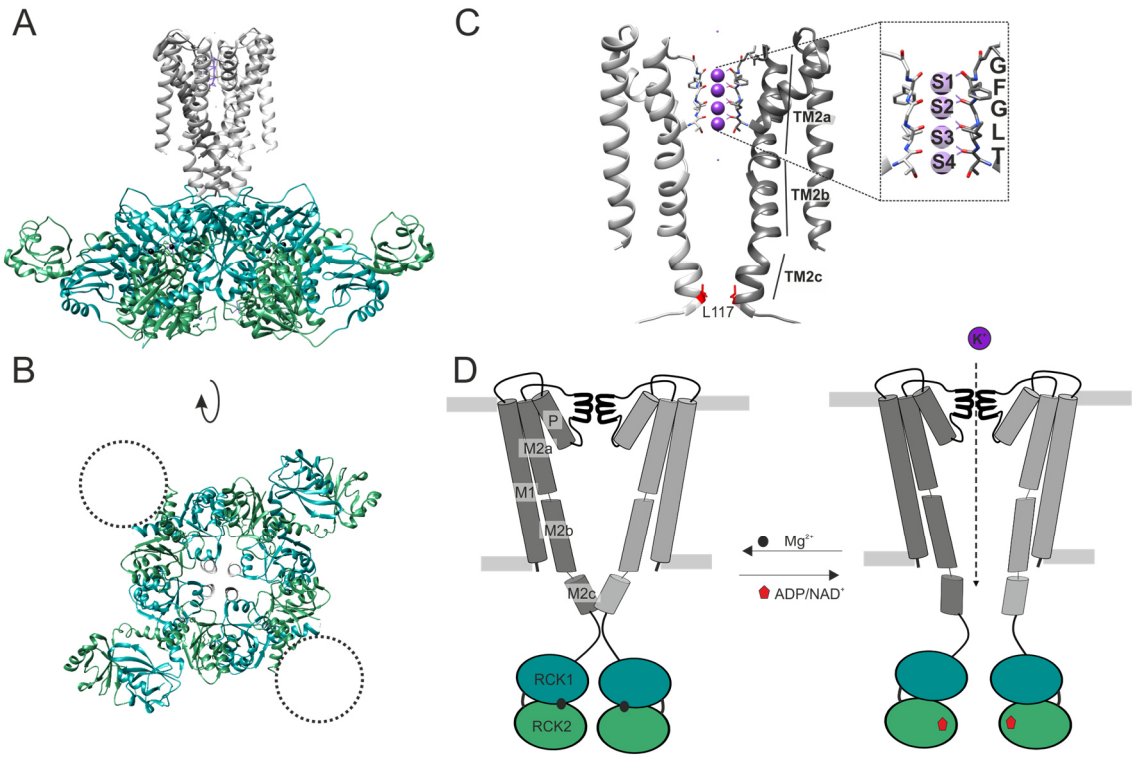

Figure 7: K^+ translocation by the Ca^{2+}- and nucleotide- regulated channel GsuK. A) Structure of GsuK from *G. sulfurreducens* in the closed, non-conductive state bound to Mg^{2+} (PDB: 4GX5). A tetrameric pore is gated by an octameric gating ring, which consist of four tandem RCK domains (RCK1 and RCK2), that are covalently fused to the transmembrane domains. B) Bottom-view of GsuK, representing the octameric ring in the inactive conformation. RCK1 and RCK2 are slightly different, which is why the ring does not adopt a two-fold symmetry. Two C lobes were not resolved in the structure, most likely due to a high flexibility (dashed circles). C) Presentation of two M1PM2 motifs to highlight the selectivity filter, in which the sequence (-TLGFG-) derivates from the classical selectivity filter, resulting in a decreased K^+ over Na^+ selectivity. The TM2 helices are longer by two helical turns when compared to MthK and can be divided in three parts: M2a, M2b and M2c. A hydrophobic residue (L117, shown in red) in each M2c helix forms the hydrophobic gate. C) Cartoon representation of the hypothesised gating mechanism. In the closed conformation (left) the RCK domain is bound to Mg^{2+}. The binding of ADP to RCK2 domains is suggested to induce expansion of the RCK ring, which in consequence relocate the M2c helices via the flexible linkers (right). This results in an open pore allowing K^+ flux.

1.7 Superfamily of K^+ transporter (SKT)

A large group of channels and transporters, which are involved in the adaptation to osmotic stress, belongs to the superfamily of K^+ transporters (SKT). These proteins are found in all kingdoms of life except animals and comprise the eukaryotic proteins HKT1,2 from plant membranes (Rubio et al, 1995; Schachtman & Schroeder, 1994; Uozumi et al, 2000), Trk1,2 from yeast (Gaber et al, 1988; Ko & Gaber, 1991), the *Tb*HKT from kinetoplasts of trypanosomes (Mosimann et al, 2010) and the prokaryotic members KtrB/D, TrkH/G and KdpA (Hesse et al, 1984; Schlösser et al, 1991; Takase et al, 1994). All members most

likely evolved from an ancestral homotetrameric 2-TM channel, by multiple gene duplications and gene fusions (Doyle et al, 1998; Schrempf et al, 1995), resulting in four nonidentical, covalently linked M1PM2 motifs, referred to as D1-D4 (Figure 8) and the four motifs are connected via cytoplasmic loops of different length and sequence. Several SKT members have partially broken transmembrane helices. Similar to the tetrameric 2-TM channel, the M1PM2 orient around a central axis and form the pathway for ions. TrkH/G and KdpA have two additional transmembrane helices, which are located in the periphery of the pore. While for KdpA it is known that they are involved in complex formation, their function in TrkH/G is unknown.

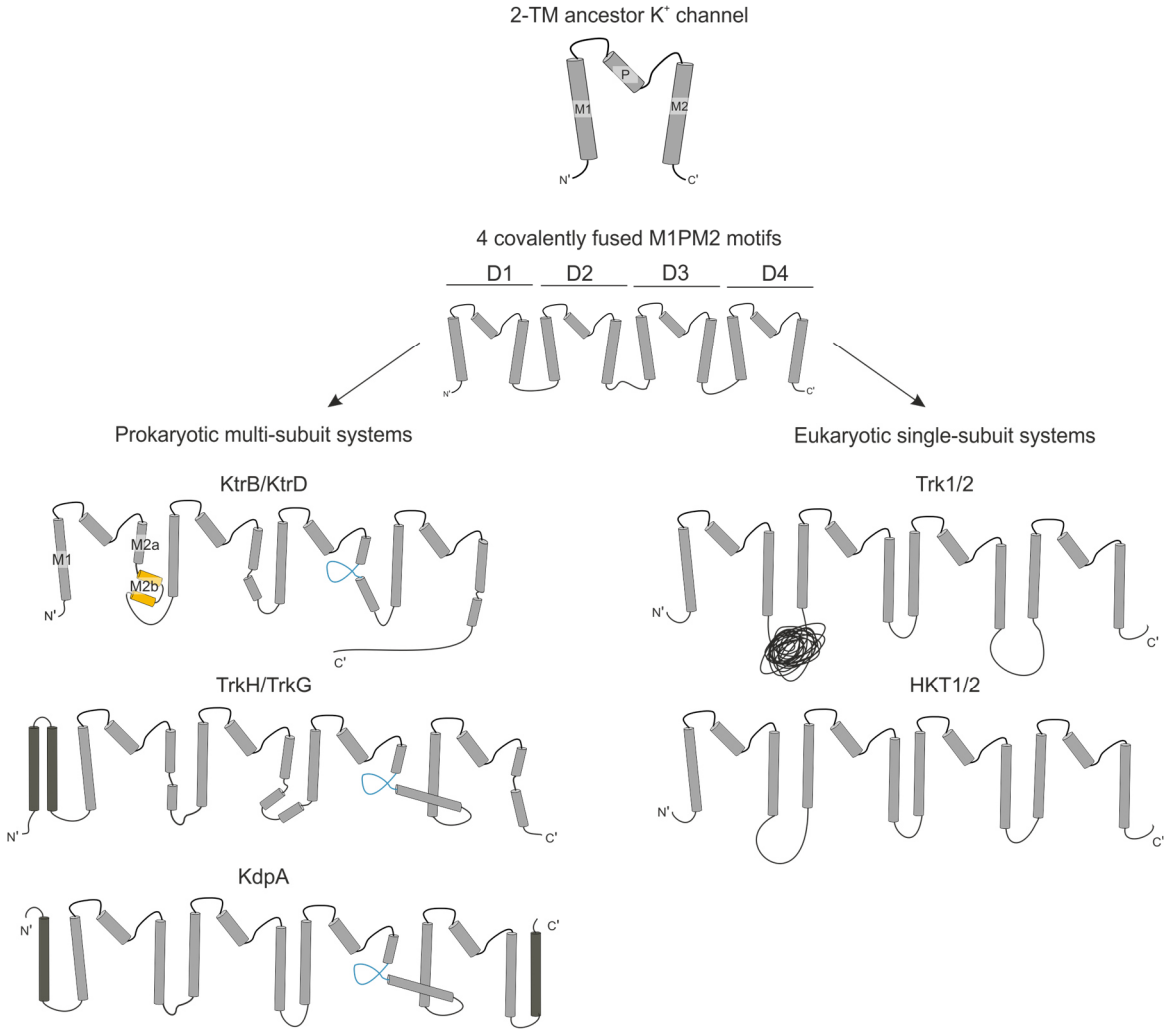

Figure 8: Superfamily of K^+ transporters (SKT). Members of the SKT most likely evolved from an ancestral 2-TM-type channel by gene duplication and fusion. In general, SKT members are formed by four non-identical covalently fused M1PM2 domains, referred as D1-D4. Therefore, a single monomer can assemble around a central axis to form a pore. Prokaryotic members are shown to form multi-subunit complexes containing regulatory subunits. In all SKT members, the selectivity filter is simplified when compared to the -TVGYG- sequence. Prokaryotic members further form an intramembrane loop, which is suggested to function as a gate (depicted in cyan). In KtrB and TrkH, all M2 helices are broken and referred to as M2a and M2b. They are suggested to play a crucial role in the translocation of K^+. Additional helices of unknown function are shown in dark grey. Eukaryotic members so far are suggested to form single-subunit systems. Figure adapted from Diskowski et al. (2015).

The selectivity filter sequence in the pore helix of each M1PM2 motif is reduced compared to KcsA, only the first glycine residue is conserved (Mäser et al, 2002; Tholema et al, 1999; Tholema et al, 2005). Here, members for which structural information is available (KtrB, TrkH and KdpA), this reduced version of the selective filter appears to form only one K^+ binding site at a position equivalent to S3 of KscA (Cao et al, 2011; Huang et al, 2017; Vieira-Pires et al, 2013). Such reduced selectivity filter would argue for a loss of selectivity for K^+ over other ions. However, this would be contradictive to the physiological role of the SKT systems, as in the context of osmoadaptation and pH homeostasis, the systems have to selectively take up potassium even at high external Na^+ concentrations.

While eukaryotic members appear to form single-subunit systems, prokaryotic members of the SKT form multi-subunit complexes with regulatory subunits. While TrkG/H and KtrB/D form a homodimer in the membrane and interact with an octameric ring of RCK domains, called TrkA and KtrA/C, respectively, KdpA forms a protein-multi-complex with the P-type ATPase subunit KdpB, the stabilising subunit KdpF, and the regulatory subunit KdpC (Cao et al, 2013; Greie, 2011; Nakamura et al, 1998). These complex-forming SKT members share a conserved structural feature: Instead of a helical bundle that regulate ions flux like in KscA, a so-called intramembrane loop restricts the central pore just below the selectivity filter. In KtrB and TrkGH, the loop is formed by small and polar residues as well as a conserved lysine of the broken transmembrane helix M2 of domain D3. Together with a highly conserved arginine from helix D4M2, the intramembrane loop forms a gate, which is suggested to be involved in gating of ion flux. Crystal structures of KtrB and TrkH showed, that the gate effectively blocks the pore (Cao et al, 2011; Vieira-Pires et al, 2013). In KdpA, the loop at the same position is composed of non-polar residues. Here it is immobile and is redirecting translocated K^+ towards the P-type ATPase KdpB. Hence, although the systems of the SKT share common features, they have developed different translocation mechanisms facilitating different functions. While the KdpFABC complex functions as an ATP-consuming high-affinity K^+ pump, KtrAB/CD and TrkAH/AG translocate K^+ as RCK-gated K^+ channels.

1.7.1 Potassium uptake by the multiligand-regulation potassium channels KtrAB and TrkAH

In most bacteria, KtrAB and TrkAH are the major K^+ uptake systems for everyday challenges (Epstein, 2003; Holtmann et al, 2003; Nakamura et al, 1998; Schlösser et al, 1995). They serve a role in general K^+ homeostasis, in osmoadaptation and potentially in the adjustment of the membrane potential (Zhang et al, 2020). The assembly of the systems is unique, as one octameric RCK ring (KtrA/TrkA), which lacks the covalent tether to a transmembrane domain, regulates two individual pores in the membrane (KtrB/TrkH). The two systems have been shown to be Na^+- or H^+-dependent, which is why KtrAB and TrkAH initially have been described to function as active transporters, coupling K^+ translocation to the transport of Na^+ or H^+, for the accumulation of K^+ against its gradient inside the cell. However, single channel recordings on TrkAH demonstrated that the system functions as channel (Cao et al, 2013). Similarly, by performing SSM-based electrophysiology and flux assays, KtrAB was shown translocate K^+ as a channel, neither symporting nor antiporting Na^+ (Mikušević et al, 2019; Vieira-Pires et al, 2013). While the transmembrane subunits KtrB and TrkH alone can translocate K^+ independent of ligands, the channel activity of the complexes has further been shown to depend on the presence of nucleotides. For both systems, ATP was shown to activate the systems, while ADP is required for the inactivation. Structural analysis of TrkAH from *Vibrio parahaemolyticus* and KtrAB from *B. subtilis* and *Vibrio alginolyticus* revealed a similar general architecture of the systems, as they both form complexes of two parallel pores made of a dimer of KtrB and TrkH, respectively, which are gated by an RCK ring formed of KtrAs and TrkAs, respectively. However, the organisation of the RCK domains as well as the interaction surface between the two subunits differ in TrkAH and KtrAB, which is why it is likely that the mechanism of gating is different.

1.7.2 H^+- and ATP-dependent K^+ translocating system TrkAH

The TrkAH complex consists of the SKT member TrkH and the regulatory cytosolic RCK protein TrkA. Two TrkH protomers assemble as a dimer in the membrane and form two individual pores for ion translocation (Cao et al, 2011). For cellular functions, TrkH is naturally associated to TrkA, which assembles as a tetrameric ring of soluble two tandem RCK domains (Figure 4 D, Figure 9 A) (Cao et al, 2013). Hence, in contrast to other tetrameric ligand gated K^+ channel like MthK and GsuK, the TrkA and TrkH are separately expressed proteins, which lack the covalent tether. The two RCK domains are referred to as RCK1 or RCK2 and each domain contains a C and an N lobe as described above (section 1.6), which are termed C1 and N1 or C2 and N2, respectively. Interaction in the tetrameric assembly of the gating ring is established by the same RCK domains, more precisely by N1 to N1 and N2 to N2, which results in two different interfaces upon

oligomerisation and a two-fold symmetry (Figure 9 B). The N lobes contain the conserved GxGxxG…D/E nucleotide binding motif and by binding of ATP or ADP to TrkA, the open probability is either increased or decreased, indicating that the channel is regulated by the binding of nucleotides (Cao et al, 2013). The selectivity filter of TrkH is simplified to the first glycine when compared to the canonical -TVGYG- sequence, like it is described for members of the SKT family (Figure 9 C). This results in a weaker selectivity for K^+ over other monovalent cations, as Rb^+ and Cs^+ are translocated with similar conductivities, while Na^+ and Li^+ have lower but still significant conductivities. The intramembrane loop below the selectivity filter, which is formed by the D3M2 helix, is involved in gating and its deletion results in a higher basal open probability and an insensitivity to ATP (Cao et al, 2013). The intramembrane gate is additionally formed by a highly conserved arginine within the same plane as the intramembrane loop and most likely acts by electrostatic interactions. Its mutation to an alanine resulted in an increase of K^+ uptake velocity, confirming its crucial role in channel gating (Cao et al, 2011).

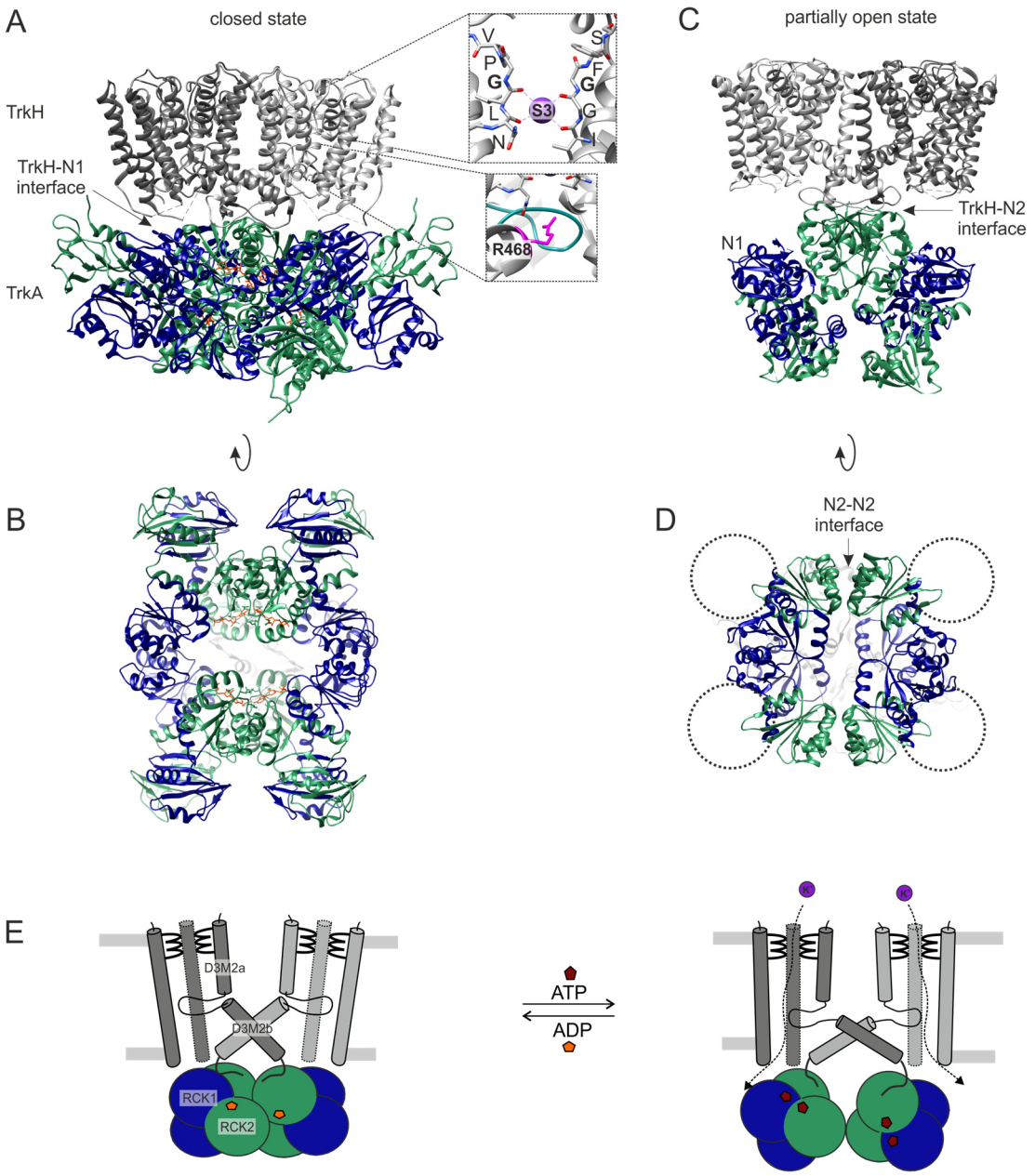

Figure 9: H^+- and ATP-dependent K^+-translocating system TrkAH. A) Structure of the TrkAH complex in the closed state (PDB: 6V4K). The dimeric TrkH pore is located in the membrane and is assembled to a ring of four TrkAs. The selectivity filter of TrkH is simplified and reduced to the first glycine of the canonical -TVGYG- sequence, which results in only one K^+ binding site (S3) (upper inset). The pore is closed, and the ion pathway is restricted by the intramembrane gate, which is formed by the intramembrane loop (dark cyan) and a conserved arginine residue (magenta) (lower inset). TrkH and TrkA interact via the interaction interface formed by N1 and N2 of TrkA B) Bottom-view of TrkAH. TrkA, consisting of RCK1 (blue) and RCK2 (green) domains adopts a two-fold symmetric tetramer, and an ADP molecule is bound to the N lobe of each RCK2 domain. The C lobes reach to the periphery. C) Structure of TrkAH in the partially open and ATP-bound conformation (PDB: 6V4J). Binding of ATP to the N lobes of both RCK1 and RCK2 domains induces the conversion of the TrkA tetramer to a dimer, which results in the loss of the interaction between N1 and TrkH. In consequence, the intramembrane loop is pulled open and ion flux is enabled. D) Bottom view of the ATP-bound conformation. Rotation of RCK2 N lobes relative to N lobes of RCK1 induces the breaking of the ring at the RCK2-RCK2 interfaces. The C lobes are not well resolved, and their locations are indicated by dashed circles. E) Cartoon illustration of the suggested gating mechanism. In the closed state (left), ADP is bound to RCK2 and the pore is restricted by the intramembrane loop and the highly conserved arginine. Upon the exchange of ADP by ATP (right), the RCK ring undergoes drastic conformational changes, which are transferred to the pore region, resulting in an open pore allowing K^+ flux. Cartoon was adapted from Stautz et al. (2021).

Molecular details on how the nucleotide binding induces the activation or inactivation of the channel were gained by obtaining structures of TrkAH from *V. parahaemolyticus* in the presence of ADP and ATP, respectively. ADP only binds to the N lobes of the RCK2 domain and enables TrkA to form a diamond shaped tetrameric ring, which is making contact to TrkH with both RCK1 and RCK2 domains (Figure 9 A, B, E) and two domains, those of the upper layer of the rings, interact with TrkH through a cytosolic loop which is connecting D3M2 with D4M1. The interface includes several salt bridges between positively charged residues of the loop and negative charged residues on TrkA. Especially, the interactions at the TrkH-N1 interface were shown to keep the pore-forming TrkH shut, as inserting mutations which are destroying this interface showed, that the ADP-induced channel closure was impaired, while the ATP-induced opening was less effected (Zhang et al, 2020). For the activation of the complex, ATP binds to both the N1 and the N2 domains, which is consistent with the available structures of the isolated TrkA ring (Figure 9 C, D, E) (Cao et al, 2013; Zhang et al, 2020). The N1 domain has a conserved arginine residue, R100 in *V. parahaemolyticus*, which allows to select for ATP by the recognition of the γ-phosphates, while the N2 domain can coordinate both nucleotides. The binding of ATP induces the rotation of each N2 domain relative to the N1 domain, which breaks the N2-N2 interfaces. This results in a splitting of the tetrameric gating ring into two dimers. While the N2 domain stays attached to TrkH, the interfaces with the N1 domains are completely abolished, which is described to pull on the D3M2b helices. Consequently, the rearrangement of these helices pull open the intramembrane loops, which leads to open pores (Figure 9). In agreement with this, single channel recordings indicate, that the two individual pores open in a mostly concerted fashion and upon activation a conductance of $3.3*10^7$ ions per seconds was determined (Cao et al, 2013). Thus, the current assumption is that the binding of ATP to the N1 domains is crucial for the activation of the TrkAH system, by inducing conformational changes within TrkA. By using a non-hydrolysable ATP homologue (ATPγS) it was ensured that only the binding and not the hydrolysis is responsible for the activation. The role of nucleotide binding to the N2 domains is less well understood, but it is suggested that the binding of ADP to the N2 sites stabilises the interaction between the N2 domains and TrkH and therefore the closed state. In addition to the conformational changes within TrkA, there is a relative rotation of the two TrkH protomers was observed during activation, which consequences are not understood so far. Interestingly, the ATP-bound structure of TrkAH is suggested to be only partially open, as the intramembrane loops still slightly restricts the pore, which is why it cannot be excluded that gating requires further conformational changes of TrkH (Zhang et al, 2020). Despite the missing details, the structural data in combination with functional data and electrophysiology allowed to paint a rather clear picture of the gating mechanism of TrkAH by now. In contrast, the detailed mechanism of its homologue KtrAB remains elusive with many more open questions.

1.7.3 KtrAB – the Na^+-, ATP- and ΔΨ-activated bacterial K^+ uptake system

The activity of the K^+ translocating system KtrAB depends on the presence Na^+ and ATP, and for efficient K^+ uptake a membrane potential is required (Kröning et al, 2007; Tholema et al, 1999). Under fully activating conditions KtrAB from *V. alginolyticus* expressed in *E. coli* cells takes up K^+ with a maximal uptake velocity (V_{max}) of 200 nmol * min^{-1} per mg cells (dry weight) and an apparent affinity (K_m) of 25 µM (Tholema et al, 2005). The system consists of the SKT member KtrB, which is embedded in the membrane as dimer, and the cytosolic RCK protein KtrA, which forms an octameric ring (Figure 10 A, C) (Holtmann et al, 2003; Nakamura et al, 1998). Like TrkH, KtrB forms two parallel pores. As expected for a member of the SKT family, KtrB contains the reduced selectivity filter when compared to the classical -TVGYG- motif, which consist of only four highly conserved glycine residues G70, G185, G290 and G402 in *V. alginolyticus*, one in each P-loop (Figure 10 C). The backbone carbonyl oxygens provide the coordination of K^+ similar to KscA, however only one binding site at a position equivalent to S3 was identified (Vieira-Pires et al, 2013). Mutations of this region demonstrated that each of the glycines determines the affinity of the KtrAB system to K^+, as an exchange of a single glycine to a serine converts the system to a Na^+-translocating system (Tholema et al, 2005). In contrast to TrkAH, a significantly different channel profile has been identified, showing that KtrB in fact functions as a K^+ selective system. While similar to TrkH all tested group 1 elements except Li^+ bind to KtrB, the translocation of ions via KtrB (in the absence of KtrA) decreased upon increasing ion size, which resulted in efficient translocation of only K^+ and Na^+. This selection is mediated by the intramembrane gate (intramembrane loop together with a highly conserved arginine residue in D4M2, R427 in *V. alginolyticus*), which limits ion passage by size restriction. Interestingly, in the presence of Na^+, the binding affinity for K^+ increases at least 10-fold resulting in preferred binding of K^+ over Na^+, which consequently allows the accumulation of K^+ under native-like mixed ion condition (Mikušević et al, 2019). The important gating function of the intramembrane loop, which is formed by the middle part of the broken D3M2 helix, was confirmed by point mutation in this region, which resulted in an increase of the V_{max} for K^+ translocation up to four-fold (Hänelt et al, 2010a; Hänelt et al, 2010b). The deletion of the complete intramembrane loop resulted in a hyperactive channel with a ten-fold higher maximal uptake velocity. In contrast, the ion binding was not affected by mutating the intramembrane loop, resulting in a similar apparent affinity for all variants. Together with the intramembrane loop, the highly conserved arginine residue is suggested to be involved in gating by electrostatic restriction of the pore (Diskowski et al, 2017; Szollosi et al, 2016; Vieira-Pires et al, 2013).

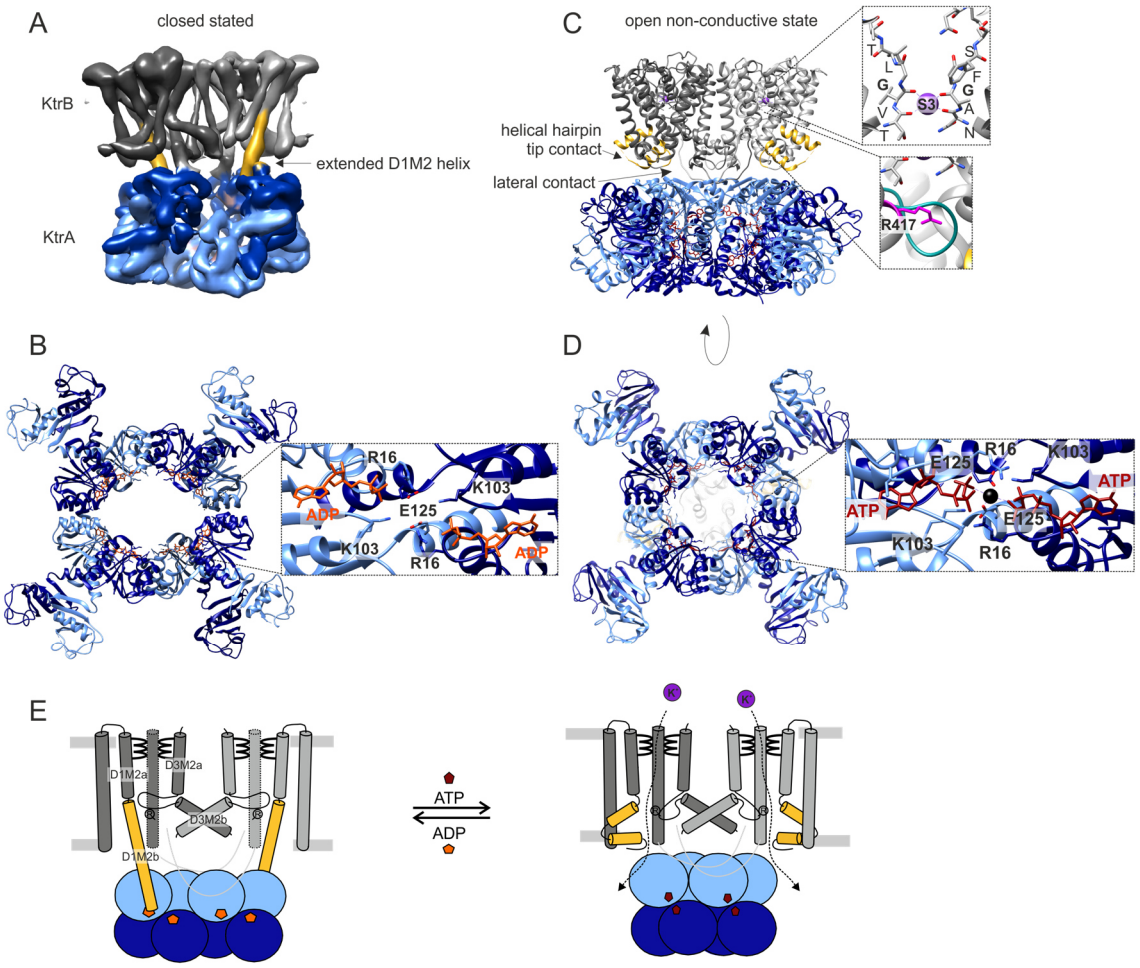

Figure 10: The Na^+-, ATP- and ΔΨ-activated bacterial K^+ uptake system KtrAB. A) 6 Å-resolution cryo-EM density map of the KtrAB complex in the ADP-bound, closed conformation (Diskowski et al, 2017). Pores are restricted by the intramembrane gate and K^+ flux is hindered. The D1M2 helices (yellow) are extended and interact with the octameric KtrA ring. The KtrA ring adopts an oval-shaped conformation and due to high flexibility, the C lobes are not well resolved. B) To analyse the coordination of ADP in the KtrA ring, the structure of the isolated KtrA ring is presented (PDB 4J91), as the resolution of the ADP-bound KtrAB complex is too low to identify residues which are involved in the coordination. Bottom-view of KtrA, representing the oval-shaped two-fold symmetric ring. ADP molecules are coordinated by the respective N lobe, mainly by interaction with the positive charges of R16 and K103. C) Structure of the ATP-bound conformation (PDB: 4J7C). Selectivity filter sequence is reduced to the first conserved glycine and K^+ is coordinated in position S3 (upper inset). Pore remains closed by the intramembrane loop (dark cyan lower inset), but D1M2 helices form a helical hairpin (yellow). D) The KtrA ring adopts a square-shaped four-fold symmetric conformation and has an ATP molecule bound to each N lobe. The ATP is coordinated by L103 from its own subunit, but it makes additional contact with R16 from the neighbouring subunit. Furthermore, a divalent cation (black ball), which is bound by E125, stabilises the square-shaped conformation. E) Cartoon illustration of hypothesised gating mechanism. Closed conformation of the KtrAB complex in the presence of ADP (left). Competitive binding of ATP results in the conformational changes in KtrA and the formation of helical hairpins, which unlocks the intramembrane loop to translocate K^+ (right). Cartoon adapted from Stautz et al. (2012).

Opening and closing of the channel is regulated by the soluble RCK protein KtrA. While KtrB alone was shown to translocate K^+ and Na^+ ions, the presence of KtrA confers Na^+ and ATP dependency to the system, increases the K^+ selectivity, and enhances the uptake velocity approximately 12-fold (Kröning et al, 2007; Tholema et al, 1999). In the absence of Na^+, the KtrAB complex is completely inactive. It is hypothesised that Na^+, in the presence of the KtrA gating domain, increases the gate's open probability (Mikušević et

al, 2019; Tholema et al, 1999; Tholema et al, 2005). While the binding site and structural consequences of Na^+ binding remain elusive, its effects on K^+ binding affinity and gating suggest that it is located within KtrB. A potential binding site located between helices D1M2 and D2M1 in close proximity to the selectivity filter, was identified by MD simulations. The potential residues are highly conserved within KtrBs. The close location to the gating region, which is regulated by conformational changes in KtrA, could explain the observed Na^+ dependency (Mikušević, 2020). However, further functional and structural evidence is required.

KtrA consists of only one soluble RCK domain (Figure 4 E), of which two form a stable dimer (Figure 5 A). For the octameric assembly, four of the dimers assemble and interact via the dimer-to-dimer interface (Figure 5 B, C). Similar to TrkA, the N lobes contain the conserved GxGxxG…D/E motif for binding of nucleotides, which induces the active or the inactive conformation (Albright et al, 2006). Structural analysis of the isolated KtrA ring and the KtrAB complex showed that upon binding of ATP and ADP, respectively, the RCK ring undergoes conformational changes (Figure 10 B, D) (Albright et al, 2006; Diskowski et al, 2017; Szollosi et al, 2016; Teixeira-Duarte et al, 2019; Vieira-Pires et al, 2013). In the inactive, ADP-bound state the ring adopts a twofold symmetric oval-shaped conformation spanning the width of the dimer interface (Figure 10 B). In KtrA from *B. subtilis* the coordination of ADP is established only by residues from the own subunit, in particular by the interaction of the β phosphates with residues R16 and K103 (Figure 10 B inset). For activation, ADP is competitively replaced by ATP, resulting in a square-shaped conformation (Figure 10 D). The square-shaped conformation is induced by changes in the intra-dimer hinge angle, which is the relative angle between the crossover helices in a dimer. The changes bring closer the two nucleotide binding sites and allows the establishment of interactions between the phosphate groups and residues of the same and the neighbouring KtrA subunit. While the coordination of the nucleotides' adenosine groups is similar to ADP, the phosphates are rearranged. In detail, residues R16 from two neighbouring KtrA subunits from *B. subtilis* are located between the two nucleotides and coordinate the closely positioned negatively charged β-phosphate groups (Figure 10 D inset). Furthermore, a highly conserved glutamate (E125 in *B. subtilis*) was identified at the dimer-to-dimer interface in close proximity to the γ-phosphates. The residue from both subunits can coordinate a divalent cation, probably Mg^{2+}, which is further stabilised by the γ-phosphates. Thus, both inter-subunit interactions tether the two ATP molecules stabilising the square-shaped, ATP-bound conformation of the octameric ring (Teixeira-Duarte et al, 2019). Further analysis showed that variants with a mutation of the arginine were still able to adopt the square-shaped conformation, while mutations of the glutamate resulted in a non-square-shaped conformation of the KtrA ring in the presence of both ADP and ATP, respectively. In line with this, liposome-based flux assays and whole-cell uptake experiments revealed that the glutamate residue is crucial for ion translocation, while the

arginine is not necessarily required for activation (Teixeira-Duarte et al, 2019). In addition to ADP, KtrAB from Gram-positive bacteria were shown to be inactivated by the second messenger c-di-AMP. C-di-AMP binds to the C lobes of the RCK domains (Stülke & Krüger, 2020). A crystal structure of a KtrA C lobe dimer from *Staphylococcus aureus* in the presence of c-di-AMP showed that it promotes a stabile interaction by binding to the dimer interface, thereby inducing conformational changes (Kim et al, 2015). However, the effect on the octameric KtrA ring remains unknown.

Since KtrA and KtrB are not covalently tethered, similar to TrkAH, complex formation requires an interaction interface of both subunits. Two distinct interaction sites have been identified from the ATP-structure of *B. subtilis* KtrAB and described as lateral contact and tip contact (Vieira-Pires et al, 2013). The lateral contact is formed by the middle part the C termini of KtrB and includes the 30 amino acid long loop, that extends to the cytoplasm interacting with the neighbouring KtrB subunit and the octameric KtrA ring (Figure 10 A). On the one hand this interaction stabilises the dimer formation, and on the other hand it establishes complex formation. In the neighbouring KtrB subunit the C-terminal carboxyl group of a highly conserved glycine (G445) is stabilised by salt bridge formation with the positively charge of the conserved lysine (K315) of the intramembrane loop. Deletion of the last four residues of the C terminus led to a non-function channel and abolished the complex formation, while a deletion of the last 10 amino acids even prevented dimer formation (Vieira-Pires et al, 2013). In line with this, the deletion of the intramembrane loop does not only affect the gating, but as well abolishes the complex formation (Hänelt et al, 2010a). The second contact was initially described as the tip contact, because in the ATP-bound conformation the helical loop between D1M2a and D1M2b of the broken D1M2 helix was shown to make direct but minor interaction with KtrA (Figure 10 C). However, a cryo-EM map of the ADP-bound conformation uncovered a much more significant interaction between the D1M2 helix and the oval-shaped KtrA ring, as the helical hairpin rearranges into an elongated subunit-interconnecting helix, extending from KtrB into KtrA (Figure 10 A, E) (Diskowski et al, 2017). Therefore, it appears that the tip contact is not only required for complex formation but presents a crucial element for controlling the allosteric coupling between the two subunits. Together with the D4M2b helix, which is also extended in the ADP-bound conformation, the ion pathway is narrowed, and the intramembrane loop is most likely locked in a ridged closed conformation. For the activation of the system, the current working model suggests, that upon stimulating conditions like hyperosmotic stress under which the internal ATP and possibly Na^+ concentration transiently increase, ADP is replaced by ATP in a competitive manner. This induces conformational changes within the RCK domain to a square-shaped gating ring. In consequence, the extended D1M2 helices form a helical hairpin, and D4M2b partially unfolds, which unlocks the intramembrane loop allowing K^+ flux (Figure 10 E). For further stabilisation of the open conformation Na^+ might bind to KtrB. Subsequently, increasing cellular K^+ concentrations induce the exchange of

ATP by ADP in KtrA, which results in adopting the closed conformation. However, the exact conditions under which the two nucleotides are exchanged remain puzzling as under all cellular conditions, the ATP concentration exceeds the ADP concentration, while similar binding affinities of both nucleotides to KtrA in the low micromolar range were determined (Diskowski et al, 2017; Kröning et al, 2007). Furthermore, it appears that at least one activation stimulus is missing, as the structure of the ATP-bound active state presents the intramembrane loop in the closed conformation, although, high concentrations of both ATP and Na^+ were present.

2 Motivation and Objectives

The bacterial lifestyle is unique and can have severe effects on human health. As highlighted in the introduction the cells can survive under constant changes in environments and their habitats include extreme conditions, for which they have developed adaptation mechanisms. For the adaptation to hyperosmotic stress, the bacterial potassium uptake system KtrAB plays a crucial role. As an initial response it rapidly takes up K^+ to avoid plasmolysis. Furthermore, KtrAB is involved in the daily K^+ homeostasis, which needs to be tightly regulated, as K^+ is involved in many essential cellular processes like pH homeostasis, membrane potential adjustments, maintaining of turgor pressure, regulation of protein synthesis and enzyme activation as well as electrical signalling in biofilms. Additionally, K^+ homeostasis has been implicated in the virulence of various pathogenic bacteria. For example, *Staphylococcus aureus* exhibits an unusual high osmo- and Na^+-tolerance, which supports human colonisation, pathogenesis, and growth on food. These tolerances are mediated by KtrAB and KdpFABC and a deletion of the Ktr system resulted in sensitivity to hyperosmotic conditions and, hyperpolarisation as well as increased susceptibility to aminoglycoside antibiotics and cationic antimicrobials (Gries et al, 2013; Price-Whelan et al, 2013).

The system consists of the K^+-translocating dimeric channel subunit KtrB and the octamer-forming cytoplasmic regulatory RCK subunit KtrA. Both subunits are not covalently linked, which strongly differs from other RCK-gated K^+ channels like MthK or GsuK, in which covalently tethered cytoplasmic RCK domains regulate a single tetrameric pore. Consequently, a modified gating mechanism is suggested. Based on functional and structural data, it is hypothesised that the activation of KtrAB depends on the binding of ATP and Mg^{2+} to KtrA, while ADP binding at the same site results in inactivation, mediated by conformational rearrangements. However, it is still poorly understood how the nucleotides are exchanged, as they were determined to have very similar affinities. In addition, it is not clear, how the resulting conformational changes in KtrA control gating in KtrB, as the present working model has various weaknesses. In the published ATP-bound structure the intramembrane loop remains in the closed conformation although the complex was prepared under activating conditions, which is why it can be speculated, that conductivity of the channel depends on at least one more activating stimulus. Furthermore, the resolution of the ADP-bound KtrAB map was too low to identify any details on the stabilisation of the closed channel.

Therefore, the aim of this Ph.D. thesis was to clarify following open questions regarding the gating mechanism of KtrAB: How does ATP and ADP bind to KtrA and how can both nucleotides be exchanged by one another? Does only the binding of nucleotides trigger conformational changes in KtrA and the KtrAB complex, or is an additional, so far unknown, stimulus required? If an additional stimulus is required, what is it? Further, it would be important to understand how are the conformational changes in the RCK domain transmitted to KtrB and how does the intramembrane loop adopt the open conformation, enabling K^+ flux? How are the ADP-bound, closed state and the ATP-bound, open state stabilised? Since the two subunits are not covalently linked, is the assembly of KtrA and KtrB is a dynamic process? And does the assembling and disassembling of the two subunits depend on the osmotic conditions? Are cellular changes upon osmotic stress, like changing lipid composition involved in the activation of the KtrAB complex? If yes, how does the protein complex interact with the lipids and how is this interaction involved in the regulation?

3 Material

3.1 Chemicals and Consumables

All basic chemicals and consumables used in this study were supplied by Carl Roth GmbH & Co. KG, Merck KGaA (Sigma-Aldrich Chemie GmbH) and VWR International GmbH, respectively. Chemicals, consumables, and kits with a different supplier are listed in Table 1.

Table 1: List of specific chemicals, consumables, and kits from different suppliers.

Chemical/Consumable/Kit	Supplier
(1-Oxyl-2,2,5,5-tetramethylpyrroline-3-methyl) methanethiosulfonate (MTS)	Toronto Research Chemicals Inc.
[2,5',8-^{3}H(N)]-ATP (^{3}H-ATP)	PerkinElmer
[2,8-^{3}H]-ADP (^{3}H-ADP)	Biotrend
[α^{32}P]-ATP	Hartmann Analytic
10 mm filter supports	Avanti® Polar Lipids, Inc.
9-Amino-6-Chloro-2-Methoxyacridine (ACMA)	Thermo Fisher Scientific Inc.
Agar	Formedium™
Amicon® Ultra-0.5/4 centrifugal filters Ultracel® (MWCO 100 kDa)	Merck Millipore Ltd.
BamHI	New England Biolabs
BioBeads SM-2	Bio-Rad Laboratories, Inc.
BN sample buffer (2x)	SERVA
Cardiolipin (*E. coli* disodium salt, 10 mg/ml) in chloroform	Avanti® Polar Lipids Inc.
Centriprep® Ultracel® YM-50 (MWCO 50 KDa)	Merck Millipore Ltd.
CF-1.2/1.3-4Cu grids	Protochips, Inc.
Cloning Enhancer	TaKaRa
Copper-chelated PVT SPA beads	PerkinElmer
DNaseI	AppliChem GmbH
dNTPs	Thermo Fisher Scientific Inc.
DpnI	Thermo Fisher Scientific Inc.
***E. coli* total lipid extract**	Avanti Polar Lipids, Inc.
EcoRI	New England Biolabs
Gel Loading Dye Purple (6x)	New England Biolabs
Gene Frame®	Thermo Scientific
GeneRuler 1kb DNA Ladder	Thermo Fisher Scientific Inc.
His-Pur™ Ni-NTA Resin	Thermo Fisher Scientific Inc.

Immobilized γ-Aminophenyl-ATP (C10-spacer)	Jena Bioscience
In-Fusion® HD Cloning Kit	TaKaRa
Native Marker, Liquid Mix for BN	SERVA
n-Dodecyl β-maltoside (DDM), Anagrade	Glycon
NEBuffer™	New England Biolabs
Nitrocellulose blotting membrane 0.45 µm	GE Healthcare
NucleoSpin® Gel and PCR Clean-up	Macherey-Nagel GmbH & Co. KG
NucleoSpin® Plasmid EasyPure	Macherey-Nagel GmbH & Co. KG
Nuclepore Track-Etch Membrane (200, 400 nm)	Whatman®
PageRuler™ prestained protein ladder	Thermo Fisher Scientific Inc.
Phusion High-Fidelity DNA Polymerase	Thermo Fisher Scientific Inc.
Pierce™ 1-Step Transfer Buffer	Thermo Fisher Scientific Inc.
Pierce™ BCA Protein Assay Kit	Thermo Fisher Scientific
Q band suprasil EPR tubes 1.6 x 1.1 x 100 R/B	Wilmad LabGlass
Q5® Site-Directed Mutagenesis Kit	New England BioLabs
SapI	NEB
Serva*Gel*™ N 4-16	SERVA
Slide-A-Lyzer™ 3.5 kDa	Thermo Fisher Scientific Inc.
Superdex® 200 Increase 10/300 GL	GE Healthcare
Superose® 6 Increase 10/300 GL	GE Healthcare
SwaI	New England Biolabs
SYPRO™ Orange dye	Thermo Fisher Scientific Inc.
T4-DNA-ligase	New England Biolabs
T4-DNA-ligase buffer	New England Biolabs
Teflon-coated microscope slides	Hendley-Essex
TLC PEI Cellulose F plates	Merck Millipore Ltd.
Ultrafree®-CL Low-binding Durapore PVDF filter	Merck Millipore Ltd.

3.2 Buffers, Solutions and Media

Buffers and solutions used for performed experiments are summarised in Table 2.

Table 2: Composition of buffers and solutions used in this thesis.

Buffer/Solution	Composition
10x TBS buffer	200 mM Tris-HCl pH 8, 1.5 M NaCl
3C protease IMAC buffer	50 mM Tris-HCl pH 8, 300 mM NaCl, 1 mM DTT, 10% glycerol (v/v)
3C protease lysis buffer	50 mM Tris-HCl pH 8, 200 mM NaCl, 1 mM DTT, 1 mM $MgCl_2$, 1 mM PMSF, 1 spatula tip of DNase I
3C protease storage buffer	50 mM Tris-HCl pH 8, 150 mM NaCl, 1 mM DTT, 10 mM EDTA, 20% glycerol (v/v)
BN-Anode buffer	500 mM BisTris pH 7.0
BN-Cathode buffer	500 mM Tricine, 150 mM BisTris
Buffer MSP1	40 mM Tris-HCl pH 8, 300 mM NaCl
Buffer MSP2	40 mM Tris-HCl pH 8, 300 mM NaCl, 1% Triton X-100 (v/v)
Buffer MSP3	40 mM Tris-HCl pH 8.9, 300 mM NaCl
Buffer MSP4	40 mM Tris-HCl pH 8.9, 300 mM NaCl, 50 mM cholic acid
Buffer MSP5	40 mM Tris-HCl pH 8.9, 300 mM NaCl, 50 mM imidazole
Buffer S	50 mM Tris-HCl pH 8, 420 mM NaCl, 180 mM KCl
Buffer W	20 mM Tris-HCl pH 8, 140 mM NaCl, 60 mM KCl
Coomassie blue buffer	40% ethanol (v/v), 10% acetic acid (v/v), 0.25% Coomassie Blue G-250 (w/v)
Cryo-EM buffer	20 mM Tris-HCl pH8, 70 mM NaCl, 30 mM KCl, 0.025% DDM (v/v)
Destaining buffer	40% ethanol (v/v), 10% acetic acid (v/v)
Dialysis buffer	40 mM Tris-HCl pH 8, 300 mM NaCl, 10% Glycerol
ECL-1	100 mM Tris-HCl pH 8, 2.5 mM Luminol, 0.4 mM p-coumaric acid
ECL-2	100 mM Tris-HCl pH 8, 0.02% H_2O_2 (v/v)
Electrophoresis buffer (10x)	250 mM Tris, 1.9 M glycine, 1% SDS (w/v)
Ethidium bromide solution	1% ethidium bromide (v/v) in ddH_2O

Inside reconstitution buffer	20 mM Hepes-HCl pH 7.4, 195 mM KCl, 5 mM NaCl, 1 mM $MgCl_2$
ITC buffer	25 mM Hepes pH 8, 140 mM NaCl, 60 mM KCl
LILBID-MS buffer	20 mM Tris-HCl pH 8, 25 mM NaCl, 15 mM KCl, 2.5 mM β-mercaptoethanol, 0.02% DDM (v/v)
Outside reconstitution buffer	20 mM Hepes-HCl pH 7.4, 195 mM sorbitol, 5 mM NaCl, 1 mM $MgCl_2$
SDS PAGE loading buffer (3x)	200 mM Tris-HCl pH 6.8, 6% SDS (w/v), 30% glycerol (v/v), 0.06% bromophenol blue (w/v), 7.5% β-mercaptoethanole (v/v)
Separation gel buffer	1.5 M Tris-HCl pH 8.8, 0.4% SDS (w/v)
Stacking gel buffer	0.5 M Tris-HCl pH 6.8, 0.4% SDS (w/v)
TBS-T buffer	1x TBS, 0.1% Tween 20 (v/v)
TCA	5% trichloracetic acid (w/v)
TEA buffer (50x)	2 M Tris-HCl pH 8.3, 1.75% AcOH (v/v), 50 mM EDTA
TES buffer	10 mM Tris-HCl pH 8, 100 mM NaCl, 1 mM EDTA

Media used for the cultivation of *B. subtilis,* and *E. coli* cells are listed in Table 3. Antibiotics and the respective concentration used for specific cells are listed in Table 4. For complementation assays (section 4.2.4), K0 medium was supplemented with different KCl concentrations from a sterile 1 M KCl stock. All used glassware, media and supplements were autoclaved, heat-sterilised or sterile filtered. To prepare solid media, 1.5% agar was added to the respective media.

Table 3: Media used for bacterial growth.

Medium	Composition
BMM-K^+ free	50 mM Tris-HCl pH 7.5, 15 mM $(NH_4)_2SO_4$, 8 mM $MgSO_4$, 7 mM Na-Citrate, 2 mM $CaCl_2$, 1 µM $FeSO_4$, 10 µM $MnSO_4$, 4.5 mM L-glutamate, 0.6 mM NaH_2PO_4, 0.78 mM L-tryptophane, 11 mM D-glucose
K0	46 mM Na_2HPO_4, 23 mM NaH_2PO_4, 7.6 mM $(NH_4)_2SO_4$, 1 mM Na-Citrate, 6 µM $FeSO_4$, 0.4 mM $MgSO_4$, 20 µg/ml methionine, 1 µg/ml thiamine, 0.2% glycerol (v/v)
K115	46 mM K_2HPO_4, 23 mM KH_2PO_4, 1 mM Na-Citrate, 7.6 mM $(NH_4)_2SO_4$
K30	34 mM Na_2HPO_4, 17 mM NaH_2PO_4, 12 mM K_2HPO_4, 6 mM KH_2PO_4, 7.6 mM $(NH_4)_2SO_4$, 1 mM Na-Citrate, 6 µM $FeSO_4$, 0.4 mM $MgSO_4$, 20 µg/ml methionine, 1 µg/ml thiamine, 0.2% glycerol (v/v)
KML	1% Trypton (w/v), 0.5% Yeast Extract (w/v), 1% KCl (w/v)
LB	1% (w/v) Trypton, 0.5% (w/v) Yeast Extract, 1% (w/v) NaCl
LB_{50KCl}	1% (w/v) Trypton, 0.5% (w/v) Yeast Extract, 0.7% NaCl (w/v), 0.3% KCl (w/v)
SMM	0.2% $(NH_4)_2SO_4$ (w/v), 1.4% K_2HPO_4 (w/v) ,0.65% KH_2PO_4 (w/v), 0.1% Na-Citrate (w/v), 0.02% $MgSO_4$ (w/v)
Transformation Medium 1	1x SSM, 0.48% glucose (v/v), 60 mM $MgSO_4$, 0.02% casamino acids (v/v), 0.02 mg/ml tryptophan, 6 µM Fe-Citrate
Transformation Medium 2	1x SSM, 0.48% glucose (v/v), 60 mM $MgSO_4$

Table 4: Used antibiotics and their respective concentrations.

Antibiotic	Stock solution	Final concentration
Ampicillin (Amp)	100 mg/ml in 50% ethanol	100 µg/ml
Kanamycin (Kan)	25 mg/ml in ddH_2O	25 µg/ml
Erythromycin (Ery)	20 mg/ml in ddH_2O	4 µg/ml
Chloramphenicol (Chl)	30 mg/ml in 50% ethanol	5 µg/ml
Spectinomycin (Spec)	100 mg/ml in ddH_2O	100 µg/ml
Tetracyclin (Tet)	6 mg/ml in 50% ethanol	6 µg/ml

3.3 Bacterial strains, plasmids, and primers

Bacterial strains used in this study are listed in Table 5. *B. subtilis* strains were used for microscopy and complementation, *E. coli* cells were used for cloning, K^+ uptake assays and protein production.

All plasmids used or cloned in this study are summarised in Table 6.

Table 5: Used *B. subtilis* and *E. coli* cells. The relevant genotype of each strain is annotated.

Strain	Relevant genotype	Reference
***B. subtilis* 168**	*trpC2*	Barbe et al, 2009*
***B. subtilis* JS03**	168, *ktrAB::kan*	This study
***B. subtilis* JS38**	168, *ktrAB::kan, kimA::ery*	This study
***B. subtilis* JS31**	168, *ktrA::pMutin4-ktrA$_{msfgGFP}$-P$_{spac}$-ktrB, erm*	This study
***B. subtilis* JS33**	kimA::chl, *ktrA::pMutin4-ktrA$_{msfgGFP}$-P$_{spac}$-ktrB, erm*	This study
***B. subtilis* JS34**	168, amyE::P$_{xyl}$-*ktrA$_{msfGFP}$-ktrB*, *spec*	This study
***B. subtilis* JS35**	JS03*, amyE::P$_{xyl}$-ktrA$_{msfGFP}$-ktrB, spec*	This study
***B. subtilis* JS41**	JS38, *amyE::P$_{xyl}$-ktrA$_{msfGFP}$-ktrB, spec*	This study
***B. subtilis* JS59**	168*, ktrAB::kan, kimA::ery, ktrD::tet,* amyE::P$_{xyl}$-KtrA$_{msfGFP}$-KtrB, *spec*	This study
***B. subtilis* JS58**	168*, ktrAB::kan, kimA::ery, ktrD::tet,* amyE::P$_{xyl}$-KtrA$_{msfGFP}$, *spec*	This study
***B. subtilis* JS46**	JS03, *amyE::P$_{xyl}$-ktrA-ktrB$_{msfGFP}$*, *spec*	This study
***B. subtilis* JS82**	168*, psd::ery, amyE::P$_{xyl}$-ktrA-ktrB$_{msfGFP}$, spec*	This study
***B. subtilis* JS87**	168*, clsA::tet, ywjE(clsB)::spec, ywjE::kan, amyE::P$_{xyl}$-ktrA-ktrB$_{msfGFP}$, spec*	This study
***E. coli* LB 2003**	F$^-$ *thi metE rpsL gal rha kup1 ΔkdpABC5 ΔtrkA*	Stumpe & Bakker, 1997
E. coli* C43 (DE3)Δ*acrAB	F$^-$ *ompT gal dcm h$_s$dS$_B$* (r$_B^-$ m$_B^-$)(DE3)*pLysS (Cm^R)*	Miroux & Walker, 1996
***E. coli* NEB5α**	*fhuA2 Δ(argF-lacZ)^{U169} phoA glnV44 Φ80 Δ(lacZ)M15 gyrA96 recA1 relA1 endA1 thi-1 hsdR17*	New England Biolabs

* Kind gift from H. Strahl, Newcastle University.

Table 6: Overview of plasmids used in this thesis. Antibiotic resistance is indicated by a superscript R.

Plasmid	Description	Reference
pMUTIN4	*bla^R, erm^R, P$_{spac}$, mcs, lacZ, lacI*	Vagner et al, 1998
pJS04	pMUTIN4 containing *ktrA'$_{msfGFP}$* for native expression and *ktrB* downstream of *P$_{spac}$*, ITPG inducible, *erm^R, bla^R*	This study
pJS03	pHJS105, with *BsktrAB* cloned into *MCS,* N-terminal *msfgfp* at *ktrA* optimised RBS	Stautz, 2016
pJS05	pJS03, Bs*ktrAB*, Δ*msfgfp*	Stautz, 2016
pJS08	pJS05, *msfgfp* fused C-terminally to *ktrA* (*BsktrA$_{msfGFP}$-ktrB)* downstream *P$_{xyl,}$* for integration at *amyE* locus, xylose-inducible, *spec^R*	Stautz, 2016
pJS09	pJS05, *msfgfp* fused N-terminally to *ktrB* (*BsktrA-$_{msfGFP}$ktrB)* downstream *P$_{xyl,}$* for integration at *amyE* locus, xylose-inducible, *spec^R*	This study
pJS11	*BsktrA$_{msfGFP}$* downstream *P$_{xyl,}$* for integration at *amyE* locus, xylose-inducible, *spec^R*	This study
pIH301-100 E449C	pBAD18 derivate coding for *his10-ktrAB* from *V. alginolyticus,* cysteine-free background*,* with point mutation E449C	This study
pEL903-100 E449C	pBAD18-derivate coding for *ktrB-his6* from *V. alginolyticus,* cysteine-free background (*ktrB*: C90S, *ktrA*: C21A/C56S/C172A), with point mutation E449C	This study
pEL901	pBAD18 derivate, *ktrB* from *V. alginolyticus, amp^R*	Tholema et al, 2005
pEL901 Δ2-19	pEL901 with deletion of amino acid 2-19, *amp^R*	Griwatz, 2021
pEL901-100 T318C	pEL901 with cysteine-free background (C90S), with point mutation T318C	This study
pEL901-100 Δ2-19 T318C	pEL901, with cysteine-free background, with deletion of amino acids 2-19 and point mutation T318C	This study
pBKtrAC3H	pBAD24 derivate, *ktrA-3C-his10* from *V. alginolyticus, amp^R*	Schrecker, 2018
pBKtrAC3H-100	pBKtrAC3H, cysteine free, C21A/C56S/C172A	This study

pBKtrANH3	pBAD24 derivate, *his10-3C-ktrA* from *V. alginolyticus, amp^R*	This study
pBKtrBC3H	pBAD24 derivate, *ktrB-3C-his10* from *V. alginolyticus, amp^R*	This study
pBKtrBNH3	pBAD24 derivate, *his10-3C-ktrB* from *V. alginolyticus, amp^R*	This study
pKT84	pHG165 derivate, *ktrAB* from *V. alginolyticus, amp^R*	Nakamura et al, 1998
pKT84 K325A	pKT84 with point mutation K325A, *amp^R*	This study
pKT84 Q99A	pKT84 with point mutation Q99A, *amp^R*	This study
pKT84 Δ2-19	pKT84 with deletion of amino acid 2-19, *amp^R*	Griwatz, 2021
pKT84 F10S/Y11S/V12S	pKT84 with point mutation F10S, Y11S, V12S, *amp^R*	Griwatz, 2021
pKT84 R7E	pKT84 with point mutation R7E, *amp^R*	Griwatz, 2021
pKT84 Δ2-15	pKT84 with deletion of amino acid 2-15, *amp^R*	This study
pKT84 R17A	pKT84 with point mutation R17A, *amp^R*	This study
pKT84 K16A/R17A/K19A/K21A	pKT84 with point mutation K16A, R17A, K19A, K21A, *amp^R*	Ohlemüller, 2021
pMSP2N2	pET vector, containing the genes for production of MSP2N2 with TEV protease site and N-terminal His_7-Tag	Addgene
pB3CNH$_6$	HRV-3C-protease with N-terminal His6-Tag	Gift from Eric Geertsma

Primer used for PCRs in this study are listed in Table 7.

Table 7: Primers used in this study.

Primer name	Sequence (5'-3')
KtrA_Fx_f	ATATATGCTCTTCTAGTAAAACAGGTGATAAGCAATTCGCTGTT
KtrA_Fx_r	TATATAGCTCTTCATGCTAATGATTTCAGCTTGTTTGCCAACTT
KtrB_Fx_f	ATATATGCTCTTCTAGTACTCAATTTCATCAGAGAGGCGTTTTT
KtrB_Fx_r	TATATAGCTCTTCATGCACCAGTAAGAACCGTGTCTTCTGGGTA
KtrA_C21A_f	GGTTTGGCGGTAGCTAAAGAATTACAAG
KtrA_C21A_r	CTTGTAATTCTTTAGCTACCGCCAAACC
KtrA_C56A_f	GTGGCAAATGCTACTCATGAAG
KtrA_C56A_r	CTTCATGAGTAGCATTTGCCAC
KtrA_C172A_f	GATTTGGCGCTGGCCAAGGTCGAAG
KtrA_C172A_r	CTTCGACCTTGGCCAGCGCCAAATC
KtrB_C90S_f	CTTCTGATGTCCTTGATGCAGATC
KtrB_C90S_r	GATCTGCATCAAGGACATCAGAAG
KtrB_Q99A_f	GCGGCTTAGGGgcAATGACCTTATCTGCG
KtrB_Q99A_r	CGCAGATAAGGTCATTGCCCCTAAGCCGC
KtrB_K325A_f	GGTGGCGGTATCGCGGTGTCTACTT
KtrB_K325A_r	AAGTAGACACCGCGATACCGCCACC
KtrB_E449C_f	GATTAAGTACCCATGTGACACGGTTCTTACTGG
KtrB_E449C_r	CCAGTAAGAACCGTGTCACATGGGTACTTAATC
KtrB_Δ2-19_f	GCGAAAGGTGGCGAACCGCGCATTATATT
KtrB_Δ2-19_r	CATGTATATCTCCTTGGTACCGAGCTCGAATTCG
KtrAB_Δ2-15_f	AAACGAGATAAAGCGAAAG
KtrAB_Δ2-15_r	CATGTATATCTCCTTGGTACCGAGCTCGAATTCG
KtrAB_R17A_f	CAGACGGCAAAGCAGATAAAGCGAAAGG
KtrAB_R17A_r	CCTTTCGCTTTATCTGCTTTGCCGTCTG
Lin_pJS05_$_{GFP}$KtrB_f	ATGACACTTCAAAAGGATAA
Lin_pJS05_$_{GFP}$KtrB_r	CCTAGGAATCTCCTTTCTCTACATCCCTTC
$_{GFP}$KtrB_f	AGAAAGGAGATTCCTAGGATGGGTACCCTGCAGAT
$_{GFP}$KtrB_r	TTATCCTTTTGAAGTGTCATGGATCCTGAGCCGCTTCCTG
Lin_pJS08_ΔB_f	GGATGTAGCGGATCCACGGGCCCCCCCTC
Lin_pJS08_ΔB_r	GGATCCGCTACATCCCTTCGTTTTCAAAACG
BamHI_msfGFP_f	GCGCGGGATCCGGAAGCGGCTCAGGAATGAGCAAAGGAGAAGAACTTTTC
msfGFP_SwaI_r	CGCGCATTTAAATTTATTTGTAGAGCTCATCCATGCC

EcoRI_KtrA'_f	GCGCGGAATTCGGGGTTAAAATCGCACAAAGCC
KtrA'_BamHI_r	GCGCGGGATCCCATCCCTTCGTTTTCAAAACG
Seq_pBAD_f	ATGCCATAGCATTTTTATCC
Seq_pBAD_r	GATTTAATCTGTATCAGG
Seq_KtrB_f	CAAGAAAGGCAATGCAACCTGCGTCG
Seq_msfGFP_f	AACTGCTGCTGGGATTACAC

4 Methods

4.1 Molecular biology

4.1.1 Isolation of genomic DNA from *B. subtilis*

To create gene deletions in *B. subtilis*, cells were transformed with the respective genomic DNA. For the isolation of genomic DNA from *B. subtilis*, 2 ml LB were inoculated with respective strains from glycerol stocks and incubated overnight at 30°C. To avoid sporulation 0.2% glucose were added to the overnight culture. To harvest the cultures, they were centrifuged at 17,000 g for 3 min and the cell pellet was resuspended in 1 ml TES buffer, and 25 µl lysozyme solution (10 mg/ml) were added. After 10 min of incubation at 37°C, 50 µl Pronase® Protease (10 mg/ml) together with 1% Sarkosyl were added, and the mixture was incubated for at least 30 min at 37°C. DNA was extracted by the addition of 250 µl phenol (50% in ethanol) and 250 µl chloroform. After centrifugation at 17,000 g for 4 min, the resulting upper layer was transferred in a new reaction tube and again mixed with 500 µl chloroform. Centrifugation was repeated and the upper layer was again transferred into a new reaction tube, which was subsequently filled with isopropanol to precipitate the DNA. The precipitate was carefully transferred to a new tube and completely dried before 100 µl of TES buffer were added. The DNA was solved by incubating at 37°C and constant shaking. Afterwards the DNA was stored at -20°C until further usage.

4.1.2 Plasmid isolation from *E. coli*

E. coli cells carrying the required plasmid were grown overnight at 37°C in 5 ml LB/KML medium supplemented with the respective antibiotic. The plasmids were isolated using the NucleoSpin® Plasmid Easy Pure Kit. Elution was performed with 50 µl of sterile ddH_2O. The concentration of the plasmid was calculated using the Beer-Lambert law, with A260 = ε * c * d (A260 = absorption at 260 nm [AU], ε = extinction coefficient [ml/(µg * cm)], c = concentration [µg/ml] and d = optical path length [cm]) by measuring absorbance at 260 nm using a NanoDrop 1000 Spectrophotometer (PeqLab Biotechnology GmbH). Finally, the sequence of the isolated plasmids was verified by Sanger sequencing (Microsynth Seqlab, Göttingen).

4.1.3 Agarose gel electrophoresis

To control the quality and the size of amplified DNA fragments, a 0.8% agarose gel was prepared in TAE buffer. Samples were mixed with Gel Loading Dye Purple and GeneRuler 1kb DNA Ladder was used to compare the size of the sample. By applying 60-120 V (peqPOWER 250V, PEQLAB), depending on gel size, the DNA fragments were separated. Afterwards, the gels were stained in 1% ethidium bromide solution for at least 30 min and subsequently visualised under UV illumination. Clean-up of PCR products from an agarose gel was executed with the NucleoSpin® Gel and PCR Clean-up according to the manufacturer's protocol.

4.1.4 Polymerase chain reaction (PCR) for site-directed mutagenesis

Plasmids encoding KtrA, KtrB or KtrAB were used to introduce site-specific mutation. Single amino acids were exchanged with primers listed in Table 7. PCR was performed using a Thermocycler peqSTAR 2X (PEQLAB) in the presence of Phusion High-Fidelity DNA Polymerase, including following steps: Initial denaturation at 98°C for 30 sec, followed by 25 cycles of denaturation, annealing and elongation. Denaturation was performed for 10 sec at 98°C, primer-specific annealing for 10 sec and elongation depending on vector size at 72°C (30sec/kb). Annealing temperatures were estimated using the NEB Tm calculator. Final extension was performed at 72°C for 10 min and the product was stored at 4°C until further usage. The reaction mixture is listed in Table 8.

Amplified products were analysed on 0.8% agarose gel (Section 4.1.3) and methylated maternal DNA was subsequently digested with DpnI/FastDigest DpnI following the manufacturer's protocol.

Table 8: Reaction mixture for site-directed mutagenesis.

Component	Volume
HF buffer (5x)	10 µl
dNTPs (2 mM)	5 µl
Forward primer (10 µM)	2.5 µl
Reverse primer (10 µM)	2.5 µl
Template DNA	1 µl
Phusion Polymerase	0.5 µl
ddH_2O	28.5 µl

For the substitution, deletion, or insertion of several adjacent amino acids, the Q5® Site Directed Mutagenesis Kit was used according to the provided manual. Primers were designed using the NEBaseChanger™ tool and are included in Table 7.

4.1.5 FX cloning

To generate plasmids encoding for KtrA and KtrB together with 3C protease-cleavable His-tags, FX cloning was performed according to the published protocols (Geertsma et al. 2011, Geertsma 2014). Initial PCR products were purified from a TAE agarose gel as described above (4.1.3). pINIT_cat was used as initial sequencing vector and after the sequences of *ktrA* and *ktrB* were verified, they were subcloned into expression vectors pBXC3H and pBXNH3. FX cloning was performed by Marina Schrecker.

4.1.6 In-Fusion® cloning to generate msfGFP fusion constructs

For fluorescence microscopy, plasmids, which contain *msfgfp* fused either C-terminally to *ktrA* or N-terminally to *ktrB*, were designed by In-Fusion® cloning following the provided protocol. For this, a vector, encoding *ktrAB*, for *amyE* integration in *B. subtilis* (pJS05) was linearised by PCR. In addition, the genes of interest were amplified with overhangs complementary to the linearised vector for insertion. In this case, *msfgfp* was amplified from plasmid pJS03. PCR was performed as described in 4.1.4. Prior to the In-Fusion® reaction, the products were treated with Cloning Enhancer by adding 2 µl Enhancer to 5 µl of PCR product. The mixture was incubated for 15 min at 37°C followed by 15 min at 80°C. Afterwards, the In-Fusion® reaction, which was modified from the manufacturer's instructions, was set up and incubated for 15 min at 50°C (Table 9).

Table 9: Modified mixture for In-Fusion® reaction.

Compound	Volume
5X In-Fusion® HD Enzyme Premix	0.5 µl
Linearised vector (50 ng)	1 µl
Insert (25 ng)	1µl

Subsequently, *E. coli* NEB5α cells were transformed with the complete reaction mixture. Plasmids were isolated and verified by sequencing.

4.1.7 Cloning of pMUTIN4 containing *ktrA*$_{msfGFP}$

To allow the native expression of *ktrA*$_{msfgfp}$ in combination with IPTG-inducible expression of *ktrB* in *B. subtilis*, a plasmid derivate of pMUTIN4 was designed (Vagner et al, 1998). Initially, *msfgfp* was cloned into the multiple cloning site (MCS) of the vector. For this, the sequence of *msfgfp* was amplified by PCR as described in 4.1.4 and restriction sites for enzymes BamHI (upstream) and SwaI (downstream) were introduced by primers. The PCR product was extracted from a 0.8% agarose gel and was, like the vector, digested with BamHI and SwaI. The reaction mixture, shown in Table 10, was incubated for 1 h at 37°C.

Table 10: Reaction mixture for digestion with restriction enzymes.

Component	Volume
Insert/Vector	X µl
NEBuffer™ (10x)	3 µl
Enzyme 1 (10 U/µl)	1 µl
Enzyme 2 (10 U/µl)	1 µl
ddH_2O	to 30 µl

Products were purified via agarose gel extraction and the assembly of the digested vector and the insert was catalysed by T4-DNA ligase. The used vector concentration was 50 ng and the amount of insert needed was calculated based on following formular:

$$amount\ of\ insert = amount\ of\ vector \times \frac{size\ of\ insert}{size\ of\ vector} \times 5$$

For the reaction, 1 µl of T4-DNA ligase (5U/µl) and 2 µl of T4 ligation buffer (10x) was mixed with respective amount of vector and insert in a final volume of 20 µl and incubated at 16°C overnight. Finally, *E. coli* NEB5α cells were transformed with the ligation reaction and the plasmids were isolated as described in 4.1.2.

In the next step, a fragment of *ktrA* (*ktrA*'), which is required for homologous recombination into the *B. subtilis* genome, was amplified by PCR and restriction sites for EcoRI (upstream) and BamHI (downstream) were introduced. As described above, the vector pMUTIN4-*msfgfp* and the ktrA' PCR product were digested with restriction enzymes followed by ligation. After transformation, the plasmid was isolated and verified via Sanger sequencing.

4.2 Microbiology

4.2.1 Preparation of *E. coli* competent cells and transformation

Chemically competent *E. coli* cells were prepared following the $CaCl_2$ method published by Sambrook et al.(1989). In short, 50 ml LB/KML medium (depending on the strain) were inoculated with 500 µl of an overnight culture of the desired cells under sterile conditions. The cells were cultured at 37°C constantly shaking at 180 rpm and harvested at an OD_{600} of 0.5-0.8. Subsequently, the cell pellet was washed in 25 ml ice-cold sterile 50 mM $CaCl_2$ and incubated on ice for 30 min. After an additional centrifugation at 5,000 g for 10 min, the cells were resuspended in 2.5 ml ice-cold 50 mM $MgCl_2$ and incubated for further 10 min on ice. Prior to flash-freezing in liquid nitrogen, 650 µl of 86% sterile glycerol were added to the cells as cryo-protectant. Aliquots of 100 µl were stored at -80°C.

For transformation, 100 µl of competent cells were slowly thawed on ice and carefully mixed with 1 µl DNA. After 30 min incubation on ice, a heat-shock was performed for 50 sec at 42°C with subsequent incubation on ice for further 10 min. The transformed cells were mixed with 1 ml of LB/KML and incubated for 45 min at 37°C under constant shaking at 180 rpm. Finally, the cells were plated on LB/KML agar plates with respective antibiotics and incubated overnight at 37°C.

4.2.2 Transformation of *Bacillus subtilis* cells

Transformation of naturally competent *B. subtilis* cells was performed following a method established by Anagnostopoulos & Spizizen (1961). *B. subtilis* cells were inoculated in 10 ml of transformation medium 1. For this, a scoop of cells from a fresh LB plate, which was incubated overnight at 37°C, was transferred into the medium. The culture was incubated at 37°C under gentle shaking. After 3 h, the culture was diluted with 10 ml of pre-warmed transformation medium 2 and incubation was continued for 2 more hours. An aliquot of 400 µl of the now competent cells was carefully mixed with 10 µl of the required plasmid and incubated for 1 additional hour. Afterwards the cells were pelleted for 1 min at 13,000 g. Carefully, 300 µl of the supernatant were removed and the cell pellet was resuspended in the remaining 100 µl. The suspension was spread on an LB agar plate containing the respective antibiotic and the plate was incubated overnight at 37°C. For transformation with genomic DNA, 2 µl DNA were mixed with 400 µl cells and after 1 h incubation, 100 µl were directly plated on a respective antibiotic-containing LB agar plate.

4.2.3 Verification of integration at the *amyE* locus by starch assay

To test whether the plasmid was integrated at the *amyE* locus in the genomic DNA of *B. subtilis* after transformation, a starch assay was performed. For this, starch resuspended in a small volume of ddH_2O was gently mixed with LB agar to a final concentration of 1%. After the plates were poured and the agar was solidified, 10 colonies from the transformation plate were picked with a sterile toothpick and resuspended in 50 µl of LB medium. From each resuspended colony, 5 µl were dropped on the starch plate and incubated overnight at 37°C. The remaining 45 µl were streaked on a LB agar plate supplemented with the respective antibiotic (60 µg/ml spectinomycin for *amyE::spec* integration vectors) for selection. The next day, the starch plates were exposed to iodine until the starch plate turned blue. For this, a few particles of iodine were placed into a lid of a fresh Petri dish and the plate was placed upside down on top of it. In case of correct integration, the complete plate turned blue as the starch cannot be degraded by the cells, whereas in case of wrong integration a clear halo appears around the colony as the AmyE activity remains intact.

4.2.4 Complementation in *B. subtilis* cells

To investigate the functionality of GFP-fused KtrAB variants, growth complementation assays at K^+ limitation were performed. The assay was adapted from a protocol established for *E. coli* cells by Tholema et al. (2005). For this, pre-cultures of different *B. subtilis* strains were grown in 2 ml KML with the respective antibiotic at 37°C for 5 hours. Afterwards, 5 ml BMM supplemented with 1 mM KCl and the respective antibiotic were inoculated with 50 µl of the pre-culture and incubated over night at 37°C under aerobic conditions. Finally, for the complementation assay, 5 ml BMM cultures were prepared with following different KCl concentration: 0.01, 0.025, 0.05, 0.075, 0.1 and 1 mM KCl. Cultures were inoculated to an initial OD_{600} of 0.1. Growth was followed for 24 hours by determination of OD_{600} after inoculation. For the first 7 h the OD_{600} was measured every hour. A final measurement was performed after 24 h.

4.2.5 Fluorescence microscopy of *B. subtilis*

For fluorescence microscopy, *B. subtilis* cells were grown to exponential growth phase at 37°C. Cultures were inoculated in 2 ml LB_{50KCl} from the respective glycerol stock or plate and incubated o/n at 30°C under constant shaking. The next day, the cultures were diluted 1:100 into fresh, pre-warmed medium. For applying K^+ limitation, different approaches were tested: Cells were either diluted in the same medium (LB_{50KCl}) and washed twice in BMM without KCl prior to microscopy, diluted in LB without potassium or already overnight grown in BMM with only 0.5 mM KCl added. All approaches resulted in the same

localisation pattern. For consistency during microscopy, the cells were grown in LB_{50KCl} overnight and for K^+ limitation diluted in LB without KCl, while for non-stressed conditions the cells were diluted in LB_{50KCl}. Cells carrying *Pxyl-ktrA*$_{msfGFP}$*-ktrB* were induced with 0.001% xylose, while cells with *Pxyl-ktrA-*$_{msfGFP}$*ktrB* were induced with 0.01% xylose as the fluorescence signal was too weak otherwise.

To perform microscopy, cells were immobilised on Teflon-coated multi-spot microscope slides covered with a thin layer of agarose. For this purpose, a solution of 1.2% electrophoresis-grade agarose was prepared in ddH_2O and cooled down to ~50°C. 400 µl of the agarose solution were spread on the Teflon-coated slide and quickly covered with another clean, uncoated microscopy slide. The agarose was allowed to solidify for 10 min at room temperature without additional applied pressure. The weight of the top slide combined with the viscosity of the solution at 50°C resulted in agarose patches with a suitable thickness. Prepared slides were either used immediately or stored maximally for 3 h in a cold humid environment in order to prevent extensive drying. Immediately before use, the slide was quickly warmed to room temperature and the uncoated top slide was removed by sliding it across the polymerised agarose surface. Subsequently, 0.5 µl of a cell culture was applied to the agarose surface, very briefly air-dried until the liquid-drop had evaporated and covered with a microscopy coverslip. Subsequently, the microscopy was carried out within a time window of 10 min after addition of the coverslip, although the applied small medium drop provided sufficient nutrients to keep the cells energised. For hyperosmotic shock experiments, agar patches were prepared in either 1 M NaCl or 1 M Sucrose instead of ddH_2O. Upon application of the cell culture to the slide, the cells got shocked.

Microscopic experiments were performed using a using a Nikon Eclipse Ti (Nikon Plan Apo ×100/1.40 Oil Ph3 objectives, CoolLED pE-4000 light source, photometrics BSI sCMOS camera) microscope. Images were acquired using Metamorph7.7 (Molecular Devices, Inc.) and analysed with FIJI/ImageJ (National Institutes of Health). For excitation a wavelength of 490 nm was used and for emission the microscope was equipped with a filter conform for GFP. Additionally, brightfield images were taken.

General membrane staining was performed by the addition of 0.5 µg/ml FM4-64 dye to 200 µl of cells, shortly before images were taken.

4.2.5.1 Abolishment of membrane potential prior to microscopy

For the dissipation of membrane potential with ionophore carbonyl cyanide-m-chlorophenylhydrazone (CCCP), 2 ml cell culture were grown until late exponential growth phase, and subsequently 500 µl were transferred into a 2 ml reaction tube. These cells were incubated with 100 µM CCCP dissolved in DMSO (0.5% final concentration of DMSO) at 37°C under constant shaking. After 5 min, 20 min, and 40 min after the addition of the ionophore the cells were applied to the microscopy slide and immediately imaged.

4.2.5.2 Time-lapse microscopy

Time-lapse microscopy was performed following the protocol published by de Jong et al. (2011) with small modifications. In short, cells were grown in LB_{50KCl} medium over night at 30°C. The next morning, the culture was diluted 1:10 in pre-warmed LB_{50KCl} and grown to mid-exponential phase at 30°C. For microscopy, the cells were diluted to an OD_{600} of 0.04. One hour before cells reach mid-exponential phase, microscope slides were prepared. For this purpose, a Gene Frame® was carefully attached in the middle of a clean glass slide and completely filled with 1.5% agarose, which was resolved in 10% LB_{50KCl} and 90% ddH_2O to avoid high background but offer enough nutrients during microscopy. Furthermore, 0.001% xylose was added to the agarose to induce gene expression. A second glass slide was quickly added on the agarose-filled Gene Chamber®. After the agarose was solidified, the upper glass slide was removed and an agar stripe of 5 mm width within the Gene Frame® was cut out, on which the cells were grown. To monitor four different strains at the same time, two stripes were cut in half, which resulted in four small squares. After 2 µl of cells were applied to the top of the agarose stripe and gently dispersed equally by turning the slide up and down, a clean microscope cover slide was added on the Gene Frame® without introducing air bubbles. The slide was pre-warmed before it was placed in a 30°C pre-warmed microscope chamber to avoid temperature fluctuations, which might cause autofocus problems during the experiment. Time-lapse microscopic experiments were performed using a using a Nikon Eclipse Ti (Nikon Plan Apo ×100/1.40 Oil Ph3 objectives, CoolLED pE-300 light source, photometrics Prime sCMOS camera) microscope. Images were acquired using Metamorph7.7 (Molecular Devices, Inc.) and analysed with FIJI/ImageJ (National Institutes of Health). For excitation a wavelength of 490 nm was used and for emission the microscope was equipped with a filter conform for GFP. Additionally, brightfield images were taken.

4.2.6 Whole-cell K^+ uptake experiments in *E. coli* LB2003 cells

Uptake of potassium via different variants of KtrAB and KtrB was investigated using a protocol modified from Bakker & Mangerich (1981). For this, potassium-free cells were produced by EDTA treatment and K^+ uptake was determined in the presence of different potassium concentrations at different time points.

4.2.6.1 Potassium-free cells

E. coli LB2003 cells were transformed with plasmids encoding different variants of KtrAB and grown in 500 ml K3 minimal medium supplemented with the respective antibiotic. For this, the cells were initially grown in 5 ml KML, followed by growth in 50 ml K30 and finally in 500 ml K3. For pKT84 constructs, instead of 0.2% glycerol, 10 mM glucose were added as carbon source. Furthermore, no arabinose was added, as the vector contains a constitutive promoter. In the late-exponential growth phase (OD_{600} between 0.6 and 0.8)

the cells were harvested and washed twice with 10 ml 120 mM Tris-HCl pH 8. The cells were adjusted to an OD_{600} of 30, which is corresponding to 10 mg dry weight (dw) of cell/ ml, and pre-warmed at 37°C for 5 min. Subsequently, the cells were depleted from intracellular K^+ and Na^+ by treatment with 1 mM EDTA for exact 7 min at 37°C and continuous shaking, since EDTA is known to permeabilise membranes of Gram-negative bacteria (Leive, 1968). To completely remove the ions and the residual EDTA, the cells were washed 3x with 200 mM HEPES-triethanolamine (TEA) pH 7.5. Finally, the OD_{600} was adjusted to 30 in 200 mM HEPES-TEA pH 7.5.

4.2.6.2 Potassium uptake assay

Uptake experiments were performed in a water bath at 25°C under constant shaking. For the experiment, cells were diluted 1:10 in 10 ml Hepes-TEA pH 7.5, corresponding to 1 mg (dw) of cells/ ml. Initially, the cells were energised with 10 mM glucose and incubated for 10 min. K^+ uptake was initiated by the addition of different KCl concentrations (0.1, 0.2, 0.4 and 1 mM). All measurements were performed in the absence and the presence of 5 mM NaCl. Prior to KCl addition, 2x 1 ml samples were taken to determine K^+ contamination and within 10 min after KCl addition, 1 ml samples were taken at different timepoints (1 min, 2 min, 3 min, 4 min, 7 min, 10 min). K^+ uptake was stopped by centrifugation of the sample through 200 µl of silicone oil (1.04 g/cm^3) in a 1.5 ml reaction tube for 2 min at 4,100 g. This separated the cells from buffer. Buffer and silicone oil were removed with a vacuum pump and the tip of the reaction tube, which contained the cell pellet, was cut off and transferred in 1 ml 5% TCA. After the pellet was dissolved, cells were disrupted by freezing at -20°C overnight, followed by cooking at 90°C for 10 min. Subsequently, 3 ml of 6.7 mM $CsCl_2$ were added and the K^+ concentration was determined by flame photometry (ELEX 6361, Eppendorf). The Michaelis-Menten constants (K_m) and the maximum uptake velocities (V_{max}) were calculated by using the Michaelis-Menten fit in GraphPad Prism5, where the following equation was applied: $Y = V_{max}*X/(K_m + X)$.

4.3 Protein biochemistry

4.3.1 SDS PAGE

For the determination of sample composition and purity, protein samples were analysed by SDS polyacrylamide gel electrophoresis (SDS PAGE) according to Laemmli (1970), utilising 5% stacking and 12% separation gels (Table 11). Samples were diluted 3:1 with 3x SDS PAGE loading buffer. Of each sample, 15 µl were loaded per lane and the proteins were separated according to their apparent molecular weight in 1x electrophoresis buffer by applying 120 V for 1:45 h (peqPOWER 250V, PEQLAB). The PageRuler™ prestained protein ladder was used a protein size standard. Afterwards the gels were treated with Coomassie blue buffer and destaining buffer for visualisation of protein signals. Alternatively, the gels were used for Western blot analysis as described in the following section (4.3.2).

Table 11: Composition of 5% stacking gels and 12% separation gels for SDS PAGE. Volumes are sufficient for pouring four 8 x 8 cm gels.

Compound	Stacking gel	Separation gel
Rotiphoresis gel 30 (30% acrylamide, 0.8% bisacrylamide)	1.3 ml	8 ml
Stacking gel buffer	2.2 ml	-
Separation gel buffer	-	8 ml
dH_2O	5.4 ml	7.8 ml
10% ammonium persulfate (APS)	90 µl	120 µl
N, N, N′, N′-tetramethylethylendiamin (TEMED)	30 µl	60 µl

4.3.2 Western blot

Western blotting from SDS PAGE gels to nitrocellulose membranes was performed using the Pierce™ 1-Step Transfer buffer with a Pierce™ Power Blotter. A pre-installed program for proteins with mixed range molecular weight in seven min was utilised. Afterwards the membranes were blocked with 10 ml of 5% powdered milk solved in TBS-T buffer for 30 min at room temperature, followed by three washing steps with 10 ml TBS-T, each for 10 min. After 1 h incubation with 10 ml of the primary antibody solution (monoclonal rabbit anti-PEG methoxy group (1: 1000 in TBS-T), followed by 3x 10 min washing steps with 10 ml TBS-T, the membranes were incubated for 1 h with 10 ml the secondary antibody (goat anti-rabbit-HRP conjugate, 1:3,00 in TBS-T). Finally, the membranes were washed again 3x 10 min with 10 ml TBS-T and subsequently 10 ml ECL-1 and 10 ml ECL-2 solutions were added to develop the blot. The signals were visualised by chemiluminescence using a Fusion Fx Spectra imager (Vilber).

4.3.3 Blue Native PAGE

With Blue Native (BN) gel electrophoresis the apparent molecular weights of protein complexes can be determined under native/non-denaturing conditions. Therefore, the protein samples were mixed with the same volume of 2x BN Sample buffer. Of each sample, 30 µl were prepared. The pre-casted gels were placed into the electrophoresis chamber. Cathode buffer containing 1% Coomassie Brilliant Blue G250 was applied to the inner chamber, while anode buffer was added to the outer chamber. Before the samples were loaded onto the gel, the wells of the pre-casted gels were carefully washed with 1x cathode buffer. Electrophoresis was carried out for 10 min at 50 V (constant) followed by 120 min at 200 V (constant) at 4°C. After 2/3 of the electrophoresis run was completed, the cathode buffer was exchanged by cathode buffer without Coomassie Brilliant Blue G250 to reduce background staining. After electrophoresis, the gels were additionally stained as described for SDS PAGE gels (4.3.1) in case the signals were too weak.

4.3.4 Purification of 3C protease

The plasmid encoding a N-terminally His_6-tagged version of the 3C protease was a gift from Dr. Eric Geertsma, Institute of Biochemistry, Goethe-University, Frankfurt. *E. coli* C43 (DE3)Δ*acrAB* cells were transformed with plasmid pB3CNH_6 and 50 ml of LB supplemented with 100 µg/ml ampicillin were inoculated with a single colony from the transformation plate and grown at 37°C and 180 rpm. After 6 h growth, 2 l of LB (100 µg/ml ampicillin) were inoculated with the preculture to an OD_{600} of 0.1 and grown at 37°C and 180 rpm. Once the OD_{600} reached 0.3, the temperature was changed to 25°C, and after approx. 30 min, the cells were induced by the addition of 0.01% of arabinose.

Subsequently, the cells were cultured o/n at 25°C and 180 rpm. Afterwards, the cells were harvested at 5,000 g and 4°C for 15 min and the cell pellet was resuspended in 3C protease lysis buffer to an OD_{600} of 100. Cells were disrupted using the 'Pressure cell' homogeniser (Stansted Fluid Power Ltd.) at 1 bar. An ultracentrifugation at 150,000 g and 4°C was performed to separate the cytoplasm from undisrupted cell, cell debris and membranes. Per litre cell culture 1 ml of Ni^{2+}-NTA agarose were equilibrated with 25x CV of ddH_2O and 25x CV of 3C protease IMAC buffer containing 10 mM imidazole. The equilibrated beads were incubated with the supernatant of the ultracentrifugation for 1 h at 4°C under gentle agitation. After incubation, the slurry was transferred into a chromatography column, and the flowthrough was collected. The Ni^{2+}-NTA agarose was washed with 25x CV of 3C protease IMAC buffer supplemented with 30 mM of imidazole. Bound proteins were eluted in six 1 ml elution steps with 3C protease IMAC buffer containing 300 mM imidazole. The protein-containing fractions were combined and further purified via SEC using a HiLoad Superdex75 16/60 column with filtered and degassed 3C protease storage buffer. Afterwards, the concentration of the protein was set to 5 mg/ml and 200 µl aliquots were flash-frozen in liquid nitrogen and stored at -20°C until further use.

4.3.5 Overproduction and purification of KtrA from *Vibrio alginolyticus*

For the expression and heterologous overproduction of KtrA from *V. alginolyticus* (VaKtrA), *E. coli* C43(DE3)Δ*acrAB* cells were transformed with plasmid pBKtrAC3H or pBKtrANH3 carrying either a C- or N- terminal His-tag on KtrA. The cells were inoculated in LB medium supplemented with 100 µg/ml ampicillin to an initial OD_{600} of 0.1 from an overnight culture and grown under aerobic conditions at 37°C. Cell growth was monitored regularly by determining the OD_{600} and at an OD_{600} of 0.6-0.8, gene expression was induced by the addition of 0.02% L-arabinose. After 1.5 hours of further growth at 37°C and 180 rpm the cells were collected by centrifugation for 15 min at 5,000 g and 4°C. Subsequently, the cells were adjusted to OD_{600} of 100 in buffer S for cell disruption. Prior to disruption with the 'Pressure cell' homogeniser (Stansted Fluid Power Ltd.) at 1 bar, the cell suspension was supplemented with a spatula tip of DNaseI, 1 mM EDTA, 100 µg/ml phenylmethylsulfonyl (PMSF) and 300 µM benzamidine. Cell debris and undisrupted cells were removed by centrifugation at 19,000 g for 15 min at 4°C. To further separate membranes from KtrA-containing cytoplasm, the supernatant was centrifuged at 130,000 g for 2 h at 4°C. Afterwards, the cytoplasm was either used for purification of the natively assembled KtrAB complex (cf. 4.3.6.3) or for the purification of the KtrA ring.

For the latter, the supernatant was incubated with 1 ml/(l cell culture) of pre-equilibrated Ni^{2+}-NTA agarose in the presence of 10 mM imidazole for at least 3 h at 4°C under gentle agitation. For equilibration, the Ni^{2+}-NTA agarose was washed with 50x column volumes (CV) ddH_2O, followed by equilibration with 50x CV buffer S. After 3 h of binding, unbound

proteins were removed by transferring the mixture to chromatography columns. The agarose was washed with 50x CV buffer W supplemented with 50 mM imidazole. Finally, the protein was eluted once with 1/2x CV and 4 times with 1x CV of buffer W containing 500 mM imidazole. Eluted fractions were concentrated to 500 µl via Amicon® Ultra-4 centrifugal filters Ultracel® (MWCO 100 kDa) and filtrated through low-binding Durapore PVDF membrane (0.22 µm) filters. Subsequently, the protein sample was further purified by size exclusion chromatography (SEC) using a Superdex® 200 Increase 10/300 GL column equilibrated with buffer W or ITC buffer, dependent on the purpose. Column was equilibrated with the respective filtered and degassed buffer.

Concentrations of the eluted samples were determined using Beer-Lambert equation $A_{280} = \varepsilon * c * d$ (A_{280} = absorption at 280 nm [AU)], ε = extinction coefficient [ml/(µg * cm)], c = concentration [µg/ml] and d = optical path length [cm]) by measuring the absorbance at 280 nm using a NanoDrop 1000 Spectrophotometer. The used molecular weight and extinction coefficient of KtrA were 25.5 kDa and 8.6 $M^{-1} * cm^{-1}$, respectively. To visualise the purification, samples for SDS PAGE ware taken at each purification step.

4.3.6 Production and purification of KtrAB/KtrB and variants thereof

4.3.6.1 Protein overproduction

For the different approaches performed in this thesis, including mixing of KtrA and KtrB, PEGylation, and reconstitution of the purified protein into liposomes, KtrAB and KtrB as well as variants thereof were purified. For this, *E. coli* LB2003 cells were transformed with the respective plasmids (Table 6).

For PEGylation, pIH301-100 E449C or pEL903-100 E449C, encoding cysteine free variants with an introduced cysteine at position E440 in KtrAB or KtrB, respectively, were used. The transformed cells were grown in KML+ 100 µg/ml ampicillin and the K^+ concentration of the medium was slowly reduced by transferring the cells first into K30 medium and finally K3 medium, both supplemented with 100 µg/ml ampicillin. More precise, cells from 5 ml KML culture were diluted 1:500 in 50 ml K30 medium and incubated for 8 h at 37°C under constant shaking at 180 rpm. The cells were then further diluted in K3 to an initial OD_{600} of 0.15 and incubated overnight at 37°C under aerobic conditions. This culture was finally used to inoculate the main cultures in K3, which were inoculated to an initial OD_{600} of 0.15 and growth was allowed for 5-7 h at 37°C under aerobic conditions. To allow the growth in K3 medium, the expression of *ktrAB*/*ktrB* was induced by the addition 0.02% L-arabinose from the beginning of the growth in both K3 cultures. At an OD_{600} of 1-1.5 the cells were harvested and disrupted as described before (4.3.3).

For mixing KtrA and KtrB and the reconstitution of KtrB into liposomes, *E. coli* LB2003 cells were transformed with plasmids pBKtrBC3H and pBKtrBNH3, respectively. Cells were grown in KML+ 100 µg/ml ampicillin, and gene expression was induced with 0.02% arabinose at an OD_{600} of 1.7. After 1.5 h growth, the cells were harvested and disrupted using the 'Pressure cell' homogeniser (Stansted Fluid Power Ltd.) at 1 bar as described above.

4.3.6.2 Solubilisation and purification of KtrAB/KtrB from isolated membranes

To remove cell debris after disruption, the solution was centrifugation at 19,000 g. Afterwards, membranes containing KtrAB and KtrB were isolated by centrifugation overnight at 130,000 g and 4°C. Afterwards membrane pellets were resuspended in buffer S to have a total membrane protein concentration of 10 mg/ml as determined by BCA assay. The membrane proteins were solubilised with 1% DDM for 1 h at 4°C under gentle agitation. Solubilised and unsolubilised fractions were separated by centrifugation at 200,000 g for 30 min at 4°C. Subsequently, the His-tagged proteins in the supernatant were bound to pre-equilibrated Ni^{2+}-NTA agarose. For a 6-litre cell culture, 1 ml CV Ni^{2+}-NTA agarose were used, which were previously washed with 50x CV ddH_2O, followed by equilibration with 50x CV buffer S. The supernatant was incubated with Ni^{2+}-NTA agarose in the presence of 10 mM imidazole. The mixture was transferred to a chromatography column and the sample was passed through to remove unbound protein. During the washing step with 50x CV of buffer W, supplemented with 50 mM imidazole and 0.04% DDM, proteins with a poor binding affinity towards the Ni^{2+}-NTA agarose were removed. Finally, protein elution was performed once with 1/2x CV and 4 times with 1x CV of buffer W supplemented with 500 mM imidazole and 0.04% DDM. Eluted fractions containing the majority of the protein were combined and concentrated to 500 µl volume via Centriprep® 30K and filtrated via low-binding Durapore PVDF membrane (0.22 µm). Subsequently, the protein sample was further purified by SEC using a Superdex® 200 Increase 10/300 GL column or Superose® 6 Increase 10/300 GL column, equilibrated with filtered and degassed buffer W supplemented with 0.025% DDM. Protein concentration was determined using Beer-Lambert equation, using M = 410 kDa and the $\varepsilon = 287\ M^{-1} * cm^{-1}$ for KtrAB, and M= 50.5 kDa and $\varepsilon = 54.4\ M^{-1} * cm^{-1}$ for the KtrB sample. Throughout the purification, samples were taken for SDS PAGE.

4.3.6.3 Production and purification of the native assembled KtrAB complex

To avoid the formation of the $KtrB_2A_8B_2$ 'sandwich' assembly, the purification of the KtrAB complex was optimised. For this purpose, KtrA and KtrB were separately produced and KtrAC3H/KtrANH3 was used to saturate KtrB in the membrane prior to solubilisation. In detail, for the production of KtrB, *E. coli* LB2003 cells were transformed with plasmid pEL901 and variants of it. As described in 4.3.6.1, the cells were initial inoculated in KML medium followed by a reduction of the KCl concentration in the medium by transferring the

cultures into K30 and finally in K3 supplemented with 0.02% arabinose for induction. After the cells reached the late-exponential growth phase at OD_{600} of 1-1.5 they were harvested, and membranes were isolated as described in section 4.3.6.2. The membrane pellet was weighted, and it was homogenised in buffer S and mixed prepared KtrA-containing cytoplasm (section 4.3.5) to have a total membrane concentration of 100 mg/ml. A membrane pellet from a 12 l *E. coli* LB2003 pEL901 culture resulted usually in a 12 g pellet, which was combined with cytoplasm from 1 l C43(DE3)ΔacrAB pBKtrAC3H/pBKtrANH3 culture with an OD_{600} of 3. After mixing the two samples, the protein was extracted from the membrane either by solubilisation with 1% DDM or 2% SMA for 6 hours at 4°C. Binding to and washing of Ni^{2+}-NTA agarose was performed as described in section 4.3.6.2, however incubation was performed overnight. Subsequently, the protein was eluted with buffer W containing 0.04% DDM and 500 mM imidazole as described before (cf. 4.3.6.2). After solubilisation with SMA, no detergent was added to the buffer.

For cryo-EM, the sample was solubilised for 2 h and bound to Ni^{2+}-NTA for 3 h. After washing, the sample was eluted from the Ni^{2+}-NTA agarose by cleavage with 3C protease. For this, 3C protease at a ratio of 1 mg of protease per litre *E. coli* C43(DE3)*ΔacrAB* pBKtrAC3H cell culture with an OD_{600} of 3 was used. The protease was resuspended in 2x CV buffer W containing 0.04% DDM and mixed with Ni^{2+}-NTA overnight at 4°C under constant rotation. Elution fractions were collected, and the agarose beads were washed twice with 1x CV buffer W containing 0.04% DDM. The protein containing fractions were combined and concentrated to 500 µl and filtered for SEC. For SEC, a Superdex® 200 Increase 10/300 GL column was equilibrated with buffer W containing 0.025% DDM or cryo-EM buffer, depending on the purpose. Throughout the purification, samples were taken for SDS PAGE.

4.3.6.4 Purification of the natively assembled complex via ATP agarose

To purify KtrAB in the ATP-bound state, the complex was further purified via agarose-immobilized γ-Aminophenyl-ATP (C10-spacer) (ATP agarose). For this purpose, the buffer of KtrAB eluted from Ni^{2+}-NTA agarose (4.3.6.3) was exchanged to buffer W with 0.04% DDM, using Zeba™ Spin Desalting Columns to remove the imidazole. Afterwards the protein was mixed with pre-equilibrated ATP agarose. Here, 4 mg $KtrA_8B_2$ were mixed with 200 µl of ATP agarose. The agarose has an ATP substitution of 20 µmol-22 µmol ATP/ml slurry. As the agarose is stored in ethanol, it was initially washed with 50x CV of ddH_2O followed by equilibration with 50x CV buffer W supplemented with 0.04% DDM. Protein mixed with the ATP agarose was incubated overnight at 4°C under gentle agitation. Subsequently, the mixture was transferred to a chromatography column, and the flowthrough was collected. The agarose beads were washed with 50x CV buffer W+ 0.04% DDM to remove unbound protein. Finally, the protein was eluted with buffer W+ 0.04%

DDM supplemented with 30 mM ATP and 2 mM $MgCl_2$ in steps similar to elution with imidazole. The fractions were combined, concentrated to 500 µl and further purified via SEC. During SEC, the ATP concentration in the buffer was reduced to 1 mM ATP. Final protein concentration was determined using the Pierce™ BCA Protein Assay Kit, as the ATP gives a strong background signal at 280 nm for NanoDrop 1000 Spectrophotometer measurements. The measurements were performed following the manufacturers protocol. Throughout the different steps, samples were taken for SDS PAGE.

4.3.7 PEGylation of KtrAB and KtrB

For PEGylation of KtrB, as a strategy to avoid 'sandwich' assembly, variants of KtrB and KtrAB were purified as described in section 4.3.6. After elution from Ni^{2+}-NTA agarose, SEC was performed using Superdex® 200 Increase 10/300 GL column with buffer W containing 0.04% DDM. Subsequently, the proteins were concentrated to 5 µM of either $KtrB_2A_8B_2$ complex or KtrB dimer and incubated with either 30 µM of 5 kDa MeO-PEG-mal or 15 µM of 10 kDa MeO-PEG-mal for 1 h at 4°C under constant rotation. The reaction was stopped by the addition of 1 mM DTT, and the samples were mixed with SDS PAGE loading buffer. Finally, the samples were analysed via SDS PAGE and Western blot.

4.3.8 Reconstitution of KtrAB/KtrB into a lipidic environment

4.3.8.1 Preparation of *E. coli* polar lipids from *E. coli* total lipid extract

For the purification of *E. coli* polar lipids, 25 mg/ml *E. coli* total lipid extract dissolved in chloroform were dried in a rotary evaporator. The flask was flushed with argon gas and the lipids were dissolved in 2 ml of chloroform. The solution was slowly titrated to 150 ml of ice-cold acetone under gentle stirring to precipitate the polar lipids. After flushing the flask with argon, it was closed and kept in the dark at 4 °C while stirring overnight. A subsequent centrifugation step at 3,000 g for 10 min was used to pellet the lipids and remove the acetone. The pellet was thoroughly dried with argon and the dried pellet was dissolved in 150 ml diethyl ether. The sample was stirred for 30 min at room temperature. A second centrifugation step at 3,000 g for 10 min followed. The supernatant, now containing the polar lipids, was dried completely in the rotary evaporator at room temperature. To determine the yield of purification, the purified lipids were weighted and dissolved in chloroform to a concentration of 100 mg/ml and stored at -20°C.

4.3.8.2 Preparation of different liposomes

To form liposomes from purified *E. coli* polar lipids, the required amount of lipids was dried under argon stream or in a rotary evaporator. To obtain different lipid compositions, the polar lipids were mixed with either 10% or 20% cardiolipin (10 mg/ml in chloroform) prior evaporation. Afterwards, the lipid films were hydrated in inside reconstitution buffer to a

final concentration of 10 mg/ml. Solutions were sonicated for 30 min in a sonication bath. Afterwards, 1 ml aliqouts were prepared and flash frozen in liquid nitrogen.

4.3.8.3 BioBeads activation

Polystyrene beads (BioBeads) were used for detergent removal. Before usage, the beads were activated by washing them twice with 4x volumes of methanol, followed by an intensive wash with ddH_2O to remove the residual methanol. Afterwards the beads were ready to use and stored at 4°C.

4.3.8.4 Reconstitution of KtrB/KtrAB into pre-formed liposomes

KtrB was reconstituted into liposomes to perform the ACMA-based flux assay. For this, the prepared liposomes containing different cardiolipin concentration were used for three cycles of freeze and thaw. To obtain unilamellar liposomes, the lipids were extruded 21 times through a 400 nm filter. The extruder was pre-equilibrated with the inside reconstitution buffer. Subsequently, the liposomes were diluted to 4 mg/ml and titrated with 10% Triton-X-100 following the absorption at 540 nm (Geertsma et al, 2008b). Titration was completed slightly after reaching the maximal absorption. Purified protein was added to the destabilised liposomes in an LPR of 100 (w/w) and the mixture was incubated at room temperature for 30 min under gentle agitation. As a control, empty liposomes were prepared by adding buffer W+ 0.04% DDM to the preformed liposomes instead of protein. For EPR measurements, the KtrAB variants were added to liposomes prepared from *E. coli* polar lipids with a LPR of 10.

To remove the detergent from the mixture and form proteoliposomes, the mix was exposed to BioBeads in several steps. With every individual addition 60 mg/ml wet weight of the beads were added. First, the mixture was incubated with BioBeads for 15 min at RT followed by addition of BioBeads for 15 min at 4°C. Afterwards the sample was incubated with fresh BioBeads for 30 minutes, 1h and overnight at 4°C. The next day, the sample was incubated one more hour after the addition of fresh BioBeads. The proteoliposome-containing supernatant was removed with a syringe, pelleted at 80,000 g for 30 min and washed twice with inside reconstitution buffer. Finally, the proteoliposomes were resuspended in inside reconstitution buffer to a lipid concentration of 10 mg/ml and either used directly or stored at -80°C until usage.

4.3.8.5 Verification of reconstitution efficiency by resolubilisation

Reconstitution efficiency was verified by performing resolubilisation of the proteoliposomes (Geertsma et al, 2008a). For this purpose, 100 µl of the proteoliposomes with a lipid concentration of 10 mg/ml were solubilised with 1% DDM for 30 min at 4°C. An aliquot of 50 µl of the solubilised sample was mixed with SDS PAGE loading dye to analyse by SDS PAGE. The remaining 50 µl were transferred to ultracentrifugation at 80,000 g for 1h and 4°C. Afterwards, the supernatant was taken and mixed with SDS PAGE loading

dye. The resulting pellet was resuspended in 50 µl of inside reconstitution buffer and mixed with the loading dye. All three fractions were compared on Coomassie-stained SDS PAGE. Signal quantification was analysed with FIJI/ImageJ (National Institutes of Health).

4.3.8.6 Production and purification of MSP2N2

MSP2N2 production and purification was carried out according to published protocols (Ritchie et al, 2009). In brief, E. coli BL21(DE3) cells transformed with pMSP2N2 were grown in TB medium supplemented with 50 µg/ml kanamycin at 37 °C. At an OD_{600} of 0.6, MSP2N2 production was induced by addition of IPTG to a final concentration of 1 mM. Growth was carried out for 4 h before cells were harvested. The harvested cells were resuspended in buffer MSP1 to an OD_{600} of 100 and disrupted with the 'Pressure cell' homogeniser (Stansted Fluid Power Ltd.) at 1 bar. Prior to cell lyses, the suspension was supplemented with a spatula tip of DNaseI, 1 mM EDTA, 100 µg/ml phenylmethylsulfonyl (PMSF) and 300 µM benzamidine. After centrifugation at 30,000 g for 30 min, the supernatant was loaded on to a pre-equilibrated Ni^{2+}-NTA agarose (1 ml CV/l culture). Pre-equilibration was performed with 20x CV buffer MSP2. After collecting the flowthrough, the beads were extensively washed: 5x CV of buffer MSP2, followed by 5x CV buffer MSP3, buffer MSP4, buffer MSP1 and buffer MSP5. The protein was finally eluted with buffer MSP1 containing 300 mM imidazole. All protein-containing fractions were combined and the protein was dialysed in a Slide-A-Lyzer™ cassette against 2x 5 l of dialysis buffer for each 12 h at 4°C. Finally, protein concentration was determined using a NanoDrop 1000 Spectrophotometer and 200 µl aliqouts were flash frozen in liquid nitrogen and stored at -80°C until further usage.

4.3.8.7 Reconstitution into MSP2N2 nanodiscs

For the reconstitution of $KtrA_8B_2$ into nanodiscs, *E. coli* polar lipids in chloroform were dried and afterwards hydrated in buffer W with a final concentration of 5 mg/ml and solubilised in 1% DDM for 3-4 h. Afterwards, detergent-solubilised native KtrAB was incubated with lipids in a molar ratio of 1:100 or 1:300 (KtrAB complex: lipids). In a standard approach, KtrAB with a concentration of around 3 mg/ml (10 µmol) was used. After 30 min incubation at room temperature and constantly mixing, MSP2N2 (1 mg/ml) was added in a molar ratio of 1:2.5:100 or 1:3:300 (KtrAB:MSP2N2:lipids). The mixture was further incubated for 30 min at 4°C. Subsequently, BioBeads were added in three steps, each 40 mg/ml wet weight and incubated for 30 min, 45 min and overnight at 4°C, respectively. BioBeads were removed, and samples were concentrated and filtered for SEC as described before.

4.4 Biochemical and biophysical methods

4.4.1 ACMA assay

To monitor KtrB-mediated K^+ fluxes, an indirect approach, which detects the vesicular acidification, was performed using the membrane permeable pH-sensitive dye 9-amino-6-chloro-2-methoxyacridine (ACMA). The assay was adapted from Teixeira-Duarte et al. (2019). For this, the prepared proteoliposomes were subjected to three freeze-thaw cycles, followed by 21x extrusion through 200 nm filters. Afterwards, 2 µl of liposomes at a lipid concentration of 10 mg/ml were diluted 1:100 in a total reaction of 200 µl into outside reconstitution buffer and mixed with 550 nM of ACMA in a fluorescence cuvette. Changes in fluorescence were monitored with an excitation wavelength of 410 nm (2 nm band width) and an emission wavelength of 550 nm (4 nm band width). After establishing a stable fluorescence signal after 150 s, the addition of 1 µM CCCP (400 µM in EtOH) initiated continuous K^+ efflux by allowing the influx of H^+. The membrane potential was clamped to 0 as for every K^+ leaving the liposomes, a proton was taken up. The protons taken up protonate the ACMA, leading to membrane impermeability and consequently quenching ACMA. Hence, ACMA quenching by H^+ indirectly informed about the K^+ flux rate of KtrB. Finally, the maximally possible ACMA quenching, as a result of the maximal possible K^+ flux, was determined by the addition of 20 nM valinomycin (8 µM in DMSO). Fluorescence traces were normalised to the fluorescence at the timepoint before CCCP addition. Evaluation of fluorescence changes and decay rates was done with GraphPad Prism 5. All measurements were performed at room temperature at the Fluorolog® 3 (Horiba Scientific) fluorescence spectrometer.

4.4.2 Isothermal titration calorimetry (ITC)

Purified KtrA was concentrated to 40-85 µM in ITC buffer. ITC measurements were performed at 24°C with a MicroCal iTC200 System (Malvern) to determine affinities towards ATP, ATP + $MgCl_2$, ADP or $MgCl_2$. The cell was loaded with 280 µl protein solution and after an initial titration step of 0.2 µl, the ligand was further titrated with a volume of 2 µl. In total 20 injections were performed with 3 min intervals between each injection. The syringe speed was set to 750 rpm. For analysis MicroCal ITC-ORIGIN Analysis Software was used and binding parameters were determined by a single-site binding fit. Exact concentration of protein and ligand are listed in Table 12.

Table 12: Protein and ligand concentration used for the performed ITC measurements.

Protein concentration	Titrant
45 µM KtrA	250 µM ATP
60 µM KtrA, 5 µM $MgCl_2$	300 µM ATP, 30 mM $MgCl_2$
30 µM KtrA	250µM ADP
85 µM KtrA	30 mM $MgCl_2$

4.4.3 Scintillation proximity assay (SPA)

Competitive nucleotide binding to KtrA was determined using SPA. For this, 200 nM purified KtrA in buffer W with 1 mM $MgCl_2$ were incubated with either 2.8 µM ATP supplemented with 0.2 µM of ^{3}H-ATP or 2.8 µM ADP supplemented with 0.2 µM of ^{3}H-ADP, each in a total volume of 55 µl. All the mixtures were prepared in buffer W containing 5% glycerol, to allow floating of the later applied SPA beads. After 30 min incubation at room temperature, 5 µl of different concentrations of ADP or ATP, ranging from 0.5 µM to 1 mM, were added to each sample for competition with pre-bound radioactive-labelled nucleotides. Samples were incubated for further 30 min at room temperate and afterwards 52.5 µl of the protein-nucleotide mixture were added to 17.5 µl of copper-chelated SPA beads which were used in a final concentration of 5 mg/ml. Prior to this, the SPA beads are washed twice with 100 volumes of ddH_2O followed by washing once with 100 volumes buffer W and once with 100 volumes buffer W containing 5% glycerol. Since KtrA contains a C-terminal His-tag it binds to the copper-chelated SPA beads. Measurement was performed at room temperature and the amount of bound radio-label was determined in cpm mode (Wallac MicroBeta). Background was determined by repeating the measurements, after incubation of the samples with 200 mM imidazole for 20 min, which should remove all of the bound KtrA from the SPA beads and allow the detection of unspecific signals. The unspecific background was finally subtracted from the measured counts to determine the total binding signal.

4.4.4 Differential scanning fluorimetry (DSF)

DSF measurements were performed to determine the effect of nucleotide binding on the melting temperature of purified KtrA/KtrAB. The method is based on the assumption that the thermo stability upon ligand binding increases. Hereby, the fluorescent dye SYPRO™ Orange was used for KtrA, which is sensitive to increasing hydrophobicity upon protein unfolding, resulting in an increased fluorescence intensity. Samples were prepared containing 5 µM KtrA in buffer W. Prior to the measurements, KtrA was supplemented with different concentrations of ADP and ATP. The total sample volume was adjusted to 27 µl

to which 3µl of 100x SYPRO™ Orange dye were added. Measurements were executed using the Rotor-Gene Q 5plex HRM System (Qiagen). The SYPRO™ Orange dye was excited at a wavelength of 470 nm and emission was measured at a wavelength of 555 nm. Before heating, the samples were kept at the pre-melting temperature of 25°C for 90 s. Subsequently, the temperature was increased by 1°C each 60 s and fluorescence intensity was recorded at temperatures between 25°C and 80°C. The gain was set to 5.

For KtrAB, CPM (7-Diethylamino- 3-(4-maleimidophenyl)-4-methylcoumarin) dye was used, which selectively binds cysteine residues. Upon protein unfolding, cysteines become accessible, which leads to an increase in fluorescence intensity. The Ni^{2+}-NTA agarose and ATP agarose purified samples were used with a concentration of 0.5 µM and 1 µM, respectively. The sample volume was adjusted to 29.5 µl and prior the measurement the sample was mixed with 0.5 µl of CPM dye (1 mg/ml in DMSO). For measurements with CPM dye an excitation wavelength of 460 nm was used and emission was measured at 510 nm. Temperatures between 25°C and 90°C were used and temperature was increased by 1°C each 30 s. Prior the measurement an automatic gain adjustment was performed.

4.4.5 Thin layer chromatography (TLC)

ATPase activity of purified KtrAB and KdpFABC was measured by hydrolysis of ^{32}P-γ-ATP (222 TBq/mmol, 370 MBq/ml) and subsequent TLC on polyethylene imine (PEI) plates (Merck Millipore) using a 0.8 M LiCl solution in acetic acid pH 3.2. Purified KdpFABC was kindly provided by Jakob M. Silberberg. Initially, 50 µl of a 10-fold cold ATP stock (30 µM), which was supplemented 1:1,000 of the radioactive tracer, was prepared. For the reaction, 0.5 µg of either KdpFABC or KtrAB was added to buffer W + 0.04% DDM to have a final volume of 15 µl, containing 1-fold of the ATP mixture (3 µM), after an initial sample of 1 µl was taken prior to hydrolysis. Samples were incubated for 30 min at 37°C, and 1 µl samples were taken after 20 sec, 40 sec, 1 min, 2 min, 4 min, 5 min, 6 min, 10 min, 15 min and 30 min. As a control for autohydrolysis, a similar reaction was set up in the absence of a protein. All 1 µl samples were immediately spotted onto the TLC PEI plates and after all samples were taken, they were separated in 0.8 M LiCl-acetic acid pH 3.2. Afterwards the plates were dried and exposed to a radio screen Exposure Cassette-K (Bio-Rad) overnight. The screens were analysed on Personal Molecular Imager System (Bio-Rad).

To investigate, if a nucleotide is co-purified with KtrAB, purified KtrAB complex comprising 2 nmol KtrA was spotted on a TLC PEI plate and subjected to the 0.8 M LiCl-acetic acid pH 3.2 buffer. For example, 10 µl of purified KtrAB with a concentration of 13 mg/ml was used to have a concentration of 2 nmol KtrA monomers. While the protein precipitates, nucleotides get separated. Visualisation of the nucleotides was achieved by illumination with UV light. As a standard, ATP and ADP were spotted to the plate.

4.4.6 Electron microscopy (EM)

Electron microscopy was performed in collaboration with the laboratory of Prof. Dr. Werner Kühlbrandt at the Max Planck Institute of Biophysics, Frankfurt. Sample freezing and microscopy was performed together with Dr. Susann Kaltwasser. Data processing and structural analysis of cryo-EM data were performed by Dr. Janet Vonck.

4.4.6.1 Preparation of negative stained samples

To analyse the quality of the protein sample prior to cryo-EM, negative stain electron microscopy was performed. For this 3 µl of the KtrAB complex with a concentration of 0.008 mg/ml was applied to glow-discharged 400 mesh carbon-coated copper grids. To determine conformational changes in KtrA, 3 µl of the purified sample was adjusted to a concentration of 0.006 mg/ml and applied to glow-discharged grids. Discharging was performed with a PELCO easiGlow device (Ted Pella, Inc.) at 15 mA for 90 s. The applied sample was incubated on the grid for 30 s at room temperature. Subsequently, the sample was removed with filter paper Nr. 4 (Whatmann®) and 3 µl of 2% uranyl formate were applied and immediately removed with the filter paper. Final staining was achieved by applying 3 µl of uranyl formate and incubating for 1 min. The stain was removed with the filter paper and the grid was air-dried to avoid liquid remnants. Grids were investigated in a Tecnai G^2 Spirit BioTWIN microscope (FEI Company) with a Rio™ 16 camera (Gatan, Inc.). EM pictures were collected by automated acquisiton using Leginon (Potter et al, 1999). Automated particle picking and 2D classification were performed with cisTEM (Grant et al, 2018). The 2D class averages obtained from negative staining were used to analyse the effect of Mg^{2+}, ATP and Mg^{2+} as well as ADP and Mg^{2+} on the conformation of KtrA. To determine if KtrA shows the oval or the square-shaped conformation, the method previously established by M. Schrecker (2018) was used. Therefore, the longest and shortest diameter of each class was measured using GIMP (gimp.org). The ratio of the diameters was calculated and compared to a set threshold of 1.115. Classes with a diameter ratio of less than 1.115 were defined to show the square-shaped conformation. For classes with a ratio of more than 1.115, the oval-shaped conformation was assumed. Sample preparation and analysis was performed by Celina Thiel, Institute of Biochemistey, Goethe-University, Frankfurt.

4.4.6.2 Sample vitrification

For cryo-EM CF-1.2/1.3-4Cu holey carbon grids (Protochips, Inc.) were glow discharged twice with a PELCO easiGlow device at 15 mA for 45 s. A volume of 3 µl sample (8-10 mg/ml) was applied on a grid immediately before plunge freezing. Samples were vitrified at 4°C and 100% humidity using a Vitrobot Mark IV device (Thermo Fisher) with blot forces of 4 and -2. Blotting times were varied from 9 -13 s, in 1 s steps, before plunge freezing in liquid ethane. Vitrified samples were stored in liquid nitrogen.

4.4.6.3 Cryo-EM image recording and processing

Images were recorded using a Titan Krios G3i microscope (Thermo Fisher Scientific) operated at 300 kV in Energy-Filtered Transmission Electron Microscopy (EFTEM) mode. Electron-optical alignments were adjusted with EPU software (Thermo Fisher Scientific). Micrographs were recorded using automated data acquisition of EPU in electron counting mode on a Gatan K3 direct electron detector at a nominal magnification of 105,000x. This corresponds to a calibrated pixel size of 0.831 Å. Dose fractionation movies were recorded at an electron flux of 13 $e^- \times pixel^{-1} \times s^{-1}$ for 2 s exposure time, corresponding to a total dose of ~40 $e^-/Å^2$. A defocus range between -0.5 and -2.5 µm was used.

To correct beam-induced motions and to generate dose-weighted images, MotionCor2 was used (Zheng et al, 2017). Next, CTFfind was used to determine the contrast transfer function (CTF) parameters and perform correction steps (Rohou & Grigorieff, 2015). Particles were automatically picked by crYOLO (Wagner et al, 2019). Cleaning the datasets by 2D and 3D classification, 3D map refinement, Bayesian polishing and correction for electron optical aberrations were performed using RELION-3.1 (Scheres, 2012; Zivanov et al, 2018). D2 symmetry was applied in case of the sandwich complex, $KtrB_2KtrA_8KtrB_2$, and C2 symmetry for the native complex, $KtrB_2KtrA_8$. The maps were further improved by density modification in Phenix (Terwilliger et al, 2020).

4.4.6.4 Model building

Atomic models were built in Coot (Emsley & Cowtan, 2004) and refined by real space refinement in Phenix (Afonine et al, 2018). As an initial model served the structure based on the 6.6 Å cryo-EM density map (EMD-3450) obtained by Diskowski et al. (2017).

4.4.7 Laser-induced Liquid Bead Ion Desorption-Mass Spectroscopy (LILBID-MS)

LILBID-MS measurements and data analysis were performed by Dr. Jan Hoffmann, Institute of Physical and Theoretical Chemistry, Goethe-University, Frankfurt. Native mass spectroscopy was performed to verify the oligomeric assembly of the purified native complex. For this, 3 µl of KtrAB at a concentration of 10 µM in LILBID buffer were analysed using a homebuilt reflection time-of-flight (TOF) setup (Morgner et al, 2007)

4.4.8 Electron paramagnetic resonance (EPR) spectroscopy

To investigate the flexibility of the intramembrane loop in the KtrAB complex under activating and inactivating conditions, as well as in the presence and absence of KtrB's N terminus, electron paramagnetic resonance (EPR) spectroscopy was performed. To measure long distances between 2 and 7 nm, double electron-electron resonance (DEER) measurements were carried out. Purification of EPR variants, measurements and evaluations of the experiments were performed together Dr. Dorith Wunnicke-Kortz, Institute of Biochemistry, Goethe-University, Frankfurt.

4.4.8.1 Purification and spin-labelling of KtrAB variants

For the EPR measurements, position T318C in the intramembrane loop of KtrB was chosen for site-directed spin-labelling, which has previously been used to successfully investigate the flexibility of the loop (Diskowski et al, 2017; Hänelt et al, 2010b). As KtrB forms a dimer, intramolecular distances can be measured between the two spin-labelled T318C residues in an otherwise cysteine free variant. The purification of the variants was performed following the protocol in section 4.3.6.3 until binding to Ni^{2+}-NTA agarose. A small deviation from the protocol occurred at the solubilisation step, in which 5 mM β-mercaptoethanol were added to the solution. After binding to Ni^{2+}-NTA agarose, the beads were washed with 50x CV of buffer W containing 0.04% DDM, 50 mM imidazole and 5 mM β-mercaptoethanol, followed by an additional wash step with 15x CV ice-cold and degassed buffer W with 0.04% DDM to remove β-mercaptoethanol. For spin-labelling, 2x CV buffer W supplemented with 0.04% DDM and 1 mM MTSSL were added to the beads and after 1 CV of buffer passed through the beads, the column was closed and incubated with the remaining buffer over night at 4°C. Subsequently, the Ni^{2+}-NTA agarose beads were extensively washed with 30 CV buffer W with 0.04% DDM to remove excessive MTSSL. The protein was finally eluted with buffer W containing 0.04% DDM and 500 mM imidazole, followed by SEC as described in section 4.3.6.2.

The samples were measured either detergent-solubilised after SEC concentrated to ~10 mg/ml or reconstituted into liposomes with a final lipid concentration of ~100 mg/ml. Reconstitution was performed as described in section 4.3.8.4

4.4.8.2 Double electron-electron resonance (DEER) measurements

The proteoliposomes were washed in inside reconstitution buffer by centrifugation at 450,000 g for 30 min. Afterwards they were resuspended in the same buffer to have a lipid concentration of 10 mg/ml. To incorporate ADP or ATP into the liposomes, 10 mM ADP and 10 mM ATP, respectively, were added to the samples and three cycles of freeze and thaw were performed. Subsequently, the samples were extruded 11 times through a 400 nm filter and centrifuged for 30 min at 450,000 g. The pellet was washed in the same volume of outside reconstitution buffer and the centrifugation step was repeated. Finally,

the proteoliposome pellet was resuspended in a minimal volume of outside reconstitution buffer to achieve a lipid concentration of ~100 mg/ml. As the outside reconstitution buffer does not contain KCl but sorbitol in comparison to the inside reconstitution buffer, an outward-directed K^+ gradient was established. Activation or inactivation was further triggered by the previous addition of 10 mM ATP or 10 mM ADP. Furthermore, 14% deuterated glycerol (Glycerol-d8) was added to each sample. To finally initiate K^+ flux at activating conditions, the built-up membrane potential was abolished by the addition of 1 µM CCCP, shortly before 15 µl of the sample were transferred into an EPR quartz tube with a 1.6 mm outer diameter and flash frozen in liquid nitrogen. Detergent-solubilised samples were concentrated to ~10 mg/ml and, after addition of 10 mM ATP + 2 mM $MgCl_2$ or 10 mM ADP + 2 mM $MgCl_2$, transferred into the EPR capillary. Samples for subsequent DEER experiments were stored at -80°C until further usage. DEER spectra were recorded using an Elexsys 580 spectrometer (Bruker Corporation) at Q-band (33.7 GHz) and 50 K. For the recording, a four-pulse sequence (Pannier et al, 2000) with a pump pulse length of 12 ns and a frequency separation of 70 MHz were applied. The resulting spectra were analysed using DeerAnalysis (Jeschke et al, 2006) and the distance distribution was determined by Tikhonov regularisation.

4.4.9 Molecular dynamics (MD) simulations of KtrB in the ADP-bound conformation

The molecular model of KtrB resulting from the cryo-EM data of the KtrAB complex (3.1 Å obtained in this thesis) was placed in a heterogenous lipid bilayer (POPE (45%), POPG (40%), and cardiolipin (15%)) and then solvated in TIP3P water with 150 mM KCl. The CHARMM36m force field was used for protein, ions, and lipid species (Best et al, 2012; Jorgensen et al, 1983; Klauda et al, 2010). An all-atom MD simulation was performed using GROMACS 2020.2 (Abraham et al, 2015). The initial system was energy-minimized for 2,000 steepest descent steps and equilibrated first for 1 ns of MD simulations in a canonical (NVT) ensemble and then for 7.5 ns in an isothermal-isobaric (NPT) ensemble under periodic boundary conditions. Positional restrains were used on the non-hydrogen protein atoms (4,000 $kJ \cdot mol^{-1} \cdot nm^2$) and during equilibration, these restraints were gradually decreased to zero. Particle-mesh Ewald summation with cubic interpolation (a 0.12-nm grid spacing) was used to treat long-range electrostatic interactions (Darden et al, 1993). The time step in the first steps of the equilibration was 1 fs, and then was increased to 2 fs during the NPT equilibration. The LINCS algorithm was used to fix all bond lengths (Hess et al, 1997). Constant temperature was set with a Berendsen thermostat (Berendsen et al, 1984), combined with a coupling constant of 1.0 ps. A semi-isotropic Berendsen barostat (Berendsen et al, 1984) was used to maintain a pressure of 1 bar. During the production run, the Berendsen thermostat and barostat were replaced by a Nosé–Hoover thermostat (Hoover, 1985) and a Parrinello–Rahman barostat (Parrinello & Rahman, 1981). A production run was performed for 1 µs.

5 Results

5.1 Localisation and assembly of KtrAB in *B. subtilis* cells

KtrAB is located within the bacterial membrane, which is why it is surrounded by lipids. In general, it is known that lipids can have drastic effects on the localisation and the activity of membrane proteins. It has been reported that bacteria can decrease or increase their membrane fluidity by forming 'lipid rafts' or 'RIFs', respectively (Bramkamp & Lopez, 2015; Strahl et al, 2014). 'Lipid rafts' have previously been described for eukaryotic cells (Simons & Ikonen, 1997), however, it has been shown that also bacteria can organise proteins into functional membrane microdomains constituted by specific lipids, reducing the membrane fluidity (Lopez & Kolter, 2010). Regions with increased fluidity (RIFs) are organised by MreB, an actin homologue, and are involved in the distribution of several membrane proteins like Fructose permease or RNase Y (Strahl et al, 2014). Furthermore, changes in phospholipid composition, headgroups, length and saturation of acyl chains, membrane tension as well as curvature can affect the function and localisation of the proteins. Especially, during the adaptation to osmotic stress, the lipid composition is drastically varied (Poolman et al, 2004). To analyse whether osmotic stress in combination with varied lipid compositions has an effect on the distribution of the KtrAB complex in the membrane, fluorescence microscopy was performed with *B. subtilis* cells. To visualise KtrAB in the bacterial cell, fluorescently labelled variants of KtrAB from *B. subtilis* were prepared. All experiments described in this chapter were performed in collaboration with Dr. Henrik Strahl at the Centre for Bacterial Cell Biology (CBCB), Newcastle University.

5.1.1 Localisation of $KtrB_{msfGFP}$ within the membrane upon osmotic stress and different lipid environments

To follow the localisation of KtrAB in the membrane, KtrB with an N-terminally fused monomeric superfolder GFP (msfGFP) was designed (Figure 11 A) and *B. subtilis ktrAB::kan kimA::ery* cells were transformed with the plasmid for integration of KtrA-$_{msfGFP}$KtrB at the *amyE* locus via homologous recombination. Correct integration was verified by testing the amylase activity. In case of correct integration, the *amyE* gene was disrupted, leading to a non-functional α-amylase, resulting in a loss of starch hydrolysis (cf. 4.2.3). To analyse the functionality of the GFP-tagged KtrB variant, the ability to complement growth at potassium limitation was investigated (Figure 11 B). While the deletion of *ktrAB::kan* and *kimA::ery* resulted in an impaired growth at all tested K^+ concentrations even after 24 h, the *ktrAB::kan kimA::ery* strain producing the GFP-tagged

version of KtrB complemented growth already at a K^+ concentrations of 0.025 mM KCl, similar to *B. subtilis* wildtype cells, indicating that KtrA-$_{msfGFP}$KtrB was functional.

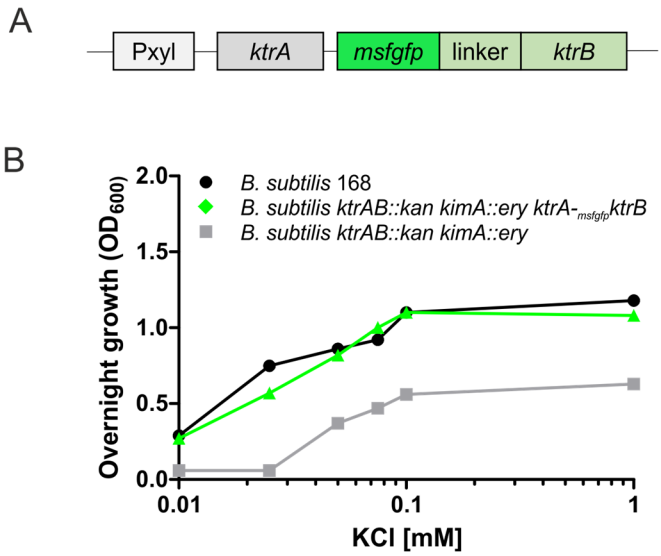

Figure 11: Growth complementation assay of *B. subtilis* cells producing KtrA-$_{msfGFP}$KtrB. A) Schematic illustration of the used $_{msfGFP}$KtrB construct. B) Growth of *ktrAB::kan kimA::ery* cells producing the GFP-fused KtrAB variant (green), wildtype *B. subtilis* cells (black) and the *ktrAB::kan kimA::ery* cells (grey), was followed for 24 h in the presence of different KCl concentrations. OD_{600} of the cells after 24 h is presented against the used potassium concentration (logarithmic presentation). Used KCl concentrations: 0.01 mM, 0.025 mM, 0.05 mM, 0.075 mM, 0.1 mM and 1 mM. While the *ktrAB::kan kimA::ery* strain shows impaired growth, wildtype and the msfGFP-fused variant revealed similar growth already at a concentration of 0.025 mM KCl.

To follow the localisation of KtrB in dependence of different osmotic conditions, the cells were exposed to potassium limitation and hyperosmotic stress during fluorescence microscopy. Here, potassium limitation was achieved by washing the cells with K^+-free medium prior to imaging. For hyperosmotic condition, microscopy slides were prepared in the presence of 1 M NaCl or 1 M sucrose, to apply osmotic shock during imaging. Under all tested conditions the localisation pattern was identical, showing a homogenous distribution of KtrB throughout the membrane (Figure 12 A). The observed small clusters in the presence of 1 M NaCl or 1 M sucrose, indicated by white arrows (Figure 12 A), were KtrB unspecific, as similar patches were identified when performing a general membrane stain by FM 4-64 (Figure 12 A, small images), a styryl dye that partitions into lipid membrane surfaces due to its intrinsic hydrophobicity (Wu et al, 2009). These results indicate, that KtrAB does not co-localise in microdomains or specific clusters upon different osmotic conditions.

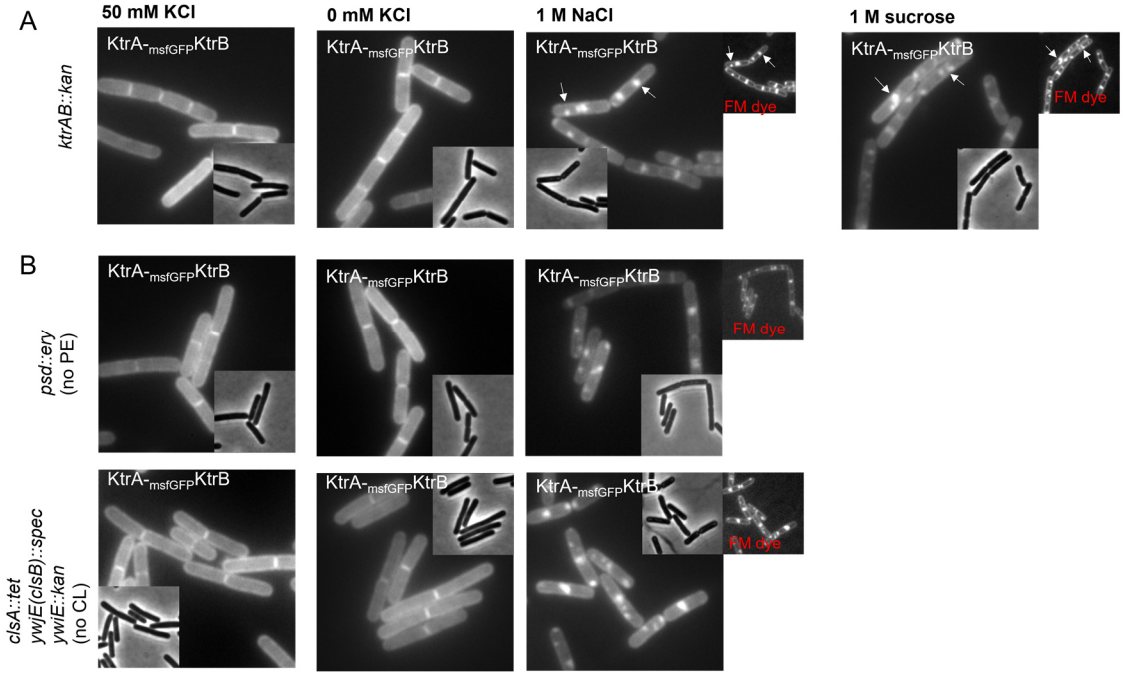

Figure 12: Distribution of KtrB$_{msfGFP}$-KtrA within the membrane comprising different lipid compositions. Cells were exposed to different osmotic stress conditions. A) Representative *B. subtilis ktrAB::kan* cells producing KtrA-$_{msfGFP}$KtrB in a native lipid environment. Different osmotic shocks were applied during microscopy (0 mM: potassium limitation, 50mM KCl: non-stress, 1 M NaCl/ 1 M sucrose: hyperosmotic shock). General lipid appearance and distribution was analysed by staining the cells with FM 4-64 (0.5 µg/ml), marked with red labels. Lipid clusters are indicated by white arrows. Representative cells were chosen, and phase-contrast images are shown in small insets. B) *B. subtilis* strains with impaired lipid synthesis were analysed: Cells containing membranes lacking PE (psd::ery) and cells without CL synthesis (clsA::tet, ywJE::spec, ywiE::kan) were used. Microscopy was performed with the help of Dr. Henrik Strahl, CBCB, Newcastle upon Tyne.

As mentioned above, a factor that changes significantly upon hyperosmotic conditions, is the composition of the plasma membrane. For various bacteria it has been shown that the content of anionic cardiolipin (CL) increased, while the amount of zwitterionic phosphatidylethanolamine (PE) decreases (Romantsov et al, 2009). In line with these changes, the activity and localisation of transport proteins that take up compatible solutes as a second response to osmotic stress, including ProP, OpuA, and BetP, have been shown to depend on the charges of phospholipid head groups (Poolman et al, 2004). For KtrAB, no such information is available. Therefore, to analyse the effect of an altered membrane lipid composition on the KtrAB system, the fluorescently-labelled version of KtrB was combined with defects in the synthesis of different lipids. Using the natural competence of *B. subtilis* either the gene for PE synthesis (*psd*::*ery*) or the genes involved in the production of CL (*clsA::tet ywjE(clsB)::spec ywiE::kan*) were deleted. To exclude that the lipid defects affect KtrAB's activity the cells were grown at K^+ limitation prior to microscopy. Here, the cells grew equally well at low potassium concentrations similar to cells with a native lipid environment. The distribution of KtrB in its native lipid environment was then compared with membranes lacking either PE or CL (Figure 12 B). Regardless of the lipid composition, KtrB was uniformly distributed in the membrane (Figure 12 A, B). In

addition, osmotic stress did not change the localisation pattern in cells with altered lipid composition.

Taken together, the results indicated that KtrB does neither colocalise with individual lipid patches nor depend on PE or CL specifically. However, whether lipids influence the activity of KtrAB in more general, e.g. via their differently charged headgroups, remains elusive and needs to be investigated.

5.1.2 Assembly of the KtrAB complex in *B. subtilis*

Since the KtrAB complex has a unique architecture, consisting of two non-covalently linked subunits, the question arises why nature has evolved this alternative system. Whether the interaction and assembly of the two subunits, KtrA and KtrB, is a dynamic process allowing the adaptation for example to changing osmotic conditions is yet unknown. For many years the KtrAB system was studied in vitro, but information on the assembly of the complex in vivo was missing. Therefore, the dynamics of the complex on a cellular level were analysed by fluorescence microscopy.

To analyse whether KtrA and KtrB assemble or disassemble depending on osmotic conditions, a fluorescently-labelled variant of KtrA was expressed in living *B. subtilis* cells, to follow its distribution *via* fluorescence microscopy. Before fluorescence microscopy was performed, it was verified that KtrA fused to msfGFP was still able to assemble to KtrB. The fusion of a msfGFP to each KtrA monomer increases the size of the KtrA ring drastically, which is why it was to be excluded that it sterically hinders the complex assembly. For this purpose, whole-cell uptake experiments were performed using *E. coli* LB 2003 cells expressing *ktrA*$_{msfgfp}$*-ktrB, ktrAB* or only *ktrB* from *B. subtilis*. In previous whole-cell uptake experiments it was observed, that KtrB from *B. subtilis* does not efficiently take up potassium, while KtrAB quickly accumulates high amounts of K^+ (Fuss, 2019). Uptake experiments were performed in the presence of 0.2 mM KCl and 5 mM NaCl, with the fusion construct KtrA$_{msfGFP}$-KtrB accumulating K^+ similar to wildtype KtrAB while KtrB hardly takes up K^+ (Figure 13). Hence, complex assembly appeared to be undisturbed.

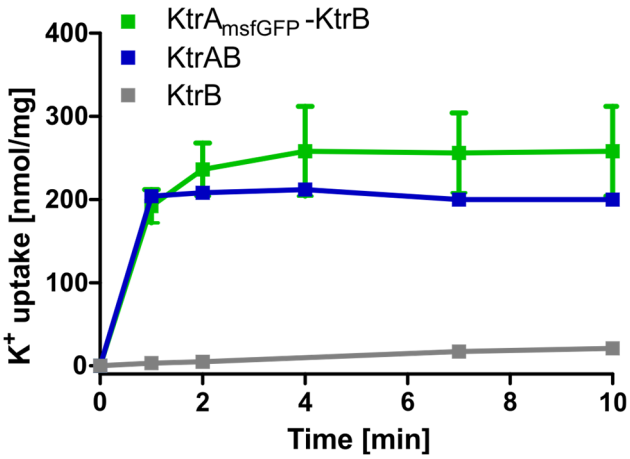

Figure 13: K^+ uptake by *E. coli* LB2003 cells producing KtrA$_{msfGFP}$KtrB from *B. subtilis*. Uptake experiments were performed to verify, if KtrA$_{msfGFP}$ can functionally associate to KtrB, allowing potassium accumulation. For this, cells were depleted of K^+ after protein production, and after 10 min incubation at room temperature, 0.2 mM KCl was added. For 10 minutes 1 ml samples were taken at different time points, and cells were separated from medium by centrifugation through silicone oil. Intracellular K^+ concentrations were determined by flame photometry. *E. coli* LB2003 cells producing KtrA$_{msfGFP}$-KtrB (green) accumulated K^+ similar to *E. coli* LB2003 cells producing KtrAB (blue), while E. *coli* LB2003 cells producing KtrB (grey) hardly take up K^+.

Since the expression levels should be comparable to wildtype expression, a variant with *ktrA* C-terminally fused to a *msfGFP* (*ktrA$_{msfGFP}$*) controlled by its native promoter, was prepared. For this the integration vector pMUTIN4 was used, which in addition introduces an inducible promoter (Pspac) for the downstream gene *ktrB* into the genome (Figure 14 A). Consequently, the resulting mutant allows to analyse changes in the localisation of KtrA in the presence and absence of KtrB. To ensure that KtrB was produced after IPTG induction, growth complementation assays were performed as described in section 4.2.4. The assay confirmed the production of KtrB, as the variant grew similar to the wildtype at K^+ limitation, while growth of the strain which was neither producing KtrB nor KimA (*ktrAB::kan kimA::ery)* was significantly reduced (Figure 14 B).

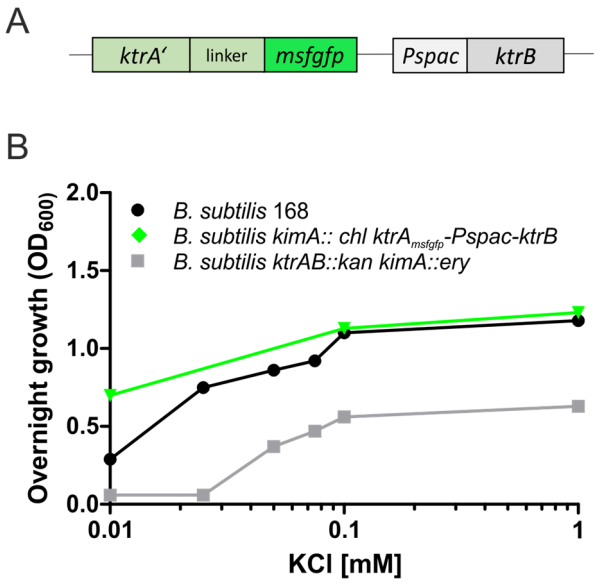

Figure 14 Growth complementation assay of *B. subtilis* cell producing KtrB under the control of an IPTG inducible promoter, while the production of KtrA is under its native promoter. A) Schematic depiction of the insert of pMUTIN4. Fluorescently-labelled subunit is highlighted in green. Pspac represents the IPTG-inducible promoter upstream of KtrB. B) Growth of *kimA::chl* cells expressing the *ktrA*$_{msfgfp}$ variant at native levels and *ktrB* by the induction of IPTG (green), wildtype *B. subtilis* cells (black) and the *ktrAB::kan kimA::ery* cells was followed for 24 h in the presence of different KCl concentration. OD_{600} of the cells after 24 h is presented against the used potassium concentration (logarithmic presentation). Used KCl concentrations: 0.01 mM, 0.025 mM, 0.05 mM, 0.075 mM, 0.1 mM, and 1 mM. While the *ktrAB::kan kimA::ery* strain shows impaired growth, *B. subtilis* wildtype and *B. subtilis* cells producing the msfGFP-fused variant revealed similar growth already at a concentration of 0.025 mM KCl, indicating the production of KtrB. Expression of *ktrB* was induced by the addition of 1 mM IPTG.

As it was confirmed that KtrB is produced upon IPTG induction and $KtrA_{msfGFP}$ can assemble to KtrB, fluorescence microscopy was applied to *B. subtilis* cells expressing *ktrA*$_{msfGFP}$. To follow the localisation of KtrA in dependence of osmotic conditions, the cells were exposed to hypo- and hyperosmotic stress conditions during fluorescence microscopy. Here, potassium limitation was achieved by washing the cells with K^+-free medium prior to imaging. In the absence of KtrB (Figure 15 A) the fluorescence signal was, as expected, diffusely distributed throughout the cytoplasm even though the cell was exposed to hypoosmotic conditions. To enable the association of KtrA to KtrB, *ktrB* gene expression was induced with 1 mM IPTG (Figure 15 B). Besides K^+ limitation, the effect of hyperosmotic stress, under which the cells need to counteract the loss of water by K^+ uptake *via* KtrAB, was tested. For this, the cells were exposed to 500 mM NaCl during imaging. In the presence of KtrB, at least under hyperosmotic conditions (500 mM NaCl and 0 mM KCl), it was expected that $KtrA_{msfGFP}$ assembles with the membrane-spanning KtrB for efficient potassium uptake, resulting in a fluorescence signal located at the membrane. Unexpectedly, though, all experiments revealed a cytoplasmic localisation of $KtrA_{msfGFP}$, indicating a missing assembly of KtrA and KtrB, as in case of assembly a signal in the membrane was expected, similar to the pattern observed in section 5.1.1.

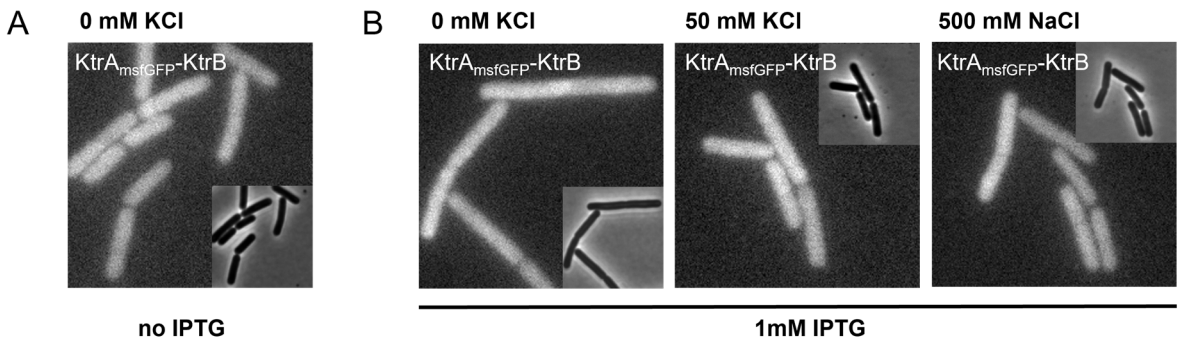

Figure 15: Expression of *ktrA$_{msfgfp}$* under its native promoter. KtrB expression was induced by the addition of IPTG. A,B) Representative selection of *B. subtilis* cells expressing *ktrA$_{msfgfp}$* in the absence of IPTG (A) and upon the induction of *ktrB* expression with 1 mM IPTG (B). The cells were exposed to different osmotic conditions (0 mM: Potassium limitation, 50 mM KCl: Non-stress, 500 mM NaCl, 0 mM KCl: Hyperosmotic shock). The small inset represents the phase contrast image of the cells. Under all conditions the fluoresence signal was observed in the cytoplasm. Microscopy was performed with the help of Dr. Henrik Strahl, CBCB, Newcastle upon Tyne.

However, the fluorescence intensity of KtrA$_{msfGFP}$ was very low due to low expression levels, so the signal in the membrane of the assembled complexes may have been too low to be detected at native expression levels. To optimise the signal-to-noise ratio, the msfGFP fusion construct was cloned under a promoter that could be fine-tuned with xylose.

5.1.3 Localisation of KtrA$_{msfGFP}$ expressed under a xylose-inducible promoter

To increase the fluorescence intensity, the *ktrA$_{msfgfp}$-ktrB* operon was cloned under a xylose-inducible promoter (Figure 16 A). Various naturally competent *B. subtilis* strains, lacking different endogenous potassium uptake systems like KtrAB, KtrCD and/or KimA, were transformed with the msfGFP fusion construct. Correct integration was verified via starch assay as described above (cf. 4.2.3). Functionality of the fusion construct was confirmed by complementation assays (Figure 16 B). Here, the production of a functional KtrA$_{msfGFP}$-KtrB variant in *ktrAB::kan kimA::ery* cells allowed growth at K^+ limitation similar to wildtype cells, indicating that the variant was functional.

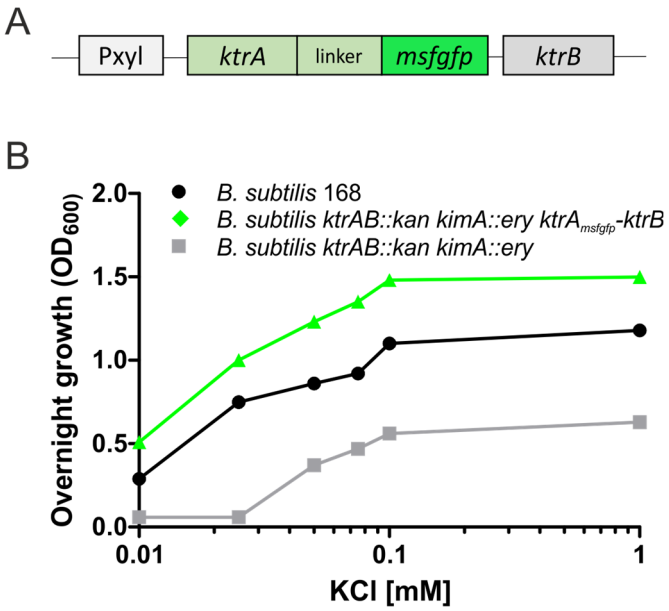

Figure 16: Growth complementation assay of *B. subtilis* cell producing KtrA$_{msfGFP}$-KtrB. A) Schematic representation of fusion construct. The construct encodes for KtrA with C-terminally fused msfGFP followed by KtrB. Both genes are under control of a xylose-inducible promoter. B) Growth of *ktrAB::kan kimA::ery* cells producing the GFP-tagged KtrAB variant (green), wildtype *B. subtilis* cells (black) and the *ktrAB::kan kimA::ery* cells (grey) was followed for 24 h in the presence of different KCl concentrations. OD_{600} of the cells after 24 h is presented against the used potassium concentration (logarithmic presentation). Used KCl concentrations: 0.01 mM, 0.025 mM, 0.05 mM, 0.075 mM, 0.1 mM and 1 mM. While the *ktrAB::kan kimA::ery* strain showed impaired growth, *B. subtilis* wildtype cells and *B. subtilis* cells producing the msfGFP-fused variant of KtrAB revealed similar growth already at a concentration of 0.025 mM KCl.

5.1.3.1 Xylose screening for optimal expression levels

To increase the signal-to-noise ratio and optimise the protein levels of KtrA$_{msfGFP}$, different xylose concentrations were screened. The aim was to increase the fluorescence intensity, but not overexpress the protein on an exceedingly high, non-native level, which would result in too high fluorescence intensity. Therefore, *ktrA$_{msfGFP}$-ktrB* was integrated into the genome of *B. subtilis* cells (Figure 16 A) and the cells were grown in LB_{50KCl} induced with either 0%, 0.0001%, 0.0005% or 0.001% xylose. Fluorescence microscopy with living cells, fixed on thin agar patches, was performed in the early-exponential growth phase (Figure 17 A).

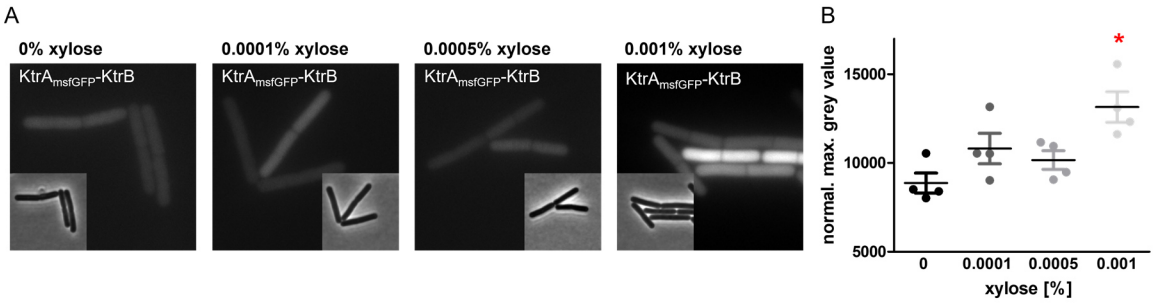

Figure 17: Xylose screening for optimal expression levels. A) Fluorescence microscopy images of representative *B. subtilis* cells, expressing *ktrA$_{msfgfp}$-ktrB*, induced with either 0%, 0.0001%, 0.0005% or 0.001% xylose. Only with 0.001% xylose a fluorescence intensity significantly higher than background signal was observed. The inset represents the phase-contrast image of the selected cells. B) Fiji was used to calculate the minimal and maximum grey values from four microscopy images of each condition. After background correction an unpaired t-test (two tailed) revealed a statistical significance (p value = 0.0060) for 0.001% xylose (indicated by the red asterisk). Microscopy was performed with the help of Dr. Henrik Strahl, CBCB, Newcastle upon Tyne.

Induction with 0.0001% and 0.0005% xylose revealed only a very weak fluorescence signal, without significant difference to uninduced cells (Figure 17 A). Using Fiji, the minimal and maximal grey values of pixels were determined for four microscopic images of each xylose concentration. After the minimal values were subtracted from the maximum value as background, the mean values were compared. While no statistically significant difference was observed between 0%, 0.0001% and 0.0005% xylose (Figure 17 B), a xylose concentration of 0.001 % showed a significantly increased signal intensity in an unpaired t-test, which was strong enough to differentiate background and fluorescence signal (Figure 17 B). Therefore, the cells for further experiments were induced with 0.001% xylose.

5.1.3.2 Effect of osmotic stress on the localisation of KtrA$_{msfGFP}$ in cells lacking endogenous uptake systems

So far, no localisation of KtrA$_{msfGFP}$ at the membrane was observed. To ensure that potassium uptake upon osmotic stress in fact relies on the KtrA$_{msfGFP}$-KtrB variant and is not mediated by any of the endogenous potassium uptake system, the distribution of the inducible KtrA$_{msfGFP}$ variant was analysed in cell backgrounds lacking the major potassium uptake systems KtrAB or KtrAB and KimA. Osmotic stress and non-stress conditions during microscopy were applied. In medium with 50 mM KCl the cells were non-stressed, while with 0 mM KCl the cells suffered potassium limitation (Figure 18 A, 1st and 2nd column, respectively). Similar to what was observed before, the fluorescence signal of KtrA$_{msfGFP}$ in the *ktrAB::kan* strain background was primarily observed in the cytoplasm. However, upon deletion of both KtrAB and KimA, small clusters of fluorescence signal

were identified independent of the osmotic condition (Figure 18 A 2nd row). To verify whether these clusters were located at the membrane because KtrA assembled to KtrB, only *ktrA*$_{msfgfp}$ was expressed under a xylose-inducible promotor in a strain background with all known potassium uptake systems (*ktrAB::kan, kimA::ery and ktrD::tet*) deleted, preventing KtrA$_{msfGFP}$ interaction either with KtrB or via crosstalk with KtrD (Figure 18 B). Again, fluorescent clusters were visible, indicating an unspecific clustering of KtrA$_{msfGFP}$ for cells with impaired potassium homeostasis. Also, hyperosmotic stress should trigger the assembly of KtrA to KtrB. Therefore, the cells were exposed to either 1 M NaCl or 1 M sucrose during microscopy (Figure 18 A, column 3 and 4). For this, the thin agar patches used on the microscope slides were supplemented with either NaCl or sucrose, to immediately image the effect of the hyperosmotic condition on the cells, as it is a very fast response. While a general effect on the cellular cytoplasm was observed, indicated by the white arrow in Figure 18 A, the distribution of KtrA$_{msfGFP}$ remained diffuse in the cytoplasm. Hence, so far, conditions under which the two subunits assemble as a complex remained elusive.

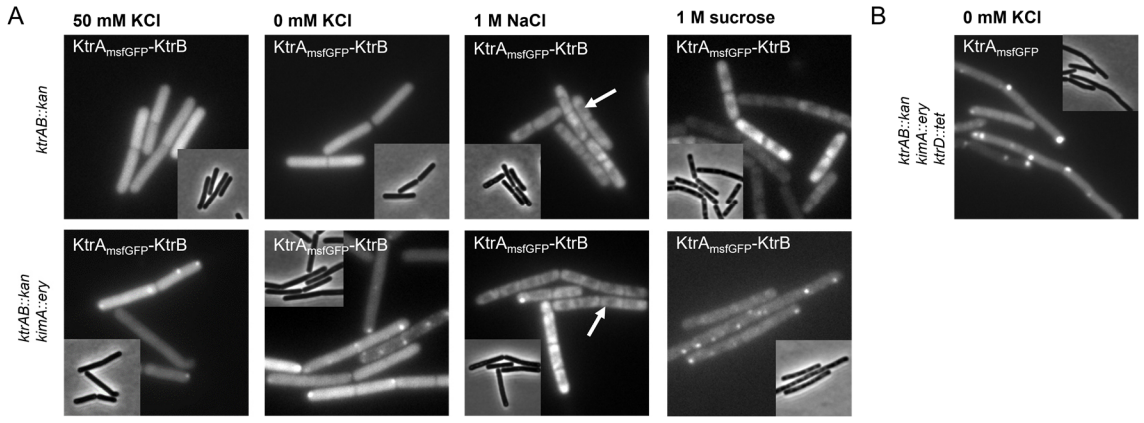

Figure 18: Distribution of KtrA$_{msfGFP}$ in different *B. subtilis* strain backgrounds and under different osmotic conditions. A) Upper row shows KtrA$_{msfGFP}$-KtrB expressed in *B. subtilis ktrAB::kan* cells exposed to different osmotic conditions: (0 mM: potassium limitation, 50mM KCl: non-stress, 1 M NaCl/1 M sucrose: hyperosmotic shock). Lower row represents KtrA$_{msfGFP}$-KtrB in *B. subtilis* lacking *ktrAB* and *kimA* at the same osmotic conditions as in the upper row. General effects of hyperosmotic conditions are indicated by a white arrow. B) Distribution of KtrA$_{msfGFP}$ in *B. subtilis* cells lacking all potassium uptake systems, including KtrB and KtrD, at potassium limitation. Representative cells of each condition were chosen, and phase-contrast images are shown as small insets. Microscopy was performed with the help of Dr. Henrik Strahl, CBCB, Newcastle upon Tyne.

5.1.3.3 Time-dependent localisation of $KtrA_{msfGFP}$-KtrB and the effect of membrane potential loss

To investigate whether the assembly occurs in a time-dependent manner, time-lapse microscopy experiments were performed. Here, the cells were monitored over 13 hours, fixed on a microscope slide. Prior to microscopy, the cells were grown in LB_{50KCl} until mid-exponential phase was reached, and subsequently immobilised on agar stripes prepared with 10% LB_{50KCl}, to offer enough nutrients during microscopy (cf. 4.2.5.2). For the first approximately 8 hours, the GFP signal was homogenously distributed in the cytoplasm as described before. Surprisingly, after 8 hours the GFP signal changed its pattern to a clustered signal, potentially localised at the cell membranes (Figure 19 A). This phenomenon was observed for all strain backgrounds, including deletions of KtrAB, KimA and/or KtrD (Figure S1). Since the clustering only appeared after several hours, I hypothesised that it could reflect oxygen limitation to the cells, which consequently would cause severe cellular stress, including a loss of membrane potential.

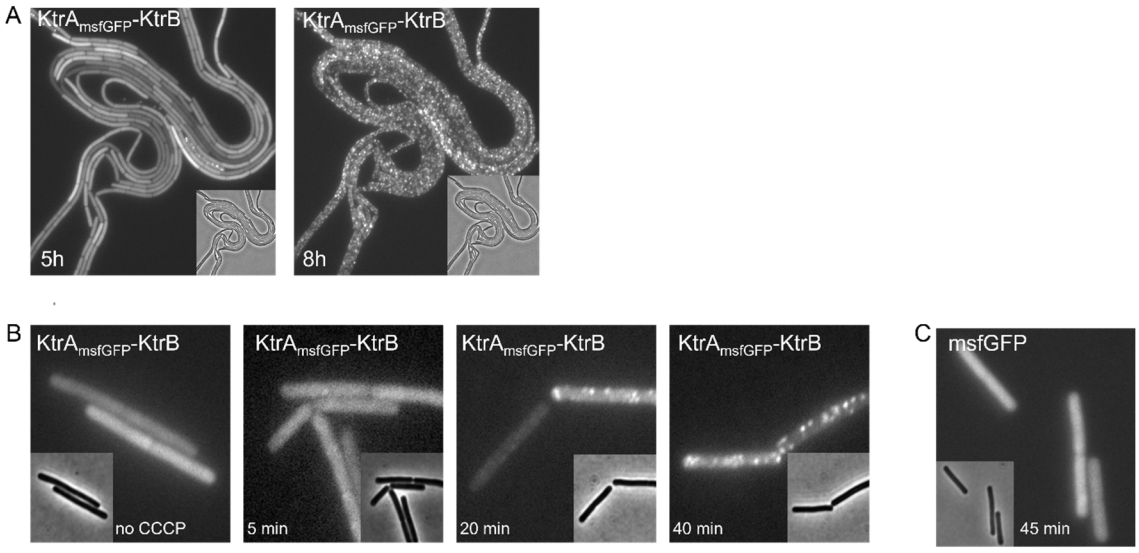

Figure 19: Time-lapse microscopy of *B. subtilis ktrAB::kan* expressing *$ktrA_{msfgfp}$-ktrB* and the effect of membrane potential loss. Representative fluorescence images of *B. subtilis* cells and the respective phase-contrast image shown in small insets. A) The localisation of $KtrA_{msfGFP}$ in *B. subtilis ktrAB::kan* cells was monitored for 13 hours. Within 8 hours the fluorescence signal was distributed diffusely in the cytoplasm. Afterwards, clusters of GFP signals located towards the membrane were identified. B) Membrane potential was abolished by the addition of 100 µM CCCP. Cells were incubated for 5, 10, 20 and 40 minutes (left to right). After 20-40 minutes similar clusters as in (A) were observed. C) As a control, only msfGFP was produced and cells were incubated with CCCP for 45 minutes. No cluster formation was observed. Control experiment was performed by James Grimshaw, CBCB, Newcastle Upon Tyne. Microscopy in general was performed in collaboration with Dr. Henrik Strahl, CBCB, Newcastle upon Tyne.

To validate if the loss of membrane potential induces cluster formation, *B. subtilis ktrAB::kan* cells expressing *$ktrA_{msfgfp}$-ktrB* under a xylose promoter, were treated with carbonyl cyanide chlorophenylhydrazone (CCCP), a proton ionophore which abolishes the membrane potential, for different periods of time, prior to analysis by fluorescence

microscopy (Figure 19 B). Interestingly, after 20 to 40 minutes, in fact, a pattern similar to that observed after 8 hours of time-lapse microscopy, was visible. As a control for unspecific clustering only *msfgfp* was expressed and the cells were incubated with CCCP for 45 minutes. In this case, no clusters were observed. However, just recently, the cluster formation of GFP-labelled proteins upon loss of membrane potential, including various cytoplasmic proteins as well as different membrane proteins, was shown to be an artificial side-effect. The proteins were observed to form aggregated clusters in the cell, often located towards the membrane. It is speculated that the clustering is caused by changes of the intracellular pH (personal communication Dr. Henrik Strahl). Therefore, the observed effect likely has no biological relevance for the assembly of KtrAB. In consequence, with all tested conditions, no unambiguous complex assembly was observed. This observation was very surprising, since previously performed in vitro structural approaches clearly revealed that the two subunits assemble (Vieira-Pires et al, 2013) and whole-cell uptake experiments here confirmed the assembly of $KtrA_{msfGFP}$ and KtrB. Therefore, it is tempting to speculate, that complex formation occurred, however, could not be resolved during microscopy. This could be due to very weak signal of KtrA at the membrane, as KtrB is homogenously distributed in the membrane as observed in section 5.1.1, avoiding the creation of any bright spots, which could be easy to detect. Furthermore, the interaction of the two subunits might be transient in vivo and therefore resulting in low signal intensity, which might not be detected. On the other hand, it can be imagined that the two subunits did not assemble as in vivo more stimuli or other conditions are required to allow complex formation.

5.2 Structural and functional analysis of the unique KtrAB complex in its native assembly

In the previous chapter the assembly and localisation of KtrAB was investigated on a cellular level. Unfortunately, no deeper mechanistical insights into the KtrAB complex could be gained. Therefore, in this part of my thesis I aimed for high-resolution structures of the KtrAB system in different conformations. In combination with further biochemical and biophysical data, this should decipher the molecular basis of potassium translocation through KtrAB, as despite the available structural and functional data of KtrAB, its gating mechanism remains largely elusive. All functional and structural experiments of this work were performed on KtrAB from *V. alginolyticus*.

5.2.1 Overcoming the non-physiological 'sandwich' assembly of the KtrAB complex

Structural analyses of KtrAB revealed that the system forms a non-physiological artefactual assembly during purification (Diskowski et al, 2017; Vieira-Pires et al, 2013), which similarly has been observed for other RCK-gated potassium channels like TrkAH and MthK (Cao et al, 2013; Jiang et al, 2002a). Due to the symmetric arrangement of the octameric RCK ring along its X-axis, a second KtrB dimer can associate to the cytoplasmically oriented side of the KtrA ring. This so-called 'sandwich' conformation is speculated to arise from the solubilisation of the complexes from the membrane. For the formation of the native complex, eight KtrAs but only two KtrBs are required, while *ktrA* and *ktrB* are localised on one operon with similarly strong ribosomal binding sites. Hence, likely an excess of KtrB dimer is produced in the cell. Whether this non-physiological assembly induces conformational artefacts is not known. Further, it interferes with the reconstitution of KtrAB into liposomes and nanodiscs. Therefore, the purification of the native KtrAB complex was the first aim of this chapter.

5.2.1.1 PEGylation of free KtrB to avoid association to the KtrAB complex

To avoid the assembly of an additional KtrB dimer to a $KtrA_8B_2$ complex, at first it was attempted to sterically hinder the association of an additional KtrB dimer. Therefore, free KtrB dimers lacking a KtrA RCK ring should be crosslinked to bulky methoxypolyethylene glycol maleimides (MeO-PEG-mal) (Figure 20 A) prior to solubilisation, while KtrB associated with KtrA and embedded in the membrane should not be accessible to MeO-PEG-mal. For this approach to be successful, it had to be ensured that crosslinking only affected free KtrB and not the native KtrAB complex, as PEGylation of the KtrAB complex would indicate that an association of a further KtrB dimer would only insufficiently be

hindered. To test this, available functional variants of $KtrBCH_6$ and $KtrANH_{10}$-KtrB, both of them containing a single cysteine at the C terminus of KtrB (E449C) in an otherwise cysteine-free protein, were used (Figure 20 B). Since the C terminus of KtrB is known to be responsible for the interaction with KtrA, a bulky MeO-PEG-mal at this position was thought to hinder the assembly. To test the accessibility of the cysteines, the proteins were overproduced and purified via affinity chromatography and size exclusion chromatography (SEC) as described in section 4.3.6. After incubation of both purified KtrB and KtrAB with six-fold and three-fold molar excess of 5 kDa or 10 kDa MeO-PEG-mal, respectively, the crosslink between the thiol group of the introduced cysteine and the MeO-PEG-mal was analysed by Coomassie-stained SDS PAGE and Western blotting. In case of PEGylation, a shift to an increased apparent molecular weight was expected. To stop the reaction before the proteins were unfolded by SDS, DTT was added. As expected for a successful PEGylation, $KtrB_{E449C}$ incubated with 5 kDa PEG migrated at an increased apparent molecular weight of ~45 kDa compared to the unmodified $KtrB_{E449C}$ at ~37 kDa, which is consistent with a crosslink of a 5 kDa MeO-PEG-mal molecule at the C terminus of KtrB (Figure 20 C). However, the majority of the protein remained unmodified, indicating an incomplete reaction. The successful PEGylation was confirmed by Western blot analysis using anti-MeO-PEG-mal antibodies to visualise PEGylated $KtrB_{E449C}$ (Figure 20 D). While no signal for PEGylated $KtrB_{E449C}$ was detected in the SDS PAGE after incubation with 10 kDa-MeO-PEG-mal, the Western blot analysis revealed a small degree of successful PEGylation, as a signal with an increased apparent molecular weight at approximately 60 kDa was identified. For $KtrAB_{E449C}$ no unambiguous signal additionally to the unmodified protein at 37 kDa was identified on the SDS PAGE (Figure 20 C). However, the Western blot analysis clearly revealed that a fraction of $KtrAB_{E449C}$ was crosslinked with the 5 kDa and 10 kDa MeO-PEG- maleimide (Figure 20 D), respectively, indicated by the signals migrating at 50 kDa and 60 kDa, respectively.

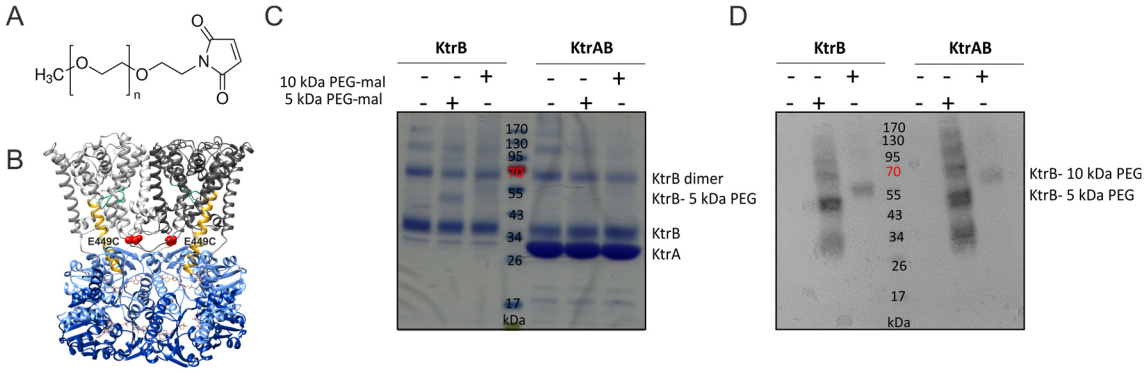

Figure 20: PEGylation of KtrB$_{E449C}$ and KtrAB$_{E449C}$. A) Chemical structure of methoxypolyethylene glycol maleimide (MeO-PEG-mal). The malemide group reacts with the thiol group of cysteines by forming a crosslink. The MeO-PEG group is a large sterical moeity, which can be varied in size. Used in this study: 5 kDa and 10 kDa MeO-PEG-mal. B) Structural representation of the introduced cysteines (ball representation, red) at the C termini of KtrBs (grey) at position 449. KtrAs are depicted in blue and the extended D1M2 helices in yellow. For representation, the model based on the low-resolution cryo-EM density map was used (Diskowski et al, 2017). The accessibility of the cysteines in both KtrB$_{E449C}$ and KtrAB$_{E449C}$ was analysed by Coomassie-stained 12% SDS PAGE (C) and Western blotting (D). For this, samples with a final concentration of 5 µM of the KtrB$_2$A$_8$B$_2$ complex and the KtrB dimer were incubated without and with either 30 µM of 5 kDa or 15 µM of 10 kDa MeO-PEG-mal for 1 h at 4°C. Before samples were mixed with SDS sample buffer, the reaction was stopped by the addition of 1 mM DTT. C) 20 µl of each sample was applied to the SDS PAGE and protein signals were visualised using Coomassie brilliant blue. D) Subsequent Western blotting of the 12% SDS PAGE was performed, and PEGylated protein was visualised with anti-MeO-PEG-mal antibodies. While the SDS PAGE was ambiguous as no obvious signals for the modified protein were visible, signals with increased apparent molecular weights in the Western blot clearly revealed PEGylation of KtrB$_{E449C}$ and KtrAB$_{E449C}$, excluding this approach for preventing the artificial sandwich assembly.

Several other residues at the interface of the complex were mutated to cysteines to increase the PEGylation of free KtrB, while showing no mass shift for the purified KtrAB complex. In detail, residue C56 in KtrA, as well as Q118C and Q122C of the extended helices in KtrB were tested (Data not shown). Unfortunately, all tested variants led to similar results, low overall PEGylation but no specific labelling of only the KtrB dimer. In conclusion, the similar PEGylation of the KtrB dimer and the assembled KtrAB complex excluded this approach for an efficient prevention of the ‘sandwich’ assembly, as the introduced cysteines were as accessible in the KtrAB complex as in the KtrB dimer and thus did not provide sufficient sterically hindrance.

5.2.1.2 Mixing of purified KtrBNH3 with an excess of purified KtrAC3H

A second approach to achieve the intact assembly of KtrAB comprised purifying the subunits individually and subsequently mixing KtrB with an excess of KtrA. In initial screenings, different combinations and conditions for the complex assembly were tested: An excess of KtrAC3H, a KtrA variant with a C-terminal cleavable His-tag, was mixed with KtrB containing either an N- or C-terminal His-tag (KtrBNH3 and KtrBC3H, respectively) and incubated for 1 hour or overnight at 4°C or room temperature (data not shown). The most promising conditions were observed for KtrBNH3 mixed with KtrAC3H incubated overnight with gentle agitation at 4°C. Consequently, a large-scale purification of both proteins was performed via Ni^{2+}-NTA agarose and SEC as described in section 4.3.6. Before mixing the purified proteins, KtrA was supplemented with 5 mM ATP to saturate the nucleotide binding sites in the RCK ring, mimicking the conditions used for the preparation of the ATP-bound structure from *B. subtilis* (Vieira-Pires et al, 2013).

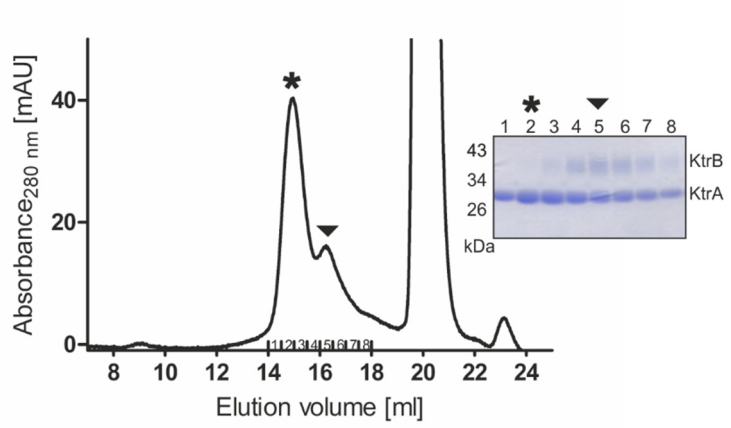

Figure 21: KtrAB assembly by mixing of individually purified KtrA and KtrB subunits. KtrAC3H and KtrBNH3 were individually produced in *E. coli* C43 and LB2003 cells, respectively, and mixed over night at 4°C after individual purification. KtrA was pre-incubated with 5 mM ATP and applied in a 13-fold molar excess compared to KtrB. After incubation, the sample was further analysed by SEC using a Superose® 6 Increase 10/300 GL column. The profile revealed two overlapping peaks, eluting at 15 ml, corresponding to KtrA (marked with *), and 16.5 ml, corresponding to KtrB (marked with ▼). Analysis of the peak fractions on a Coomassie-stained 12 % SDS PAGE confirmed that the two subunits did not assemble and eluted as separate subunits.The assembled complex would elute at smaller elution volumes. In contrast, separate signals for KtrAC3H (*) and KtrBNH3 (▼) were observed at an apparent molecular weight of 28 kDa and 37 kDa, respectively. The peak at 20 ml corresponded to ATP and as its absorbance exceeds 400 mAU, the y-axis was cropped at 50 mAU for easier representation.

After incubation of KtrA and KtrB an additional size-exclusion chromatography was performed, to analyse if complex formation occurred. The analysis revealed that both proteins still eluted separately at 15 ml for KtrA and 16.5 ml for KtrB (Figure 21). A successfully assembled complex would result in an additional peak, eluting at smaller elution volumes, as the hydrodynamic radius of the complex is bigger than of the single subunits. The respective SDS PAGE of all SEC fractions showed in most of the samples, signals for both subunits (Figure 21, lane 3-8), which is due to the overlap of the two peaks

and not based on assembly. The subunits of the assembled KtrAB complex would co-migrate at a smaller elution volume, if present. However, the strongest signals of the individual proteins (Figure 21 lanes 2 and 3 for KtrA, lanes 5 and 6 for KtrB), corresponding to the central peaks of the SEC, were well separated. This confirmed an unsuccessful assembly of the complex, which was also observed for all other tested conditions. Therefore, a different strategy was considered.

5.2.1.3 Pull-out purification of tag-less KtrB with KtrAC3H

As it was speculated that the 'sandwich' assembly occurred during solubilisation by the association of a free KtrB dimer to the native KtrAB complex, the next approach was to saturate all KtrBs within the membrane with KtrAs prior to solubilisation. In addition, to exclude that the His-tag on KtrB interfered with the assembly of the complex, a tag-less variant of KtrB was chosen. This further had the advantage that only tag-less KtrB assembled with a tagged KtrA ring could be purified via affinity chromatography. To this end, the pull-out of KtrB from the membranes by variants of KtrA with cleavable N- (KtrANH3) or C- (KtrAC3H) terminal His-tags was tested. At first, KtrB-containing membranes were prepared from *E. coli* LB2003 cells transformed with pEL901, which encodes tag-less KtrB. Subsequently, homogenised membranes were mixed with cytoplasm from *E. coli* C43(DE3)*ΔacrAB* cells, which overexpressed either *ktrAC3H* or *ktrANH3*. After homogenisation, the membranes were further divided for the solubilisation of the membrane protein with either 2% SMA or 1% DDM for 6 hours. Further purification steps were performed as described in section 4.3.6.3. Analysis of an SDS PAGE presenting samples from the purification revealed that, after extraction with SMAs, no signal with the apparent molecular weight of KtrB (37 kDa) was detected after elution from Ni^{2+}-NTA agarose (Figure 22 A, left panel: E2 and E3). KtrANH3 and KtrAC3H, on the other hand, were enriched at their apparent molecular weight of 28 kDa. This suggests that either the extraction of KtrB from the membrane was not successful, or that complex assembly was disrupted after KtrB was extracted by SMAs. Therefore, the samples were not further considered. Upon solubilisation with DDM, both KtrAC3H and KtrANH3 (28 kDa) and KtrB (37 kDa) were enriched in the elution fractions after Ni^{2+}-NTA (Figure 22 A, right panel: E2 and E3). This indicated a successful complex assembly, as tag-less KtrB could only be eluted from the Ni^{2+}-NTA agarose when it was assembled with His-tagged KtrA. Of the two KtrA constructs, KtrAC3H showed a much stronger signal compared to KtrANH3, reflecting a higher protein production, as the same amount of cytoplasm was used. However, the signal intensity for co-eluted KtrB was similar.

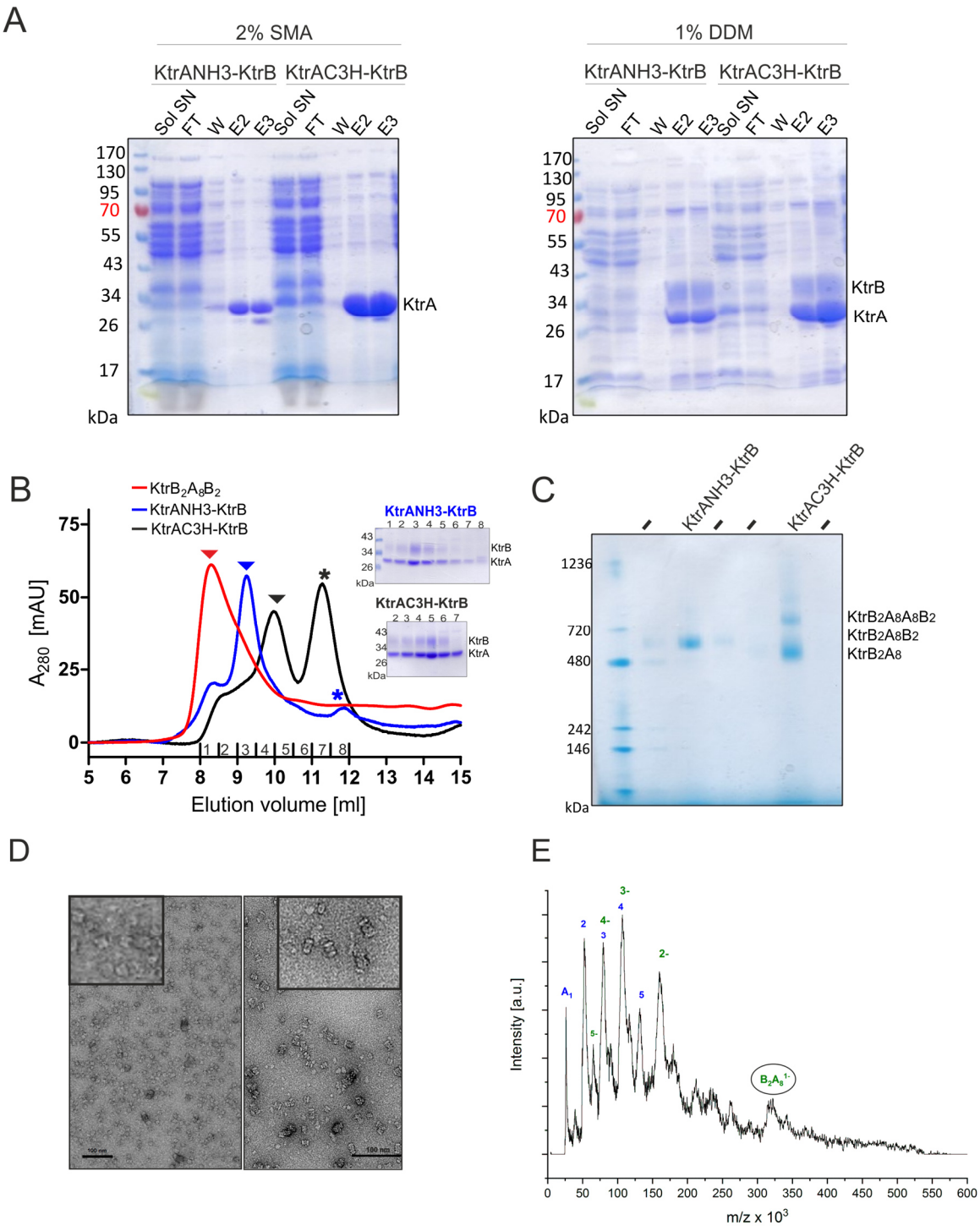
A
2% SMA
1% DDM
KtrANH3-KtrB
KtrAC3H-KtrB
Sol SN
FT
W
E2
E3
170
130
95
70
55
43
34
26
17
kDa
KtrA
KtrB
B
KtrB2A8B2
KtrANH3-KtrB
KtrAC3H-KtrB
A280 [mAU]
Elution volume [ml]
C
1236
720
480
242
146
KtrB2A8A8B2
KtrB2A8B2
KtrB2A8
D
E
Intensity [a.u.]
m/z x 10^3

Figure 22: Establishing a pull-out purification of tag-less KtrB with His-tagged KtrA to saturate all KtrB dimers within the membrane. Tag-less KtrB was produced in *E. coli* LB2003 cells, and membranes thereof were isolated. Separately, KtrAC3H or KtrANH3 were overproduced in *E. coli* C43*ΔacrAB* cells and the isolated KtrA-containing cytoplasm was mixed with the KtrB membranes prior to solubilisation. A) Samples were collected during purifications and 10 µl of each purification step were analysed on a Coomassie-stained 12% SDS PAGE: Supernatant of solubilised sample after centrifugation (SOL-SN), flowthrough (FT), wash fraction (W) and two elution fraction (E2, E3) from Ni^{2+}-NTA agarose affinity purification. Solubilisation was performed with 2% SMA (left) or 1% DDM (right). Pull-out was performed with both KtrANH3 and KtrAC3H. Solubilisation with SMA was unsuccessful, indicated by the missing KtrB signal at an apparent molecular weight of 37 kDa. Membranes solubilised with 1% DDM resulted in enriched signals of KtrA (28 kDa) and KtrB (37 kDa) after elution. For the pull-out with KtrANH3 and KtrAC3H, the signal intensity for KtrB remained the same, while KtrAC3H seemed to be more enriched compared to KtrANH3. The elution fractions for each KtrA variant were combined and concentrated for further analysis via SEC using a Superdex® 200 Increase 10/300 GL column. B) SEC profiles of both KtrANH3-KtrB (blue) and KtrAC3H-KtrB (black) in comparison with an elution profile of $KtrB_2A_8B_2$ (red). The elution profile of KtrAC3H-KtrB clearly differentiated from the 'sandwich' assembly, eluting at 10 ml, while the range of elution volume for KtrANH3-KtrB (9.2 ml) was within the broad elution volume of the 'sandwich' assembly. The 12% SDS PAGE containing the SEC fractions verified the presence of KtrA (28 kDa) and KtrB (37 kDa) in the first peaks (marked with ▼in the respective colours) and free KtrA at 11.5 ml (marked with *). KtrAB-containing peak fractions were further characterised by a blue native PAGE. C) 15 µl of the samples were mixed with 2x BN sample buffer and separated according to their native apparent molecular weight. The samples migrated at different apparent molecular weights, indicating a varied complex assembly. The smaller molecular weight signal of KtrAC3H-KtrB was suggested to represent the intact $KtrB_2A_8$ complex. D) Negative staining with 2% uranyl formate of KtrAC3H-KtrB at a concentration of 0.008 mg/ml revealed particles of smaller size (left image, inset) and missing the typical 'sandwich' shape from previous samples of $KtrB_2A_8B_2$ (right image, inset). Electron microscopy and negative staining were performed with the help of Dr. Susann Kaltwasser, Max Planck Institute of Biophysics, Frankfurt and Marina Schrecker, Institute of Biochemistry, Goethe-University, Frankfurt. E) LILBID-MS measurements of purified KtrAC3H-KtrB indicate that the 1-fold negatively charged intact $KtrB_2A_8$ assembly (highlighted by a circle) was the highest oligomeric state in the sample. LILBID-MS analysis was performed by Dr. Jan Hoffmann, Institute of Physical and Theoretical Chemistry, Goethe-University, Frankfurt.

To analyse the two assemblies (KtrANH3-KtrB and KtrAC3H-KtrB) further in comparison to the formerly purified $KtrB_2A_8B_2$ sandwich assembly, SEC was performed (Figure 22 B). For KtrANH3-KtrB, a main signal centred at 9.2 ml was identified with a minor secondary signal at around 8.2 ml. The elution volume lies within the broad elution profile of the $KtrB_2A_8B_2$ assembly, indicating a similar hydrodynamic radius of the protein particles. SDS PAGE of the peak fractions verified that both contained KtrA and KtrB. An additional minor signal was identified at around 11.5 ml, corresponding to unbound KtrA (Figure 22 B lane 8). A more significant effect was observed in the elution profile of KtrAC3H-KtrB, which eluted at 10 ml, showing only a minor remaining signal at 8.5 ml. Like for KtrANH3-KtrB, an additional peak was observed at an elution volume of 11.5 ml (Figure 22 B). The peak fractions were analysed by SDS PAGE and revealed the presence of KtrA and KtrB at an elution volume of 10 ml and only KtrA at an elution volume of 11.5 ml. The higher elution volume of the KtrA- and KtrB-containing fraction at 10 ml compared to the 'sandwich' assembly suggests a smaller hydrodynamic radius of the protein, which could indicate a modified complex assembly. To ensure that the samples are indeed different in molecular weight, a blue native (BN) PAGE was performed using the 9.2 ml peak fraction of KtrANH3-KtrB and the 10 ml KtrAC3H-KtrB peak fraction (Figure 22 C). The BN PAGE revealed signals of different sizes for the two samples: KtrANH3-KtrB migrated at an apparent molecular weight between 480 kDa and 720 kDa, which corresponds to the $KtrB_2A_8B_2$ sandwich assembly. KtrAC3H-KtrB showed two signals, one smaller than the

protein band of KtrANH3-KtrB and one bigger, which are approximately double in molecular weight compared to each other. This could indicate the presence of the native $KtrB_2A_8$ complex and another assembly artefact, $KtrB_2A_8A_8B_2$, which has been described previously (Diskowski et al, 2017). Experiments were continued with KtrAC3H-KtrB, as in addition to likely containing the native complex assembly, the placement of the His-tag at the C terminus of KtrA was also structurally preferable as it would interfere less with complex formation.

To validate the presence of the physiological assembly $KtrA_8B_2$, negative staining EM and native mass spectrometry (MS) (Laser-Induced Liquid Bead Ion Desorption MS (LILBID-MS)) were performed (Figure 22 D, E). The particles observed in the negatively stained sample were smaller compared the ‘sandwich’ particles (Figure 22 D, inset). Furthermore, the sample was pure and homogenous, however, containing some obvious larger particles, which most likely represent protein in the $KtrB_2A_8A_8B_2$ assembly. Complementary to this, LILBID-MS verified that the $KtrA_8B_2$ assembly was the highest oligomeric state (Figure 22 E), validating the native assembly. All together, these results confirmed that the pull-out strategy of tag-less KtrB with KtrAC3H enabled the purification of KtrAB in the physiological assembly. Consequently, the protocol was adopted for further structural and functional approaches.

5.2.2 Optimising single-particle cryo-EM analysis of the native KtrAB assembly

All previously published structures of KtrAB are limited by several weaknesses. The cryo-EM map of KtrAB from *V. alginolyticus* in the ADP-bound conformation represented a non-physiological assembly and was resolved only to a resolution of 6 Å. The high-resolution X-ray structure of KtrAB from *B. subtilis* in its ATP-bound conformation was prepared by separately purified subunits, with its RCK domains pre-bound to ATP. While the RCK domain in the sandwich assembly adopts a square-shaped conformation and the D1M2b helices of KtrB form a helical hairpin, which were described as typical features of the active state, the intramembrane loop is stabilised in the closed conformation, indicating that KtrAB is not fully in the active and conductive state. Therefore, to decipher the complete gating mechanism of KtrAB, high-resolution structures of the physiological complex assembly in its fully active or inactive state were required. While an ADP-bound conformation at a low resolution already existed, no ATP-bound structure from *V. alginolyticus* was available; therefore, resolving the active state was prioritised.

5.2.2.1 Cryo-EM maps of the KtrAB complex

For structural investigations by cryo-EM, a large amount of protein was required. Therefore, the protocol for the purification of the native complex was adapted for large-scale purification. A 12 l *E. coli* LB2003 pEL901 culture grown to an OD_{600} of approx. 1.4 yielded around 12 g membrane pellet. This pellet was combined with the cytoplasm from 1 l *E. coli* C43(DE3)*ΔacrAB* pBKtrAC3H culture, which was grown to a final OD_{600} of at least 3 after expression of *ktrA*, to ensure adequate excess of the RCK ring to saturate all KtrB dimers in the membrane. After homogenisation, the sample was solubilised with 1% DDM for at least 2 hours. Purification was performed via Ni^{2+}-NTA affinity chromatography and subsequently the protein was cleaved overnight with 3C protease for elution to increase the purity of the eluate and remove the C-terminal His-tag on KtrA. The sample was further purified by SEC (Figure 23 A). The main signal at 9.5 ml corresponded to $KtrA_8B_2$, and an additional peak at 11 ml corresponded to the excess of free KtrA, as described above (cf. 5.2.1.3). To avoid unbound KtrA rings from the overlapping elution fraction in the cryo-EM sample, only the front peak (elution fraction 1, Figure 23 A) containing the native assembly was concentrated to a final concentration of 8 mg/ml to proceed with single-particle cryo-EM. Grids were prepared as previously described by Schrecker (2018).

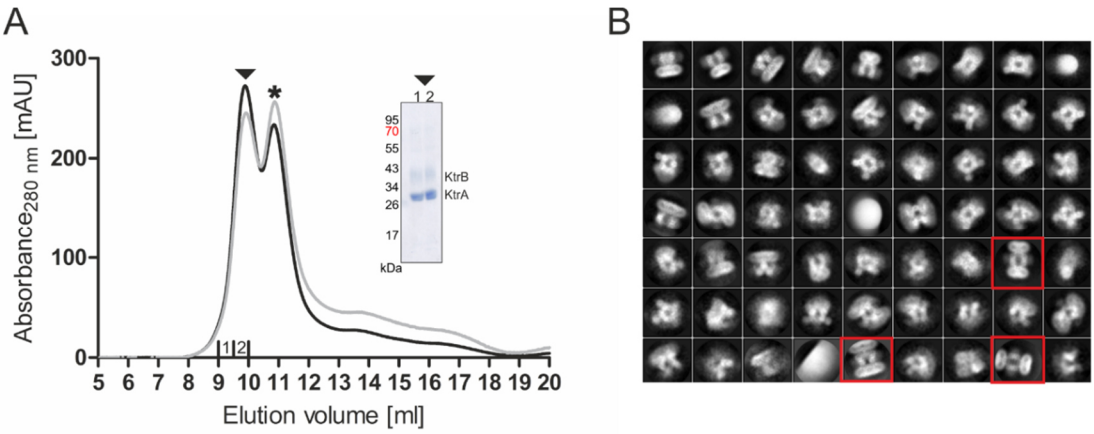

Figure 23: Large-scale purification of the native KtrAB complex assembly for cryo-EM analysis. A) SEC profile of the complex performed on a Superdex® 200 Increase 10/300 GL column. The peak fractions correspond to KtrAB (▼) and excessive KtrA (*). Sample composition of the KtrAB peak fractions was analysed on a Coomassie-stained 12% SDS PAGE (inset) and the presence of KtrA and KtrB was confirmed. B) Exemplary 2D class averages of the native KtrAB assembly. Data collection was performed on a Titan Krios microscope (Thermo Fisher Scientific) operating at 300 kV and a magnification of 130,000x. Classes containing particles remaining in the 'sandwich assembly' were highlighted in red. Grid preparation and data collection were performed with the help of Dr. Susann Kaltwasser, Max Planck Institute of Biophysics, Frankfurt and Marina Schrecker, Institute of Biochemistry, Goethe-University, Frankfurt. Classification and structural analysis were performed by Dr. Janet Vonck, Max Planck Institute of Biophysics, Frankfurt.

For comparison with the previously obtained $KtrB_2A_8B_2$ map (Diskowski et al, 2017), an initial dataset of the native KtrAB assembly was collected using a Titan Krios G3i operating at 300 kV in the presence of ADP. Over 125,000 particles were automatically picked from the micrographs and subjected to 2D classification (Figure 23 B). The 2D classes clearly demonstrated the native $KtrB_2A_8$ composition, displaying different orientations of the single particles, which were crucial for the 3D reconstruction of the complex. Interestingly, few classes still showed particles in the non-physiological 'sandwich' assembly, but their contribution was less than 10% and they were excluded from the subsequent refinement. In a first approach, a low-resolution density map with a final resolution of 7.0 Å was achieved (Schrecker, 2018). Overall, this density map of the $KtrB_2A_8$ assembly showed an architecture comparable to the available map of the $KtrB_2A_8B_2$ complex with characteristic extended D1M2 helices of the ADP-bound state (Figure 24 A). However, to further illuminate the molecular details of the system, a higher resolution was required. To achieve a high-resolution density map of the native complex, the sample and grid quality needed to be improved. It was important that sufficient protein particles were randomly oriented and evenly distributed in the vitrified ice, which is why grid preparation and plunge freezing conditions were optimised. First, deposition of the sample was tested on several grid types, containing different hole sizes, and blotting forces and blotting times were varied with different filter papers. Screening of the grids prior to data collection resulted in most promising conditions using C-flat 1.2/1.3 4Cu grids blotted for 12 seconds with a blotting force of 4 and Whatman blotting paper Nr. 1 at the FEI Vitrobot Mark IV. With these conditions, the ice was as thin as possible while still allowing all protein orientations and a

homogenous distribution throughout the hole. All samples were supplemented with 1 mM ATP and 2 mM $MgCl_2$ with the goal of achieving a high-resolution structure of the active, open conformation. With the optimised conditions, a first dataset of only 25,000 particles revealed a promising density map limited to 4.5 Å due to a low quantity of particles per micrograph (Figure 24 B). Therefore, a sample was prepared with an increased protein concentration of 9.5 mg/ml to obtain more particles in the ice. The new dataset comprised 6,336 micrographs, of which 211,602 particles contributed to a much more detailed 3.1 Å density map (Figure 24 C, Figure S2, Table S1). The increase in detail within the densities upon increased resolution is highlighted in a zoomed section of each density map (Figure 24, insets). At 7 Å, a 'sausage-like' straight density was observed, while at 4.5 Å helical features already become visible. A tremendous difference can be identified upon the resolution improvement to 3.1 Å, as side chain information becomes visible. Performing density modification of the cryo-EM map with resolve_cryo_em (Terwilliger et al, 2020) improved the final resolution even further to 2.8 Å (Figure 24 D).

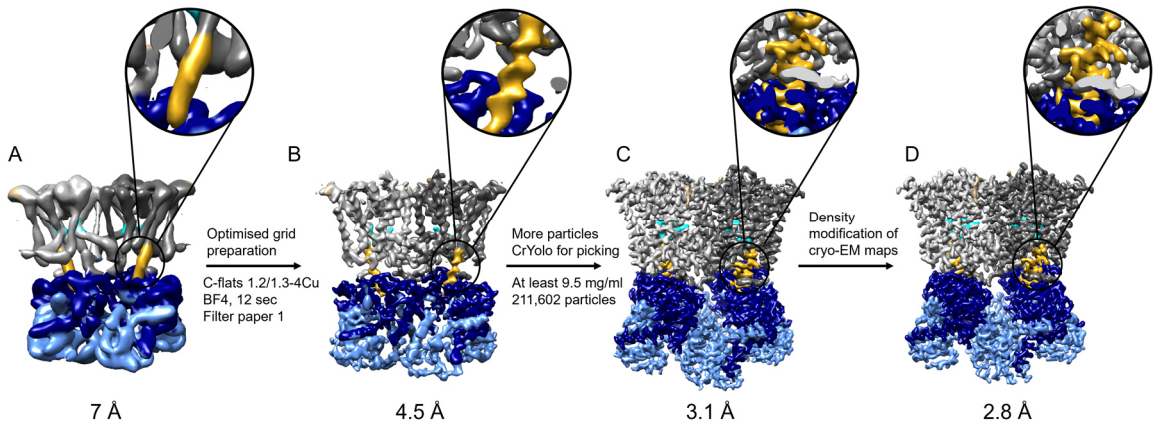

Figure 24: The resolution revolution in cryo-EM maps of the native KtrAB assembly. A) The first dataset of the native KtrAB complex resulted in 7 Å resolution map (Schrecker, 2018). B) After optimisation of grid preparation and automated data acquisition at a Titan Krios G3i with the help of Dr. Susann Kaltwasser, Max Planck Institute of Biophysics, Frankfurt, a small dataset of only 25,000 particles resulted in a 4.5 Å map. C) By increasing the protein concentration and the number of picked particles as well as performing automated particle picking using crYolo (Wagner et al, 2019) instead of RELION (Scheres, 2012), the resolution was improved to 3.1 Å. D) With density modification of cryo-EM maps (Terwilliger et al, 2020) the map was further improved to a resolution of 2.8 Å. The inset (A-D, circle) shows an enlarged view of a section from the protein, highlighting the improvement of the densities. While a largely amorphous rod-like density was observed at 7 Å, side chain information became visible in the 2.8 Å map. Data processing and structural analysis were performed by Dr. Janet Vonck, Max Planck Institute of Biophysics, Frankfurt.

Surprisingly, the general architecture of the complex in all maps strongly resembles the previously resolved ADP-bound conformation. Based on the published ATP-bound crystal structure (Vieira-Pires et al, 2013), the D1M2 helix was expected to form a helical hairpin, while the KtrA ring should adopt a square-shaped conformation. Instead, a closer inspection of the 2.8 Å density map (Figure 25 A, B) clearly highlights the features that define the ADP-bound state (Diskowski et al, 2017), particularly the extended D1M2 helix

and the oval-shaped KtrA ring, even though the samples were all supplemented with ATP and $MgCl_2$. Moreover, the dimensions of the KtrA ring were identical to the previous low-resolution structure, with 6.3 nm in one direction and 7.8 nm in the other direction (Figure 25 B). Finally, a more detailed analysis of the KtrA gating ring revealed a non-protein density corresponding to an ADP molecule bound to the N lobe of each of the eight KtrA subunits (Figure 25 C, D, E). In comparison to the described coordination of ADP for *Bs*KtrA slight variations were observed. While the positive charge of residue K103 (corresponds to K102 in *V. alginolyticus*) seemed to play a role in coordination in *Bs*KtrA, this was not observed for *Va*KtrA. Here, instead, residue R40 seemingly interacts with the negative charge of the phosphate (Figure 25 D). Furthermore, an additional small non-protein density was identified and assigned as a Mg^{2+}, which also appears to be involved in coordination of the β-phosphate. Therefore, with the described three positive charges all negative charges of the ADP are coordinated. Interestingly, in alternating KtrA subunits, residue R15 is further involved in the coordination of the ADP molecule, as previously described for *Bs*KtrA, which adds an additional positive charge to the binding site (Figure 25 E). The glutamate, which has been shown to be involved in the coordination of the Mg^{2+} in the ATP-bound structure (Teixeira-Duarte et al, 2019), is oriented too far to make contact with the magnesium ion in the presented structure. Hence, instead of the active, ATP-bound complex, the structure of the inactive, ADP-bound state has been obtained. Therefore, further modifications were implemented to the purification process with the goal of binding ATP to KtrA and triggering the active, open conformation.

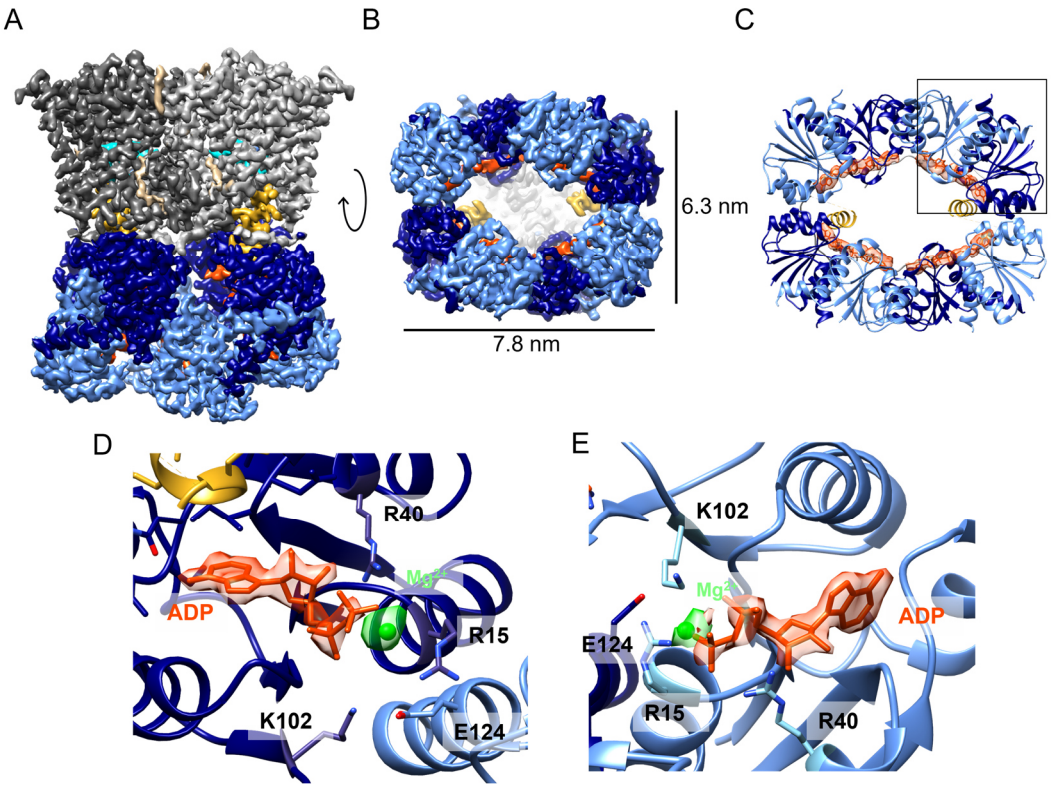

Figure 25: Cryo-EM structure of the native KtrAB complex assembly with a resolution of 2.8 Å. A) Analysis of the 2.8 Å density map indicated that the extended helices (yellow) were present. B) The KtrA ring adopted the dimensions of the previously described closed conformation, with 6.3 nm on the short axis and 7.8 nm on the long axis. C) At the resolution of 2.8 Å, one ADP molecule was identified at each KtrA N lobe (orange). D) The positive charge of resiude R40 in KtrA coordinates one of the phosphates of the ADP. Furthermore, a non-protein denisty was assigned to a Mg^{2+} (green), which is involved in the coordination of the β-phosphate. E) In alternating KtrA subunits residue R15 is further involved in the coordination of the negative charge of a phosphate. Cryo-EM grid preparation and data acquisition were performed with the help of Dr. Susann Kaltwasser, Max Planck Institute of Biophysics, Frankfurt. Data processing and structural analysis were performed by Dr. Janet Vonck, Max Planck Institute of Biophysics, Frankfurt.

5.2.2.2 Cryo-EM map of KtrAB complex purified via ATP agarose

To ensure that the KtrA ring bound ATP during the purification, the complex was purified via ATP-agarose affinity chromatography, from which it was eluted by competition with free ATP. For this, the native complex assembly was purified as described before, and, after elution from Ni^{2+}-NTA agarose, bound to pre-equilibrated ATP agarose overnight. After washing the agarose to remove unbound protein, bound complexes were eluted with buffer containing ATP and $MgCl_2$. Initial tests revealed that elution from the ATP-agarose was less efficient with ATP compared to ADP, which is why a high concentration of 30 mM ATP was used. As this concentration of ATP leads to a strong background in cryo-EM samples (personal communication Marina Schrecker, Janet Vonck), it was reduced to 1 mM ATP with 2 mM $MgCl_2$ during SEC. The ATP, whose absorption maximum lies at 259 nm, has a strong residual absorption at 280 nm, which resulted in a high background absorption affecting the quality of the SEC profile (Figure 26 A). Nonetheless, a protein signal was identified at an elution volume of around 10 ml. The signal at 8.5 ml elution

volume suggests the additional presence of the $KtrB_2A_8B_2$ assembly. For the cryo-EM sample, SEC fractions 3 and 4 were concentrated to a final concentration of 6 mg/ml. Analysis of samples from the purification by SDS PAGE revealed that, even after elution, the majority of the protein remained bound to the ATP-agarose (Figure 26 B), explaining the low yield after SEC. Nevertheless, the SEC fractions showed signals for both KtrA and KtrB, indicating successful isolation of the complex with high purity. To further test if this optimisation favours ATP binding, differential scanning fluorimetry (DSF) was performed. This method is based on the observation that the stability of many proteins increases after ligand binding, which can be determined by changes in the denaturation temperature of the protein. For this, the thermostability of KtrAB eluted from ATP-agarose was compared to that of KtrAB eluted from Ni^{2+}-NTA (Figure 26 C). Changes in fluorescence were detected by using the dye CPM, which gets strongly fluorescent upon binding to accessible cysteines of unfolding proteins. Here, the melting temperature of KtrAB eluted from ATP agarose was shifted to 62.5°C, 9°C higher than the 53.5°C after elution from Ni^{2+}-NTA agarose, indicating a higher stability for KtrAB eluted from ATP-agarose. However, the melting curve contained several populations at different temperatures, indicating a mixed stabilisation of the protein. To ensure a high quality of the purified sample, it was evaluated by negative staining (Figure 26 D) prior to cryo-EM. Negative staining displayed a homogeneous sample, allowing subsequent single particle cryo-EM using the established conditions. From a dataset of 73,965 particles from 5,956 micrographs, a cryo-EM map with a resolution of 2.5 Å was obtained (Figure 26 E, F, Figure S2, Table S1).

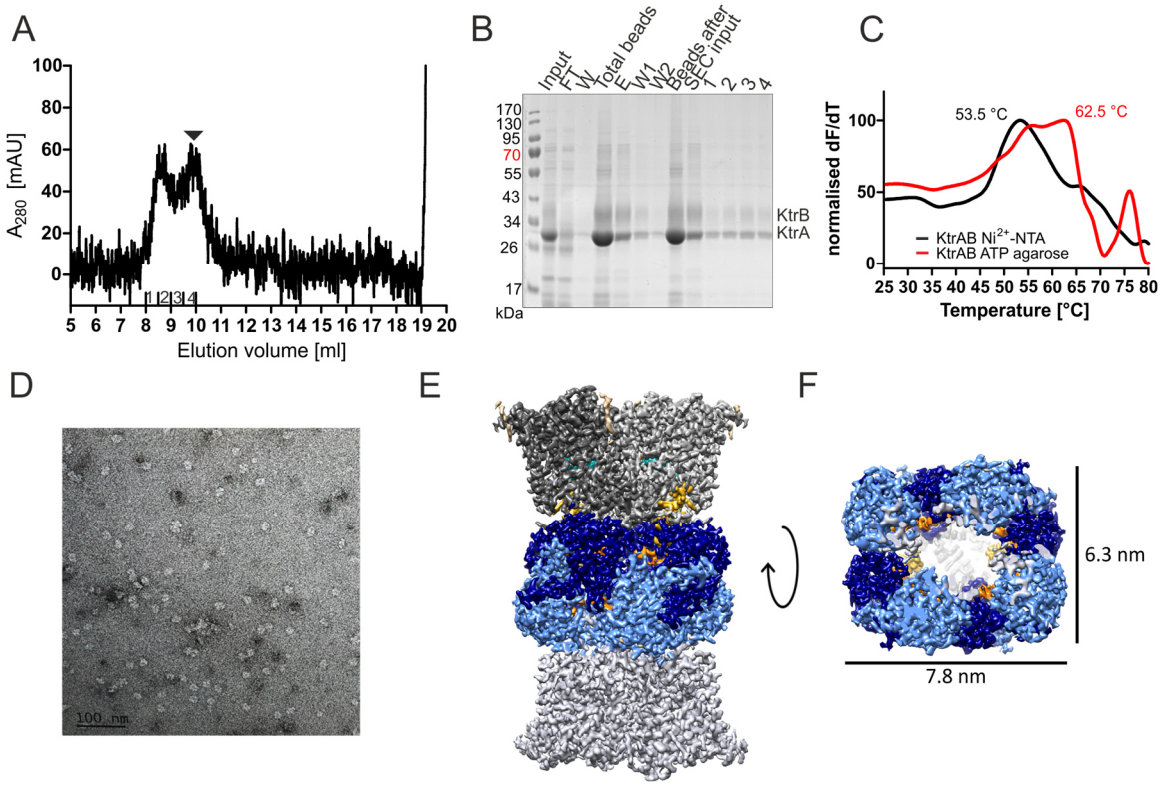

Figure 26: Purification of KtrAB via ATP agarose for cryo-EM. KtrAB was purified as described above with an additional purification step of binding to ATP agarose. Elution was performed competitively with 30 mM ATP and 2 mM $MgCl_2$. A) SEC profile of KtrAB eluted from ATP agarose. SEC was performed using Superdex® 200 Increase 10/300 GL column for higher purity and to exchange the buffer to a lower ATP concentration (1 mM ATP and 2 mM $MgCl_2$) to reduce the background on cryo-EM micrographs. Fraction used for sample preparation are indicated by ▼. The high noise of the SEC profile is caused by background ATP absorption from the SEC buffer. B) Sample composition was analysed on a Coomassie-stained 12% SDS PAGE. 10 µl of each sample were applied: Purified KtrAB used to bind to the ATP agarose (Input), flowthrough (FT), wash (W), total ATP agarose beads with KtrAB bound (Total beads), KtrAB eluted with 30 mM ATP (El), wash fractions 1 and 2 (W1, W2), ATP agarose beads after elution with 30 mM ATP (Beads after), concentrated sample for SEC (Input SEC), SEC fractions (1-4). Signals migrating at the apparent weight of KtrA (28 kDa) and KtrB (37 kDa) were identified. Fractions 3 and 4 were used for further experiments. C) Thermostability of Ni^{2+}-NTA agarose-purified KtrAB (black) compared with ATP agarose-purified KtrAB (red) by DSF. A shift to a higher melting temperature was observed in the presence of ATP. Yet, several populations at different temperatures were observed, indicating different stabilised states of the protein. D) To control the quality of the sample, negative staining with 2% uranyl formate was performed together with Dr. Susann Kaltwasser, Max Planck Institute of Biophysics, Frankfurt. The sample showed appropriate quality to proceed with single particle cryo-EM. E, F) 2.5 Å cryo-EM map of KtrAB purified via ATP agarose. The complex adopts the ADP-bound conformation, with extended D1M2 helices (yellow) in KtrB (grey) and an oval-shaped KtrA ring (blue). Non-protein densities corresponding to ADP (orange) were identified in all eight KtrA subunits. The complex assembled in the non-physiological $KtrB_2A_8B_2$ 'sandwich' assembly. Data acquisition was performed at the Titan Krios G3i operating at 300 kV, 73,965 particles from 5,956 micrographs were processed to yield the 2.5 Å resolution map. Cryo-EM grid preparation and data acquisition were performed with the help of Dr. Susann Kaltwasser, Max Planck Institute of Biophysics, Frankfurt. Data processing and structural analysis were performed by Dr. Janet Vonck, Max Planck Institute of Biophysics, Frankfurt.

The cryo-EM map revealed that the complex again adopted the non-physiological 'sandwich' assembly, most likely due to an insufficient excess of KtrA prior solubilisation. Although the fractions, which were eluting at 10 ml, were used, they contained an increased number of particles in the 'sandwich' assembly, most likely by overlap with the fractions at 8.5 ml. Unfortunately, despite the additional purification steps intended to favour ATP binding, the map again represents the ADP-bound conformation (Figure 26 E,

F) and ADP molecules were assigned to non-protein densities in the N lobes of all KtrA subunits. It appears that the exchange of ADP to ATP in the detergent-solubilised KtrAB complex was incomplete and only few ATP molecules were bound to the octameric ring. Since the few binding positions might be randomised, they were not identified during 3D classification of the cryo-EM sample, as the processing procedure averaged them out. For conformational changes of the RCK ring, however, it seems that all binding sites need to be occupied by ATP, which could not be achieved in the here-performed structural approaches.

5.2.2.3 Conformational flexibility of the intramembrane gating loop in the dependence of nucleotides

By performing EPR measurements, it was further verified, that the detergent-solubilised KtrAB complex, does not undergo conformational rearrangements in the presence of ATP or ADP. As in response to changes in the RCK ring upon binding of nucleotides, channel gating, which is mediated by the intramembrane loop in the centre of KtrB, was so far supposed to open and close the pore, the flexibility of the intramembrane loop was analysed in the presence of nucleotides (Diskowski et al, 2017; Hänelt et al, 2010b; Szollosi et al, 2016). In a previous study by Diskowski et al. (2017), nucleotide-dependent conformational changes in the intramembrane loop were determined by site-specifically spin-labelling position T318C (located in the intramembrane loop) in an otherwise cysteine-free KtrAB variant and performing pulsed electron paramagnetic resonance (EPR) spectroscopy. Since KtrB assembles as a dimer, the intermolecular distance between the labelled residues in each protomer could be measured. While in the presence of ADP a defined mean distance distribution was observed, in the presence of ATP a broader distance distribution, which reflects higher flexibility of the loop, was identified (Diskowski et al, 2017). However, the measurements were performed with detergent-solubilised KtrAB in the ‘sandwich’ assembly, which is why three different distances between the spin labels can contribute to the distance distribution. Therefore, the measurements were repeated with the detergent-solubilised native assembled KtrAB complex in the presence of 10 mM ATP or 10 mM ADP. At both conditions, a weak oscillation in the dipolar evolution functions and consequently broad distance distributions were observed, indicating a high flexibility of the intramembrane loop (Figure 27). More specifically, in the presence of ADP, the solubilised KtrAB complex revealed a broad distance distribution, ranging from 1.5 nm up to 4 nm with a major mean distance at 3.3 nm (Figure 27, upper row). Since the sample conditions were similar to the conditions used in cryo-EM, this mean distance at 3.3 nm most likely corresponds to a stabilisation of the intramembrane loop in the inactive, closed conformation. In the presence of ATP, again,

a broad distance distribution with a range of 1.5 nm to 4 nm was visible, indicating a similar conformation of the intramembrane loop (Figure 27 lower row).

Together with the cryo-EM data, it is obvious, that the KtrAB complex in a detergent micelle does not undergo conformational changes in the presence of ATP. Therefore, the binding of ATP and ADP to the regulatory subunit KtrA was investigated in further detail.

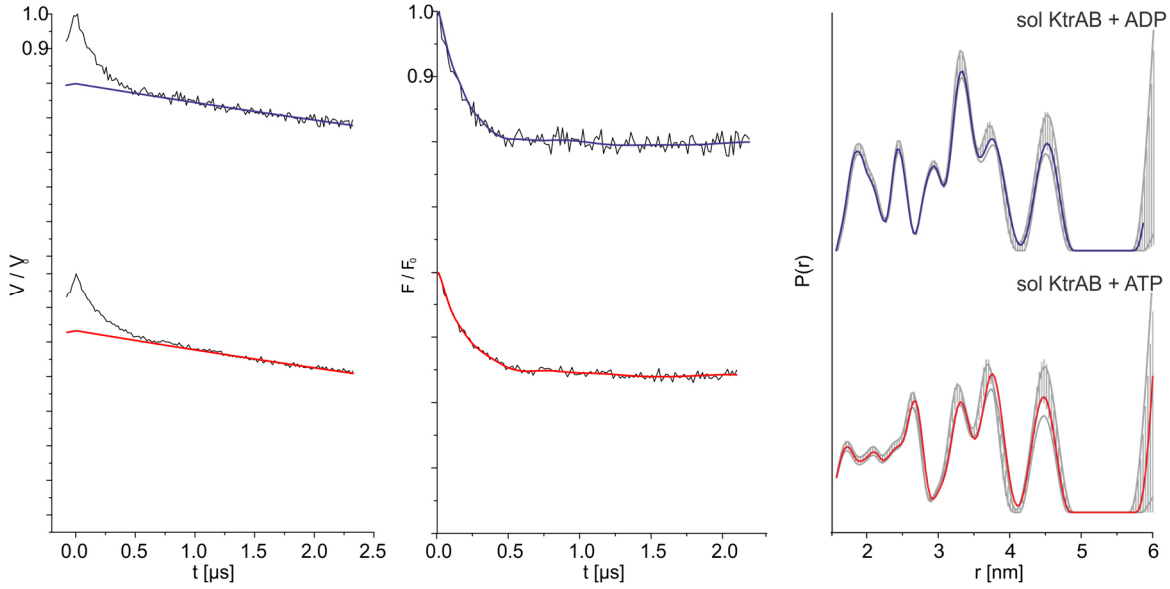

Figure 27: Dynamics of the intramembrane loop of detergent-solubilised KtrAB in the dependence of nucleotides. DEER measurements of $KtrAB_{T318CR1}$ variant (R1 indicates, that the variant is spin-labelled) in the presence of 10 mM ADP (blue) or 10 mM ATP (red). Left panels: Experimental raw data V(t) with fitted background function; middle panels: Background-corrected dipolar evolution function F(t); right panels: Interspin distance distribution P(r) obtained by Tikhonov regularisation. Grey areas represent the full variation of possible distance distributions. The lower and upper error estimates (grey lines) represent the respective mean values minus and plus twice the standard deviation. Distance is measured between the labelled residues in both KtrB protomers. At both conditions a broad distance distribution was observed, indicating a high flexibility of the intramembrane loop. The mean distance distribution at 3.3 nm most likely correspond to the closed, inactive conformation of the intramembrane loop. Sample preparation was performed together with Dr. Dorith Wunnicke-Kortz, Institute of Biochemistry, Goethe-University, Frankfurt, who performed the pulsed EPR measurements and data evaluation.

5.2.3 Analysis of nucleotide binding to KtrA to illuminate regulation by ATP and ADP

In previous studies, it was shown that KtrAB is regulated by binding of ATP and ADP without performing ATP hydrolysis (Kröning et al, 2007). Binding affinities for both nucleotides were determined in the low micromolar range, with a slight preference for ATP (Diskowski et al, 2017). Recently, it has been reported that binding of divalent cations, especially Mg^{2+}, to a conserved site in KtrA, together with ATP, was required for activation (Teixeira-Duarte et al, 2019). Surprisingly, in all structural approaches in this thesis, no binding of ATP was observed, even though different steps were taken during sample preparation to support the ATP-bound state. Therefore, I took a step back and further analysed nucleotide binding to KtrA using different techniques. Since the nucleotides bind to the N lobes of KtrA, only the RCK protein was used for most approaches, because KtrA can be achieved in much higher yield compared with the KtrAB complex. Purification was performed via Ni^{2+}-NTA affinity chromatography with subsequent SEC as described in section 4.3.5.

5.2.3.1 Isothermal titration calorimetry to determine affinity of KtrA for ATP and ADP

Isothermal titration calorimetry (ITC) measurements with purified KtrA were performed for ATP, ATP+$MgCl_2$, ADP, and $MgCl_2$ to determine the K_D values for the different nucleotides/ions. Here, no significant difference in affinity was observed between ATP (3.6 µM ± 0.11 µM) and ATP+$MgCl_2$ (3.4 µM ± 0.76 µM) (Figure 28 A, B). As Mg^{2+} has been shown to stabilise the ATP-bound conformation, it was tested whether $MgCl_2$ itself binds to KtrA in the absence of ATP. Since the published structures show that Mg^{2+} is involved the coordination of the γ-phosphates of ATP, it is not surprising, that for $MgCl_2$ by itself, no binding was detected (Figure 28 D) (Schrecker, 2018; Teixeira-Duarte et al, 2019)). For ADP, a K_D of 2.4 µM ± 0.06 µM was determined (Figure 28 C), which indicates a slightly higher affinity than for ATP, but still in a similar low micromolar range. Similar affinities have been observed in ITC measurements on the KtrAB complex and previous published data on the KtrA ring (Diskowski et al, 2017; Kröning et al, 2007), however in those measurement a slight preference for ATP over ADP was observed.

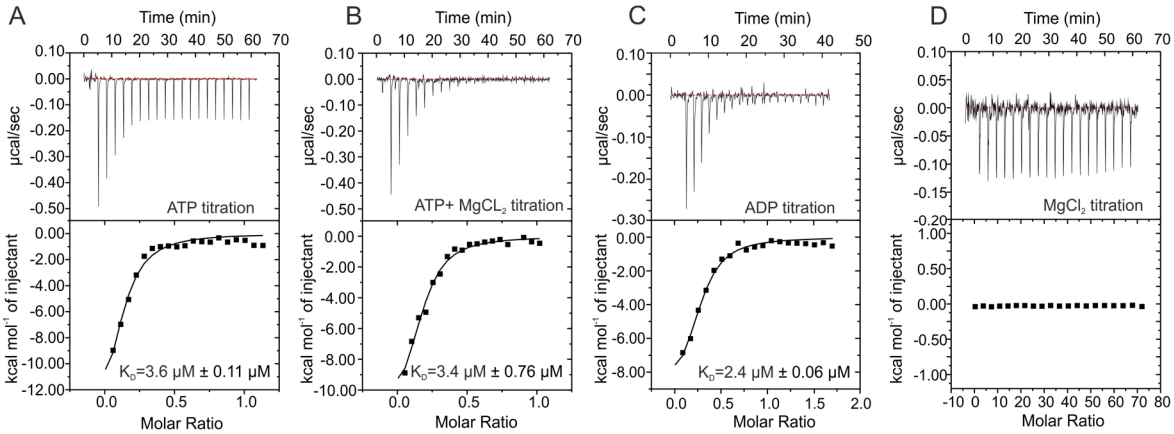

Figure 28: Binding affinities of regulatory nucleotides ATP and ADP and $MgCl_2$ to KtrAC3H examined by ITC. The upper panel shows the raw heat exchange data of (A) ATP (250 µM ATP to 45 µM KtrA), (B) ATP+$MgCl_2$ (300 µM ATP +30 mM $MgCl_2$ to 60 µM KtrA+ 5 mM $MgCl_2$), (C) ADP (250 µM ADP to 30 µM KtrA) and (D) $MgCl_2$ (30 mM $MgCl_2$ to 85 µM KtrA) binding to KtrA. The lower panels present the integrated injection heat pulses, normalised per mole of injection. Obtained binding curves were fitted by a one-site binding model, resulting in the indicated dissociation constants (K_D).

The N-values, which indicate the stoichiometry of binding, varied between measurements, even within replicates. In all measurements the values were lower than 1, ranging from 0.04-0.2, while 1 was the expected stoichiometry as the protein concentration was adjusted according to a KtrA monomer, each contains one nucleotide binding site. Therefore, it is tempting to speculate that not all KtrA molecules were active, or that KtrA binding sites were partially pre-occupied by a co-purified nucleotide. As in all cryo-EM samples ADP was bound, even though it was not supplemented, ADP might be co-purified, resulting in an affected N-value. However, the N-values require careful evaluation, as the data forms a non-sigmoidal curve, which is not optimal for fitting. For fits reaching saturation very early, similar to the presented fits, the N-values appear to be very small (Milev, 2015). Nonetheless, the K_D values obtained from replicate measurements were reproducible, indicating an adequate reliability.

5.2.3.2 Competitive nucleotide binding analysed by Scintillation Proximity Assay

The binding behaviour of ATP and ADP to KtrA was further assessed by scintillation proximity assay (SPA). A competitive binding assay was performed to determine the IC_{50} values of the different nucleotides. To this end, purified KtrA with a final concentration of 200 nM was pre-incubated with either 3 µM ATP or ADP doped with 6.7% radioactively labelled ^{3}H-ATP or ^{3}H-ADP, respectively, as a tracer. The protein was then coupled via its His-tag to the Copper-chelated PVT SPA beads and increasing concentrations of the non-radioactive competitor were added. Optimal amounts of beads, radioligand and protein concentration were adapted from previously established protocols (Stefan et al, 2020). Competitive displacement of the pre-bound radioligand could be observed for both ATP and ADP in SPA measurements (Figure 29). To fully out-compete the pre-bound

nucleotides, around 1 mM of the respective competitor was required, while the determined IC_{50} values describe the concentrations of the competing cold ligands which displace 50% of the pre-bound radioligand. Independent of the pre-bound radiolabelled nucleotide, the IC_{50} value for cold ADP was lower compared to ATP. An IC_{50} for cold ADP of 4 µM for the displacement of pre-bound ^{3}H-ADP and of 3 µM for the displacement of pre-bound ^{3}H-ATP was determined (Figure 29, blue curves), while the competition with cold ATP resulted in an IC_{50} value of 11 µM with pre-bound ^{3}H-ADP and of 10 µM with pre-bound ^{3}H-ATP (Figure 29, red curves). This indicated that, in both cases, a little less ADP than ATP was required to out-compete the pre-bound nucleotide, which is in good agreement with the ITC measurements. However, the IC_{50} values are all in the low micromolar range, hence both nucleotides should be replaceable by one another at moderate competing concentrations. Therefore, it remains confusing why all structural approaches feature ADP-bound KtrA, even when samples were prepared in the presence of ATP. It is tempting to speculate, that the nucleotide binding in the presence of channel subunit KtrB in the KtrAB complex requires an additional stimulus.

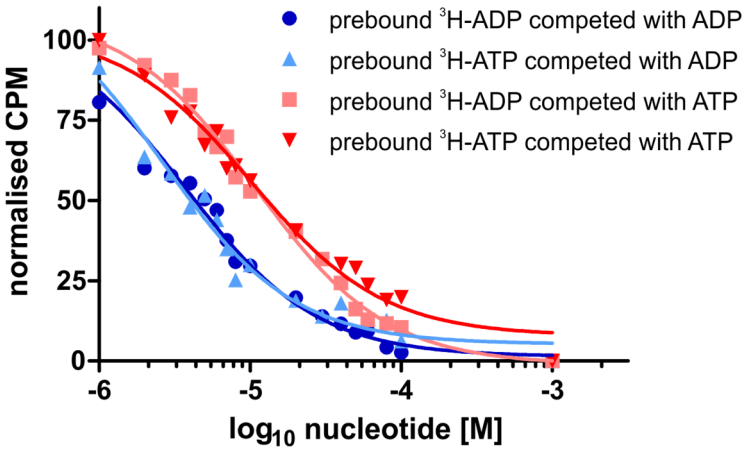

Figure 29: Determination of IC_{50} values using SPA competition assay. Purified KtrAC3H was pre-incubated with 3 µM ATP or ADP doped with 6.7% radioactively labelled ^{3}H-ATP or ^{3}H-ADP as a tracer. Subsequently, the protein was incubated with copper-chelated PVT SPA beads (final concentration of 5 mg/ml). Cold nucleotides (ATP and ADP) were added in increasing concentrations from 0.5 µM to 1000 µM for competition. Competition with cold ADP for KtrAC3H pre-bound with ^{3}H-ADP or ^{3}H-ATP is shown in dark and light blue, respectively. Competition with cold ATP after pre-incubation with ^{3}H-ADP or ^{3}H-ATP is represented in light and dark red, respectively. To determine unspecific counts, the protein was eluted from SPA beads with 500 mM imidazole after measurements. Background was subtracted from each measure point.

5.2.3.3 Effect of nucleotides on the thermostability of KtrA

As no significant difference in the affinity of KtrA for ATP or ADP was determined in ITC measurements, and similar IC_{50} values were shown with SPA, it was aimed to be identified, whether the binding of one or the other nucleotide has a different effect on the KtrA ring. Therefore, the effect of these nucleotides on the thermostability of KtrA was analysed. For this purpose, DSF measurements were used to identify the denaturation temperature (melting temperature) of KtrA in the presence of ATP or ADP. As shortly introduced above (cf. 5.2.2.2), upon binding to a folded protein most ligands stabilise the protein, leading to an increased melting temperature. For the detection of protein unfolding, the commonly used dye SyproOrange® was applied whose fluorescence is quenched in an aqueous environment, but which becomes strongly fluorescent when it binds to exposed hydrophobic regions of an unfolded protein (Bai et al, 2019).

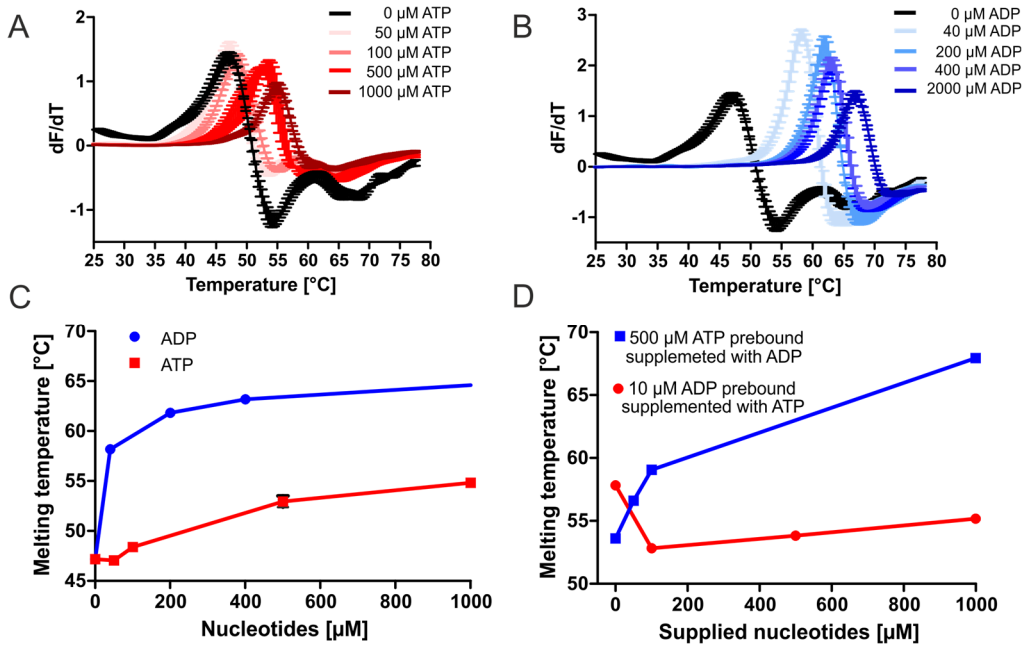

Figure 30: Differential scanning fluorimetry of KtrA in the presence of ATP and ADP. Purified KtrA was mixed with different concentrations of ATP (red) or ADP (blue) and changes in SyproOrange fluorescence (λ_{ex} 470 nm; λ_{em} 555 nm) were detected over a temperature increase from 25 - 80 °C. A, B) First derivative of the raw data (dF/dT), in which the peak indicates the melting point of the protein. Error bars indicate the standard deviation from technical triplicates. A) ATP concentrations ranging from 50 µM (lightest red) to 1000 µM (darkest red) were added to 5 µM KtrA. Melting curve of KtrA without nucleotide added shown in black. B) ADP concentrations ranging from 40 µM (lightest blue) to 2000 µM (darkest blue) were added to 5 µM KtrA. Melting curve of KtrA without nucleotide added shown in black. C) Melting temperatures of KtrA in the presence of different concentrations of ATP or ADP. ADP binding leads to a higher stability. Data point of 2000 µM ADP is not shown. D) To test ATP/ADP displacement, competitive binding experiments were performed. 5 µM KtrA were pre-incubated with either 500 µM ATP (blue graph) or 10 µM ADP (red graph) and supplied with different concentrations of ADP and ATP, respectively. Competition between both nucleotides was observed.

Before adding nucleotides, purified KtrA showed a melting temperature at around 47°C (Figure 30 A, B, black), which was increased upon addition of both ATP and ADP, illustrated by the peak shift of the melting curves towards higher temperatures, respectively (Figure 30 B, C). Interestingly, addition of ADP led to much higher melting temperatures than addition of ATP. While a maximum melting temperature of 55°C was determined in the presence of 1 mM ATP, already 40 µM ADP (Figure 30 A, C) led to a melting temperature of 58°C, which increased up to 67°C at higher ADP concentrations (Figure 30 B, C). These results imply that, while both nucleotides directly interact with KtrA as they both showed a stabilising effect, ADP causes a stronger stabilisation of KtrA than ATP. Hence, for the first time, a fundamental difference in the binding of ATP and ADP to KtrA was demonstrated. Similar measurements were performed in combination with $MgCl_2$ (up to 1 mM), which showed no further effect on the melting temperatures (data not shown). To test whether the observed stabilising effects were reversible by competition of the nucleotides, KtrA was pre-incubated either with 500 µM ATP or 10 µM ADP. As the two nucleotides induce very different stabilities of the KtrA ring, different concentrations of ATP and ADP were chosen for pre-incubation, to have a comparable strong stabilisation of the KtrA ring for the competition experiment. Subsequently, the samples were supplemented with different concentrations of ADP and ATP, respectively (Figure 30 D). KtrA pre-bound to 500 µM ATP showed an increased stabilisation upon increasing ADP concentrations, hence ADP successively out-competed ATP (Figure 30 D). Interestingly, in reverse order, the melting temperature did not decrease successively, but first dropped to the lowest melting temperature of 52°C, while it subsequently increased to a maximum of 55°C (Figure 30 D). This might indicate that a heterogeneous occupancy of the binding sites is unfavourable leading to destabilisation.

5.2.3.4 Nucleotide-induced conformational changes of KtrA

All described experiments before show that both nucleotides ATP and ADP bind to the isolated KtrA ring. To analyse, whether KtrA undergoes conformational changes upon binding of nucleotides and $MgCl_2$, the conformation of KtrA was visualised via negative staining electron microscopy. Based on the published structures, two distinct nucleotide-dependent conformations were expected. In the ATP-bound state the KtrA ring adopts a square-shaped conformation, while in the ADP-bound state the ring has an oval shape (Albright et al, 2006; Teixeira-Duarte et al, 2019). In previous studies performed by M. Schrecker, several conditions have already been investigated. They revealed, that only in the presence of 1 mM ATP and 2 mM $MgCl_2$, 89% of the particles adopt the square-shape conformation, while in the presence of only 1 mM ATP, 1 mM ADP, and 1 mM ATP with 2 mM EDTA, the majority of the particles were obtained in the oval-shaped conformation (Schrecker, 2018). Interestingly, in the absence of any supplied nucleotide, the majority of the KtrA rings (72%) adopt the oval-shaped conformation. To complete and confirm the data, purified KtrA was supplemented with either or 1 mM ATP and 2 mM $MgCl_2$ or 1 mM ADP and 2 mM $MgCl_2$. Furthermore, a sample was prepared in the presence of only 2 mM $MgCl_2$, to investigate its effect on the conformation of KtrA. For this purpose, KtrA was purified as described in section 4.3.5 and protein concentration was adjusted to 0.006 mg/ml, prior the sample was supplemented with the respective ligands. Negative staining grids were prepared (cf. 4.4.6.1), and images were acquired using Leginon with a Tecnai G^2 spirit Biotwin Microscope operating at 120 kV and a magnification of 30,000x (Potter et al, 1999). From over 500 micrographs per sample, particles were automatically picked and analysed with *cis*TEM (Grant et al, 2018). The particles were sorted into 30 2D classes and the conformations of KtrA rings from selected classes were analysed (Figure 31 A, B, C, Table S1-S6).

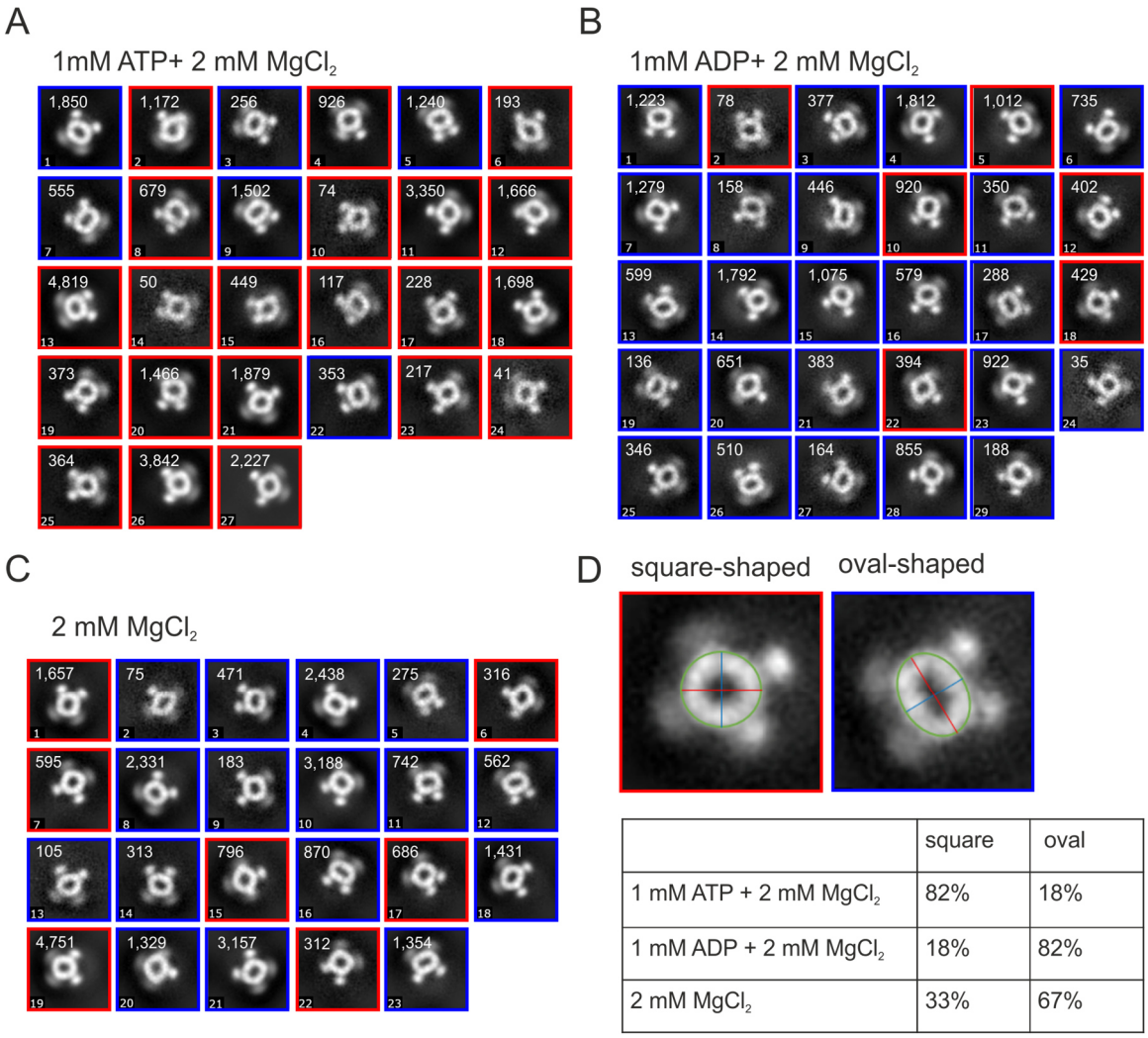

	square	oval
1 mM ATP + 2 mM $MgCl_2$	82%	18%
1 mM ADP + 2 mM $MgCl_2$	18%	82%
2 mM $MgCl_2$	33%	67%

Figure 31: 2D class averages of KtrA in the presence of different ligands. KtrA was purified via SEC and the protein at a final concentration of 0.006 mg/ml was incubated with either (A) 1 mM ATP+ 2 mM $MgCl_2$, (B) 1 mM ADP+ 2 mM $MgCl_2$ or (C) 2 mM $MgCl_2$. 3 µl of the samples were applied on a carbon-coated copper grid and stained with 2% uranyl formate. Images were acquired using a Tecnai G^2 Spirit Biotwin microscope, and a Rio16 camera at a magnification of 42,000 x. Particle picking and 2D classification were performed with cisTEM. The best out of 30 classes are shown. D) To determine the conformation of the particles from all classes, the ratio between the longest x-diameter (red line) and the shortest y-diameter (blue line) was compared. A threshold was set to 1.115, therefore classes with a ratio greater than 1.115 were defined as oval-shaped (blue frame), and classes with a ratio smaller than 1.115 were defined as square-shaped (red frame). Numbers of particles from each class are indicated on the top of the respective image. The calculation of the diameter revealed, that only in the presence of 2 mM $MgCl_2$ and 1 mM ATP majority (82%) of the particles are in the square-shaped conformation. Purification of KtrA and evaluation of the data was performed by Celina Thiel, Institute of Biochemistry, Goethe-University, Frankfurt, under my supervision. Data collection was performed together with Dr. Susann Kaltwasser, Max Planck Institute of Biophysics, Frankfurt.

For this purpose, the ratio between the longest x-diameter and the shortest y-diameter was determined (Figure 31 D) and a threshold of 1.115 was set. Therefore, classes with a ratio greater than 1.115 were defined as oval-shaped, while classes with a ratio smaller than 1.115 were defined as square-shaped KtrA rings. Evaluation of the data revealed, that, similar to the observations by M. Schrecker (2018), in the presence of ATP and $MgCl_2$ majority (82%) of the particles adopt the square-shaped conformation (Figure 31 A, D, Table S3, Table S4). In the presence of ADP and $MgCl_2$, 82% of the KtrA particles

displayed a significant shift to the expected oval-shaped conformation (Figure 31 B, D, Table S4, Table S5). Similar, in the presence of only $MgCl_2$, 67% of the particles represent the oval-shaped conformation, reflecting the distribution of KtrAs conformation in the absence of any supplied nucleotide (Figure 31 C, D, Table S6, Table S7) (Schrecker, 2018). This indicates that the binding of $MgCl_2$ itself does not induce conformational changes, which is in line with the ITC data, as no direct binding of $MgCl_2$ to KtrA was observed (cf. 5.2.3.1).

Taken together, the data clearly shows, that the isolated KtrA ring can adopt different conformations upon binding of nucleotides, while for the KtrAB complex nucleotide-dependent conformational changes in the KtrA ring could not be obtained.

5.2.3.5 Excluding ATP hydrolysis during sample preparation

A possibility not addressed so far is that ATP get hydrolysed during sample preparation by KtrAB, resulting in the continually obtained ADP-bound states. Although this is unlikely because KtrAB possesses no innate ATPase function, the hydrolysis of [α-^{32}P]-ATP in the presence of purified KtrAB was monitored for 30 min by thin layer chromatography (TLC). As expected, no protein-mediated hydrolysis or autohydrolysis of ATP were observed, as only [α-^{32}P]-ATP and no [α-^{32}P]-ADP was detected (Figure 32 A, middle and lower row). As a positive control, the hydrolysis of [α-^{32}P]-ATP by the P-type ATPase KdpFABC was detected (Figure 32 A, upper row). Here, ATP was hydrolysed over time, indicated by an increasing signal for [α-^{32}P]-ADP in the TLC. Complete hydrolysis was observed after around 4 min. To finally exclude that the ATP hydrolysis is involved in constantly obtaining ADP-bound states in cryo-EM, KtrAB was purified in the presence of the non-hydrolysable ATP analogue AMPPCP. To provide the nucleotide in excess during the purification, 100 mM AMPPCP and 2 mM $MgCl_2$ were added to the elution fractions from Ni^{2+}-NTA agarose. Aferwards, the protein was further purified via SEC, during which the AMPPCP concentration was reduced to 3 mM to decrease the background on cryo-EM micrographs. Similar to the sample obtained from ATP agarose, the quality of the SEC profile was very low due to the nucleotide-containing SEC buffer, but the expected peak centred at 10 ml elution volume was still identified (data not shown). The peak fraction was concentrated and used for cryo-EM. The dataset resulted in a 3.6 Å resolution map of KtrAB in the ‘sandwich’ assembly and was again obtained in the ADP-bound conformation showing the extended helices and the oval-shaped KtrA ring, with ADP-bound to all KtrA subunits (Figure 32 B).

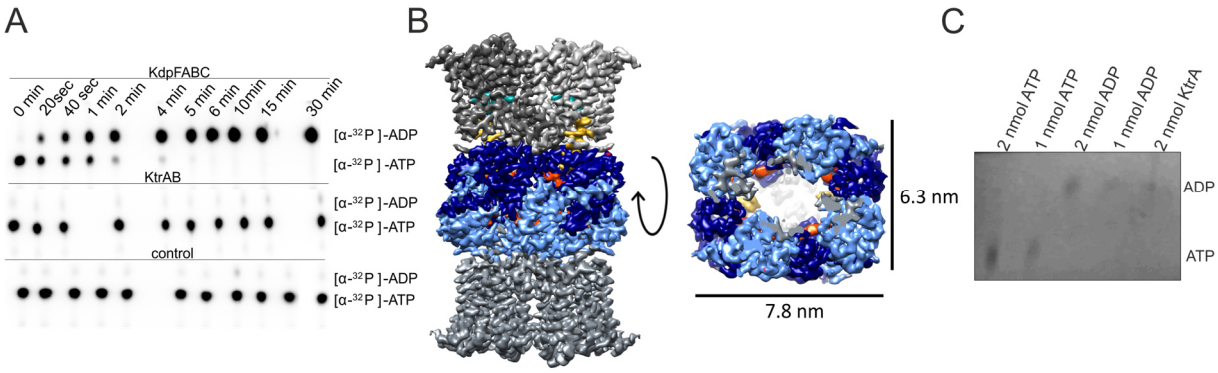

Figure 32: Elimination of possible ATP hydrolysis during KtrAB sample preparation for cryo-EM. A) Autoradiogram of a thin layer chromatography separating [α-^{32}P]-ATP and [α-^{32}P]-ADP. ATP hydrolysis by 0.5 µg of the P-type ATPase KdpFABC serves as a positive control (upper panel). KtrAB did not hydrolyse [α-^{32}P]-ATP, and no significant autohydrolysis was observed in the absence of protein. Purified KdpFABC was kindly provided by Jakob Silberberg, Institute of Biochemistry, Goethe-University, Frankfurt. B) Cryo-EM density map of KtrAB obtained in the presence of the non-hydrolysable ATP analogue AMPPCP at a resolution of 3.6 Å. The complex again adopted the ADP-bound conformation. Non-protein densities in KtrA's N lobe confirmed ADP binding. C) An UV-illuminated thin layer chromatography revealed the presence of ADP in the purified KtrAB sample. Cryo-EM grid preparation and data acquisition were performed with the help of Dr. Susann Kaltwasser, Max Planck Institute of Biophysics, Frankfurt. Data processing and structural analysis were performed by Dr. Janet Vonck, Max Planck Institute of Biophysics, Frankfurt.

Altogether, it appears likely that pre-bound ADP is co-purified with KtrA. To test this, a TLC was performed with KtrAB purified as for cryo-EM to determine whether nucleotides were co-purified. Nucleotides were detected by auto-fluorescence under illumination with UV light, revealing a weak signal for ADP in the KtrAB sample (Figure 32 C). This supports the idea of co-purified ADP. The unsuccessful displacement attempts in structural experiments, together with the performed DSF measurements, suggest that the inactive, ADP-bound state is the more stable and most likely the energetically preferred conformation. Since nucleotide triggered conformational changes were observed for the isolated KtrA ring (cf. 5.2.3.4), it appears likely that an additional factor is required to exchange ADP for ATP during the activation of the KtrAB complex, although the identity of this trigger or condition remains unclear.

5.2.4 Detailed structural analysis of the high-resolution structure of KtrAB in the ADP-bound state

The 6 Å cryo-EM density map of KtrAB obtained in the presence of ADP revealed major rearrangements in KtrB and KtrA when compared to the ATP-bound structure, yet it did not allow to resolve the molecular details of inactive state (Diskowski et al, 2017). The cryo-EM density map of the native KtrAB assembly at a resolution of 2.8 Å (cf. 5.2.2.1), in combination with the 2.5 Å resolution map of the $KtrB_2A_8B_2$ 'sandwich' (cf. 5.2.2.2), both presented in this thesis, finally allow the structural evaluation of the ADP-bound, inactive conformation. The high-resolution density maps enabled the optimisation and correction of the previously built model of KtrAB, as most backbone carbonyls (missing residues 1-7, 17-20 and 123-131) and a high level of side chain information became visible (Figure 33 A, B). An overlay of the models obtained from the native and the 'sandwich' assembly confirmed that both share the same conformation (Figure 33 C, D). Only small rotations in the two KtrA subunits (Figure 33 D, asterisk) that actually bind the extra KtrB dimer in the sandwich assembly were observed. However, these alterations did not have a significant impact on the remaining overall structure and the ADP coordination.

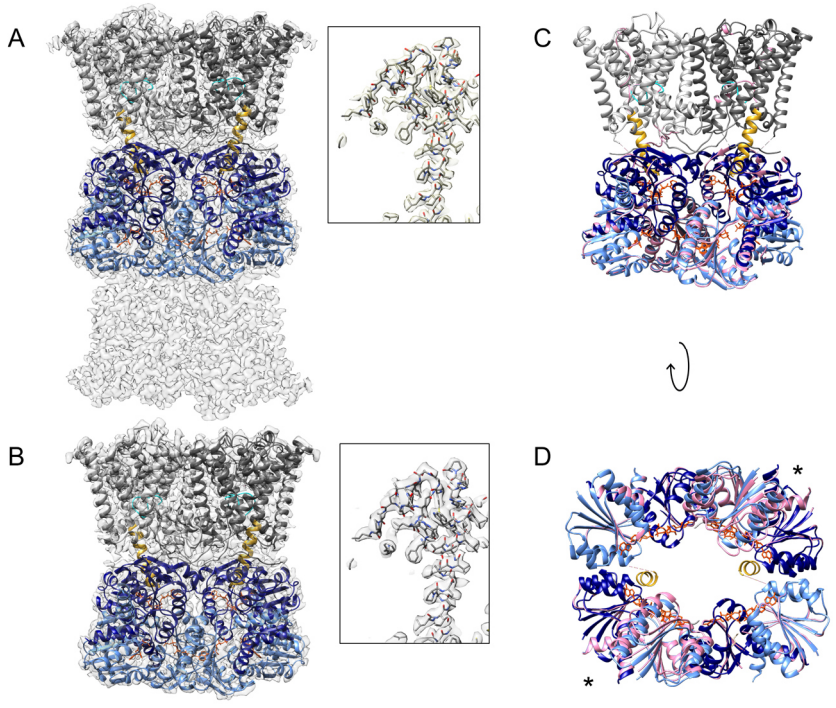

Figure 33: High-resolution structures of KtrAB in the artificial $KtrB_2A_8B_2$ assembly compared to the native $KtrB_2A_8$ assembly. A) Overlay of the KtrAB model (coloured) and the 2.5 Å density map of the artificial sandwich assembly (transparent grey). B) Overlay of the KtrAB model (coloured) and the obtained 2.8 Å density map of the intact native assembly. Due to the high resolution, previously unresolved backbone carbonyls and side chain information became visible (A, B, inset). C) Overlay of both models ('sandwich' coloured, native pink) showed that they share the same overall conformation. D) The bottom view revealed small rotations in the two KtrA subunits, in which the extra KtrB dimer of the 'sandwich' assembly binds (indicated by *).

Since the two structures are basically identical, the structure resulting from the ‘sandwich’ assembly was used for further analysis, as it represents the highest-resolution structure of ADP-bound KtrAB. As already mentioned above (cf. 5.2.2.1), the overall architecture represents the closed conformation of the system, possessing typical features like the extended D1M2 helices and the oval-shaped KtrA ring. Similar to previously published KtrAB structures, the C lobes of KtrA remain unsolved as they appear to be very flexible. The coordination of ADP in the octameric KtrA ring has been described in detail in the past as highlighted in the introduction. Above, the described binding site has been confirmed in the presented structures, yet with slight variations (cf. Figure 25). In the following sections, I will discuss which interactions and features of the system are important for the stabilisation of the closed conformation and how those relate to ADP binding.

5.2.4.1 Regulation of K^+ flux by the selectivity filter and the intramembrane loop

The selectivity filter (SF) and the intramembrane loop of KtrB play a crucial role in ion selectivity and gating in KtrAB (Mikušević et al, 2019). However, the molecular basis for the selectivity and gating remains elusive. At a resolution of 2.5 Å, both structural features are well resolved. Further, within the selectivity filter of KtrB three additional non-protein densities are visible, which could present potassium ions or water molecules. However, unambiguously identifying densities as ions in cryo-EM remains difficult (Vonck & Mills, 2017). The strongest and most defined density was observed at the position corresponding to the S3 binding site of the classical K^+ channel selectivity filter in KcsA. Here, the backbone carbonyl oxygens of residues V68 and T69 from D1, residues N183 and A184 from D2, residues T288 and A289 from D3, and residues T400 and V401 from D4 shape the narrowest section of the pore and are positioned to coordinate the non-protein density, mimicking the coordination geometry of the first hydration shell for a K^+ ion. As this site has already been described as a K^+ binding site in KtrB and its homolog TrkH, it was assigned as K^+ (Figure 34 B) (Cao et al, 2011; Vieira-Pires et al, 2013). Below and above the S3 site, in positions corresponding to the S4 and S2 sites in classical KcsA SF, additional densities were observed. As these densities were much weaker and less defined, they were annotated as coordinating water molecules (Figure 34 B). However, it cannot be entirely excluded that potassium ions contribute to the densities, as lower occupancy or statistical effects would weaken the density. Just below the selectivity filter, the intramembrane loop (Figure 34 C) was resolved in a closed conformation. Calculating the radii along the pore of KtrB with HOLE clearly reveals a constriction at the intramembrane loop with a diameter as small as 0.18 Å, preventing the passage even of a dehydrated K^+ ion (Figure 34 E, F).This closed conformation is mainly stabilised by a hydrophilic interaction between the hydroxyl group of the T318 in the intramembrane loop and the side chain of M100 of the D1M2 helix. Furthermore, the backbone carbonyl of G96

in the extended helix interacts with the backbone of T320. The positively charged K325 from the intramembrane loop forms a salt bridge (3.1 Å) with the backbone carboxylate of the highly conserved, C-terminal G455 of the neighbouring KtrB, restricting the pathway further. The C terminus extends from the neighbouring KtrB into the cytoplasm, making lateral contact with KtrA, from where it enters the pore (Figure 34 C, D). The interaction between K325 and C terminus of the neighbouring subunit was previously observed in KtrAB from *B. subtilis* (Vieira-Pires et al, 2013). In addition to this sterically hindrance, the conserved R427 from the D4M2b helix extends into the centre of the pore, potentially forming an electrostatic barrier for K^+ passage (Figure 34 C). The orientation of R427 is stabilised by hydrophilic interactions with the backbone of two glycines (G95 and G96) in the D1M2 helix. Furthermore, a glutamine (Q99) in the D1M2 helix likewise extends into the pore, making close contact to R427 via extensive hydrophilic interactions.

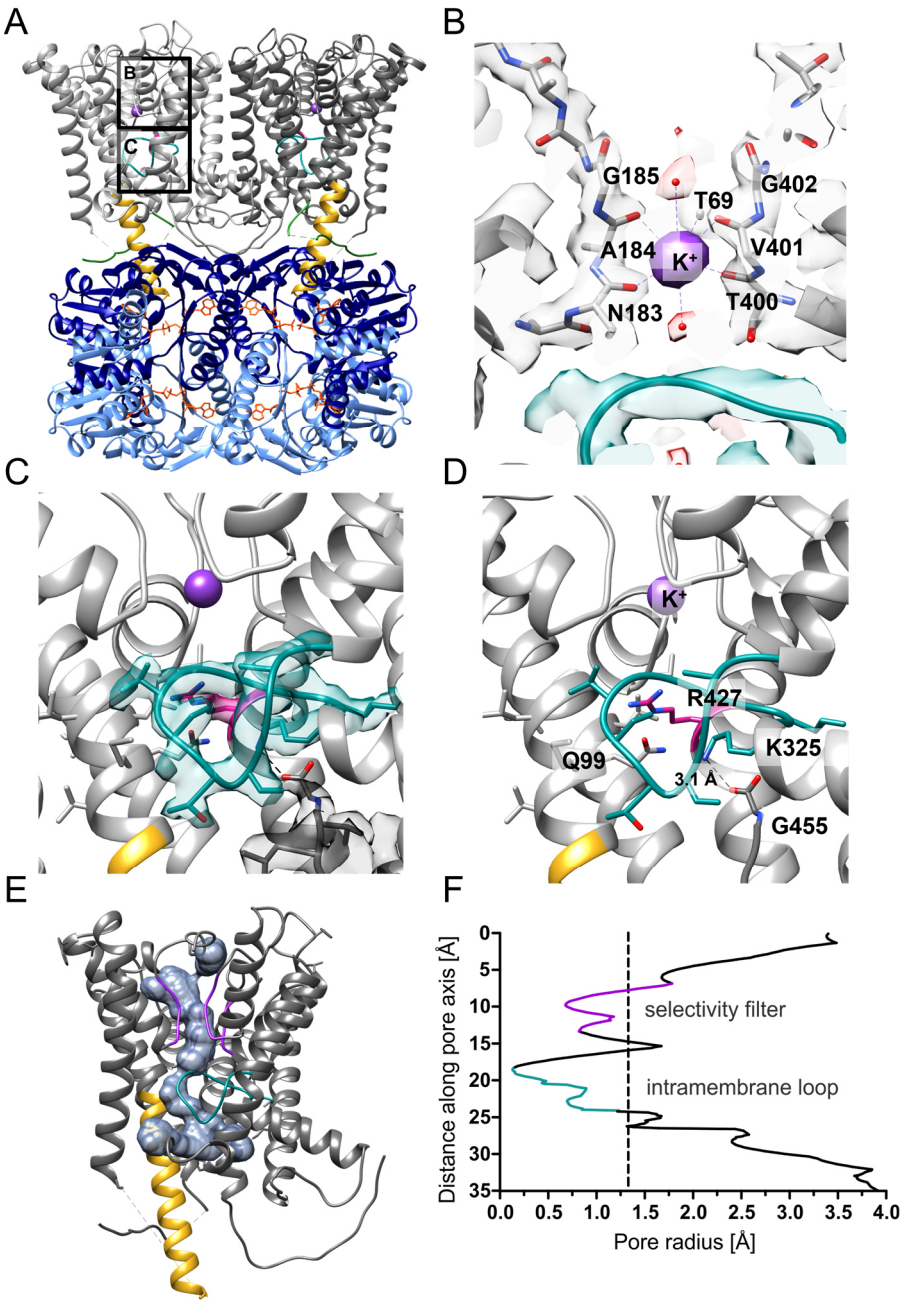

Figure 34: **Structural details of the selectivity filter and the intramembrane loop of KtrB in the ADP-bound KtrAB complex.** A) Structural model of KtrAB in the ADP-bound conformation, built according to the 2.5 Å resolution map. B) Close-up view of the coordination of an identified potassium density (purple) in the selectivity filter (SF) at the S3 binding site. Two additional non-protein densities in the SF were assigned as water molecules. D1 and D3 are not shown for better visualisation. C) Close-up view of the intramembrane loop (cyan). Densities of the intramembrane loop and the C-terminal G455 are shown in the respective colours to highlight the orientation of the side chains. D) Same close-up view of the intramembrane loop presenting the residues, which are involved in its stabilisation. It is stabilised in the closed conformation mainly by hydrophilic interactions with the backbone of the extended D1M2 helix and a salt bridge between the K325 and the C-terminal backbone carboxylate of G455 from the neighbouring KtrB monomer. The conserved R427 (magenta), which is stabilised by Q99 forms an additional electrostatic barrier for potassium flux. Densities are shown in respective transparent colour to highlight the exact position of side chains. Data processing and model building were performed by Dr. Janet Vonck, Max Planck Institute of Biophysics, Frankfurt. E) Structure of a KtrB monomer with SF shown in purple and intramembrane loop in dark cyan. Graphical representation of the calculated pore pathway surface (blue transparent density) generated by HOLE (Smart et al, 1996). F) Calculated pathway radii through the pore of a KtrB monomer along the central axis. The radius of a dehydrated K^+ is shown as a dashed line. The pathway is clearly restricted by the intramembrane loop. Radii were calculated using HOLE.

Initially, the role of the intramembrane loop as a gate was suggested because various mutations in the predicted intramembrane loop of KtrB caused increased K^+ uptake velocities (V_{max}), while the apparent affinity (K_m) was not affected (Hänelt et al, 2010a). To analyse the importance of the here-identified K325 and Q99 for the stabilisation of the inactive KtrAB complex, uptake of K^+ by KtrAB variants featuring alanine substitutions in these positions was determined in a whole-cell uptake assay in the presence of four different KCl concentrations (0.1, 0.2, 0.4, and 1 mM). All measurements were performed in the absence and in the presence of 5 mM NaCl to verify the characteristic Na^+ dependency of KtrAB. Both variants retained the Na^+ dependency and showed an increase in K^+ uptake at increasing K^+ concentrations (Figure 35 A, B, Figure S3). Michaelis-Menten kinetics were determined from the initial uptake velocities at different K^+ concentrations. In fact, the V_{max} of both KtrAB variants significantly increased compared to wildtype KtrAB (Figure 35 C, D, Figure S3), while the K_m remained similar (Figure 35 D). This is in good agreement with the data observed for several loop variants tested in KtrB alone (Hänelt et al, 2010a), and indicates that mutating K325 and Q99, respectively, causes the intramembrane loop to be less stabilised in its closed conformation, therefore allowing faster K^+ uptake.

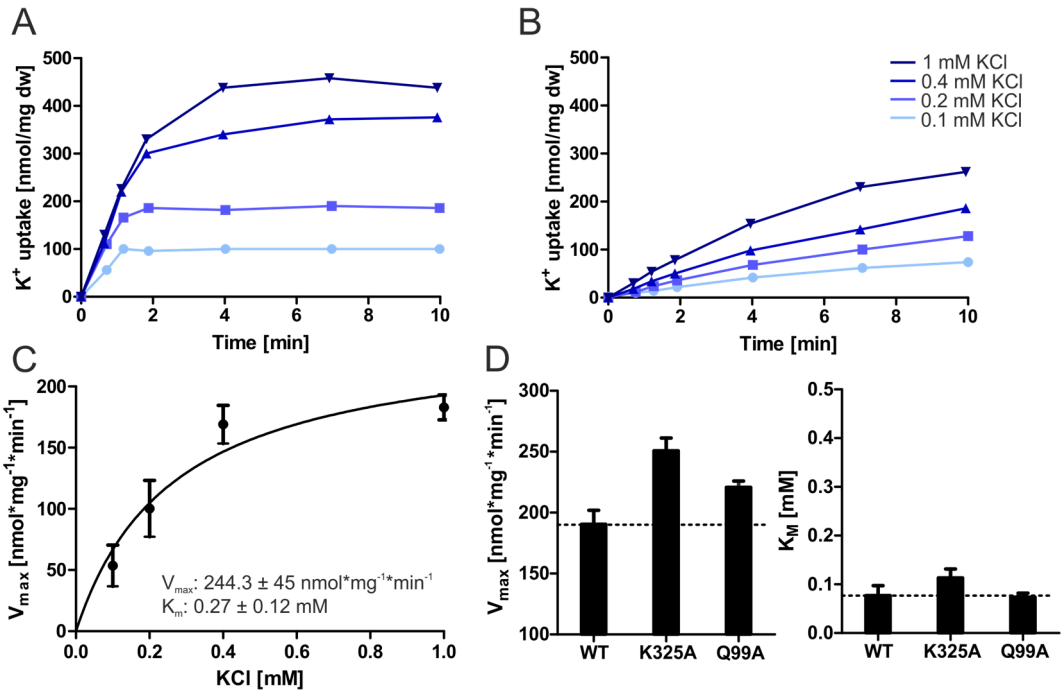

Figure 35: K^+ uptake by *E. coli* LB2003 cells producing KtrAB pore variants. A) After protein production, *E. coli* LB2003 cells were depleted of K^+ and, after 10 min incubation at room temperature, different K^+ concentrations (0.1, 0.2, 0.4, and 1 mM, different shades of blue) and 5 mM NaCl were added. 1 ml samples were taken at different time points, and cells were separated from medium via centrifugation through silicone oil. Cellular potassium content was determined by flame photometry. Exemplary, the uptake curves for *E. coli* LB2003 pKT84_KtrB$_{K325A}$ are shown. Uptake experiments were performed in triplicates. B) Similar measurements were performed in the absence of NaCl. All variants shows Na^+-dependent K^+ uptake. C) Slopes from initial uptake velocities are plotted against the used KCl concentration. Michaelis-Menten fit was performed to determine V_{max} and K_m. Exemplary, the Michaelis-Menten fit for *E. coli* LB2003 pKT84_KtrB$_{K325A}$ is shown. C, D) Average Michaelis-Menten kinetics for potassium uptake through *E. coli* LB2003 cells producing WT KtrAB, KtrAB$_{K325A}$, and KtrAB$_{Q99A}$, respectively, derived from triplicates. Both variants revealed increased V_{max} values. (C) The K_m values remained similar (D). Uptake experiments were performed in triplicates with the help of David Griwatz, Institute of Biochemistry, Goethe-University, Frankfurt under my supervision.

5.2.4.2 Stabilisation of the inter-subunit connecting D1M2 helix

The most obvious, directly visible interaction between KtrA and KtrB in the inactive state is mediated by the extended D1M2 helices from KtrB, reaching from the transmembrane domain into the KtrA ring (Diskowski et al, 2017). However, so far, the resolution was too low to identify the residues involved in stabilising this conformation. Now, the high-resolution map obtained in this thesis revealed that the coordination of the extended D1M2 helices within the KtrA gating ring is established by several hydrophobic interactions and hydrogen bonds between KtrAs and the helices (Figure 36 B, C). Further, inter-subunit salt bridges between the conserved residues R117 (KtrBs) and E38 (KtrAs) become apparent. The distance between the charged groups of the arginine and the glutamate is 3.4 Å, which is ideal for an electrostatic interaction (Barlow & Thornton, 1983). In contrast, extended helices D1M2 are not in direct contact with the bound ADP, although they protrude into KtrA close to the conserved nucleotide binding site. Thus, the extended helices are mainly

stabilised by the N lobe of KtrA and a series of events, i.e., ligand exchange and the subsequent conformational change of the KtrA gating ring, is required to transmit the activating signal to KtrB.

Surprisingly, in all cryo-EM maps obtained within this thesis so far unknown densities were observed near the extended D1M2 helices, lying flatly on top of the KtrA ring (Figure 36 D). The moieties share an interaction interface with both KtrA and the extended D1M2 helices, potentially making them important building blocks of the regulatory mechanism of KtrAB.

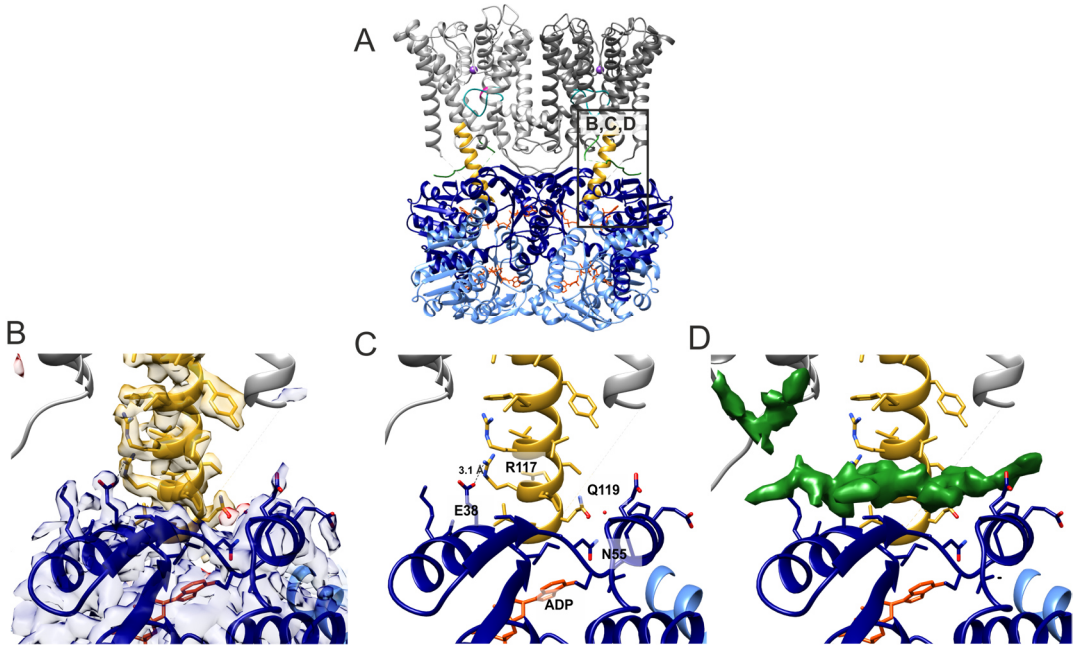

Figure 36: Stabilisation of the extended D1M2 helices of KtrB within the KtrA subunits. A) Structure of KtrAB in the ADP-bound conformation. B) Overlay of the density map (transparent in respective colours) and the model of KtrAB to highlight the orientation of side chains relevant to the KtrA/KtrB interaction. C) Extended helices (yellow) are stabilised by several hydrophobic interactions and hydrogen bonds with KtrAs (blue). A salt bridge was observed between R117 (KtrB) and E38 (KtrA) (distance 3.4 Å). D) Unknown densities at the interface of KtrB and KtrA (green), in close proximity to the extended helices, were identified, suggesting an important role in the interaction of both subunits.

5.2.4.3 Identification of a new feature in the KtrAB complex: The N temini of KtrB

Detailed investigations of the additional densities identified at the interface of KtrA and KtrB (Figure 37) revealed that they correspond to the N termini of both KtrB subunits, which were previously unresolved. The obtained density map allowed the building of a segment from R7 to D14, while residues G15 to A20 remained unresolved. Structural analysis of this newly resolved region indicated an extensive interaction network with both the N lobe of KtrA and the extended D1M2 helix of KtrB. In particular, a hydrophobic patch, V9-P13, forms several hydrophobic interactions with the extended helix and residues from KtrA (Figure 37). Residue Y11 additionally forms backbone to backbone hydrogen bonds with

V53 of KtrA. Furthermore, the positive charge of R7 is in close contact with the negative charge of E64 from KtrA, forming a salt bridge. Due to the intensive interaction network, I hypothesised that the N terminus might play a further role in the stabilisation of KtrAB in the closed conformation. Alternatively, it could be important for the conformational rearrangement to the active state or play a general role for the assembly of the two subunits.

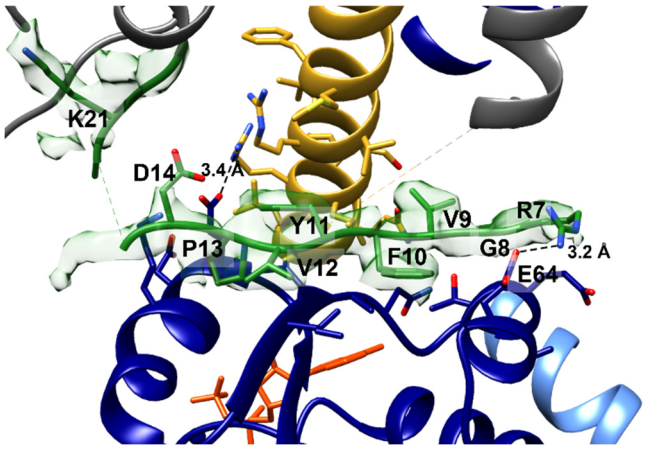

Figure 37: Newly resolved N terminus of KtrB forms an extensive interaction network with KtrA and KtrB. R7 from the KtrB N terminus (green) forms a stabilising salt bridge with E64 from KtrA (blue). A following hydrophobic patch from V9 to P13 interacts with the extended helix (indicated in yellow) and KtrA via hydrophobic interactions and hydrogen bonds. A motif of four positive residues in the N terminus (K16, R17, K19, K21) was not resolved.

To investigate this hypothesis structurally, a variant with a deletion of residues 2-19 (ΔNterm) was designed (Griwatz, 2021). The variant was purified via the established pull-out protocol for subsequent cryo-EM analysis. Size exclusion chromatography indicated that the protein eluted at the same volume as the full-length complex at 10 ml followed by a peak corresponding to free KtrA (Figure 38 A). The protein yield after SEC was comparable to the yield observed for the wildtype purification, indicating similar expression levels. The composition of the SEC fractions was investigated by a Coomassie-stained SDS PAGE and showed the presence of both KtrA and KtrB. This indicates that the N terminus is not required for a successful complex assembly (Griwatz, 2021). For cryo-EM sample preparation, the variant was incubated with 1 mM ATP + 2 mM $MgCl_2$, in order to stabilise the activated, open conformation. A dataset of 7,109 movies was collected from which 525,000 particles were automatically picked. After 2D classification, a density map with a resolution of 3.6 Å was obtained (Figure 38 B, Table S1). The 3D map of $KtrAB_{\Delta 2\text{-}19}$ variant shows the artificial ‘sandwich’ assembly. Furthermore, the map resembles the same conformation observed in all previous obtained maps: The KtrA ring adopts an oval shape, and the D1M2 helices remain extended, showing no effect of N terminus truncation. An ADP molecule is bound in each KtrA N lobe, even though the sample was supplemented with ATP. As expected, no density was observed for the N terminus (Figure

38 C). Consequently, the N terminus is not required for stabilisation of the inactive ADP-bound state, as the variant still exhibits all previously described features. This leaves the possibility that the N terminus plays a role for the activation of KtrAB.

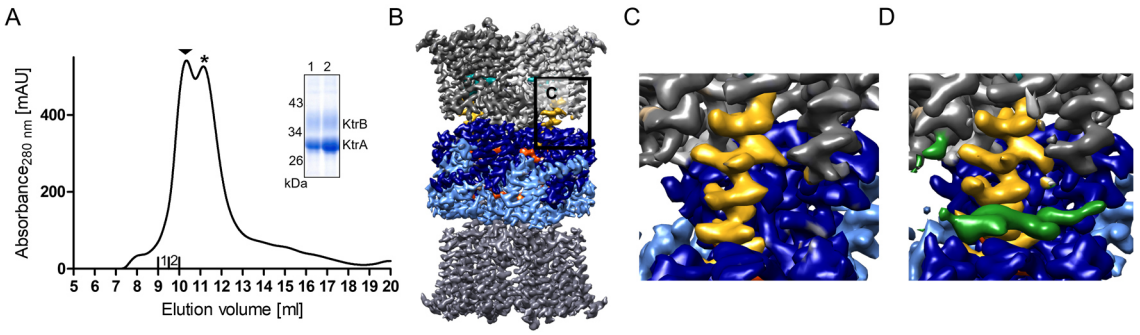

Figure 38: Structural effect of N terminus deletion on the KtrAB complex. A) SEC profile of KtrAB$_{\Delta 2\text{-}19}$ performed on a Superdex® 200 Increase 10/300 GL column. Signals for KtrAB (▼) and excessive KtrA (*) similar to the full length protein were observed. Sample composition of KtrAB peak fractions was analysed on a Coomassie-stained 12% SDS PAGE (inset) and the presence of KtrA and KtrB was confirmed. B) 3.6 Å density map resulting from single-particle cryo-EM, obtained in the artificial 'sandwich' assembly. The absence of the N terminus showed no effect on the conformation of the system, which was again obtained in the ADP-bound state (ADP indicated in orange, closed intramembrane loop in cyan). C) Zoom at the KtrA-KtrB interface as indicated in B. While the system adopts the ADP-bound conformation, including the extended helices and the oval-shaped KtrA ring, the densities for the N termini are lacking. D) For comparison, a close-up view of full-length KtrAB low-pass filtered to the same resolution (3.6 Å) is shown, presenting the density of the N terminus. Sample preparation for cryo-EM was performed by David Griwatz, Institute of Biochemistry, Goethe-University, Frankfurt during his Master thesis under my supervision. Grid preparation and data acquisition were performed in collaboration with Dr. Susann Kaltwasser, Max Planck Institute of Biophysics, Frankfurt. Data analysis, processing and model building were performed by Dr. Janet Vonck, Max Planck Institute of Biophysics, Frankfurt.

The hypothesis, that the N termini are involved in the activation of the KtrAB system, is supported by in vivo K^+ uptake experiments performed with *E. coli* LB2003 cells expressing a tag-less KtrAB$_{\Delta 2\text{-}19}$ variant (pKT84_KtrB$\Delta_{2\text{-}19}$). Interestingly, in the absence of the N terminus, the V_{max} was significantly reduced from 190 nmol*mg^{-1}*min^{-1} to 46 nmol*mg^{-1}*min^{-1} when compared to wildtype KtrAB (Figure 39 A, Figure S4), while the K_M remained similar (Figure 39 B). The reduced uptake velocity in fact could indicate an important role of the N terminus on the activation of the system. All uptake experiments were performed in the presence and absence of 5 mM NaCl. The uptake remained Na^+ dependent, confirming the assembly of the complex, which was in line with the structural observations.

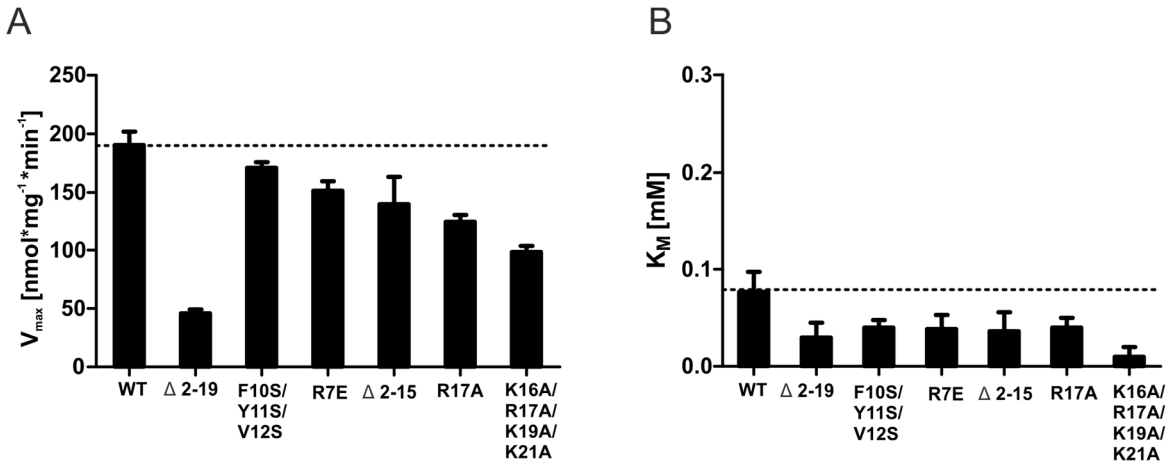

Figure 39: K^+ uptake by KtrAB variants with modified N termini. Uptake experiments were performed as described previously. *E. coli* LB2003 cells were transformed with pKT84 (tag-less KtrAB) and variants thereof. K^+-free cells were prepared, and K^+ uptake was measured in the presence of 0.1, 0.2, 0.4 and 1 mM KCl. All experiments were performed in the presence and absence of 5 mM NaCl. No uptake was observed without Na^+ (cf. Figure S4). For all measurements the Michaelis-Menten kinetics were determined using initial uptake velocities. A) V_{max} values and B) K_M values for all variants were determined. Dashed lines represent Michaelis-Menten kinetics of the wildtype. Measurements were performed in triplicates by David Griwatz and his Bachelor student Katja Ohlemüller, Institute of Biochemistry, Goethe-University, Frankfurt.

To identify the crucial residues responsible for the reduced uptake in the N terminus deletion variant, different structurally important residues were mutated and whole-cell K^+ uptake experiments were performed (Figure 39 A, B). Surprisingly, mutating the hydrophobic patch involved in nonpolar interactions with KtrA and the extended helix to polar serines (F10S, Y11S, V12S) did not significantly affect uptake. The exchange of residue R7, which most likely forms a salt bridge with E64 in KtrA, to an alanine slightly reduced the uptake velocity from 190 nmol*mg^{-1}*min^{-1} to 150 nmol*mg^{-1}*min^{-1}. The third striking feature removed in the $KtrB_{\Delta 2\text{-}19}$ variant is a cluster of positive charges at the end of the N-terminal loop (K16, R17, K19), which was not resolved in the available structures. Remarkably, a shorter deletion variant (Δ2-15), which retains these charges, showed only a slight reduction in V_{max} compared to the drastic effect of the full deletion (Δ2-19), indicating an involvement of the positively charged region in the activation. To test this further, the positive residues were mutated in the full-length construct. Already the neutralisation of R17 reduced the V_{max} to 125 nmol*mg^{-1}*min^{-1}. The neutralisation of all four positive residues resulted in a further reduction of the V_{max} to half the maximal velocity of the wildtype. These results suggest that the positively charged residues of the N terminus play a crucial role in the activation of KtrAB system. A possible scenario could be that a reorientation of the N terminus, most importantly of the positive charges, would allow conformational rearrangements of the remaining KtrAB complex, which ultimately would lead to the opening of the pore and the stabilisation of the open, active state. It was speculated that the positively charged residues of the N termini could interact with the negatively charged lipid headgroups of the membrane. To investigate this hypothesis,

molecular dynamics (MD) simulation of KtrB in a lipid environment were performed, analysing the localisation of the N termini.

5.2.5 MD simulations of the KtrB dimer in a lipid environment

Preliminary MD simulations were provided by Dr. Ahmad Reza Mehdipour, Center for Molecular Modeling, Ghent University. For the simulations the structural model of a KtrB dimer, resulting from the 3.1 Å cryo-EM density map of KtrAB obtained within this thesis, was placed in a heterogenous lipid bilayer consisting of 45% POPE, 49% POPG and 15% CL. An all-atom simulation was started with the N termini located in the position as observed in the obtained structure of the KtrAB complex (Figure 40 A). During initial equilibration of the systems, both N termini of the KtrB dimer slightly rearranged, establishing first interactions with the membrane, but in general remaining in a similar position compared to the initial position (Figure 40 B). After the equilibration, the localisation of KtrBs' N termini with regard to the membrane was analysed for 1 µs and revealed, that both N termini frequently interact with the membrane, as shown by the increase in number of contacts after approximately 200 ns (Figure 40 C). Here, a protein residue and a lipid molecule were counted to be in contact when at least one heavy-atom pair was within 3.5 Å in distance. Additionally, analysis of the distance of the N termini from the membrane in the Z direction demonstrates, that in correlation with the increased number of contacts, the centre of the mass of at least one N terminus moves very close to the lipid headgroups after 200 ns, which remains stable within the remaining simulation time (Figure 40 D, green). This strong interaction is as well reflected by the snapshot taken at the end of the simulation, in which the N terminus is very close to the membrane (Figure 40 E). The second N terminus, however, appears to remain in its initial position. Yet, the increased number of contacts and the snapshot taken at the end of the simulation show, that this N terminus as well interacts with the membrane (Figure 40 F). As the analysis of the distance shows the location of the centre of the mass of the complete N terminus, it does not resolve movements of individual parts from the N terminus towards the membrane. In general, the observed interactions of both N termini were especially established by the positively charged residues R7, K16, R17 and K19 with the negatively charged phospholipid headgroups. Additionally, the hydrophobic residues V9 and F10 were shown to dive deep into the membrane interacting with the acyl chains. However, it has to be considered that the KtrA ring was not present during the simulation. Therefore, the N termini were not able to establish the interaction with the KtrA ring as observed in the cryo-EM structure. In further MD simulation, the localisation of the N termini towards the membrane should be analysed in the presence of KtrA.

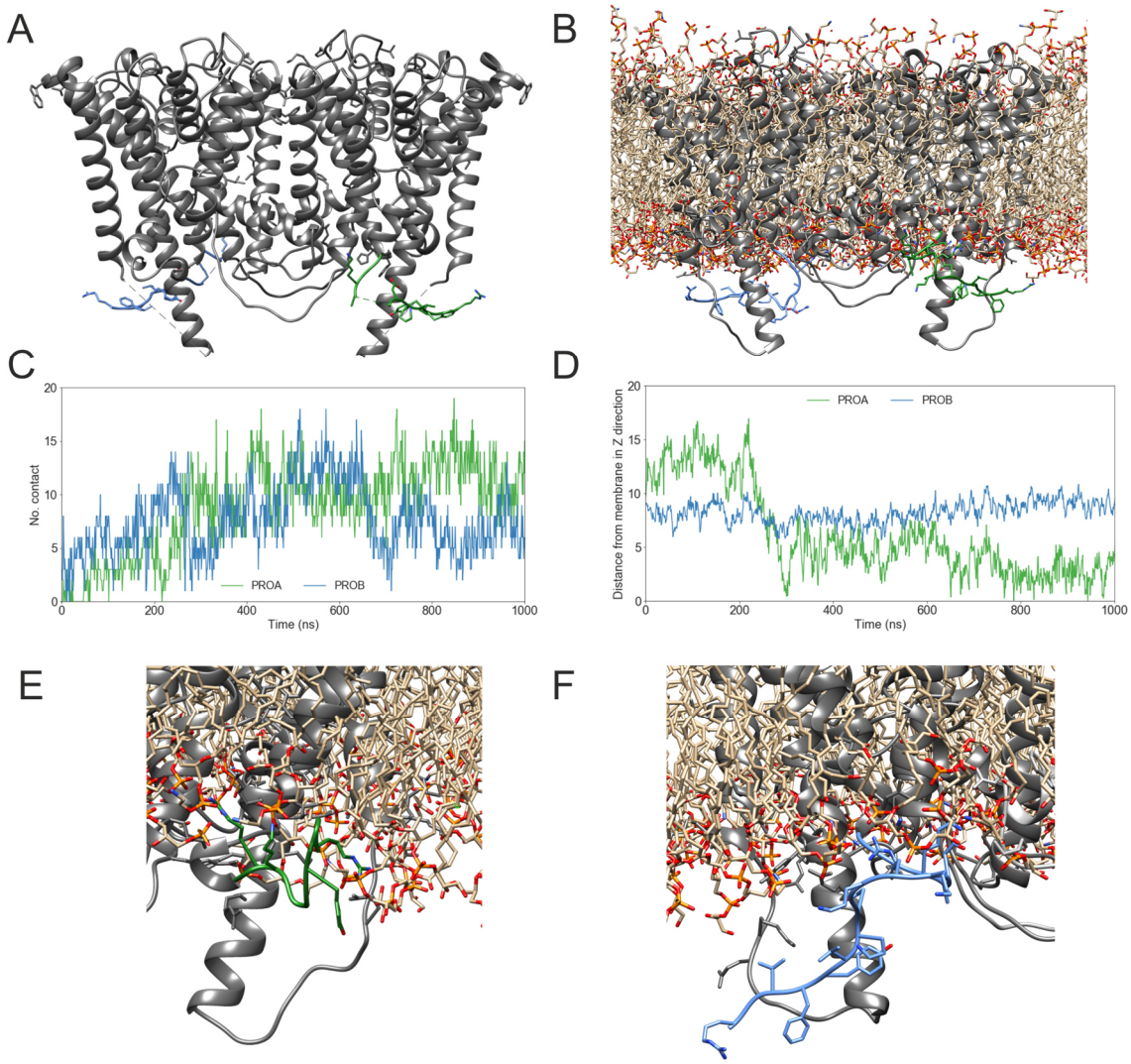

Figure 40: All-atom MD simulations of a KtrB dimer in a lipid environment. For the simulation a heterogenous lipid bilayer consisting of 45% POPE, 49% POPG and 15% CL was used. The simulations was performed for 1 µs analysing the localisation of the N termini of a KtrB dimer (green and blue) towards the membrane. A) Structure of the KtrB dimer obtained from the cryo-EM data of the KtrAB complex. In the complex the N termini lie flat on the KtrA ring, which is not shown. B) Snapshot of the simulation, showing the position of the N termini after an initial equilibration of the system. C) Analysis of the MD simulation revealed that the number of residue-residue interactions between both N termini und the lipids increases after approximately 200 ns. D) Furthermore, the distance of the centre of mass of the two N termini (green and blue) from the membrane in the z direction was determined and revealed, that at least one N termini moves close to the membrane surface after approximately 200 ns. E) Zoom into the N terminus of one protomer (green) showing a strong interaction with the lipid membrane. F) The N terminus of the other protomer (blue) interacts only partially with the membrane, most likely with the positively charged residues. ProA (green) and ProB (blue) represent the N terminus of a KtrB protomer, respectively. MD simulations and analysis were performed by Dr. Ahmad Reza Mehdipour, Center for Molecular Modeling, Ghent University.

5.2.6 Conformational flexibility of the intramembrane gating loop in the dependence of lipids and KtrB's N terminus

The decreased K^+ uptake by the KtrAB N terminus variants implies an effect of the mutations on the gating of the channel. Since the positive charged residues strongly contribute to this effect, it was suggested that the N terminus interacts with the lipid environment, which is in line with the pre-liminary MD simulations. Therefore, the flexibility of the intramembrane loop was analysed in a lipid environment via DEER measurements, using the $KtrAB_{T318C}$ variant, as described in section 5.2.2.3. For providing native-like conditions, the purified and spin-labelled native $KtrA_8B_2$ assembly was reconstituted into *E. coli* polar lipid (ECPL) liposomes. To induce nucleotide-dependent conformational changes, the samples were supplied with either 10 mM ADP or 10 mM ATP. K^+ translocation through KtrAB across the membrane was initiated by the addition of CCCP, which is abolishing the emerging membrane potential. In the presence of ADP (Figure 41, 1st row), the $KtrAB_{T318CR1}$ variant showed a clear oscillation in both the experimental raw data and the dipolar evolution function F(t), resulting in a distance distribution centred at 3.3 nm and featuring a small distribution width. As described for the detergent-solubilised KtrAB complex, this distance most likely corresponds to the closed conformation, in which the intramembrane loop blocks the pore (cf. 5.2.2.3). The clear oscillation indicates a dominant fraction of the sample in this conformation, suggesting a highly restricted loop. Only a minor fraction was observed at a larger distance of 3.7 nm. In the presence of ATP, a clear shift of the mean distance distribution was observed (Figure 41, 2nd row). The oscillation observed in the experimental raw data and dipolar evolution function resulted in a shift of the major fraction to larger interspin distances of 3.7 nm, indicating a stabilisation of the intramembrane loop in another, probably the open conformation, which has not been observed in the detergent-solubilised sample. Only a marginal signal was still observed at 3.3 nm, indicating that a minor fraction of the complex remains in its inactive state. These data confirm that a lipid membrane is required to stabilise the intramembrane loop in an open conformation, which seem to be triggered by ATP-dependent conformational changes within the KtrA ring.

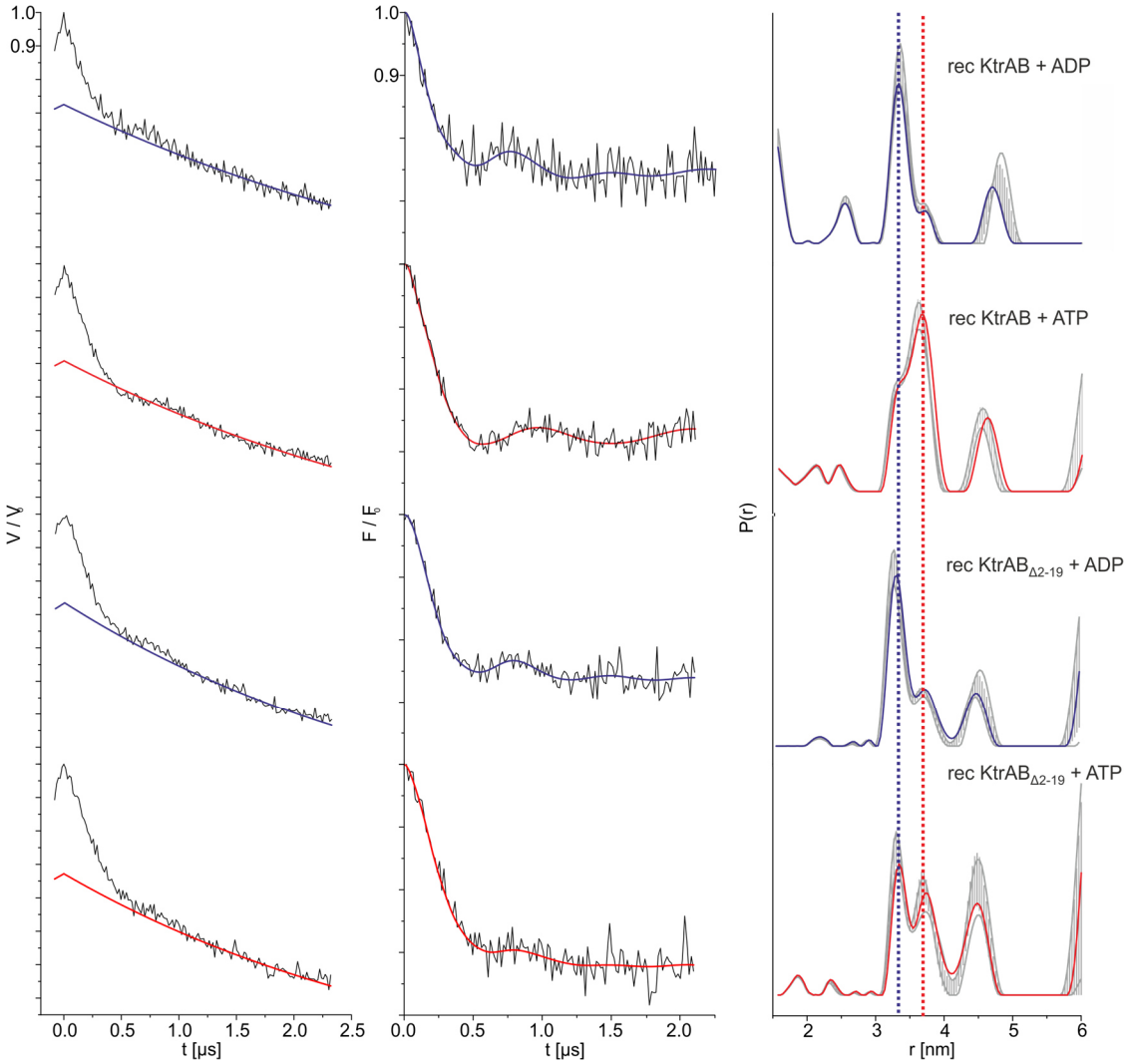

Figure 41: Dynamics of the intramembrane loop of KtrAB in the dependence of KtrBs' N termini and a lipid environment. DEER measurements of the full-length KtrAB$_{T318CR1}$ and the KtrAB$_{T318CR1_\Delta 2-19}$ variant in the presence of 10 mM ADP (blue) or 10 mM ATP (red) and 2 mM $MgCl_2$. Left panels: Experimental raw data V(t) with fitted background function; middle panels: Background-corrected dipolar evolution function F(t); right panels: Interspin distance distribution P(r) obtained by Tikhonov regularisation. Grey areas represent the full variation of possible distance distributions. The lower and upper error estimates (grey lines) represent the respective mean values minus and plus twice the standard deviation. Distances are measured between the labelled residues in both KtrB protomers. A distance of 3.3 nm (blue dashed line) most likely corresponds to the closed conformation of the intramembrane loop, a distance of 3.7 nm (red dashed line) is suggested to represent the open conformation. Mean distance distribution centred around 4.5 nm corresponds to the background signal resulting from a d2 time of 2.4 µs, which was used for all measurements, indicating reliable distance distributions up to 4.5 nm. KtrAB$_{T318CR1}$ and KtrAB$_{T318CR1_\Delta 2-19}$ were reconstituted in ECPL liposomes with a LPR of 10. In full-length KtrAB, ATP induces a transition to the open loop conformation. In the ΔN term variant, the transition to the open conformation is impaired. Sample preparation was performed together with Dr. Dorith Wunnicke-Kortz, Institute of Biochemistry, Goethe-University, Frankfurt, who performed the pulsed EPR measurements and data evaluation.

To understand the role of the N termini in the gating of the channel, in a similar approach the effect of the N terminus deletion (Δ2-19) on the flexibility of the intramembrane loop was analysed. Interestingly, in the presence of ADP, a similar distance distribution for $KtrAB_{T318CR1\_\Delta2\text{-}19}$ was observed when compared to full-length $KtrAB_{T318CR1}$. Here, the mean distance distribution again centred at 3.3 nm, indicates a closed conformation of the intramembrane loop (Figure 41 3rd row). These results confirmed the observation from cryo-EM that the closed ADP-bound conformation is not influenced by the deletion of KtrBs' N termini. On the other hand, in the presence of ATP, the $KtrAB_{T318CR1\_\Delta2\text{-}19}$ variant showed a much broader distance distribution, with roughly equal occupancy of the open conformation at 3.7 nm and the closed conformation at 3.3 nm (Figure 41, 4th row), similar to the detergent-solubilised sample (cf. Figure 27). This suggests that the conformational transition of the intramembrane loop from the closed to the open conformation, as observed for full length $KtrAB_{T318CR1,}$ is impaired in the absence of KtrB's N terminus, thus less frequently allowing the channel opening and potassium flux. This explanation is in line with the lowered V_{max} of the $KtrAB_{\Delta2\text{-}19}$ variant in the K^+ uptake experiments (cf. Figure 39). Taken together, it can be concluded, that removing the N termini has a similar effect as observed in the absence of a membrane environment, supporting the hypothesis, that conformational changes triggered by ATP and an interaction between the N terminus and the membrane play an important role in the conformational transition to the open state during channel gating. However, the underlying mechanism of channel gating and how the N terminus in detail interacts with the membrane remain elusive and requires further investigation.

5.2.7 Lipids and their role in regulating KtrAB

Alongside previous EPR studies (Diskowski et al, 2017), the data of this thesis revealed that lipids might play a crucial role in the regulation of the KtrAB system. I hypothesise that the N terminus of KtrB, which has been shown to be dispensable for complex assembly and stabilisation of the inactive conformation, interacts with the membrane and thus influences the opening of the KtrAB potassium channel. Hence, the role of lipids was further investigated by both functional and structural approaches.

5.2.7.1 Effect of cardiolipin on the activity of KtrB

Based on the results presented in this thesis, the most likely interaction between KtrB's N terminus and the membrane is between the cluster of positive charges between K16 and K21 and negatively charged lipid head groups at the membrane surface. Incidentally, the concentration of negatively charged lipids, especially cardiolipin (CL), increases in the membrane upon osmotic stress, which corresponds to the conditions of KtrAB activation. To understand the role of the lipids in detail, the effect of a varied lipid composition on the activity of the channel subunit KtrB was tested using a liposome-based flux assay. For this, liposomes were prepared from ECPL supplemented with 0%, 10% or 20% CL, and purified KtrB was reconstituted at an LPR of 100. Before performing the ACMA-based flux assay, the reconstitution efficiency was verified by resolubilisation to ensure that the reconstitution worked similar for all liposomes containing different lipid compositions (Geertsma et al, 2008a). The resolubilisation relies on the assumption that only well reconstituted protein remains folded upon detergent removal and thus can be solubilised, while the other protein would precipitate and remain in the pellet after resolubilisation. Quantification of the SDS PAGE analysis of all samples revealed that independent of the lipid composition 70-80% of the protein was well reconstituted (Figure 42 A). The established ACMA-based flux assay was adjusted according to the protocol published by Teixeira-Duarte et al. (Teixeira-Duarte et al, 2019). In short, liposomes were loaded with buffer containing 20 mM Hepes pH 7.4, 195 mM KCl, 5 mM NaCl and 1 mM $MgCl_2$, while in the outside buffer KCl was replaced by 195 mM sorbitol, creating a KCl gradient across the membrane. Addition of CCCP, which clamps the membrane voltage to 0, initiates continuous flux of K^+ through open channels until an electrochemical equilibrium is reached (Figure 42 B). Empty liposomes (eLS) indicated as pale traces (Figure 42 A), served as negative controls, where flux was only observed upon the addition of K^+ ionophore valinomycin. Interestingly, for the KtrB-containing liposomes, increasing CL concentrations resulted in faster K^+ fluxes. Determining the rate constant of the ACMA quenching (k), which is an indirect indicator of K^+ flux, revealed an increase of the rate constant by a factor of 2 or 3 for liposomes supplied with either 10 or 20% CL, respectively,

compared to only ECPL (Figure 42 C). These results show for the first time that lipids, more precisely cardiolipin, influence the K^+ permeability of reconstituted KtrB.

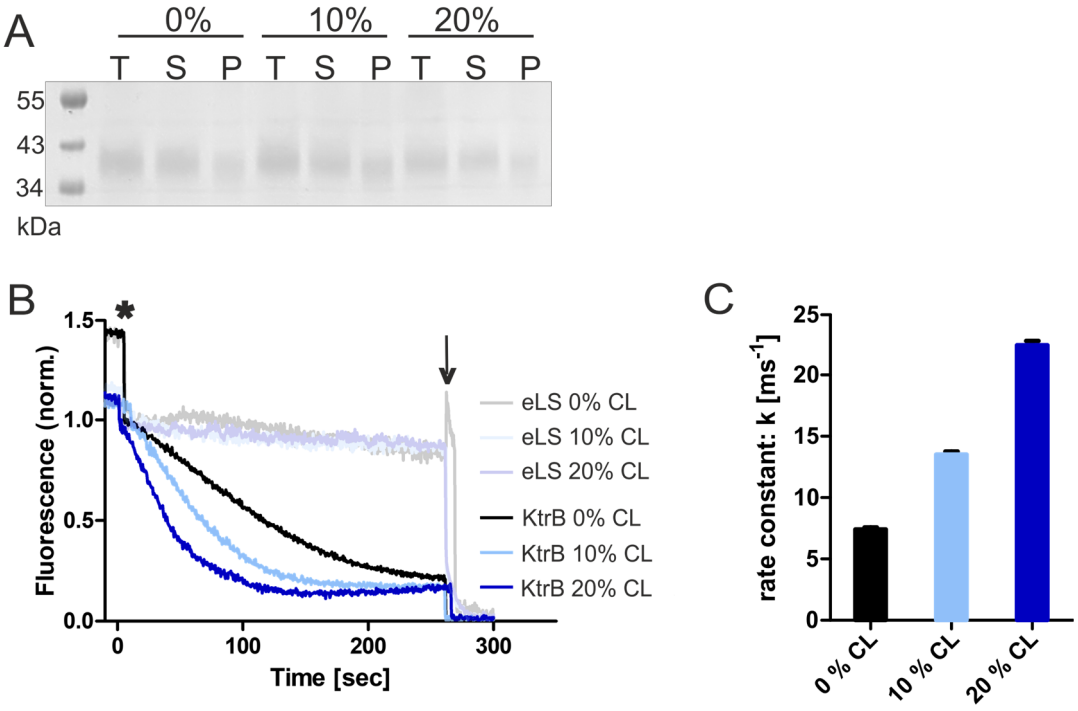

Figure 42: ACMA-based flux assay to analyse the effect of cardiolipin on the activity of KtrB. KtrBC3H was purified and reconstituted in liposomes, containing different percentages of CL, at an LPR of 100. A) 12% SDS PAGE of samples after resolubilisation of KtrB-containing liposomes with 1% DDM. Signal intensities of total sample (T), supernatant (S) and pellet (P) after solubilisation were compared and revealed a reconstitution efficiency between 70%-80% quantified by Fiji/ImageJ. B) Proteoliposomes were loaded with KCl and diluted in K^+-free buffer, containing 195 mM sorbitol. K^+ flux was initiated by addition of the H^+ ionophore CCCP (marked by *). Changes in fluorescence (λ_{ex} 410 nm; λ_{em} 500 nm) were detected for 250 sec. For determining the maximal potassium release from the liposomes, the K^+ ionophore valinomycin was added (indicated by arrow). Empty liposomes were used as negative controls, presented in respective pale colours. C) Decay rates ($k=1/t_1$) for one-phase exponential decays were determined for proteoliposomes with different CL concentrations, revealing an increasing rate constant for increasing CL concentrations.

Unfortunately, it was not possible to establish the ACMA-based flux assay for KtrAB, as the reconstitution efficiency of the assembled complex was insufficient. Furthermore, the regulatory nucleotides ATP and ADP interfere with ACMA fluorescence, which increased the struggles for successful and reproducible measurements. Therefore, an alternative assay needs to be established in the future.

5.2.7.2 Reconstitution of KtrAB in nanodiscs for structural analysis

Based on the results of the transport and EPR measurements studying the role of KtrB's N terminus, it was speculated that the lipid environment might be the missing stimulus for sufficient ATP binding and the subsequent conformational change towards the active state. Therefore, providing a lipid environment could help to solve the structure of KtrAB in the ATP-bound conformation and to understand the role of the N terminus in the full translocation mechanism of the complex. To structurally analyse the effect of the lipids on the KtrAB complex and investigate the role of the KtrB's N terminus in this regard, a reconstitution protocol for KtrAB in nanodiscs was established. For this, the membrane scaffold protein (MSP) 2N2 was chosen, as it was described to generate nanodiscs with a diameter of 15 - 16.5 nm. KtrB has a diameter of 8.3 nm on the long axis, hence the nanodisc should provide a sufficient lipid environment for interaction between the protein and the lipids. In addition to the selection of the scaffold protein, the MSP-to-lipid and protein-to-lipid ratios play a crucial role for successful reconstitution. In an initial trial, $KtrB_2A_8$:MSP2N2:lipid ratios of 1:3:500/1000 (molar ratios) were tested, which resulted mainly in aggregated protein. Protein aggregation was previously reported to be caused by a high excess of lipids, which results in the production of large polydisperse liposome-like particles that induce aggregation (Bao et al, 2012). Therefore, for further trials the molar ratio was adapted to 1:2.5:100 or 1:3:200. Purified KtrAB was mixed with pre-solubilised lipids and MSP2N2. Subsequently, the remaining detergent was removed by the addition of BioBeads. The sample was concentrated and further purified via SEC to separate empty nanodiscs from KtrAB-containing nanodiscs. Unfortunately, after concentration, the protein partially precipitated, which could be separated from the remaining reconstituted fraction by centrifugation (Figure 43 A). The remaining reconstituted protein was subjected to SEC. Both tested ratios revealed similar elution profiles, each showing three signals eluting at 15 ml, 16.5 ml and 18.2 ml, with in general slightly higher absorbance for the sample reconstituted with a molar ratio of 1:2.5:100 (Figure 43 B). Therefore, the molar ratio of 1:2.5:100 was used for further experiments. The sample compositions of the different SEC peaks were analysed by 12% SDS PAGE, and the first peak was identified to contain both KtrAB and MSP2N2, the latter of which runs at an apparent molecular weight of 45 kDa (Figure 43 B). Additional signals migrating at higher apparent molecular weights indicated contaminations. Further quality control of the sample was performed via negative staining, from which reasonable 2D classes allowed to proceed with single particle cryo-EM (data not shown). For this purpose, the protein was concentrated to 2.2 mg/ml and grids were prepared as described above for the detergent-solubilised sample. To induce the active conformation, 1 mM ATP and 2 mM $MgCl_2$ were added prior to plunge freezing. From an initial dataset, 375,000 particles were automatically picked and a 2D classification revealed classes of KtrAB in different orientations but also several classes of unknown particles (Figure 43 C). These

contaminations most likely were co-purified with MSP2N2 and could not be excluded during several subsequent purification steps. Nevertheless, particles from classes containing KtrAB were used for 3D reconstruction, resulting in a 6 Å resolution density map (Figure 43 D, Table S1). The transmembrane helices of the KtrB dimer were tightly surrounded by MSP2N2, which was surprising, as the MSP2N2 nanodiscs were expected to form much larger nanodiscs. KtrAB assembled in the native $KtrB_2A_8$ complex, comprising all previously known features. However, although ATP was added to the sample, the complex again adopted the closed conformation, in which the prominent D1M2 extended helices reach from the transmembrane domain of KtrB into the KtrA ring (Figure **43** D, red asterisks). Even though the resolution was too low to identify the bound nucleotide, the KtrA ring clearly adopted the oval-shaped conformation with the same dimensions observed before. Thus, no significant influence of the nanodiscs on the structure of KtrAB was observed. A possible explanation for that unfortunate outcome could be that still not enough lipids surrounded the complex for the KtrB N terminus to interact, as MSP2N2 tightly associated with KtrAB. Therefore, in further approaches, the reconstitution into nanodiscs needs to be improved to achieve deeper insights into the role of lipids on the structural rearrangements of KtrAB during channel gating. In addition to advantages for structural approaches, a successful reconstitution would be beneficial for other future biophysical and biochemical approaches like ITC, SPA or EPR.

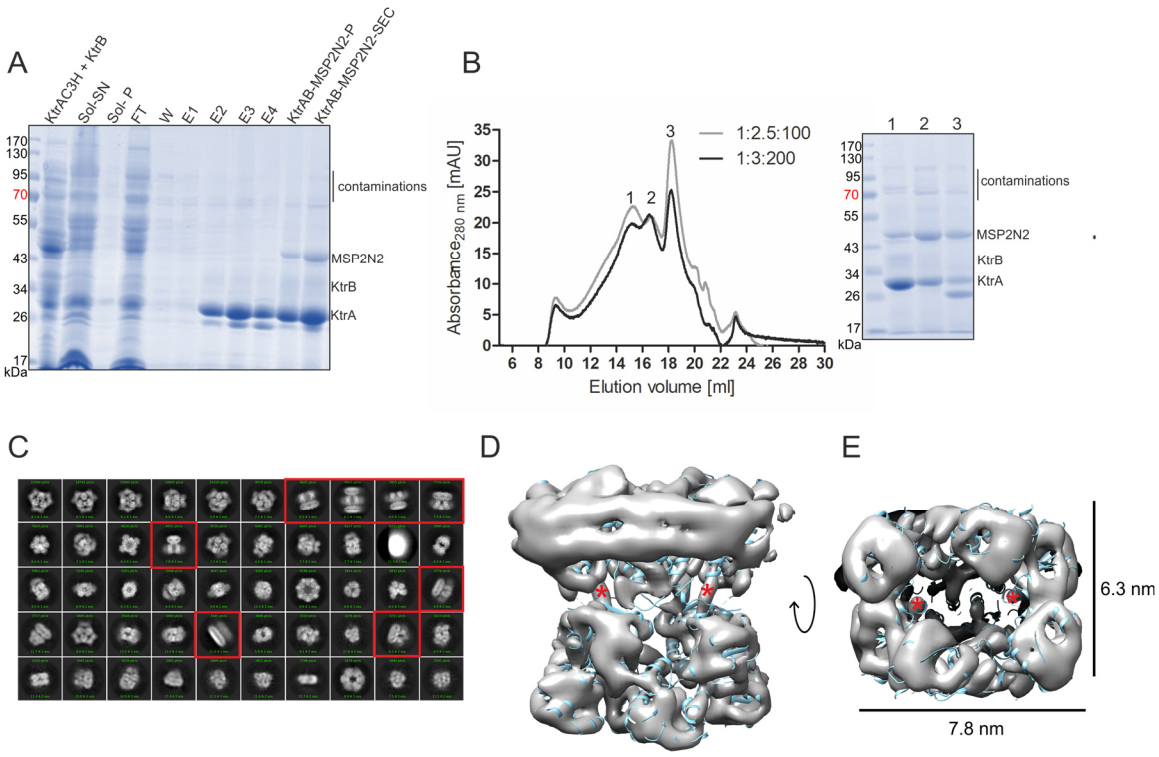

Figure 43: Reconstitution of KtrAB into MSP2N2 nanodiscs for structural analysis. KtrAB was purified via the established pull-out procedure and, after elution from Ni^{2+}-NTA agarose, the protein was reconstituted in MSP2N2 nanodiscs in the presence of ECPL. Two different molar ratios of KtrAB:MSP2N2:lipids (1:2.5:100 and 1:3:300) were tested and further purified via SEC. A) Coomassie-stained 12% SDS PAGE to analyse the composition of samples collected from purification: Mixture of KtrAC3H cytoplasm and KtrB-containing membranes (KtrAC3H+KtrB), supernatant of solubilised sample after centrifugation (Sol-SN), pellet of solubilised sample after centrifugation (Sol-P), flowthrough (FT), wash fraction (W), and four elution fractions from Ni^{2+}- NTA agarose affinity purification. After reconstitution of elution fraction E2 and E3, the sample partially aggregated and aggregates were seperated by centrifugation (KtrAB-MSP2N2-P). Remaining protein was analysed by SEC. B) The SEC profile revealed three signals for each ratio. Composition of each peak fraction was identified by a Coomassie-stained 12% SDS PAGE. While peak 1 from SEC contains KtrAB and MSP, peak 2 lacks KtrB and peak 3 contains various contaminations. Peak fraction 1 was concentrated to 2.2 mg/ml and a cryo-EM sample was prepared as described before. C) A dataset was obtained using a Titan Krios G3i, and 2D classes of automatically picked particles by crYOLO resulted in several classes of KtrAB in different orientations (highlighted in red), but also several classes with other particles, resulting from contaminations during purification. D, E) KtrAB-containing classes were used to perform 3D reconstruction and resulted in a low-resolution 6 Å map (grey). The MSP2N2 was tightly wrapped around the transmembrane helices of KtrB, with little to no surrounding membrane surface. Superposition of the map and the ADP-bound model of KtrAB (light blue) revealed that the map was obtained in the same architecture as observed before. E) The KtrA ring clearly adopts the oval-shaped conformation. Grid preparation and data acquisition were performed with the help of Dr. Susann Kaltwasser, Max Planck Institute of Biophysics, Frankfurt. Data analysis and processing were performed by Dr. Janet Vonck, Max Planck Institute of Biophysics, Frankfurt.

6 Discussion

The goal of this Ph.D. thesis was to decipher the molecular details of the K^+ gating mechanism by the unique bacterial potassium channel KtrAB. In vivo fluorescence microscopy with living *B. subtilis* cells was performed to gain insights into the localisation and the assembly of the two individual subunits KtrA and KtrB under different osmotic conditions on a cellular level. For structural and functional approaches, the purification of KtrAB from *V. alginolyticus* was optimised to obtain its native $KtrA_8B_2$ assembly. In total, 6 cryo-EM structures, all aiming for the ATP-bound active conformation, were obtained in the ADP-bound inactive state. Biochemical analysis, which focused on nucleotide binding, revealed that ADP seemed to preferably bind to KtrA and the nucleotide was co-purified with the KtrAB complex, not allowing the complete exchange to ATP under the tested conditions. However, ATP was observed to bind to the isolated KtrA RCK ring, inducing the expected square-shaped conformation. The structures obtained in this thesis revealed the previously unresolved N termini of the KtrB dimer, disclosing a yet unknown interaction platform between KtrA and KtrB, which was subsequently shown to play a crucial role in the gating mechanism of KtrAB in a lipid environment. The results indicate an allosteric network, combining nucleotide-triggered changes within KtrA and conformational rearrangements in KtrBs' N termini and transmembrane domains, which are required to stabilise the active, conducting state of the KtrAB system.

6.1 New structural and functional insights lead to an adapted proposed gating mechanism for KtrAB from *V. alginolyticus*

The data presented within this thesis allows to expand the existing gating mechanism of KtrAB (Figure 44). In the inactive state, ADP is bound to KtrAB. Based on the data presented in this thesis, this is most likely the energetically preferred and most stable conformation. The KtrA ring adopts an oval shape, and one ADP molecule is bound to each of the KtrA subunits, as seen in the 2.5 Å resolution cryo-EM density map (cf. 5.2.2.2). The D1M2 helix of each KtrB protomer is extended and protruding from the membrane into one KtrA subunit, where it is stabilised by hydrophobic interactions and a salt bridge between the conserved residue R117 of KtrB and residue E38 in the N lobe of KtrA. At the interface of the KtrB dimer and the octameric gating ring, the newly identified N termini of both KtrBs lie flat on the KtrA ring and are in contact with both KtrA and KtrB, mainly via hydrophobic interactions and salt bridges between R7 of the N termini and E64 in two KtrA subunits. The intramembrane loop is locked in a closed conformation, stabilised by hydrophobic interactions with the backbone of the D1M2 helix. These

stabilising interactions of all features could be clearly identified in the 2.5 Å structure of KtrAB (cf. 5.2.4). Together with the highly conserved positive charged residue R427, which forms an electrostatic barrier, the gate blocks the pore for K^+ flux, which was confirmed by the calculated pore radius (cf. 5.2.4.1). In line with this, MD simulations revealed that the water accessibility within the pore is drastically reduced in this conformation (Diskowski et al, 2017).

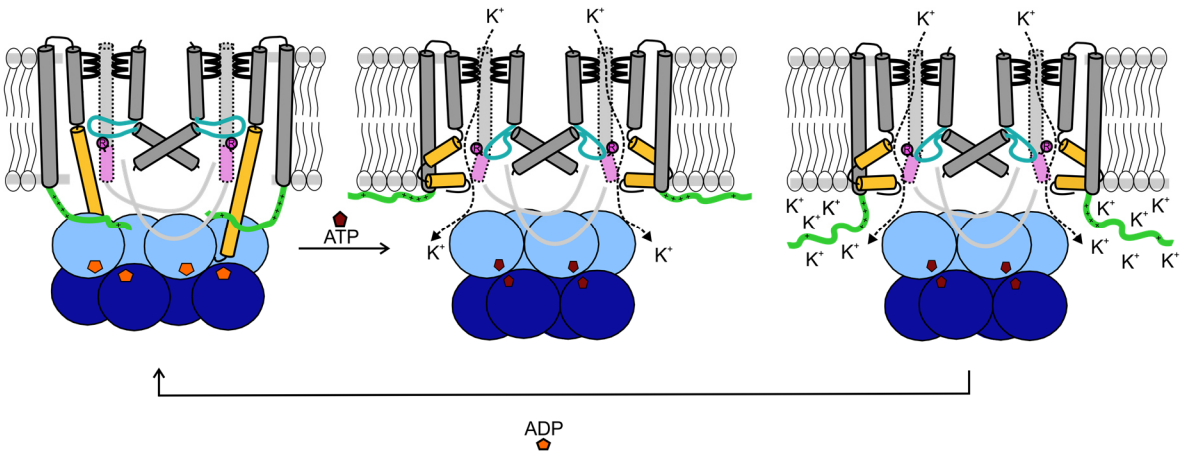

Figure 44: Suggested gating mechanism of the KtrAB complex. Cartoon representing an allosteric network in which the interaction of KtrBs' N termini with the membrane, together with ATP- and Mg^{2+}-triggered conformational changes within KtrA, induce the activation of the KtrAB system. In the ADP-bound conformation (left, ADP in orange), the RCK domain adopts an oval-shape conformation (blue) and the D1M2 helices are extended (yellow), reaching into the KtrA ring. The N termini of KtrB (green) lie flat on the KtrA ring and the intramembrane loop (turquoise) blocks potassium flux. Upon activation, the N termini relocate towards the membrane, establishing electrostatic contacts with the negatively charged phospholipid headgroups via a number of positive charges. This induces conformational rearrangements in KtrB (grey): The D1M2 helices break (yellow) and helices D4M2 containing R427 (pink) relocate away from the pore. In KtrA, ADP is replaced by ATP (dark red) and Mg^{2+}, resulting in a square-shaped KtrA ring. Consequently, potassium uptake increases the intracellular positive charge, which locally shields the negatively charged membrane surface, leading to release of the N termini. This is the first step of restoring the inactive, ADP-bound conformation to avoid the K^+ mediated cytotoxic processes of unhindered uptake.

Activation of the system occurs as a consequence of cellular changes upon osmotic stress, including changes in ionic strength, ΔpH, lipid composition, membrane potential and turgor pressure, as well as the intracellular ATP concentration. I suggest that in this process, an allosteric network triggers channel opening: On the one hand, the increased ATP concentration allows the exchange of few ADP molecules for ATP, which in consequence destabilises the KtrA ring, as was observed in the DSF measurements (cf. 5.2.3.3). This instability of the ring, on the other hand, likely affects the whole KtrAB complex, including the extended helices and KtrBs' N termini. The rearrangements of the octameric ring might displace the N termini from their position on KtrA, possibly by interacting with their cluster of positively charged residues with the negatively charged headgroups of the lipid membrane. This suggestion is supported by preliminary MD simulations showing the preferred orientation of the N termini towards the membrane (cf. 5.2.5). In vivo, this displacement might be supported by the hyperpolarisation, increased ionic strength and/or

excess of anionic membrane lipids, which is in line with the ΔΨ-dependent activation observed for KtrAB (Kröning et al, 2007). As a consequence of the reorientation, the N termini actively pull on the transmembrane helices of KtrB, especially the D1M1 helices to which they are connected. This possibly induces destabilisation and small conformational changes of the extended D1M2 helices, which unleashes the KtrA ring, allowing the exchange of all remaining ADP to ATP in a competitive manner. This exchange likely induces the adoption of the square-shaped conformation of the KtrA ring, which entirely displaces the extended helices. Whether the extended helices break and form a helical hairpin or just reorient within the membrane plane, as suggested by M. Schrecker (2018), remains under debate and was not focus of this work. However, an overlay of *Va*KtrB in the ADP-bound conformation and *Bs*KtrA in the ATP-bound state revealed that the extended helices of KtrB are incompatible with the ATP-bound, square-shaped KtrA ring due to steric hindrance. This shows that the conformational changes of the RCK and channel subunits need to be strictly synchronised and that a reorientation of the extended helices is required to allow conformational changes within KtrA or vice versa (Diskowski et al, 2017). The complete rearrangement of the D1M2 helices into the broken helices or a relocation within the membrane plane unlock the intramembrane loop, thus opening the steric gating component. Conformational changes of the D4M2b helix likewise reorient the conserved R427 from the pore, removing the electrostatic barrier. Together, these concerted conformational changes result in an open pore, allowing potassium flux. This hypothesis is supported by the performed EPR measurements, as they have shown, that both the lipid environment and the presence of the N termini are required to induce a conformational flexibility of the intramembrane loop in the presence of ATP (cf. 5.2.6).

As an alternative, it can be speculated that the N termini of KtrB continuously interact with the membrane, and the gating is mainly controlled by the competitive exchange of ADP and ATP in KtrA. The interaction of the N termini with the membrane, however, is mandatory to allosterically induce conformational changes in KtrB, which in consequence unblocks the pore for K^+ translocation as indicated by the EPR data. In this case, the observed position of the N termini in the cryo-EM structure would be artificial, as the required membrane surface was missing in the detergent-solubilised sample. The rest of the described regulatory mechanism could be comparable and for both possibilities, the KtrA ring plays an essential role in the regulation of gating. This is emphasised by DEER experiments comparing the conformational flexibility of the intramembrane loop of the KtrAB complex and KtrB only, which showed a defined conformation of the intramembrane loop only in the presence of KtrA (Diskowski et al, 2017). It can be speculated, that the C termini of KtrB play an important role for these observations. As they are described to form the lateral contact between KtrA and KtrB, slight rearrangement upon structural changes in KtrA could induce the destabilisation of the salt bridge with K325 of the neighbouring subunit or reorient the loop into the open state by pulling or pushing on the salt bridge.

Opening of KtrAB results in an increase of the intracellular potassium concentration, under specific conditions up to molar concentrations (Epstein, 1986), which is why a rapid inactivation is important to prevent excessive ion flux. I hypothesise that this influx of positive charges shields the negative membrane surface, releasing the N termini from the membrane as an initial step of channel inactivation. Within the KtrA ring, ATP is replaced by ADP as the ATP concentration drops, which consequently leads to the oval-shaped conformation, so that the D1M2 helices can extend and re-establish the interactions with KtrA. The N termini interact with KtrA ring via their hydrophobic patches and the positive residues. Thereby, the intramembrane loop is again locked in the closed conformation, obstructing the pore together with the positive gating arginine to finally achieve the energetically preferred inactive conformation.

6.2 Interaction of KtrB's N terminus with the membrane

As an integral membrane protein, KtrB is embedded in the lipidic bilayer and therefore surrounded by a shell of lipid molecules. Accordingly, the lipid composition and distribution can have a major effect on the regulation of the channel. Membranes of most bacteria predominantly consist of phosphatidylethanolamine (PE), phosphatidylglycerol (PG) and cardiolipin (CL) (Romantsov, 2017), but their ratios vary widely. In many species, the proportion of anionic phospholipid (PG and CL) increases in high salinity, at the expense of zwitterionic phospholipids (PE), indicating that the increase in negatively charged lipids could play an important role in the adaptation to osmotic stress (Romantsov et al, 2009). For many membrane proteins, it has been shown that an interaction with the membrane affects the activity of the protein. This can occur by different mechanisms: Proteins can either be affected by binding of lipids specific sites or by general physiological membrane properties like thickness, lateral pressure, fluidity, or surface charges. The latter is observed for example for osmoregulatory transporters like the glycine betaine (GB)-translocating ABC (ATP-binding cassette) transporter OpuA from *Lactococcus lactis* (Biemans-Oldehinkel et al, 2006; Sikkema et al, 2020), the Na^+/GB symporter BetP from *Corynebacterium glutamicum* (Ochrombel et al, 2011; Rübenhagen et al, 2000) and the H^+/proline symporter ProP from *Escherichia coli (*Culham et al, 2018; Romantsov et al, 2007) as summarised in the introduction. These are well studied systems, all of which are responsible for uptake of compatible solutes as a second response to hyperosmotic stress. In OpuA, for example, a C-terminal domain called CBS (Cystathionine β-Synthase), which is fused to the NBDs (nucleotide binding domains), has been described to interact with the anionic membrane surface directly or indirectly, and upon high ionic strength rearrangements of the CBS domains are transmitted to the NBDs of the protein, thereby affecting the translocation activity (Karasawa et al, 2011). Recently it was shown that, in addition to the CBS domain, a series of positively charged residues in a helix-turn-helix

(HTH) motif of the NBD, which are only conserved within osmoregulatory homologues, are positioned in close proximity to the membrane. Here, they interact with the negatively charged lipids, forming a sensor for ionic strength to regulate the activity of the transporter. The increase in intracellular ionic strength weakens the interaction of the cationic HTH motif with the membrane, leading to the activation of OpuA (Sikkema et al, 2020). In this mechanism, the threshold of activation strongly depends on the fraction of anionic lipids in the surrounding membrane environment. The transmission of the osmotic signals to the protein via an interaction between charged residues of an osmosensor domain and the negatively charged headgroups of membrane lipids is similar to the suggested mechanism for the regulation of KtrAB. Since KtrAB is responsible for the initial and rapid adaption to hyperosmotic stress, the system is deactivated when the compatible solute transporters are activated, necessitating an inverse regulation. Here, the identified N termini appear to interact with the lipid environment during the activation of the system. It appears plausible that both processes are mediated by sensing of the ionic strength and the interaction with the surrounding lipids. However, KtrAB requires an interaction of the N terminus with the membrane for the activation, which occurs at low ionic strength, while the interaction between the lipids and the osmosensors are weakened for the activation of the osmolyte transporters, which occurs by charge shielding at high ionic strength, hence when KtrAB is inactivated. In vitro liposome-based potassium flux assays showed that an increased fraction of CL within liposomes led to an increased activity of reconstituted KtrB from *V. alginolyticus*. This indicates that CL influences the activity of KtrB, most likely by increasing the negative charge on the membrane surface, which agrees well with the proposed function of the N terminus in the KtrAB gating mechanism. In line with this, the whole-cell K^+ uptake assays performed within this thesis revealed, that especially the positively charged residues of KtrBs' N termini are required to maintain channel activity, which appears to be dependent on an interaction with the membrane. Interestingly, not only the presence, but also the position of the basic residue cluster seems to be critical, as a repositioning of the residues within the N terminus did not recover channel activity, shown by similarly decreased uptake velocities in whole-cell K^+ uptake experiments (Ohlemüller, 2021). I suggest that the close proximity of the positively charged residues to the TM helices is required to generate an immediate pulling force, which is otherwise not strong enough to relocate the helices of KtrB.

The anionic phospholipid CL has often been observed to be involved in the regulation of membrane proteins, which are implemented in osmotic stress response. In many bacteria, the CL concentration in the membrane increases upon osmotic stress. This increase in CL can have significant regulatory effects on membrane proteins. For example, ProP was shown to co-localise with CL at the cell poles and it was demonstrated that an interaction of a C-terminal domain with the CL-enriched membrane is required for protein activation (Romantsov et al, 2007). However, for KtrB from *B. subtilis*, microscopy experiments

analysing the localisation of the channel depending on the lipid composition in vivo revealed that the channel is homogenously distributed within the membrane, independent of the membrane composition. This excludes the co-localisation with specific lipid domains (cf. 5.1.1).

In addition to these general effects of membrane physiology, the phospholipid CL has been described to play a regulatory role as a specific ligand for several membrane proteins in *E. coli*, including the ammonium transporter AmtB, the translocon SecYEG or the leucine transporter LeuT (Corey et al, 2018; Gupta et al, 2017; Patrick et al, 2018). Recently, it was also shown that CL binds to the potassium transporter KdpFABC from *E. coli* with high-affinity, stimulating ATPase activity (Silberberg et al, 2021). More generally, binding sites for CL in the TM domains of these proteins were described to be characterised by following features: Several basic residues are located in close proximity, a glycine residue is present in the same plane as well as aromatic amino acids like phenylalanine (Corey et al, 2021). Although KtrB's N terminus formally contains these elements, a specific binding of CL does not seem to be the case in KtrAB. Instead, the protein-lipid interplay is rather mediated by non-specific, electrostatic interactions. The best-resolved cryo-EM density map at 2.5 Å resolution contains several additional non-protein densities in the inner and outer leaflet of KtrB. However, all identified densities were assigned to DDM molecules, as each density shows only one tail, while for phospholipids two acyl chains would be expected (Figure 45). Especially cardiolipin molecules were excluded, as four hydrocarbon tails would have been easily identified at the present resolution of 2.5 Å.

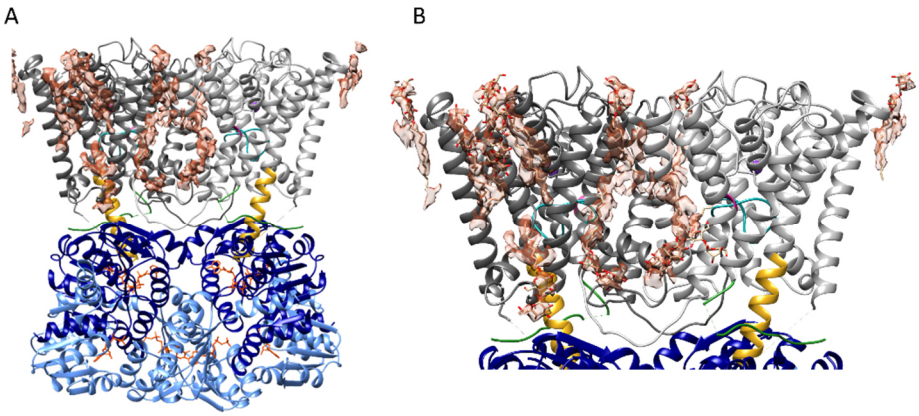

Figure 45: Addititonal non-protein densities were obtained within the cryo-EM density map of KtrAB. A) Densities in the inner and outer leaflet of KtrB were assigned to detergent molecules. B) Zoom-in of KtrB and overlay of densities and DDM molecules. No direct lipid-protein interaction was identified.

To structurally resolve the proposed membrane interactions of KtrAB a lipid surface surrounding the protein in cryo-EM samples will be required. To achieve this, first steps towards the reconstitution of KtrAB in nanodiscs were established (cf. 5.2.7.2). In addition to providing a platform to observe the proposed gating mechanism, this approach has the advantage of providing more physiological membrane properties. This has led to breakthroughs in systems, which are dependent on specific membrane attributes. For example, the bacterial mechanosensitive channels MscS and MscL, which are involved in the adaption to hypoosmotic stress, sense mechanical forces in cell membranes, and are regulated by the membrane tension (Levina et al, 1999). Recently, the complete conformational cycle of MscS in different lipid environments was structurally elucidated by reconstitution of the protein into nanodiscs. Mimicking membrane tension in combination with different lipid compositions illuminated the critical role of bound lipids (Zhang et al, 2021). Similarly, nanodiscs of different sizes and with varied lipid compositions would be helpful to understand the role of lipids and a membrane-like environment on the conformational rearrangements in KtrAB during activation and deactivation of the system. Unfortunately, first trials revealed that the MSPs are tightly wrapped around the transmembrane domain, not allowing for a significant lipid surface surrounding the protein. However, this tightness of the MSPs seems to be a general observation, independent of the predicted size of the nanodiscs, as it has as well been observed for other membrane proteins like Glt_{TK} (Arkhipova et al, 2020). As it is suggested that the N terminus electrostatically interacts with the membrane surface to induce conformational rearrangements in KtrB, the nanodiscs might not have provided enough space to allow the conformational change. With varied MSP to lipid ratios, it should be tested, whether larger nanodiscs can be generated. In case this is unsuccessful, lipid bicelles should be tested, as they form larger particles with a diameter of 20-50 nm (Dufourc, 2021). If yet the active-state cannot be achieved, cryo-electron tomography using KtrAB reconstituted in liposomes should be considered for further structural investigations, as the nucleotide-dependent conformational changes not yet observed in cryo-EM were visible in EPR for liposome-reconstituted KtrAB (cf. 5.2.6).

6.3 Possible role of KtrB's N terminus in channel inactivation

Just as important as the activation of a K^+ channel is its inactivation, as unhindered K^+ flux would induce K^+-mediated cytotoxic processes. While for KtrAB it is suggested that inactivation is mainly facilitated by the exchange of ATP for ADP in KtrA, for other systems it has been shown that they can be rapidly desensitised while the stimuli for channel opening are still present. As the inactivation by RCK domains seems to be rather slow (110 seconds for the recovery from the active to the inactive state in MthK (Kuo et al, 2007)), an additional fast inhibitory mechanism within milliseconds to seconds (Kuo et al,

2008; Xu & McDermott, 2019) appears to be necessary, as otherwise a cell would massively depolarise at an ion flux of around 10^7-10^8 ions per second, ultimately leading to cell death (Stautz et al, 2021).

Here, two distinct mechanisms have been described for the inactivation of several K^+ channels: The N-type inactivation is a fast, autoinhibitory process, where an N-terminal peptide binds to the pore, blocking ion flux. In contrast, in a C-type inactivation, the flux of ions is hindered by conformational changes blocking the selectivity filter (Hoshi & Armstrong, 2013; Kurata & Fedida, 2006). Neither of the two mechanisms has been described for KtrAB so far, however it is plausible that a rapid inactivation for the fast ion flux through KtrAB is required, to rapidly control K^+ uptake to avoid large effects on the membrane potential and cell function. I suggest that KtrB's N terminus, which apparently is crucial for activation of KtrAB, could also be involved in the rapid inactivation of the channel, which would expand the working hypothesis for KtrAB regulation by one additional step (Figure 46). Upon an increase of the internal K^+ concentration by its uptake through open KtrAB, the negative charge of the membrane is shielded, resulting in the repulsion of the N termini from the lipid surface. As a consequence, the N termini relocate, but instead of binding to the KtrA-KtrB interface, as described above, one further possibility is that the N termini intrude into the pores of the KtrB dimer and interact by their hydrophobic patches with the pore. Similar as described for MthK, these interactions would induce a desensitised state of the channel by sterically blocking the translocation pathway. In this model, the N termini would serve a double regulatory role as an osmosensor: At low ionic strength, they interact with the membrane and allows the activation of the channel together with Mg^{2+}-ATP binding to the RCK ring, while at high ionic strength, they could induce an N-type inactivation by plugging the pore upon their release from the membrane. The relocation of the N-terminal peptide into the pore could trigger the exchange of ATP for ADP in the RCK ring, allowing the restoration of energetically preferred inactive state. Although this theory sounds plausible, no experimental proof is available so far. Future experiments, including single channel recordings in a black lipid membrane (BLM) setup, could validate this hypothesis.

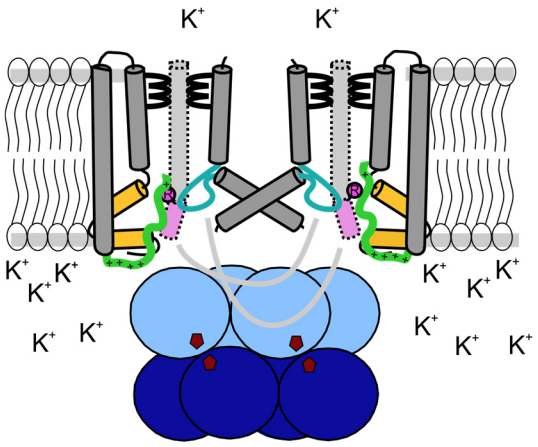

Figure 46: Hypothesised N-type inactivation of KtrAB by the N termini of KtrB. After K^+ flux is enabled by the activation of KtrAB, the increasing internal K^+ concentration locally shields the negative charge of the membrane, inducing repulsion of the N termini, as described in Figure 44. To rapidly inactivate the channel, the N terminus could reorient into the pore, blocking further K^+ uptake, similar to the N-type inactivation observed for other K^+ channels. This restructuring could induce ADP binding in the RCK ring, and the resulting conformational changes required to restore the closed, inactive conformation.

6.4 Conservation of KtrBs' N termini within KtrAB homologues

Whether the proposed gating mechanism, especially the role of the N termini, is specific for KtrAB from Gram-negative organisms like *V. alginolyticus* or a common mechanism for all KtrAB homologues is yet unclear. Using the PROMALS3D server, a tool for multiple sequence and structure alignment, the length of the unstructured N termini from different organisms was identified, by determining the beginning of the first N terminal helices (Figure 47). Comparing the sequence of KtrBs' N termini from Gram-positive and Gram-negative bacteria, revealed that it is not highly conserved. A particularly significant difference was observed in the length of the N terminal peptide. Here, most Gram-positive bacteria possess a shorter N terminus compared to Gram-negative bacteria.

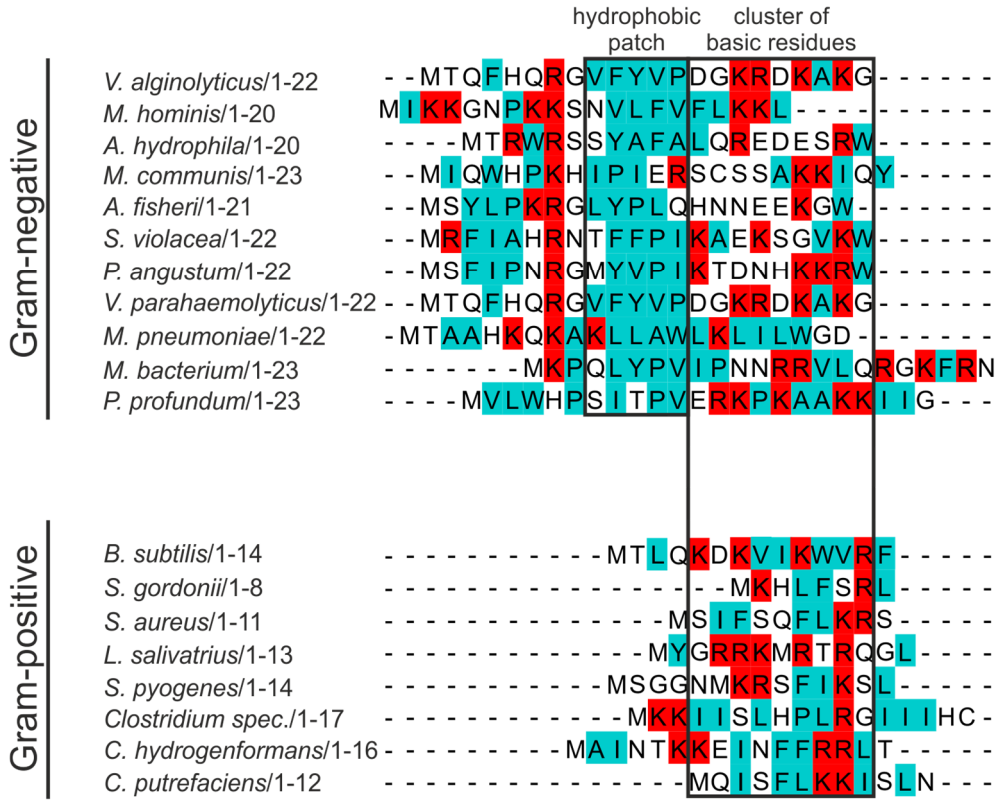

Figure 47: Sequence alignments of KtrB N termini from Gram-positive and Gram-negative bacteria. The extent of the unstructured N termini in each homologue was determined using the PROMALS3D server, a tool for multiple sequence and structure alignment, by identifying the beginning of the first TM helix. The alignment was performed with Clustal Omega and adjusted with Jalview. Basic residues are highlighted in red, while hydrophobic residues are indicated in turquoise. The conserved hydrophobic patch of Gram-negative bacteria and the conserved cluster of basic residues of Gram-negative and Gram-positive bacteria are highlighted by a black box. Amino acid sequences from following species are shown: Gram-negative: *Vibrio alginolyticus*, *Mycoplasma hominis*, *Aeromonas hydrophila* , *Marinomonas communis*, *Aliivibrio fisheri*, *Shewanella violacea*, *Photobacterium angustum*, *Vibrio parahaemolyticus*, *Mycoplasma pneumoniae*, *Methylococcaceae bacterium*, *Photobacterium profundum*. Gram-positive: *Bacillus subtilis*, *Streptococcus gordonii*, *Staphylococcus aureus*, *Lactobacillus salivarius*, *Streptococcus pyogenes*, *Clostridium spec.*, *Carboxydothermus hydrogenoformans*, *Clostridium putrefaciens*.

Besides the different lengths of the N termini, the alignment shows that all species contain several positively charged amino acids just prior to the start of the first TM helix, as well as earlier in the N terminus. This suggests a possible conservation of the proposed role of the N terminus. Interestingly, R7 (*V. alginolyticus*), which has been described to form a salt bridge with KtrA, is conserved as a positive amino acid within most of Gram-negative bacteria. In general, positively charged residues at the N terminus of membrane proteins are a widespread universal pattern with various functions, including correct membrane insertion according to the positive-inside rule (von Heijne, 1989). However, it is not excluded that these residues fulfil additional functions in KtrAB. In fact, the whole-cell uptake experiments performed within this thesis (cf. 5.2.4.3) revealed that at least for KtrAB from *V. alginolyticus* the positive residues play a crucial role in the activation of the system, as the uptake velocity is drastically reduced upon their neutralisation. Since neither the mutation of the positively charged cluster nor of the conserved R7 individually abolishes the activity as much as the deletion of the complete N terminus, a synergic effect of all residues is suggested. Interestingly, the hydrophobic patch, which seemed to be less important for KtrAB activation, is conserved within most of the Gram-negative but not Gram-positive bacteria. It is possible that the hydrophobic patch is important to reacquire the inactive, ADP-bound state by interacting with the oval-shaped KtrA ring or the pores of KtrB. In Gram-positive bacteria the inactivation of KtrAB is not only achieved by ADP binding but also by the binding of cyclic di- AMP to the C lobes of the gating ring (Corrigan et al, 2013). Most Gram-negative bacteria do not synthesise c-di-AMP, and it remains elusive whether another cyclic nucleotide or a comparable ligand binds to the C lobes of KtrA from *V. alginolyticus*. Therefore, a varied mechanism for Gram-positive and Gram-negative bacteria could be plausible. However, as the positively charged residues are conserved within all shown bacteria, it is likely that the activation of the KtrAB systems from Gram-positive bacteria also depend on the interaction of the N termini with the membrane.

6.5 New insights into KtrAB gating by nucleotide binding to the N lobes of the RCK ring

While the crucial role of KtrBs' N termini in the regulation of KtrAB was observed for the first time in this thesis, the effect of nucleotide binding to the KtrA ring has already been known for a long time (Albright et al, 2006). Previously published data on the affinity of the nucleotides towards KtrAB indicated a slight preference for ATP over ADP (Diskowski et al, 2017; Kröning et al, 2007). In this thesis, similar affinities for both nucleotides towards the KtrA ring were observed, albeit showing a small preference for ADP. Physiologically, a similar affinity for both nucleotides would probably lead to a permanently open ion channel, as the cytosolic ATP concentration in most bacteria is around 5 to 10 times higher compared to ADP (1.5 mM - 3 mM ATP vs. 400 µM ADP), and this disparity increases even further in the first 10 minutes of hyperosmotic stress by *de novo* ATP synthesis (Bennett et al, 2009; Jensen et al, 1999; Kashket, 1982; Ohwada & Sagisaka, 1987). Unhindered K^+ influx through a constantly open channel, however, would induce cytotoxic processes that would kill the cell. Therefore, it appears that nucleotide binding needs to be controlled by an additional factor. A recent study on the activation of KtrAB from *B. subtilis* revealed that Mg^{2+} is required to stabilise the ATP-bound, square-shaped conformation by coordinating the γ-phosphates of ATP in KtrA. This was confirmed by negative staining EM data on the isolated KtrA gating ring by Schrecker (2018) and within this thesis, where only in the presence of Mg^{2+} and ATP the square-shaped conformation of KtrA from *V. alginolyticus* was induced. In all cryo-EM approaches of KtrAB within this study, both $MgCl_2$ and ATP were supplied to the sample. However, this did not allow binding of ATP to the KtrAB complex. Rather, ADP was bound in all structures, which remained in the inactive conformation, although ADP was never added to any sample. Thin layer chromatography confirmed that ADP was co-purified together with KtrAB and it appeared that it could not be exchanged in the cryo-EM samples. To be precise, it is not clear if all binding sites in the complex were occupied or bound to ADP, it is in fact possible that already partial binding of ADP results in the oval-shaped conformation. As cryo-EM analysis generates an average map from a large dataset, it is possible that a partial, randomly distributed occupancy of binding sites in the KtrA ring by ADP leads to a density suggesting that all binding sites are occupied. Particularly if, on average, more ADP is bound than ATP, individual ATP-bound sites do not become visible in the density map.

To gain insights in how nucleotides can be exchanged, experiments to analyse the binding behaviour of ATP and ADP were performed on the isolated KtrA ring. Although ADP seems to be tightly pre-bound, the DSF competition experiments and SPA showed that the nucleotides bound to the isolated KtrA ring can be exchanged (cf. 5.2.3.2 and 5.2.3.3). In detail, DSF measurements of KtrA pre-incubated with saturating concentrations of either ADP or ATP revealed, that upon addition of the competing nucleotide the observed melting

temperature could be shifted toward the melting temperatures of the competitor. This means, while the stability of the KtrA-ADP sample decreased after addition of ATP, the melting temperature of KtrA-ATP increased after addition of ADP, indicating an at least partial exchange. Already a concentration of 50 µM ADP significantly increased the melting temperature, even though the protein was pre-incubated with a ten-fold higher ATP concentration (cf. 5.2.3.3). This indicates, that compared to ATP, the binding of ADP, even if only partial, could induce a much more stable KtrA ring, most likely stabilised in the oval-shaped conformation. This is in line with the assumption that the ADP-bound state is the most stable conformation. By increasing the ADP concentrations, the oval-shaped KtrA ring seemed to be further stabilised, as higher melting temperatures were determined. Furthermore, SPA measurements revealed that ADP binding seemed to be preferred over ATP binding, as the IC_{50} values for ADP were 50% lower than the IC_{50} values determined for ATP (cf. 5.2.3.2).

In contrast, when outcompeting ADP with ATP, the opposite was observed: For KtrA pre-incubated with 10 µM ADP (two-fold excess compared to KtrA monomer), the KtrA ring is expected to be present in the stable oval-shaped conformation as highlighted above. Upon addition of 100 µM ATP a reduction of the melting temperature is induced, indicating a decreased stability of the KtrA ring. Here, the observed destabilisation could have different reasons: 1) In the presence of both nucleotides, partial exchange of ADP by ATP could induce partial conformational changes within the respective KtrA dimers in an unconcerted fashion, causing a distortion of the ring, which is neither adopting the oval-shaped nor the square-shaped conformation. 2) Binding of ATP to several binding sites in the KtrA ring does already induce a concerted switch to the square-shaped conformation, which in general is less stable, as observed in the DSF measurements. Upon occupancy of all binding sites the square-shaped KtrA ring is further stabilised as reflected by the increasing melting temperatures upon increasing ATP concentrations. 3) Partial binding of ATP to the KtrA ring does not induce conformational changes but causes a relocation of the negative charges from the β- to the γ- phosphates in the subunits which have ATP bound. Here, the oval-shaped conformation would be retained until all binding sites are occupied by ATP, as only allosteric binding of ATP to all subunits triggers the adaptation of the square-shaped conformation. While among all available crystal structures none of the KtrA rings have been solved in the mixed state as suggested in scenario 1, crystal structures of the isolated *Bs*KtrA rings supporting scenario 3 are available (i.e. PDB: 2HMU) (Albright et al, 2006; Teixeira-Duarte et al, 2019). Here, the KtrA rings have been solved in the oval-shaped conformation but with ATP bound. In these structures, the shape of the KtrA ring and the coordination of the bound ATP are identical to the KtrA ring obtained in the 2.5 Å resolution structure of the ADP-bound KtrAB complex presented in this thesis, leaving the γ-phosphates uncoordinated (Figure 48). This indicates that this arrangement can exist. However, the DSF measurements suggest, that the ring is less stable compared to both,

the ADP-bound, oval-shaped ring, and the square-shaped, ATP-bound ring. This third possibility would be in agreement with the hypothesised adapted gating mechanism (cf. 6.1).

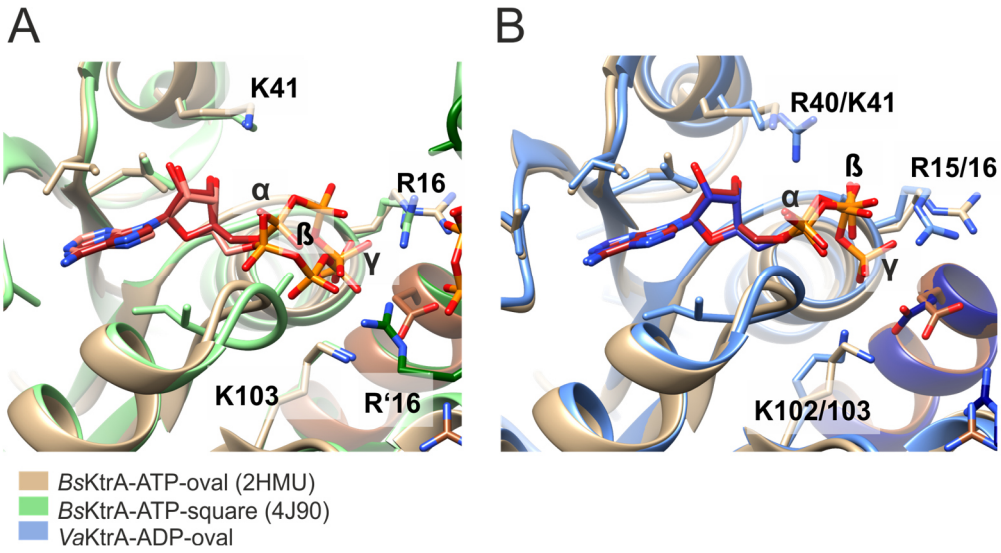

Figure 48 Coordination of ADP/ATP in the KtrA ring. Available structures of the KtrA ring reveal that an oval-shaped KtrA ring can bind ADP as well as ATP. A) An overlay of the nucleotide binding site from an oval-shaped *Bs*KtrA ring with ATP (light/dark brown, PDB: 2HMU) and square-shaped, ATP-bound KtrA ring (light/dark green, PDB: 4J90). In the square-shaped conformation, the R'16 of the neighbouring subunit is involved in the ATP coordination, while in the oval-shaped conformation the ATP is only coordinated within its own subunit. B) By comparison of the oval-shaped, ADP-bound KtrA ring of the *Va*KtrAB structure obtained in this thesis with the oval-shape isolated KtrA ring from *B. subtilis* with ATP-bound (light/dark blue), it was identified that both nucleotides are similarly coordinated.

To investigate which of the above-mentioned scenarios is more likely, additional DSF measurements should be performed. Here, KtrA, pre-incubated with saturating ADP concentrations, should be used for competition with ATP in lower concentrations than used so far. If partial binding does not induce conformational changes, the melting temperature should decrease stepwise by increasing ATP concentrations, as more and more sites would get occupied by ATP, resulting in the delocalisation of the negative charges. Only the occupancy of all sites with ATP would result in the adoption of the square-shaped conformation, consequently increasing the melting temperature. In contrast, if ATP binding to only few binding sites induces the square-shaped conformation, changes in the melting temperature are only expected at a specific ATP concentration.

It is, however, important to emphasise that all binding studies and previously published structures are based on the isolated KtrA ring. Even the available structure of the ATP-bound KtrAB complex from *B. subtilis* was prepared by assembling individually isolated KtrB with KtrA that was previously bound to ATP. Thus, it cannot be excluded that the obtained KtrAB-ATP conformation is an artificial assembly, as KtrB was missing, while the binding sites in the RCK ring were saturated with ATP. Thus, taken together, all results suggest that the binding or exchange of ADP and ATP, and the corresponding

conformational changes, are possible in the isolated KtrA ring, while the binding of nucleotides in the assembled KtrAB complex appears to be more complex and requires an additional trigger. One possible trigger is the conformational change of the KtrB N terminus, as described in the hypothesised gating mechanism. In addition, although there is no direct interaction of the extended helices with the nucleotide, a displacement of the helices might be required to change the microenvironment of the binding site, allowing the binding of ATP. Unfortunately, the available data does not fully resolve the remaining questions about nucleotide binding in the KtrAB complex but does reinforce the notion that an allosteric network is required to enable ATP binding, explaining why the exchange of ADP to ATP in cryo-EM approaches was unsuccessful so far.

6.6 Features of KtrAB gating are shared among potassium channels

Allosteric networks including ligand binding and conformational rearrangements in a regulatory domain as well as in the transmembrane domain, to obtain fully active and fully inactive states, have been observed for many other K^+ channels and show a number of parallels to the proposed mechanism for KtrAB. For MthK, several structures of the Ca^{2+}-bound active state and one distinct closed conformation were determined in nanodiscs, illuminating the full Ca^{2+}-mediated gating cycle (Fan et al, 2020). In the closed state, the octameric RCK ring adopts a four-fold symmetric arrangement, and the pore is blocked. MD simulations of the protein in this state revealed a dynamic rocking of the entire gating ring, showing interactions of the RCK domains with the surrounding membrane. The rigid body tumbling is enabled by a flexible C-linker (residue 115-117), which connects transmembrane helix 2 (TM2) and the RCK domain. Interestingly, the linker lies flat on the N lobe of the RCK domain, interacting via several hydrophobic interactions and possible salt bridges (Figure 49). This arrangement is strongly reminiscent of the conformation observed for the N terminus of KtrB. MD simulations revealed an alternating interaction of the C-linker with the N lobe and the phospholipid headgroups of the membrane, similar to the membrane interactions suggested for the N termini of KtrBs. Like the KtrB N terminus, the MthK C-linker contains several positive residues (K105, K114, R116), which could interact with the phospholipid headgroups. Even at inactive conditions, the interaction of MthK's C-linker with the membrane induces a displacement of the adjacent TM2, which results in an increase of the lower pore radius. Although the channel remains closed, the rearrangements in this region hint at the conformational changes that the system undergoes during activation. Multiple cryo-EM structures of the Ca^{2+}-bound, active states show strongly tilted gating rings with respect to the membrane plane, suggesting a high flexibility upon binding of Ca^{2+}. The movement induces a loss of the four-fold symmetry of the RCK ring by a slight shift at the four dimer-to-dimer interfaces. The large tilts and the resulting conformational changes of the RCK domains pull at the C-linker, which, in

consequence, detaches from the N lobe. This leads to a reorientation of the adjacent helix, pulling the helical bundle open, allowing the opening of the pore. Unfortunately, the majority of the active Ca^{2+}-bound structures do not resolve the C-linker, not allowing a detailed structural analysis of its conformational changes upon activation. Although the C-linker and the N termini share several parallels, it seems that the conformational changes in KtrA upon binding of ATP and ADP depend on the relocation of the N termini towards the membrane, which in consequence induces changes in KtrB resulting in an open pore. However, as the N termini of KtrB and KtrA are not tethered, it is plausible that the activation mechanism of KtrAB varies compared to MthK.

The inactivation of MthK, in addition to Ca^{2+} release from the RCK domains, involves steric blocking of the translocation pathway by a strong density inside the pore. This density was assigned to the first 17 residues of the N terminal peptide, which are connected to TM1. It has been shown that, after activation of the channel, the N terminus refolds into the pore, thus inducing rapid inactivation. This avoids excessive uptake of K^+. A similar mechanism could exist for KtrAB by N-type inactivation as suggested above (cf. 6.3).

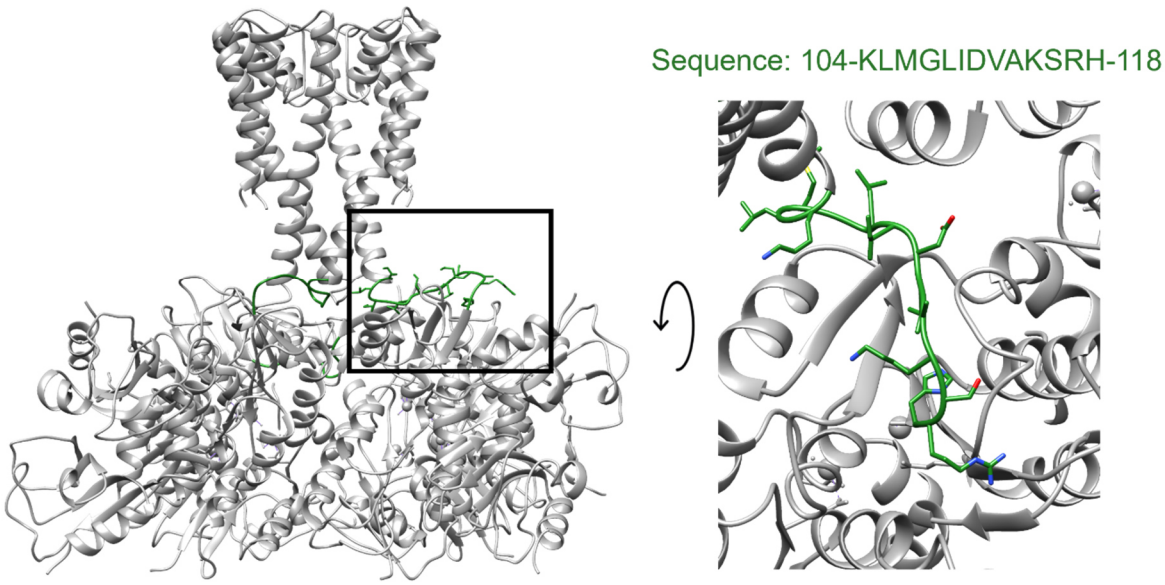

Figure 49: Structure of closed MthK K^+ channel (PDB 6U5R). The flexible C-linker (green), which connects the TM domain with the RCK domain, lies flat on the N lobe of the RCK domain, associated via hydrophobic interactions and salt bridges. Upon movement of the RCK domains, the interaction of the C-linker alternates between the N lobe and the membrane surface.

A further example of a K^+ channel, for which an allosteric network of interactions and conformational changes is required to achieve full activation and inactivation, is the bacterial uptake system TrkAH, a homologue of KtrAB. In general, the system has a similar architecture to KtrAB. However, the organisation of the RCK ring and the interaction surface between the RCK domains and the TrkH dimer differs from KtrAB. The RCK ring consists of different RCK1 and RCK2 domains, which have slightly varied binding sites for ADP and ATP. This allows ATP to bind in both subunits, while ADP only binds to the N lobes of RCK2 domains. Upon activation and binding of ATP to all N lobes, the tetrameric ring is split in two dimers. This in consequence disrupts the interface between TrkA and TrkH, pulling on the D3M2b helix and thus relocates the intramembrane loop, which in consequence opens the pore for K^+ translocation (Zhang, et al. 2020). This shows that ligand binding induces large conformational changes of the RCK domain, which in turn exert a pulling force on the transmembrane helices to finally open the pore. Similary large conformational changes have been observed for KtrC, a homologue of KtrA, for which different oligomeric states have been described. Here, the ADP-bound state shows an octameric state similar to KtrA, while, in the presence of ATP, the octameric ring is disrupted, forming different oligomeric species, most likely tetramers with a similar assembly to the split TrkA RCK ring (Rocha et al, 2019). Such large conformational changes, particularly including disruptions or changes in the oligomeric state of the RCK ring, are so far not known for KtrA. On the contrary, all available KtrA structures from *B. subtilis* in the presence of ADP and ATP, respectively, indicate an octameric assembly. In line with this, the 2D classes of negatively stained KtrA from *V. alginolyticus* show exclusively octameric rings, with the largest conformational change being the switch between the square-shaped and oval-shaped states depending on the nucleotide added.

Altogether, the highlighted mechanisms clearly show, that ligand binding to the regulatory gating rings is not sufficient to trigger the activation of the channels. Rather, all systems, including KtrAB, require an allosteric network for the transmission between open and closed states.

6.7 Outlook

So far, the regulation of KtrAB was described to occur upon conformational changes within the KtrA RCK ring by binding of either ADP or ATP. However, it appears that the ADP/ATP binding model is insufficient, and an additional trigger is needed to transmit the signal to the pore region. In this thesis, the N termini of the KtrB dimer were shown to be involved in an unforeseen allosteric network, which is required to achieve the activated, conductive state of the KtrAB channel. This newly suggested mechanism (Figure 44) is based on the structural data in combination with functional and EPR data presented in this work. I propose an interaction of the N termini with the membrane, which in consequence leads to rearrangements in the system, finally resulting in an open pore. However, I do neither have a direct proof for the protein-lipid interaction, nor data on how exactly the N termini interact with the lipid environment. To achieve those data, the N terminal peptide (amino acids 1-21) and variants of it could be synthesised, purified and used in biochemical as well as biophysical experiments. Several experimental techniques have been developed in the last decades, with the aim to understand binding, location, and orientation of a peptide relative to a lipid bilayer, including ITC, EPR, NMR and MD simulations. (Galdiero et al, 2013). Binding properties for different variants of the N-terminal peptide towards liposomes can be determined using ITC. Reducing the number of positive charges, increasing the ionic strength, or rising the negative charges of lipids in liposomes could provide insights into the stimuli that trigger an interaction of the N termini with the membrane. To understand the detailed interaction between the N termini and the lipid bilayer, solid-state NMR should be considered. For this, either phospholipids or peptides can be labelled with NMR-active nuclei. ^{31}P or ^{2}H labelling of lipids can provide insights into the response of lipids when they interact with peptides. Specific labelling of peptides with ^{2}H-, ^{13}C-, or ^{15}N-labels could give direct information about the peptide conformation, orientation, and mobility in the presence of a membrane (Strandberg, 2018). To provide further detailed information at a molecular level, MD simulations in the presence of KtrA should be performed to analyse the localisation of the N termini, as here the N termini could still establish the contacts in the KtrA-KtrB interface, which was observed in the structure obtained in this thesis. For MthK, MD simulations strongly supported the experimental data elucidating the gating mechanism including the interaction of the C linker with the membrane (Fan et al, 2020).

However, to fully understand the gating mechanism of KtrAB, determining a structure of the ATP-bound active state remains crucial. With this, many open questions concerning the conformational changes in KtrB upon ATP binding, especially the movement of the extended D1M2 helices, the relocation of the N termini and the stabilisation of the intramembrane loop could be addressed. Yet, if the activation requires the large allosteric network suggested in this thesis, single particle cryo-EM might be limited in terms of

structurally resolving the activation process, as in membrane scaffolds like nanodiscs not all required triggers can be applied. Therefore, cryo-ET of KtrAB reconstituted in liposomes could be helpful. On the one hand this approach provides the larger membrane surface that is required and on the other hand enables the application of ion gradients generating a membrane potential applied as a potential trigger.

Whether KtrBs' N termini have an additional role in N-type inactivation could be analysed with single channel recordings, similar to studies published for MthK (Kuo et al, 2007; Kuo et al, 2008). Here, in case the KtrAB complex is desensitised by the N termini of KtrB, a rapid inactivation of channel activity should be observed, which could be abolished upon mutation or deletion of the N terminus. By supplying the N-terminal peptide, the desensitisation should be recovered. For this, BLM measurements need to be established for the KtrAB complex.

The question whether the proposed mechanism is specific for KtrAB from Gram-negative organisms like *V. alginolyticus* or a common gating regulation of KtrAB, can be tackled by performing whole-cell K^+ uptake experiments with N termini variants of KtrAB from *B. subtilis* expressed by *E. coli* LB2003 cells. For *B. subtilis* wildtype KtrAB, this has already been established (Fuss, 2019) and has been used to verify the functionality of the GFP-variant of KtrAB in this thesis (Figure 13).

Taken together, the new insights gained within this thesis, uncover that the gating mechanism of KtrAB most likely requires an allosteric network to allow the transition between an inactive and active, conductive state.

7 Supplementary Information

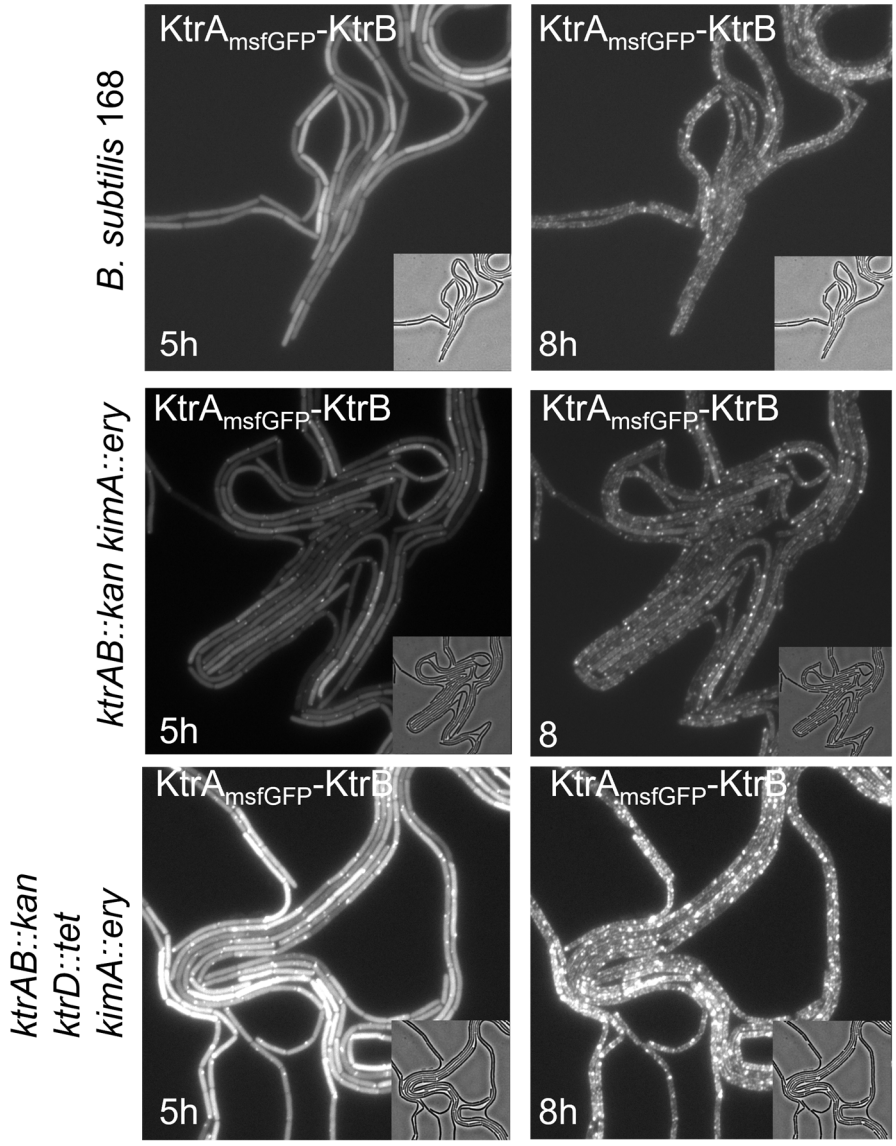

Figure S1: Time-lapse microscopy of *B. subtilis ktrAB::kan* expressing *ktrA$_{msfgfp}$-ktrB*. Representative fluorescence images of *B. subtilis* cells and the respective phase-contrast image shown in small insets. The localisation of KtrA$_{msfGFP}$ in *B. subtilis* 168 cells, *ktrAB::kan kimA::ery* cells and *ktrAB::kan ktrD::tet kimA::ery* cells was monitored for 13 hours. Within 8 hours the fluorescence signal was distributed diffusely in the cytoplasm. Afterwards, clusters of GFP signals located towards the membrane were identified. Microscopy was performed with the help of Dr. Henrik Strahl, Centre for Bacterial Cell Biology (CBCB), Newcastle upon Tyne.

Table S1: Cryo-EM data collection and refinement statistics

	$KtrB_2A_8B_2$	**$KtrB_2A_8$**	**KtrAB in nanodiscs**	**$KtrAB_{\Delta 2\text{-}19}$**
Data collection				
Microscope	FEI Titan Krios	FEI Titan Krios	FEI Titan Krios	FEI Titan Krios
Camera	Gatan K3 Summit	Gatan K3 Summit	Gatan K3 Summit	Gatan K3 Summit
Voltage (kV)	300	300	300	300
Nominal magnification	105,000x	105,000x	105,000x	105,000x
Calibrated pixel size (Å)	0.837	0.837	0.837	0.837
Electron exposure ($e^-/Å^2$)	40.0	40.0	40.0	40.0
Exposure time total (s)	2	2	2	2
Number of frames per image	40	40	40	40
Defocus range (μm)	-1.0 – -2.5	-0.8 – -2.5		-0.5 – -2.2
Image processing				
Motion correction software	*MotionCor2*	*MotionCor2*	*MotionCor2*	*MotionCor2*
CTF estimation software	*Gctf*	*Gctf*	*Gctf*	*Gctf*
Particle selection software	*crYOLO*	*crYOLO*	*crYOLO*	*crYOLO*
Micrographs (no.)	5,956	3,663	10,315	7,109
Initial particle images (no.)	198,298	394,476	374,333	211,579
Final particle images (no.)	73,965	211,602	59,348	58,420
Symmetry	D2	C2	C1	D2
Applied *B*-factor ($Å^2$)	-65	-100	-443	-160
Final resolution (Relion) (Å)	2.8	3.1	6.0	3.6
Final resolution (denmod) (Å)	2.5	2.8	ND	ND

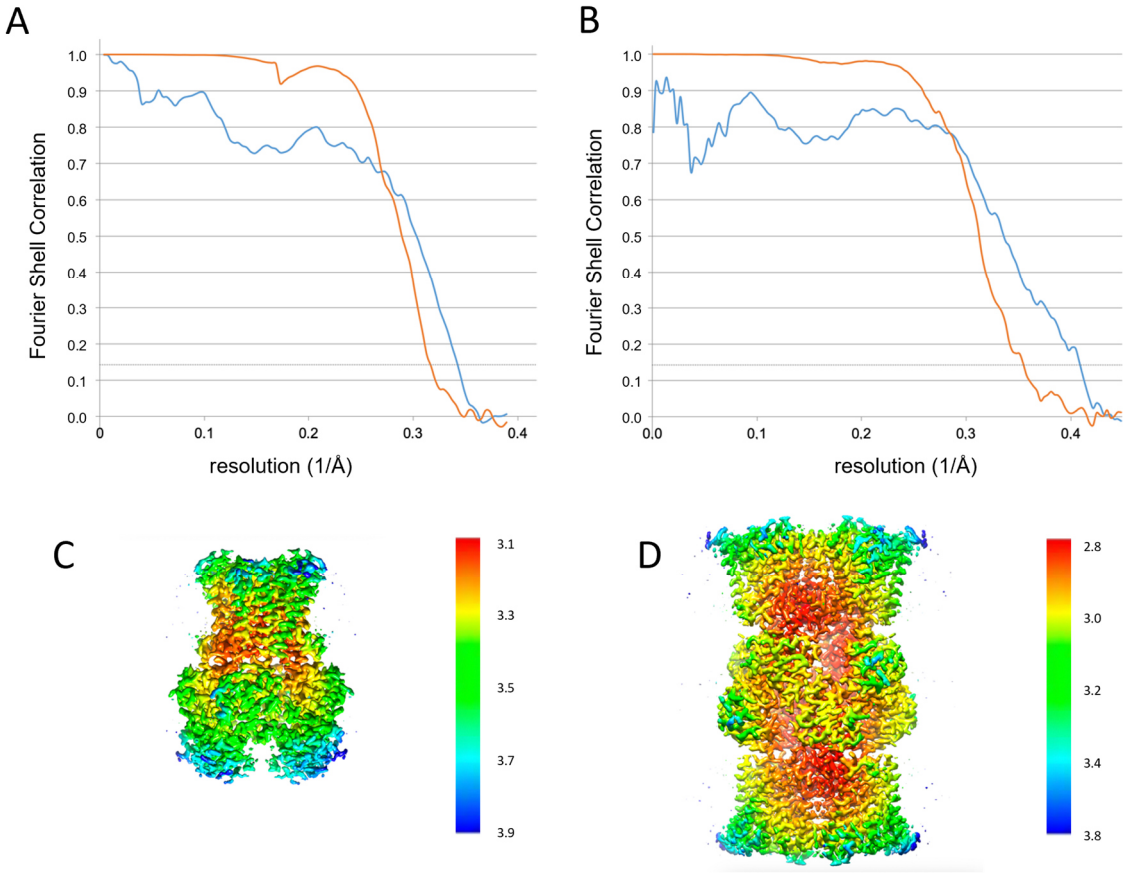

Figure S2: Cryo-EM map validation. A) FSC plots for resolution estimation and model validation of native KtrAB complex (C2 symmetry). Gold-standard FSC plot between two half-maps separately refined in Relion (orange) indicates a resolution of 3.2 Å (0.143 threshold). Map-to-model FSC for the final refined model and the Relion map (blue) indicates a resolution of 3.3 Å (0.5 FSC criterion). B) FSC plots for the sandwich KtrAB complex (D2 symmetry). Gold-standard FSC (orange curve): 2.82 Å, map-to-model FSC (blue): 2.96 Å. C) Native and D) 'sandwich' cryo-EM map colored by local resolution as determined in Relion. Color scale in Å.

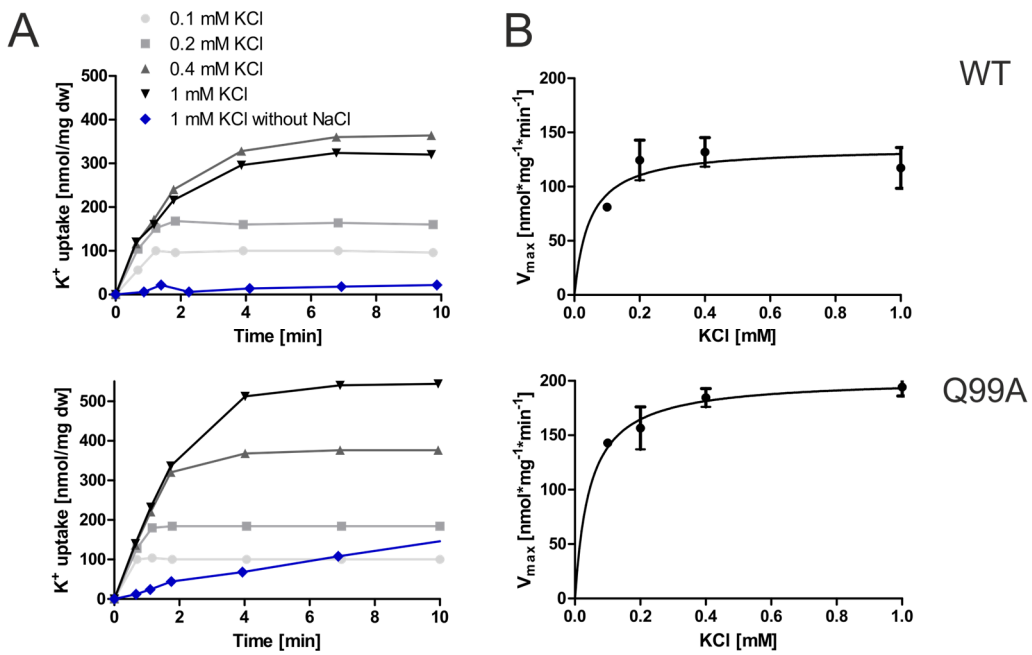

Figure S3: K^+ uptake by *E. coli* LB2003 cells producing KtrAB pore variants. A) After production of different KtrAB pore variants, *E. coli* LB2003 cells were depleted of K^+ and, after 10 min incubation at room temperature, different K^+ concentrations (0.1, 0.2, 0.4, and 1 mM, different shades of black) were added. For 10 min, 1 ml samples were taken at different time points, and cells were separated from medium via centrifugation through silicone oil. Intracellular potassium concentrations were determined by flame photometry. All experiments were performed in the presence and absence of 5 mM NaCl. Only in the presence of NaCl, K^+ is taken up. K^+ uptake in the presence of 1 mM KCl and in the absence of NaCl is exemplary shown blue. B) Initial uptake velocities are plotted against the used KCl concentration. Michaelis-Menten fit was performed to determine V_{max} and K_m. Experiments were performed in triplicates and average K_m and V_{max} values are represented in the main text (cf. Figure 35).

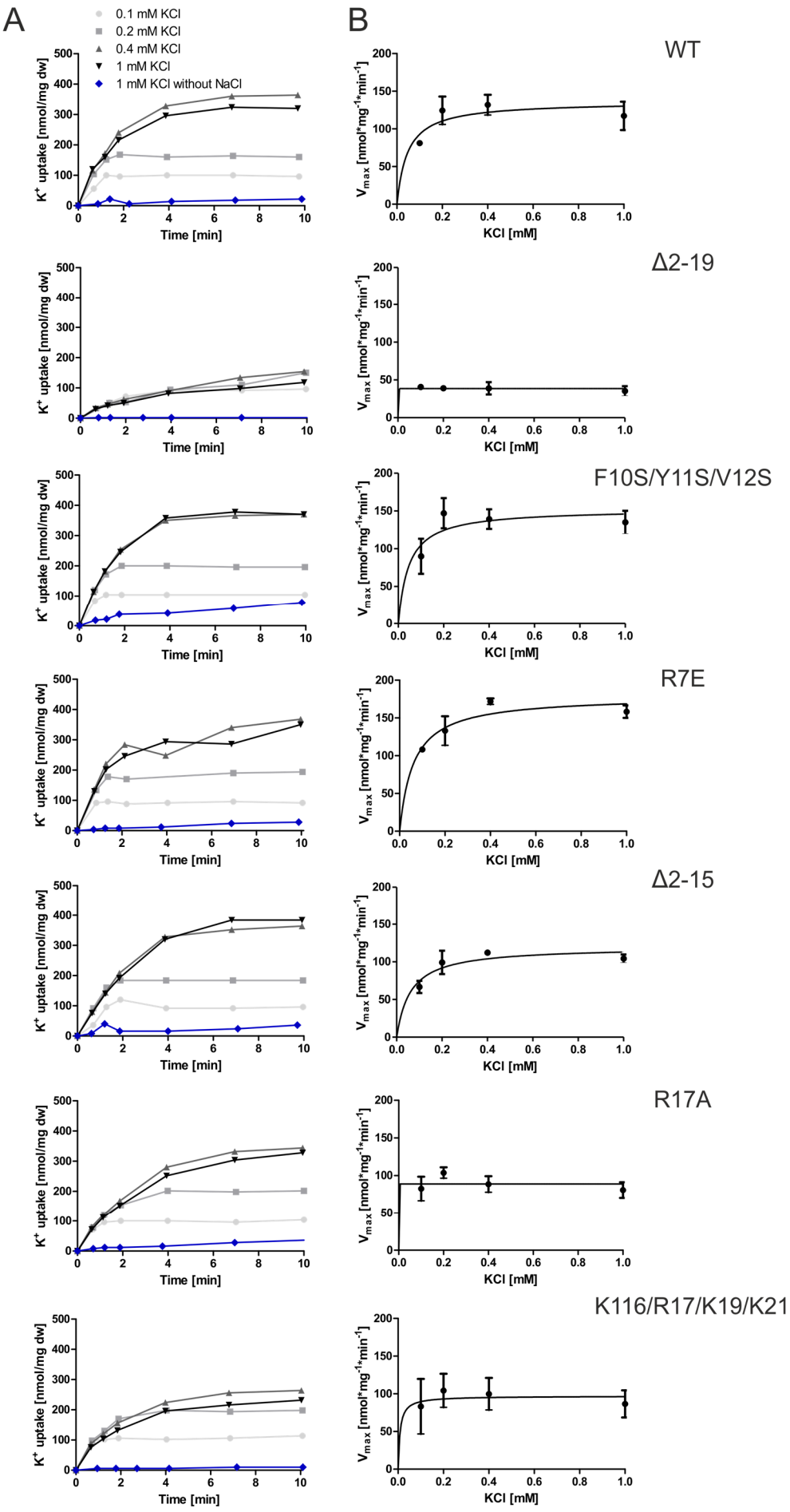
A
B
0.1 mM KCl
0.2 mM KCl
0.4 mM KCl
1 mM KCl
1 mM KCl without NaCl
K+ uptake [nmol/mg dw]
Time [min]
Vmax [nmol*mg-1*min-1]
KCl [mM]
WT
Δ2-19
F10S/Y11S/V12S
R7E
Δ2-15
R17A
K116/R17/K19/K21

Figure S4: K^+ uptake by *E. coli* LB2003 cells producing KtrAB with variations in the N terminus of KtrB. A) After production of different KtrAB with different mutations in the N terminus, *E. coli* LB2003 cells were depleted of K^+ and, after 10 min incubation at room temperature, different K^+ concentrations (0.1, 0.2, 0.4, and 1 mM, different shades of black) were added. For 10 min, 1 ml samples were taken at different time points, and cells were separated from medium via centrifugation through silicone oil. Intracellular potassium concentrations were determined by flame photometry. All experiments were performed in the presence and absence of 5 mM NaCl. Only in the presence of NaCl, K^+ is taken up. K^+ uptake in the presence of 1 mM KCl and in the absence of NaCl is exemplary shown blue. B) Initial uptake velocities are plotted against the used KCl concentration. To determine V_{max} and K_m a Michaelis-Menten fit was performed. Experiments were performed in triplicates and average K_m and V_{max} values are represented in the main text (cf. Figure 39).

Table S2: Calculated diameter ratios, conformations, and number of particles for the classes of purified KtrA in the presence of 1 mM ATP and 2 mM $MgCl_2$. All classes with a diameter ratio below 1.115 were defined as square-shaped (S) and all with a ratio above 1.115 were defined as oval-shaped (O).

Class	Diameter ratio a/b	Oval (O) or Square (S) conformation	No of particles	
1	1.140	**O**	1,850	
2	1.018	**S**	1,172	
3	1.097	**O**	256	
4	1.030	**S**	926	
5	1.131	**O**	1,240	
6	1.056	**S**	193	
7	1.209	**O**	555	
8	1.104	**S**	679	
9	1.280	**O**	1,502	
10	1.074	**S**	74	
11	1.040	**S**	3,350	
12	1.110	**S**	1,666	
13	1.071	**S**	4,819	
14	1.043	**S**	50	
15	1.021	**S**	449	
16	1.108	**S**	117	
17	1.039	**S**	288	
18	1.000	**S**	1,698	
19	1.076	**S**	372	
20	1.020	**S**	1,466	
21	1.031	**S**	1,879	
22	1.161	**O**	353	
23	1.051	**S**	217	
24	1.020	**S**	41	
25	1.009	**S**	364	
26	1.098	**S**	3,842	
27	1.008	**S**	2,227	
Total Number of Particles			**31,645**	
Thereof	**square**		25,889	**82%**
	oval		5,756	**18%**

Table S3: Evaluation of 2D classes of KtrA in the presence of 1 mM ATP and 2 mM $MgCl_2$. Determined x-and y-diameters and the corresponding ratios are shown

Class	a (long)	b (short)	Ratio
1	81.4	71.4	1.140
2	80.0	78.6	1.018
3	75.6	68.9	1.097
4	75.8	73.6	1.030
5	77.6	68.6	1.131
6	75.4	71.4	1.056
7	86.6	71.6	1.209
8	82.0	74.3	1.104
9	84.2	65.8	1.280
10	72.2	67.2	1.074
11	73.6	70.8	1.040
12	78.6	70.8	1.110
13	75.0	70.0	1.071
14	72.2	69.2	1.043
15	67.8	66.4	1.021
16	73.6	66.4	1.108
17	75.0	72.2	1.039
18	73.6	73.6	1.000
19	70.8	65.8	1.076
20	71.4	70.0	1.020
21	73.6	71.4	1.031
22	78.0	67.2	1.161
23	73.6	70.0	1.051
24	71.4	70.0	1.020
25	70.0	69.4	1.009
26	79.3	72.2	1.098
27	71.4	70.8	1.008

Table S4: Calculated diameter ratios, conformations, and number of particles for the classes of purified KtrA in the presence of 1 mM ADP and 2 mM $MgCl_2$. All classes with a diameter ratio below 1.115 were defined as square-shaped (S) and all with a ratio above 1.115 were defined as oval-shaped (O).

Class	Diameter ratio a/b	Oval (O) or Square (S) conformation	No of particles	
1	1.241	**O**	1,223	
2	1.013	**S**	78	
3	1.156	**O**	377	
4	1.167	**O**	1,812	
5	1.083	**S**	1,012	
6	1.164	**O**	735	
7	1.256	**O**	1,279	
8	1.264	**O**	158	
9	1.342	**O**	446	
10	1.088	**S**	920	
11	1.288	**O**	350	
12	1.035	**S**	402	
13	1.245	**O**	599	
14	1.225	**O**	1,792	
15	1.328	**O**	1,075	
16	1.280	**O**	579	
17	1.331	**O**	288	
18	1.105	**S**	429	
19	1.371	**O**	136	
20	1.216	**O**	651	
21	1.174	**O**	383	
22	1.110	**S**	394	
23	1.156	**O**	922	
24	1.371	**O**	35	
25	1.227	**O**	346	
26	1.208	**O**	510	
27	1.195	**O**	164	
28	1.134	**O**	855	
29	1.178	**O**	188	
Total Number of Particles			**18,138**	
Thereof	**square**		3,235	**18%**
	oval		14,903	**82%**

Table S5: Evaluation of 2D classes of KtrA in the presence of 1 mM ADP and 2 mM $MgCl_2$. Determined x-and y-diameters and the corresponding ratios are shown.

Class	a (long)	b (short)	Ratio
1	67.0	54.0	1.241
2	62.2	61.4	1.013
3	63.6	55.0	1.156
4	65.8	56.4	1.167
5	65.0	60.0	1.083
6	65.2	56.0	1.164
7	62.8	50.0	1.256
8	67.0	53.0	1.264
9	66.3	49.4	1.342
10	62.1	57.1	1.088
11	67.0	52.0	1.288
12	62.2	60.1	1.035
13	63.6	51.1	1.245
14	58.8	48.0	1.225
15	60.8	45.8	1.328
16	64.0	50.0	1.280
17	70.0	52.6	1.331
18	60.8	55.0	1.105
19	57.7	42.1	1.371
20	63.7	52.4	1.216
21	62.2	53.0	1.174
22	59.4	53.5	1.110
23	63.6	55.0	1.156
24	63.6	46.4	1.371
25	63.3	51.6	1.227
26	59.9	49.6	1.208
27	62.4	52.2	1.195
28	60.8	53.6	1.134
29	60.8	51.6	1.178

Table S6: Calculated diameter ratios, conformations, and number of particles for the classes of purified KtrA in the presence of 2 mM $MgCl_2$. All classes with a diameter ratio below 1.115 were defined as square-shaped (S) and all with a ratio above 1.115 were defined as oval-shaped (O).

Class	Diameter ratio a/b	Oval (O) or Square (S) conformation	No of particles	
1	1.084	**S**	1,657	
2	1.165	**O**	75	
3	1.159	**O**	471	
4	1.141	**O**	2,438	
5	1.133	**O**	275	
6	1.000	**S**	316	
7	1.000	**S**	595	
8	1.176	**O**	2,331	
9	1.130	**O**	183	
10	1.219	**O**	3,188	
11	1.232	**O**	742	
12	1.253	**O**	562	
13	1.210	**O**	105	
14	1.270	**O**	313	
15	1.108	**S**	796	
16	1.363	**O**	870	
17	1.100	**S**	686	
18	1.119	**O**	1,431	
19	1.013	**S**	4,751	
20	1.165	**O**	1,329	
21	1.157	**O**	3,157	
22	1.110	**S**	312	
23	1.270	**O**	1,354	
Total Number of Particles			**27,937**	
Thereof	**square**		9,113	**33%**
	oval		18,824	**67%**

Table S7: Evaluation of 2D classes of KtrA in the presence of 2 mM $MgCl_2$. Determined x-and y-diameters and the corresponding ratios are shown.

Class	a (long)	b (short)	Ratio
1	82.2	75.8	1.084
2	79.9	68.6	1.165
3	81.5	70.3	1.159
4	80.8	70.8	1.141
5	79.9	70.5	1.133
6	75.0	75.0	1.000
7	73.6	73.6	1.000
8	81.4	69.2	1.176
9	79.2	70.1	1.130
10	83.6	68.6	1.219
11	85.1	69.1	1.232
12	84.8	67.7	1.253
13	77.9	64.4	1.210
14	80.8	63.6	1.270
15	83.4	75.3	1.108
16	89.4	65.6	1.363
17	79.4	72.2	1.100
18	80.8	72.2	1.119
19	78.0	77.0	1.013
20	86.8	74.5	1.165
21	83.5	72.2	1.157
22	78.6	70.8	1.110
23	62.1	48.9	1.270

8 References

Abraham M.J., Murtola T., Schulz R., Páll S., Smith J.C., Hess B., Lindahl E. (2015) GROMACS: High performance molecular simulations through multi-level parallelism from laptops to supercomputers. *SoftwareX* 1-2: 19-25

Afonine P.V., Poon B.K., Read R.J., Sobolev O.V., Terwilliger T.C., Urzhumtsev A., Adams P.D. (2018) Real-space refinement in PHENIX for cryo-EM and crystallography. *Acta crystallographica Section D, Structural biology* 74: 531-544

Albright R.A., Ibar J.L., Kim C.U., Gruner S.M., Morais-Cabral J.H. (2006) The RCK domain of the KtrAB K^+ transporter: multiple conformations of an octameric ring. *Cell* 126: 1147-1159

Anagnostopoulos C., Spizizen J. (1961) Requirements for Transformation in *Bacillus Subtilis*. *Journal of bacteriology* 81: 741-746

Aono R., Aibe K., Inoue A., Horikoshi K. (1991) Preparation of Organic Solvent-tolerant Mutants from *Escherichia coli* K-12. *Agricultural and Biological Chemistry* 55: 1935-1938

Arkhipova V., Guskov A., Slotboom D.J. (2020) Structural ensemble of a glutamate transporter homologue in lipid nanodisc environment. *Nature communications* 11: 998

Armstrong C.M., Bezanilla .F (1973) Currents Related to Movement of the Gating Particles of the Sodium Channels. *Nature* 242: 459-461

Bai N., Roder H., Dickson A., Karanicolas J. (2019) Isothermal Analysis of ThermoFluor Data can readily provide Quantitative Binding Affinities. *Scientific reports* 9: 2650

Bakker E.P., Booth I.R., Dinnbier U., Epstein W., Gajewska A. (1987) Evidence for multiple K^+ export systems in *Escherichia coli*. *Journal of bacteriology* 169: 3743-3749

Bakker E.P., Mangerich W.E. (1981) Interconversion of components of the bacterial proton motive force by electrogenic potassium transport. *Journal of bacteriology* 147: 820-826

Bao H., Duong F., Chan C.S. (2012) A step-by-step method for the reconstitution of an ABC transporter into nanodisc lipid particles. *J Vis Exp*: e3910

Barbe V., Cruveiller S., Kunst F., Lenoble P., Meurice G., Sekowska A., Vallenet D., Wang T., Moszer I., Medigue C., Danchin A. (2009) From a consortium sequence to a unified sequence: the *Bacillus subtilis* 168 reference genome a decade later. *Microbiology* 155: 1758-1775

Barlow D.J., Thornton J.M. (1983) Ion-pairs in proteins. *Journal of molecular biology* 168: 867-885

Beagle S.D., Lockless S.W. (2020) Unappreciated Roles for K^+ Channels in Bacterial Physiology. *Trends Microbiol*

Beales N. (2004) Adaptation of Microorganisms to Cold Temperatures, Weak Acid Preservatives, Low pH, and Osmotic Stress: A Review. *Comprehensive reviews in food science and food safety* 3: 1-20

Bennett B.D., Kimball E.H,. Gao M., Osterhout R., Van Dien S.J., Rabinowitz J.D. (2009) Absolute metabolite concentrations and implied enzyme active site occupancy in *Escherichia coli*. *Nature chemical biology* 5: 593-599

Berendsen H.J.C., Postma J.P.M., Gunsteren W.Fv., DiNola A., Haak J.R. (1984) Molecular dynamics with coupling to an external bath. *The Journal of Chemical Physics* 81: 3684-3690

Best R.B., Zhu X., Shim J., Lopes P.E.M., Mittal J., Feig M., MacKerell A.D. (2012) Optimization of the Additive CHARMM All-Atom Protein Force Field Targeting Improved Sampling of the Backbone ϕ, ψ and Side-Chain χ1 and χ2 Dihedral Angles. *Journal of chemical theory and computation* 8: 3257-3273

Biemans-Oldehinkel E., Mahmood N.A., Poolman B. (2006) A sensor for intracellular ionic strength. *Proceedings of the National Academy of Sciences of the United States of America* 103: 10624-10629

Blake K.L., O'Neill A.J. (2013) Transposon library screening for identification of genetic loci participating in intrinsic susceptibility and acquired resistance to antistaphylococcal agents. *The Journal of antimicrobial chemotherapy* 68: 12-16

Booth I.R. (1985) Regulation of cytoplasmic pH in bacteria. *Microbiological reviews* 49: 359-378

Bramkamp M., Lopez D. (2015) Exploring the existence of lipid rafts in bacteria. *Microbiology and molecular biology reviews : MMBR* 79: 81-100

Buda R,. Liu Y., Yang J., Hegde S., Stevenson K., Bai F., Pilizota T. (2016) Dynamics of *Escherichia coli's* passive response to a sudden decrease in external osmolarity. *Proceedings of the National Academy of Sciences* 113: E5838-E5846

Cao Y., Jin X., Huang H., Derebe M.G., Levin E.J., Kabaleeswaran V., Pan Y., Punta M., Love J., Weng J., Quick M., Ye S., Kloss B., Bruni R., Martinez-Hackert E., Hendrickson W.A., Rost B., Javitch J.A., Rajashankar K.R., Jiang Y., Zhou M. (2011) Crystal structure of a potassium ion transporter, TrkH. *Nature* 471: 336-340

Cao Y., Pan Y., Huang H., Jin X., Levin E.J., Kloss B., Zhou M. (2013) Gating of the TrkH ion channel by its associated RCK protein TrkA. *Nature* 496: 317-322

Carden D.E., Walker D.J., Flowers T.J., Miller A.J. (2003) Single-cell measurements of the contributions of cytosolic Na^+ and K^+ to salt tolerance. *Plant physiology* 131: 676-683

Chakrapani S., Perozo E. (2007) How to gate an ion channel: lessons from MthK. *Nature structural & molecular biology* 14: 180-182

Checchetto V., Formentin E., Carraretto L., Segalla A., Giacometti G.M., Szabo I., Bergantino E. (2013) Functional characterization and determination of the physiological role of a calcium-dependent potassium channel from cyanobacteria. *Plant physiology* 162: 953-964

Cheng Y., Feng G., Moraru C.I. (2019) Micro- and Nanotopography Sensitive Bacterial Attachment Mechanisms: A Review. *Frontiers in microbiology* 10

Cordero-Morales J.F., Cuello L.G., Perozo E. (2006) Voltage-dependent gating at the KcsA selectivity filter. *Nature structural & molecular biology* 13: 319-322

Corey R.A., Pyle E., Allen W.J., Watkins D.W., Casiraghi M., Miroux B., Arechaga I., Politis A,. Collinson I. (2018) Specific cardiolipin-SecY interactions are required for proton-motive force stimulation of protein secretion. *Proceedings of the National Academy of Sciences of the United States of America* 115: 7967-7972

Corey R.A., Song W., Duncan A.L., Ansell T.B., Sansom M.S..P, Stansfeld P.J. (2021) Identification and assessment of cardiolipin interactions with *E. coli* inner membrane proteins. *bioRxiv*: 2021.2003.2019.436130

Corrigan R.M., Campeotto I., Jeganathan T., Roelofs K.G., Lee V.T., Gründling A. (2013) Systematic identification of conserved bacterial c-di-AMP receptor proteins. *Proceedings of the National Academy of Sciences of the United States of America* 110: 9084-9089

Cox G., Wright G.D. (2013) Intrinsic antibiotic resistance: mechanisms, origins, challenges and solutions. *International journal of medical microbiology : IJMM* 303: 287-292

Cruden D.L., Wolfram J.H., Rogers R.D., Gibson D.T. (1992) Physiological properties of a *Pseudomonas* strain which grows with p-xylene in a two-phase (organic-aqueous) medium. *Appl Environ Microbiol* 58: 2723-2729

Cuello L.G., Cortes D.M., Perozo .E (2017) The gating cycle of a K^+ channel at atomic resolution. *eLife* 6

Cuello L.G., Jogini V., Cortes D.M., Pan A.C., Gagnon D.G., Dalmas O., Cordero-Morales J.F., Chakrapani S., Roux B., Perozo E. (2010a) Structural basis for the coupling between activation and inactivation gates in K^+ channels. *Nature* 466: 272-275

Cuello L.G., Jogini V., Cortes D.M., Perozo E. (2010b) Structural mechanism of C-type inactivation in K^+ channels. *Nature* 466: 203-208

Culham D.E., Marom D., Boutin R., Garner J., Ozturk T.N., Sahtout N., Tempelhagen L., Lamoureux G., Wood J.M. (2018) Dual Role of the C-Terminal Domain in Osmosensing by Bacterial Osmolyte Transporter ProP. *Biophysical journal* 115: 2152-2166

Darden T., York D., Pedersen L. (1993) Particle mesh Ewald: An N·log(N) method for Ewald sums in large systems. *The Journal of Chemical Physics* 98: 10089-10092

de Jong I.G., Beilharz K., Kuipers O.P., Veening J-W. (2011) Live Cell Imaging of *Bacillus subtilis* and S*treptococcus pneumoniae* using Automated Time-lapse Microscopy. *Journal of visualized experiments : JoVE*: 3145

Diskowski M., Mehdipour A.R., Wunnicke D., Mills D.J., Mikušević V., Bärland N., Hoffmann J., Morgner N., Steinhoff H.J., Hummer G., Vonck J., Hänelt I. (2017) Helical jackknives control the gates of the double-pore K^+ uptake system KtrAB. *eLife* 6

Donlan R.M. (2002) Biofilms: microbial life on surfaces. *Emerg Infect Dis* 8: 881-890

Doyle D.A., Morais Cabral J, Pfuetzner RA, Kuo A, Gulbis JM, Cohen SL, Chait BT, MacKinnon R (1998) The structure of the potassium channel: molecular basis of K^+ conduction and selectivity. *Science* 280: 69-77

Dufourc E.J. (2021) Bicelles and nanodiscs for biophysical chemistry11A tribute to Prof Michèle Auger, University Laval, Canada. *Biochimica et Biophysica Acta (BBA) - Biomembranes* 1863: 183478

Eisenberg D., Crothers D. (1979) *Physical chemistry with applications to the life sciences*.

Emsley P., Cowtan K. (2004) Coot: model-building tools for molecular graphics. *Acta Crystallogr D Biol Crystallogr* 60: 2126-2132

Epstein W. (1986) Osmoregulation by potassium transport in *Escherichia coli*. *FEMS microbiology reviews* 2: 73-75

Epstein W. (2003) The roles and regulation of potassium in bacteria. *Progress in nucleic acid research and molecular biology* 75: 293-320

Epstein W., Buurman E., McLaggan D., Naprstek J. (1993) Multiple mechanisms, roles and controls of K^+ transport in *Escherichia coli*. *Biochem Soc Trans* 21: 1006-1010

Epstein W., Kim B.S. (1971) Potassium transport loci in *Escherichia coli* K-12. *Journal of bacteriology* 108: 639-644

Fajardo A., Martinez-Martin N., Mercadillo M., Galan J.C., Ghysels B., Matthijs S., Cornelis P., Wiehlmann L., Tummler B., Baquero .F, Martinez J.L. (2008) The neglected intrinsic resistome of bacterial pathogens. *PloS one* 3: e1619

Fan C., Sukomon N., Flood E., Rheinberger J., Allen T.W., Nimigean C.M. (2020) Ball-and-chain inactivation in a calcium-gated potassium channel. *Nature* 580: 288-293

Felle H., Porter J., Slayman C., Kaback H. (1980) Quantitative measurements of membrane potential in *Escherichia coli*. *Biochemistry* 19: 3585-3590

Follmann M., Becker M., Ochrombel I., Ott V., Kramer R., Marin K. (2009) Potassium transport in *corynebacterium glutamicum* is facilitated by the putative channel protein CglK, which is essential for pH homeostasis and growth at acidic pH. *Journal of bacteriology* 191: 2944-2952

Fuss M.F. (2019) The functional characterization of the potassium uptake system KtrAB from *Bacillus subtilis*. Institute of Biochemistry, Johann Wolfgang Goethe-University Frankfurt

Gaber R.F., Styles C.A., Fink G.R. (1988) TRK1 encodes a plasma membrane protein required for high-affinity potassium transport in *Saccharomyces cerevisiae*. *Molecular and cellular biology* 8: 2848-2859

Gadsby D.C. (2009) Ion channels versus ion pumps: the principal difference, in principle. *Nature reviews Molecular cell biology* 10: 344-352

Galdiero S., Falanga A., Cantisani M., Vitiello M., Morelli G., Galdiero M. (2013) Peptide-lipid interactions: experiments and applications. *International journal of molecular sciences* 14: 18758-18789

Geertsma E.R., Groeneveld M., Slotboom D-J., Poolman B. (2008a) Quality control of overexpressed membrane proteins. *Proceedings of the National Academy of Sciences* 105: 5722-5727

Geertsma E.R., Nik Mahmood N.A,. Schuurman-Wolters G.K., Poolman B. (2008b) Membrane reconstitution of ABC transporters and assays of translocator function. *Nat Protoc* 3: 256-266

Goldstein S.A., Wang K.W., Ilan N., Pausch M.H. (1998) Sequence and function of the two P domain potassium channels: implications of an emerging superfamily. *Journal of molecular medicine (Berlin, Germany)* 76: 13-20

Gomez M.J., Neyfakh A.A. (2006) Genes involved in intrinsic antibiotic resistance of *Acinetobacter baylyi*. *Antimicrobial agents and chemotherapy* 50: 3562-3567

Gorecki K., Hagerhall C., Drakenberg T. (2014) The Na^+ transport in gram-positive bacteria defect in the Mrp antiporter complex measured with ^{23}Na nuclear magnetic resonance. *Analytical biochemistry* 445: 80-86

Gouaux E., Mackinnon R. (2005) Principles of selective ion transport in channels and pumps. *Science* 310: 1461-1465

Grant T., Rohou A., Grigorieff N. (2018) *cis*TEM, user-friendly software for single-particle image processing. *eLife* 7: e35383

Greie J.C. (2011) The KdpFABC complex from *Escherichia coli*: a chimeric K^+ transporter merging ion pumps with ion channels. *European journal of cell biology* 90: 705-710

Gries C.M., Bose J.L., Nuxoll A.S., Fey P.D., Bayles K.W. (2013) The Ktr potassium transport system in *Staphylococcus aureus* and its role in cell physiology, antimicrobial resistance and pathogenesis. *Molecular microbiology* 89: 760-773

Griwatz D. (2021) Elucidating the role of KtrB's N terminus in the nucleotide dependent K^+ translocation by KtrAB. Institute of Biochemistry, Johann Wolfgang Goethe-University Frankfurt

Gundlach J., Herzberg C., Kaever V., Gunka K., Hoffmann T., Weiss M., Gibhardt J., Thurmer A., Hertel D., Daniel R., Bremer E., Commichau F.M., Stülke J. (2017) Control of potassium homeostasis is an essential function of the second messenger cyclic di-AMP in *Bacillus subtilis*. *Sci Signal* 10

Gundlach J., Krüger L., Herzberg C., Turdiev A., Poehlein A., Tascon I., Weiss M., Hertel D., Daniel R., Hänelt I., Lee V.T., Stülke J. (2019) Sustained sensing in potassium homeostasis: Cyclic di-AMP controls potassium uptake by KimA at the levels of expression and activity. *The Journal of biological chemistry*

Gupta K., Donlan J.A.C., Hopper J.T.S., Uzdavinys P., Landreh M., Struwe W.B., Drew D., Baldwin A.J., Stansfeld P.J., Robinson C.V. (2017) The role of interfacial lipids in stabilizing membrane protein oligomers. *Nature* 541: 421-424

Hänelt I., Lochte S., Sundermann L., Elbers K., Vor der Brüggen M, Bakker E.P. (2010a) Gain of function mutations in membrane region M2C2 of KtrB open a gate controlling K^+ transport by the KtrAB system from *Vibrio alginolyticus*. *The Journal of biological chemistry* 285: 10318-10327

Hänelt I., Wunnicke D., Müller-Trimbusch M., Vor der Brüggen M., Kraus I., Bakker E.P., Steinhoff H.J. (2010b) Membrane region M2C2 in subunit KtrB of the K^+ uptake system KtrAB from *Vibrio alginolyticus* forms a flexible gate controlling K^+ flux: an electron paramagnetic resonance study. *The Journal of biological chemistry* 285: 28210-28219

Harro J.M., Peters B.M., O'May G.A., Archer N., Kerns P., Prabhakara R., Shirtliff M.E. (2010) Vaccine development in *Staphylococcus aureus*: taking the biofilm phenotype into consideration. *FEMS Immunology & Medical Microbiology* 59: 306-323

Healy J., Ekkerman S., Pliotas C., Richard M., Bartlett W., Grayer S.C., Morris .GM., Miller S., Booth I.R., Conway S.J., Rasmussen T. (2014) Understanding the Structural Requirements for Activators of the Kef Bacterial Potassium Efflux System. *Biochemistry* 53: 1982-1992

Hess B., Bekker H., Berendsen H.J.C., Fraaije J.G.E.M. (1997) LINCS: A linear constraint solver for molecular simulations. *Journal of computational chemistry* 18: 1463-1472

Hesse J.E., Wieczorek L., Altendorf K., Reicin A.S., Dorus E., Epstein W. (1984) Sequence homology between two membrane transport ATPases, the Kdp-ATPase of *Escherichia coli* and the Ca^{2+}-ATPase of sarcoplasmic reticulum. *Proceedings of the National Academy of Sciences of the United States of America* 81: 4746-4750

Hibino H., Inanobe A., Furutani K., Murakami S., Findlay I., Kurachi Y. (2010) Inwardly rectifying potassium channels: their structure, function, and physiological roles. *Physiological reviews* 90: 291-366

Hille B. (1970) Ionic channels in nerve membranes. *Progress in biophysics and molecular biology* 21: 1-32

Hille B. (1971) The permeability of the sodium channel to organic cations in myelinated nerve. *The Journal of general physiology* 58: 599-619

Hille B. (1973) Potassium channels in myelinated nerve. Selective permeability to small cations. *The Journal of general physiology* 61: 669-686

Hirano M., Onishi Y., Yanagida T., Ide T. (2011) Role of the KcsA Channel Cytoplasmic Domain in pH-Dependent Gating. *Biophysical journal* 101: 2157-2162

Hite R.K., MacKinnon R (2017) Structural Titration of Slo2.2, a Na^+-Dependent K^+ Channel. *Cell* 168: 390-399 e311

Hodgkin A.L., Huxley A.F. (1952) A quantitative description of membrane current and its application to conduction and excitation in nerve. *J Physiol* 117: 500-544

Holtmann G., Bakker E.P., Uozumi N., Bremer E. (2003) KtrAB and KtrCD: two K^+ uptake systems in *Bacillus subtilis* and their role in adaptation to hypertonicity. *Journal of bacteriology* 185: 1289-1298

Hoover W.G. (1985) Canonical dynamics: Equilibrium phase-space distributions. *Physical Review A* 31: 1695-1697

Hoshi T., Armstrong C.M. (2013) C-type inactivation of voltage-gated K^+ channels: pore constriction or dilation? *The Journal of general physiology* 141: 151-160

Huang C.S., Pedersen .BP., Stokes D.L. (2017) Crystal structure of the potassium-importing KdpFABC membrane complex. *Nature* 546: 681-685

Imai S., Osawa M., Takeuchi K., Shimada I. (2010) Structural basis underlying the dual gate properties of KcsA. *Proceedings of the National Academy of Sciences* 107: 6216-6221

Inoue A., Horikoshi, K. (1989) A *Pseudomonas* thrives in high concentrations of toluene. *Nature* 338: 264–266

Iwamoto M., Oiki S. (2013) Amphipathic antenna of an inward rectifier K^+ channel responds to changes in the inner membrane leaflet. *Proceedings of the National Academy of Sciences* 110: 749-754

Jensen P.R., Van Der Weijden C.C., Jensen L.B., Westerhoff H.V., Snoep J.L. (1999) Extensive regulation compromises the extent to which DNA gyrase controls DNA supercoiling and growth rate of *Escherichia coli*. *European journal of biochemistry* 266: 865-877

Jeschke G., Chechik V., Ionita P., Godt A., Zimmermann H., Banham J., Timmel C.R., Hilger D., Jung H. (2006) DeerAnalysis2006 - a comprehensive software package for analyzing pulsed ELDOR data. *Applied Magnetic Resonance* 30: 473-498

Jiang Y., Lee A., Chen J., Cadene M., Chait B.T., MacKinnon R. (2002a) Crystal structure and mechanism of a calcium-gated potassium channel. *Nature* 417: 515-522

Jiang Y., Lee A., Chen J., Cadene M., Chait B.T., MacKinnon R. (2002b) The open pore conformation of potassium channels. *Nature* 417: 523-526

Jiang Y., Pico A., Cadene M., Chait B.T., MacKinnon R. (2001) Structure of the RCK domain from the *E. coli* K^+ channel and demonstration of its presence in the human BK channel. *Neuron* 29: 593-601

Jorgensen W.L., Chandrasekhar J., Madura J.D., Impey R.W., Klein M.L. (1983) Comparison of simple potential functions for simulating liquid water. *The Journal of Chemical Physics* 79: 926-935

Karasawa A., Erkens G.B., Berntsson R.P., Otten R., Schuurman-Wolters G.K., Mulder F.A., Poolman B. (2011) Cystathionine beta-synthase (CBS) domains 1 and 2 fulfill different roles in ionic strength sensing of the ATP-binding cassette (ABC) transporter OpuA. *The Journal of biological chemistry* 286: 37280-37291

Kashket E.R. (1982) Stoichiometry of the H^+-ATPase of growing and resting, aerobic *Escherichia coli*. *Biochemistry* 21: 5534-5538

Kim D.M., Nimigean C.M. (2016) Voltage-Gated Potassium Channels: A Structural Examination of Selectivity and Gating. *Cold Spring Harbor perspectives in biology* 8

Kim H., Youn S.J., Kim S.O., Ko J., Lee J.O., Choi B.S. (2015) Structural Studies of Potassium Transport Protein KtrA Regulator of Conductance of K^+ (RCK) C Domain in Complex with Cyclic Diadenosine Monophosphate (c-di-AMP). *The Journal of biological chemistry* 290: 16393-16402

Klauda J.B., Venable R.M., Freites J.A., O'Connor J.W., Tobias D.J., Mondragon-Ramirez C., Vorobyov I., MacKerell A.D., Pastor R.W. (2010) Update of the CHARMM All-Atom Additive Force Field for Lipids: Validation on Six Lipid Types. *The Journal of Physical Chemistry B* 114: 7830-7843

Ko C.H., Gaber R.F. (1991) TRK1 and TRK2 encode structurally related K^+ transporters in *Saccharomyces cerevisiae*. *Molecular and cellular biology* 11: 4266-4273

Kong C., Zeng W., Ye S., Chen L., Sauer D.B., Lam Y., Derebe M.G., Jiang Y. (2012) Distinct gating mechanisms revealed by the structures of a multi-ligand gated K^+ channel. *eLife* 1: e00184

Kopec W., Köpfer D.A., Vickery O.N., Bondarenko A.S., Jansen T.L.C., de Groot B..L, Zachariae U. (2018) Direct knock-on of desolvated ions governs strict ion selectivity in K^+ channels. *Nature chemistry* 10: 813-820

Köpfer D.A., Song C., Gruene T., Sheldrick G.M., Zachariae U., de Groot B.L. (2014) Ion permeation in K^+ channels occurs by direct Coulomb knock-on. *Science* 346: 352-355

Kröning N., Willenborg M., Tholema N., Hänelt I., Schmid R., Bakker E.P. (2007) ATP binding to the KTN/RCK subunit KtrA from the K^+ -uptake system KtrAB of *Vibrio alginolyticus*: its role in the formation of the KtrAB complex and its requirement *in vivo*. *The Journal of biological chemistry* 282: 14018-14027

Krüger L., Herzberg C., Warneke R., Poehlein A., Stautz J., Weiss M., Daniel R., Hänelt I., Stülke J. (2020) Two ways to convert a low- to a high-affinity potassium channel: Control of *Bacillus subtilis* KtrCD by glutamate. *Journal of bacteriology*

Krulwich T.A., Sachs G., Padan E. (2011) Molecular aspects of bacterial pH sensing and homeostasis. *Nature Reviews Microbiology* 9: 330-343

Kubo Y., Baldwin T.J., Jan Y.N., Jan L.Y. (1993) Primary structure and functional expression of a mouse inward rectifier potassium channel. *Nature* 362: 127-133

Kuo M.M., Baker K.A., Wong L., Choe S. (2007) Dynamic oligomeric conversions of the cytoplasmic RCK domains mediate MthK potassium channel activity. *Proceedings of the National Academy of Sciences of the United States of America* 104: 2151-2156

Kuo M.M., Maslennikov I., Molden B., Choe S. (2008) The desensitization gating of the MthK K^+ channel is governed by its cytoplasmic amino terminus. *PLoS biology* 6: e223

Kurata H.T., Fedida D. (2006) A structural interpretation of voltage-gated potassium channel inactivation. *Progress in biophysics and molecular biology* 92: 185-208

Laemmli U.K. (1970) Cleavage of structural proteins during the assembly of the head of bacteriophage T4. *Nature* 227: 680-685

Lee AG (2003) Lipid–protein interactions in biological membranes: a structural perspective. *Biochimica et Biophysica Acta (BBA) - Biomembranes* 1612: 1-40

Leive L. (1968) Studies on the permeability change produced in coliform bacteria by ethylenediaminetetraacetate. *The Journal of biological chemistry* 243: 2373-2380

Levina N., Totemeyer S., Stokes N.R., Louis P., Jones M.A., Booth I.R. (1999) Protection of *Escherichia coli* cells against extreme turgor by activation of MscS and MscL mechanosensitive channels: identification of genes required for MscS activity. *The EMBO journal* 18: 1730-1737

Liu A., Tran L., Becket E., Lee K., Chinn L., Park E., Tran K., Miller J.H. (2010) Antibiotic sensitivity profiles determined with an *Escherichia coli* gene knockout collection: generating an antibiotic bar code. *Antimicrobial agents and chemotherapy* 54: 1393-1403

Lopez D., Kolter R. (2010) Functional microdomains in bacterial membranes. *Genes & development* 24: 1893-1902

Loukin S.H., Kuo M.M-C., Zhou X-L, Haynes W.J., Kung C., Saimi Y. (2005) Microbial K^+ Channels. *Journal of General Physiology* 125: 521-527

Mäser P., Hosoo Y., Goshima S., Horie T., Eckelman B., Yamada K., Yoshida K., Bakker E.P., Shinmyo A., Oiki S., Schroeder J.I., Uozumi N. (2002) Glycine residues in potassium channel-like selectivity filters determine potassium selectivity in four-loop-per-subunit HKT transporters from plants. *Proceedings of the National Academy of Sciences of the United States of America* 99: 6428-6433

Matsuda N., Kobayashi H., Katoh H., Ogawa T., Futatsugi L., Nakamura T., Bakker E.P., Uozumi N (2004) Na^+-dependent K^+ uptake Ktr system from the cyanobacterium *Synechocystis sp.* PCC 6803 and its role in the early phases of cell adaptation to hyperosmotic shock. *The Journal of biological chemistry* 279: 54952-54962

Merino N., Aronson H.S., Bojanova D.P., Feyhl-Buska J., Wong M.L., Zhang S., Giovannelli D. (2019) Living at the Extremes: Extremophiles and the Limits of Life in a Planetary Context. *Frontiers in microbiology* 10: 780

Mikušević V. (2020) Ion selectivity of the unusual K^+ channel KtrAB. Institute of Biochemistry, Johann Wolfgang Goethe-University Frankfurt,

Mikušević V., Schrecker M., Kolesova N., Patino-Ruiz M., Fendler K., Hänelt I. (2019) A channel profile report of the unusual K^+ channel KtrB. *The Journal of general physiology* 151: 1357-1368

Milev S. (2015) N-value ITC data. https://www.materials-talks.com/2015/04/23/dont-throw-away-your-bad-n-value-itc-data/,14.12.2021, 5:15 pm.

Miroux B., Walker J.E. (1996) Over-production of proteins in *Escherichia coli*: mutant hosts that allow synthesis of some membrane proteins and globular proteins at high levels. *Journal of molecular biology* 260: 289-298

Morais-Cabral J.H., Zhou Y., MacKinnon R. (2001) Energetic optimization of ion conduction rate by the K^+ selectivity filter. *Nature* 414: 37-42

Morgner N., Kleinschroth T., Barth H.D., Ludwig B., Brutschy B. (2007) A novel approach to analyze membrane proteins by laser mass spectrometry: from protein subunits to the integral complex. *Journal of the American Society for Mass Spectrometry* 18: 1429-1438

Mosimann M., Goshima S., Wenzler T., Luscher A., Uozumi N., Maser P. (2010) A Trk/HKT-type K^+ transporter from *Trypanosoma brucei*. *Eukaryotic cell* 9: 539-546

Munns R, Tester M (2008) Mechanisms of salinity tolerance. *Annual review of plant biology* 59: 651-681

Nakamura T., Yuda R., Unemoto T., Bakker E.P. (1998) KtrAB, a new type of bacterial K^+-uptake system from *Vibrio alginolyticus*. *Journal of bacteriology* 180: 3491-3494

Nelson J.W., Sudarsan N., Furukawa K., Weinberg Z., Wang J.X., Breaker R.R. (2013) Riboswitches in eubacteria sense the second messenger c-di-AMP. *Nature chemical biology* 9: 834-839

Nikaido H. (1994) Prevention of drug access to bacterial targets: permeability barriers and active efflux. *Science* 264: 382-388

Nissen P., Hansen J., Ban N., Moore P.B., Steitz T.A. (2000) The structural basis of ribosome activity in peptide bond synthesis. *Science* 289: 920-930

Niu X., Qian X., Magleby K.L. (2004) Linker-gating ring complex as passive spring and Ca^{2+}-dependent machine for a voltage- and Ca^{2+}-activated potassium channel. *Neuron* 42: 745-756

Ochrombel I., Becker M., Kramer R., Marin K. (2011) Osmotic stress response in *C. glutamicum*: impact of channel- and transporter-mediated potassium accumulation. *Archives of microbiology* 193: 787-796

Ohlemüller K. (2021) Deciphering the role of KtrB‘s N terminus in channel gating of KtrAB. Institute of Biochemistry Johann Wolfgang Goethe University-Frankfurt

Ohwada T., Sagisaka S. (1987) An immediate and steep increase in ATP concentration in response to reduced turgor pressure in *Escherichia coli* B. *Archives of biochemistry and biophysics* 259: 157-163

Öster C., Hendriks K., Kopec W., Chevelkov V., Shi C., Michl D., Lange S., Sun H., Groot B.Ld, Lange A. (2019) The conduction pathway of potassium channels is water free under physiological conditions. *Science advances* 5: eaaw6756

Paje M.L.F., Neilan B.A., Couperwhite L. (1997) A *Rhodococcus* species that thrives on medium saturated with liquid benzene. *Microbiology* 143 (Pt 9): 2975-2981

Pannier M., Veit S., Godt A., Jeschke G., Spiess H.W. (2000) Dead-time free measurement of dipole-dipole interactions between electron spins. *Journal of magnetic resonance* 142: 331-340

Parrinello M., Rahman A. (1981) Polymorphic transitions in single crystals: A new molecular dynamics method. *J Appl Phys* 52: 7182-7190

Patrick J.W., Boone C.D., Liu W., Conover G.M., Liu Y., Cong X., Laganowsky A. (2018) Allostery revealed within lipid binding events to membrane proteins. *Proceedings of the National Academy of Sciences of the United States of America* 115: 2976-2981

Pau V.P., Abarca-Heidemann K., Rothberg B.S. (2010) Allosteric mechanism of Ca^{2+} activation and H^+-inhibited gating of the MthK K^+ channel. *The Journal of general physiology* 135: 509-526

Pau V.P., Smith F.J., Taylor A.B., Parfenova L.V., Samakai E., Callaghan M.M., Abarca-Heidemann K., Hart P.J., Rothberg B.S. (2011) Structure and function of multiple Ca^{2+}-binding sites in a K^+ channel regulator of K^+ conductance (RCK) domain. *Proceedings of the National Academy of Sciences of the United States of America* 108: 17684-17689

Poolman B., Spitzer J.J., Wood J.M. (2004) Bacterial osmosensing: roles of membrane structure and electrostatics in lipid-protein and protein-protein interactions. *Biochimica et biophysica acta* 1666: 88-104

Potter C.S., Chu H., Frey B., Green C., Kisseberth N., Madden T.J., Miller K.L., Nahrstedt K., Pulokas J., Reilein A., Tcheng D., Weber D., Carragher B. (1999) Leginon: a system for fully automated acquisition of 1000 electron micrographs a day. *Ultramicroscopy* 77: 153-161

Price-Whelan A., Poon C.K., Benson M.A., Eidem T.T., Roux C.M., Boyd J.M., Dunman P.M., Torres V.J., Krulwich T.A. (2013) Transcriptional profiling of *Staphylococcus aureus* during growth in 2 M NaCl leads to clarification of physiological roles for Kdp and Ktr K^+ uptake systems. *MBio* 4

Prindle A., Liu J., Asally M., Ly S., Garcia-Ojalvo J., Suel G.M. (2015) Ion channels enable electrical communication in bacterial communities. *Nature* 527: 59-63

Rhoads D.B., Epstein W. (1977) Energy coupling to net K^+ transport in *Escherichia coli* K-12. *The Journal of biological chemistry* 252: 1394-1401

Ritchie T.K., Grinkova Y.V., Bayburt T.H., Denisov I.G., Zolnerciks J.K., Atkins W.M., Sligar S.G. (2009) Chapter 11 - Reconstitution of membrane proteins in phospholipid bilayer nanodiscs. *Methods in enzymology* 464: 211-231

Rocha R., Teixeira-Duarte C.M., Jorge J.M.P., Morais-Cabral J.H. (2019) Characterization of the molecular properties of KtrC, a second RCK domain that regulates a Ktr channel in *Bacillus subtilis*. *Journal of structural biology* 205: 34-43

Rohou A., Grigorieff N. (2015) CTFFIND4: Fast and accurate defocus estimation from electron micrographs. *Journal of structural biology* 192: 216-221

Romantsov T., Guan Z., Wood J.M. (2009) Cardiolipin and the osmotic stress responses of bacteria. *Biochim Biophys Acta* 1788: 2092-2100

Romantsov T., Helbig S., Culham D.E., Gill C., Stalker L., Wood J.M. (2007) Cardiolipin promotes polar localization of osmosensory transporter ProP in *Escherichia coli*. *Molecular microbiology* 64: 1455-1465

Romantsov T., Wood J. M. (2017) Contributions of Membrane Lipids to Bacterial Cell Homeostasis upon Osmotic Challenge. In *Handbook of Hydrocarbon and Lipid Microbiology*, Otto G (ed), Biogenesis of Fatty Acids, Lipids and Membranes, pp 1-23. Springer, Cham.

Roosild T.P., Castronovo S., Healy J., Miller S., Pliotas C., Rasmussen T., Bartlett W., Conway S.J., Booth I.R. (2010) Mechanism of ligand-gated potassium efflux in bacterial pathogens. *Proceedings of the National Academy of Sciences of the United States of America* 107: 19784-19789

Rothschild L.J., Mancinelli R.L. (2001) Life in extreme environments. *Nature* 409: 1092-1101

Rozov A., Khusainov I., El Omari K., Duman R., Mykhaylyk V., Yusupov M., Westhof E., Wagner A., Yusupova G. (2019) Importance of potassium ions for ribosome structure and function revealed by long-wavelength X-ray diffraction. *Nature communications* 10: 2519

Rübenhagen R., Morbach S., Krämer R. (2001) The osmoreactive betaine carrier BetP from *Corynebacterium glutamicum* is a sensor for cytoplasmic K^+. *The EMBO journal* 20: 5412-5420

Rübenhagen R., Ronsch H., Jung H., Kramer R., Morbach S. (2000) Osmosensor and osmoregulator properties of the betaine carrier BetP from *Corynebacterium glutamicum* in proteoliposomes. *The Journal of biological chemistry* 275: 735-741

Rubio F., Gassmann W., Schroeder J.I. (1995) Sodium-driven potassium uptake by the plant potassium transporter HKT1 and mutations conferring salt tolerance. *Science* 270: 1660-1663

Russell N.J. (1990) Cold adaptation of microorganisms. *Philos Trans R Soc Lond B Biol Sci* 326: 595-608, discussion 608-511

Sambrook J., Fritsch, E. F. & Maniatis, T. (1989) Molecular cloning: A laboratory manual.

Sardessai Y., Bhosle S. (2002) Tolerance of bacteria to organic solvents. *Research in Microbiology* 153: 263-268

Sardessai Y., Bhosle S. (2003) Isolation of an organic-solvent-tolerant cholesterol-transforming *Bacillus* species, BC1, from coastal sediment. *Marine biotechnology* 5: 116-118

Sato Y., Nanatani K., Hamamoto S., Shimizu M., Takahashi M., Tabuchi-Kobayashi M., Mizutani A., Schroeder J.I., Souma S., Uozumi N. (2014) Defining membrane spanning domains and crucial membrane-localized acidic amino acid residues for K^+ transport of a Kup/HAK/KT-type *Escherichia coli* potassium transporter. *J Biochem* 155: 315-323

Schachtman D.P., Schroeder J.I. (1994) Structure and transport mechanism of a high-affinity potassium uptake transporter from higher plants. *Nature* 370: 655-658

Scheres S.H. (2012) RELION: implementation of a Bayesian approach to cryo-EM structure determination. *Journal of structural biology* 180: 519-530

Schleyer M., Bakker E.P. (1993) Nucleotide sequence and 3'-end deletion studies indicate that the K^+-uptake protein kup from *Escherichia coli* is composed of a hydrophobic core linked to a large and partially essential hydrophilic C terminus. *Journal of bacteriology* 175: 6925-6931

Schlösser A., Kluttig S., Hamann A., Bakker E.P. (1991) Subcloning, nucleotide sequence, and expression of trkG, a gene that encodes an integral membrane protein involved in potassium uptake via the Trk system of *Escherichia coli*. *Journal of bacteriology* 173: 3170-3176

Schlösser A., Meldorf M., Stumpe S., Bakker E.P., Epstein W. (1995) TrkH and its homolog, TrkG, determine the specificity and kinetics of cation transport by the Trk system of *Escherichia coli*. *Journal of bacteriology* 177: 1908-1910

Schrecker M. (2018) Exploring the structural and mechanistic basis of K^+ translocation by the KtrAB system Institute of Biochemistry, Johann Wolfgang Goethe-University Frankfurt,

Schrecker M., Wunnicke D., Hänelt I. (2019) How RCK domains regulate gating of K^+ channels. *Biological chemistry* 400: 1303-1322

Schrempf H., Schmidt O., Kummerlen R., Hinnah S., Müller D., Betzler M., Steinkamp T., Wagner R. (1995) A prokaryotic potassium ion channel with two predicted transmembrane segments from *Streptomyces lividans*. *The EMBO journal* 14: 5170-5178

Schultz S.G., Solomon A.K .(1961) Cation transport in *Escherichia coli*. Intracellular Na^+ and K^+ concentrations and net cation movement. *The Journal of general physiology* 45: 355-369

Sikkema H.R., van den Noort M., Rheinberger J., de Boer M., Krepel S.T., Schuurman-Wolters G.K., Paulino C., Poolman B. (2020) Gating by ionic strength and safety check by cyclic-di-AMP in the ABC transporter OpuA. *Science advances* 6

Silberberg J.M., Corey R.A., Hielkema L., Stock C., Stansfeld P.J., Paulino C., Hänelt I. (2021) Deciphering ion transport and ATPase coupling in the intersubunit tunnel of KdpFABC. *Nature communications* 12: 5098

Simons K., Ikonen E. (1997) Functional rafts in cell membranes. *Nature* 387: 569-572

Sleator R.D., Hill C. (2002) Bacterial osmoadaptation: the role of osmolytes in bacterial stress and virulence. *FEMS microbiology reviews* 26: 49-71

Smart O.S., Neduvelil J.G., Wang X., Wallace B.A., Sansom M.S. (1996) HOLE: a program for the analysis of the pore dimensions of ion channel structural models. *J Mol Graph* 14: 354-360, 376

Smith K., Hunter I.S. (2008) Efficacy of common hospital biocides with biofilms of multi-drug resistant clinical isolates. *Journal of Medical Microbiology* 57: 966-973

Sohlenkamp C. (2017) Membrane Homeostasis in Bacteria upon pH Challenge. In *Biogenesis of Fatty Acids, Lipids and Membranes*, Geiger O (ed), pp 1-13. Cham: Springer International Publishing

Sohlenkamp C., Geiger O. (2016) Bacterial membrane lipids: diversity in structures and pathways. *FEMS microbiology reviews* 40: 133-159

Stautz J. (2016) Regulation and organistation of KtrAB in the lipid bilayer in vivo and in vitro. Institute of Biochemistry Johann Wolfgang Goethe University-Frankfurt

Stautz J., Hellmich Y., Fuss M.F., Silberberg J.M., Devlin J.R., Stockbridge R.B., Hänelt I. (2021) Molecular Mechanisms for Bacterial Potassium Homeostasis. *Journal of molecular biology* 433: 166968

Stefan E., Hofmann S., Tampe R. (2020) A single power stroke by ATP binding drives substrate translocation in a heterodimeric ABC transporter. *eLife* 9

Stewart P.S., William Costerton J. (2001) Antibiotic resistance of bacteria in biofilms. *The Lancet* 358: 135-138

Stock C., Hielkema L., Tascon I., Wunnicke D., Oostergetel G.T., Azkargorta M., Paulino C., Hänelt I. (2018) Cryo-EM structures of KdpFABC suggest a K^+ transport mechanism via two inter-subunit half-channels. *Nature communications* 9: 4971

Strahl H., Burmann F., Hamoen L.W. (2014) The actin homologue MreB organizes the bacterial cell membrane. *Nature communications* 5: 3442

Strandberg E. (2018) Solid-State NMR for Studying Peptide Structures and Peptide-Lipid Interactions in Membranes. In *Modern Magnetic Resonance*, Webb GA (ed), pp 1985-1996. Springer

Stülke J., Krüger L. (2020) Cyclic di-AMP signaling in bacteria. *Annual review of microbiology* 74: 159-179

Stumpe S., Bakker E.P. (1997) Requirement of a large K^+-uptake capacity and of extracytoplasmic protease activity for protamine resistance of *Escherichia coli*. *Archives of microbiology* 167: 126-136

Sukharev S.I., Blount P., Martinac B., Blattner F.R., Kung C. (1994) A large-conductance mechanosensitive channel in *E. coli* encoded by mscL alone. *Nature* 368: 265-268

Szollosi A., Vieira-Pires R.S., Teixeira-Duarte C.M., Rocha R., Morais-Cabral J.H. (2016) Dissecting the Molecular Mechanism of Nucleotide-Dependent Activation of the KtrAB K^+ Transporter. *PLoS biology* 14: e1002356

Takase K., Kakinuma S., Yamato I., Konishi K., Igarashi K., Kakinuma Y. (1994) Sequencing and characterization of the ntp gene cluster for vacuolar-type Na^+-translocating ATPase of *Enterococcus hirae*. *The Journal of biological chemistry* 269: 11037-11044

Tascon I., Sousa J.S., Corey R.A., Mills D.J., Griwatz D., Aumüller N., Mikušević V., Stansfeld P.J., Vonck J., Hänelt I. (2020) Structural basis of proton-coupled potassium transport in the KUP family. *Nature communications* 11: 626

Teixeira-Duarte C.M., Fonseca F., Morais-Cabral J.H. (2019) Activation of a nucleotide-dependent RCK domain requires binding of a cation cofactor to a conserved site. *eLife* 8

Terwilliger T.C., Sobolev O.V., Afonine .PV., Adams P.D., Read R.J. (2020) Density modification of cryo-EM maps. *Acta crystallographica Section D, Structural biology* 76: 912-925

Tholema N., Bakker E.P., Suzuki A., Nakamura T. (1999) Change to alanine of one out of four selectivity filter glycines in KtrB causes a two orders of magnitude decrease in the affinities for both K^+ and Na^+ of the Na^+ dependent K^+ uptake system KtrAB from *Vibrio alginolyticus*. *FEBS letters* 450: 217-220

Tholema N., Vor der Bruggen M., Maser P., Nakamura T., Schroeder J.I., Kobayashi H., Uozumi N., Bakker E.P. (2005) All four putative selectivity filter glycine residues in KtrB are essential for high affinity and selective K^+ uptake by the KtrAB system from *Vibrio alginolyticus*. *The Journal of biological chemistry* 280: 41146-41154

Thompson A.N., Posson D.J., Parsa P.V., Nimigean .CM. (2008) Molecular mechanism of pH sensing in KcsA potassium channels. *Proceedings of the National Academy of Sciences* 105: 6900-6905

Torres S., Pandey A., Castro G.R. (2011) Organic solvent adaptation of Gram positive bacteria: Applications and biotechnological potentials. *Biotechnology Advances* 29: 442-452

Trchounian A., Kobayashi H. (1999) Kup is the major K^+ uptake system in *Escherichia coli* upon hyper-osmotic stress at a low pH. *FEBS letters* 447: 144-148

Tsatskis Y., Khambati J., Dobson M., Bogdanov M., Dowhan W., Wood J.M. (2005) The Osmotic Activation of Transporter ProP Is Tuned by Both Its C-terminal Coiled-coil and Osmotically Induced Changes in Phospholipid Composition. *Journal of Biological Chemistry* 280: 41387-41394

Tuson H.H., Weibel D.B. (2013) Bacteria–surface interactions. *Soft matter* 9: 4368-4380

Uozumi N., Kim E.J., Rubio F., Yamaguchi T., Muto S., Tsuboi A., Bakker E.P., Nakamura T., Schroeder J.I. (2000) The Arabidopsis HKT1 gene homolog mediates inward Na^+ currents in xenopus laevis oocytes and Na^+ uptake in *Saccharomyces cerevisiae*. *Plant physiology* 122: 1249-1259

Uysal S., Vásquez V., Tereshko V., Esaki K., Fellouse F.A., Sidhu S.S., Koide S., Perozo E., Kossiakoff A. (2009) Crystal structure of full-length KcsA in its closed conformation. *Proceedings of the National Academy of Sciences* 106: 6644-6649

Vagner V., Dervyn E., Ehrlich S.D. (1998) A vector for systematic gene inactivation in *Bacillus subtilis*. *Microbiology* 144 (Pt 11): 3097-3104

Ventosa A., Nieto J.J., Oren A. (1998) Biology of moderately halophilic aerobic bacteria. *Microbiol Mol Biol R* 62: 504

Vieira-Pires R.S,. Szollosi A., Morais-Cabral J.H. (2013) The structure of the KtrAB potassium transporter. *Nature* 496: 323-328

von Heijne G. (1989) Control of topology and mode of assembly of a polytopic membrane protein by positively charged residues. *Nature* 341: 456-458

Vonck J., Mills D.J. (2017) Advances in high-resolution cryo-EM of oligomeric enzymes. *Current opinion in structural biology* 46: 48-54

Wagner T., Merino F., Stabrin M., Moriya T., Antoni C., Apelbaum A., Hagel P., Sitsel O., Raisch T., Prumbaum D., Quentin D., Roderer D., Tacke S., Siebolds B., Schubert E., Shaikh T.R., Lill P., Gatsogiannis C., Raunser S. (2019) SPHIRE-crYOLO is a fast and accurate fully automated particle picker for cryo-EM. *Communications biology* 2: 218

Wang Q,. Cen Z., Zhao J. (2015) The Survival Mechanisms of Thermophiles at High Temperatures: An Angle of Omics. *Physiology* 30: 97-106

Wierenga R.K., Terpstra P., Hol W.G.J. (1986) Prediction of the occurrence of the ADP-binding βαβ-fold in proteins, using an amino acid sequence fingerprint. *Journal of molecular biology* 187: 101-107

Wilson M.E., Maksaev G., Haswell E.S. (2013) MscS-like mechanosensitive channels in plants and microbes. *Biochemistry* 52: 5708-5722

Wood J.M. (1999) Osmosensing by bacteria: signals and membrane-based sensors. *Microbiology and molecular biology reviews : MMBR* 63: 230-262

Wu Y., Yeh F.L., Mao F., Chapman E.R. (2009) Biophysical characterization of styryl dye-membrane interactions. *Biophysical journal* 97: 101-109

Xu Y., McDermott A.E. (2019) Inactivation in the potassium channel KcsA. *Journal of structural biology: X* 3: 100009

Ye S., Li Y., Chen L., Jiang Y. (2006) Crystal structures of a ligand-free MthK gating ring: insights into the ligand gating mechanism of K^+ channels. *Cell* 126: 1161-1173

Yin W., Wang Y., Liu L., He J. (2019) Biofilms: The Microbial "Protective Clothing" in Extreme Environments. *International journal of molecular sciences* 20: 3423

Zakharyan E., Trchounian A. (2001) K^+ influx by Kup in *Escherichia coli* is accompanied by a decrease in H^+ efflux. *FEMS microbiology letters* 204: 61-64

Zhang H., Pan Y., Hu L., Hudson M.A., Hofstetter K.S., Xu Z., Rong M., Wang Z., Prasad B.V.V., Lockless S.W., Chiu W., Zhou M. (2020) TrkA undergoes a tetramer-to-dimer conversion to open TrkH which enables changes in membrane potential. *Nature communications* 11: 547

Zhang Y., Daday C., Gu R.X., Cox C.D., Martinac B., de Groot B.L., Walz T. (2021) Visualization of the mechanosensitive ion channel MscS under membrane tension. *Nature* 590: 509-514

Zheng S.Q., Palovcak E., Armache J.P., Verba K.A., Cheng Y., Agard D.A. (2017) MotionCor2: anisotropic correction of beam-induced motion for improved cryo-electron microscopy. *Nat Methods* 14: 331-332

Zhou Y., Morais-Cabral J.H., Kaufman A., MacKinnon R. (2001) Chemistry of ion coordination and hydration revealed by a K^+ channel-Fab complex at 2.0 Å resolution. *Nature* 414: 43-48

Zivanov J., Nakane T., Forsberg B., Kimanius D., Hagen W.J.H., Lindahl E., Scheres S.H.W. (2018) RELION-3: new tools for automated high-resolution cryo-EM structure determination. *bioRxiv*

9 Abbreviations

Abbreviation	Meaning
ABC	ATP-binding cassette
ACMA	9-Amino-6-Chloro-2-Methoxyacridine
ADP	Adenosine diphosphate
AMP	Adenosine monophosphate
AMPPCP	Adenosine-5'-[(β,γ)-methyleno]triphosphate
amp^R	Ampicillin resistance
APS	Ammonium persulfate
ATP	Adenosine triphosphate
B. subtilis	*Bacillus subtilis*
BetP	Glycine betaine transporter
bla^R	β-lactam resistance
BN	Blue native
***Bs*KtrAB**	KtrAB from *Bacillus subtilis*
Ca^{2+}	Calcium ion
CBS	Cystathionine-β-synthase
CCCP	Carbonyl cyanide-m-chlorophenylhydrazone
c-di-AMP	Cyclic di-adenosine monophosphate
CL	Cardiolipin
CPM	7-Diethylamino- 3-(4-maleimidophenyl)-4-methylcoumarin
Cryo-EM	Cryogenic electron microscopy
CTF	Contrast transfer function
CV	Column volume
ddH_2O	Double-distilled water
DDM	n-Dodecyl β-maltoside
DEER	Double electron-electron resonance
DMSO	Dimethylsulfoxid
DNA	deoxyribonucleic acid
dNTPs	Desoxynucleotide-5-triphosphate
DSF	Differential scanning fluorimetry
DTT	Diethiothreitol
E. coli	*Escherichia coli*
ECPL	*E. coli* polar lipids
EDTA	Ethylenediaminetetraacetic acid
EM	Electron microscopy
EPR	Electron paramagnetic resonance
EPS	Extracellular polymeric substances
erm^R	Erythromycin resistance

ETC	Electron transport chain
FM4-64	N-(3-Triethylammoniumpropyl)-4-(6-(4-(Diethylamino) Phenyl) Hexatrienyl) Pyridinium Dibromide
FT	Flowthrough
FX	Fragment exchange
GL	Glycolipids
GLP	Glycophospholipids
GsuK	Channel of *Geobacter sulfurreducens*
H^+	Proton
HOP	Hopanoids
HTH	Helix-turn-helix
IC_{50}	Half maximal inhibitory concentration
IPTG	Isopropyl-beta-D-thiogalactopyranoside
ITC	Isothermal titration calorimetry
K^+	Potassium ion
KcsA	K^+ channel of *Streptomyces lividans* A
K_D	Equilibrium dissociation constant
KdpFABC	K^+ dependent P-type ATPase (FABC)
Kef	K^+ efflux system
KhtSTU	K^+/H^+ transport STU
KimA	K^+ importer A
K_m	Michaelis-Menten constant
KtrAB/CD	K^+ transporter AB/CD
Kup	K^+ uptake
LeutT	Leucine transporter
Li^+	Lithium ion
LILBID	Laser-induced liquid bead ion desorption
M. thermoautotrophicus	*Methanothermobacter thermoautotrophicum*
MCS	Multiple cloning site
MD	Molecular dynamics
MDR	Multi-drug resistant
MeO-PEG-mal	Methoxypolyethylene glycol maleimides
Mg^{2+}	Magnesium ion
MreB	Cell shape-determining protein
MS	Mass spectroscopy
MscL	Large-conductance mechanosensitive channel
MscM	Miniconductance mechanosensitive channel
MscS	Small-conductance mechanosensitive channel
msfGFP	Monomeric superfolder green fluorescent protein
MSP	Membrane scaffold protein
MthK	K^+ channel of *Methanobacterium thermoautotrophicum*

MTS (SL)	(1-Oxyl-2,2,5,5-tetramethylpyrroline-3-methyl) methanethiosulfonate (spin label)
MWCO	Molecular weight cut-off
Na^+	Sodium ion
NAD(H)	Nicotinamide adenine dinucleotide (hydrogen)
NBD	Nucleotide binding domain
Ni^{2+}-NTA	$Nickel^{2+}$-charged nitrilotriacetic acid
OD	Optical density
OL	Ornithine lipids
OpuA	Proline/betaine transporter
P	Pore
PA	Phosphatidic acid
PAGE	Polyacrylamide gel electrophoresis
PCR	Polymerase chain reaction
PE	Phosphatidylethanolamine
PG	Phosphatidylglycerol
pmf	Proton motif force
PMSF	Phenylmethylsulfonyl
P_{open}	Open probability
ProP	Glycine betaine/carnitine/choline ABC transporter
PS	Phosphatidylserine
PVT	Polyvinyl toluene
RCK	Regulator of conductance of K^+
RIF	Regions with increased fluidity
RNA	Ribonucleic acid
Rpm	Revolutions per minute
SDS	Sodium dodecylsulfate
SEC	Size exclusion chromatography
SF	Selectivity filter
SKT	Superfamily of potassium transporter
SL	Sphingolipids
SMA	Styrene-maleic acid
SPA	Scintillation proximity assay
***spec*^{R}**	Spectinomycin resistance
TAE	Tris-Acetat-EDTA
TCA	Trichloroacetic acid
TEMED	N, N, N′, N′-tetramethylethylendiamin
tet^R	Tetracyclin resistance
TLC	Thin layer chromatography
TM	Transmembrane
TrkAH/G/1,2	Transport of K^+ (AH)
UV	Ultraviolet

V. alginolyticus	*Vibrio alginolyticus*
***Va*KtrAB**	KtrAB from *Vibrio alginolyticus*
$\mathbf{V_{max}}$	Maximal uptake velocity
VSD	Voltage sensor domain
$\mathbf{Zn^{2+}}$	Zinc ion
ΔΨ	Membrane potential